Experimental Protocols and Analysis Methods for Real-Time Assessment of Cardiac Metabolism

Mariotti, Erika

Awarding institution:
King's College London

Experimental Protocols and Analysis Methods for Real-Time Assessment of Cardiac Metabolism

Erika Mariotti

A thesis submitted to the University of London for the degree of

Doctor of Philosophy in Imaging Sciences and Biomedical Engineering

Division of Imaging Sciences and Medical Engineering, King's College, St. Thomas's Hospital, London.

February 2014

Declaration

I, Erika Mariotti, declare that the PhD thesis entitled *“Experimental Protocols and Analysis Methods for Real-Time Assessment of Cardiac Metabolism*” is no more than 100,000 words in length including quotes and exclusive of tables, figures, appendices, bibliography, references and footnotes. This thesis contains no material that has been submitted previously, in whole or in part, for the award of any other academic degree or diploma. Except where otherwise indicated, this thesis is my own work.

Abstract

Cardiovascular disease remains the primary cause of death worldwide. Medical imaging plays a critical and increasing role in both its diagnosis and characterisation. Recent advances in hyperpolarised ^{13}C Magnetic Resonance (MR) allow, for example, imaging an injected molecule and its downstream metabolites to uncover biochemical changes in the myocardium. On the other hand, radionuclide imaging using Positron Emission Tomography (PET) and Single Photon Emission Computed Tomography (SPECT) has significantly higher sensitivity than MR, but the signals from injected tracers and their metabolites are indistinguishable. All these imaging modalities are able to produce dynamic data containing information of the kinetics of their respective tracers. In order to relate the measured signal or activity to the underlying physiological or biochemical processes mathematical models have to be used.

In this thesis, experimental protocols have been developed and semi-quantitative and quantitative methods have been evaluated for the analysis of hyperpolarised ^{13}C dynamic time-series and time-activity curves of PET tracers acquired *ex vivo* from Langendorff perfused rat hearts. A number of compartmental models were explored to fit *in vitro* and *ex vivo* hyperpolarised ^{13}C time-series acquired for pyruvate and its downstream metabolites to derive apparent rates of the enzymatic reactions involved in pyruvate metabolic pathways. Compartmental modelling was also used in combination with Monte Carlo simulations to explore the detection limits of transmural cardiac ischemia

in vivo in small rodents using hyperpolarised ^{13}C spectroscopic imaging. The feasibility of using a model free maximum entropy/nonlinear least square method (MEM/NLS) for the kinetic analysis of hyperpolarised ^{13}C dynamic data was explored in this thesis for the first time and validated using Monte Carlo simulations and experimental hyperpolarised ^{13}C *in vitro* time-series. Finally, the feasibility of extending the analysis methods validated for *in vivo* PET experiments (spectral-based algorithm, Patlak graphical plot and the semi-quantitative index RATIO) to the kinetic analysis of time-activity curves of PET tracers acquired *ex vivo* was also assessed in this thesis.

Acknowledgements

The first person I want to thank is my first PhD supervisor Dr. Thomas Eykyn. Tom is one of the most helpful people I have ever met in my life. I have walked into his office a countless number of times and he was ALWAYS available for a discussion. I want to thank him for giving me the opportunity to pursue my PhD, for guiding me throughout my project, for being patient during some difficult moments and for understanding my English even when it was not even clear to me.

Another special thanks goes to my second PhD supervisor Dr. Richard Southworth. Thank you for your guidance and your support which has always motivated me to do better. I would like also to thank you for consuming your index finger in order to make my paper one of the most downloaded in the journal and for teaching me how to say "lipophilicity" with the help of a pint or two.

I really think I was very lucky student in having two supervisors as you two and I will be always grateful to you for contributing to make me the scientist and person that I am now. GRAZIE!

A special thanks also goes to Prof. Phil Blower who always supported me.

The realisation of this PhD thesis would not have been possible without the help and collaboration of all the members of my group. Thank you very much Dr. Maxwell Handley and Dr. Rodolfo Medina for helping me in the lab when things were too "screaming" for me and thank you for our interesting conversations in front of a beer. Thank you Zaitul for our chats, your smile and enthusiasm often have made my day. Last but not least thank you very much to my soon to be

Doctor Miss Diamond Fiona. You have been not just a colleague for me but a faithful friend who helped me when everything was going wrong.

We have been a pretty cool group for the last four years. I will miss you all guys.

Thank you very much to Dr. Joel Dunn and Dr. Mattia Veronese for your help in developing the analysis methods used in this thesis. It was a pleasure to work with you two and I hope there will be the possibility to collaborate again in the future.

A big thanks goes to Prof. Sebastian Kozerke who allowed me to spend three months in his lab in Zurich. It was a great experience from both my professional and personal growth and allowed me to work with Dr. Kilian Weiss. Kilian immensely helped me during the months I spent in Zurich and for this reason he deserves a special thanks. He is a great scientist and a great friend and I really hope there will be the possibility to work together again one day.

Thank you to my friends Davide and Adelaide for supporting me throughout my PhD. I will miss our Italian gossip at lunch time. You have to keep me updated!!

Thank you to all the other KCL people which have been part of my daily life for the last four years. Thank you Jennifer (or Dr. Dr. Dr. Dr. Williams??) for all the laughs and glasses of wine we had together, thank you David Thakor for all your help with the lab and please remember that I have eaten the radioactive form. It was pretty good actually. Thank you to Karen & Karen for our girly chats in the lab. Thanks Claudia for your advices and all the nice dinners out.

A special thanks also goes to all my friends that have been supported me throughout my PhD. Thank you to my lifelong friends Flavia and Anna Chiara for always being there. Thank you to my female other half Francesca without

you it would not be the same. Thank you to Amalia who helped me so many times that I have lost count and to Elisa for our chats.

An enormous thanks goes to my mum, dad and granny. There are no words to describe how grateful I am to you for everything you have done for me, for helping me in difficult times and celebrating with me all my little achievements.

My PhD was the most beautiful experience of my life not only for the many things I learned but also because it allowed me to meet the person who has completely changed my life: my husband Tobias. Mo, thank you for making my life wonderful and full of love and thank you for being very very very close to me during the writing of this Encyclopedia (as you call it).

List of Contents

List of Figures

Chapter 1

Chapter 2

Chapter 3

Chapter 4

Chapter 5

Chapter 6

Chapter 7

List of Tables

List of Abbreviations

ADP : adenosine diphosphate

ALT : alanine transaminase

ATP : adenosine triphosphate

AUC : area under the curve

CA : carbonic anhydrase

CAD : coronary artery disease

CAT : carnitine translocase

CK : creatine kinase

CPS : counts per second

CPT : carnitine palmitoyltransferase

Cr : creatine

DCE : dynamic contrast enhancement

DNP : dynamic nuclear polarisation

ECG : electrocardiography

EM : electromagnetic

EPSI : echo planar spectroscopic imaging

ESR : electron spin resonance

ETC : electron transport chain

FACS : fatty acyl-CoA synthase

FDG : fluorodeoxyglucose

FUM : fumarase

GLUT : glucose transporter

LCE : late contrast enhancement

LDH : lactate dehydrogenase

LVDEP : left ventricle end diastolic pressure

LVDP : left ventricle develop pressure

MEM : maximum entropy method

MI : myocardial ischemia

MR : magnetic resonance

MRI : magnetic resonance imaging

MRS : magnetic resonance spectroscopy

MRSI : magnetic resonance spectroscopic imaging

NA : normalised activity

NLS : nonlinear least square

NLSA : nonlinear spectral analysis

ns : number of spectra

P : pressure

PC : pyruvate carboxylase

PCr : phosphocreatine

PDH : pyruvate dehydrogenase

PET : positron emission tomography

PHIP : para-hydrogen induced polarisation

Pi : inorganic phosphate

ROI : region of interest

RF : radiofrequency

SA : spectral analysis

SNR : signal-to-noise ratio

SPECT : single photon emission computed tomography

SUV : standard uptake value

T : temperature

TE : echo time

TR : repetition time

TSP : trimethylsilyl propionate

T_{ss} : solid-state build-up time constant

VTI : variable temperature insert

ω_e : Larmor frequency of carbon 13

ω_e : Larmor frequency of electrons

Chapter 1 : Introduction

1.1 Aims

This thesis aims at the development of acquisition protocols and analysis methods for real-time assessment of cardiac metabolism using molecular imaging in Langendorff perfused rat hearts.

For many years imaging techniques such as positron emission tomography (PET), single-photon emission computed tomography (SPECT), magnetic resonance imaging (MRI) and ultrasound were almost exclusively used to obtain anatomical and physiological information of the heart (Saraste et al. 2009). Since its introduction in the early 1990's, molecular imaging has greatly improved our understanding of the pathogenesis of many cardiac diseases as well as illuminating on new treatment targets by allowing the imaging of biological processes that take place at cellular and subcellular levels in the myocardium (Massoud and Gambhir 2003; Osborn and Jaffer 2013).

The Langendorff perfused heart has been the model of reference in cardiac research for many years and greatly contributed to the understanding of cardiac physiology. Section 1.2 presents a comparison between this experimental model and the physiological perfusion of the heart. In this thesis Langendorff

perfused studies were carried out both in healthy and hypoxic/ischemic hearts. A definition of cardiac hypoxia and ischemia is presented in Section 1.3.

In order to understand the importance of molecular imaging techniques able to measure cardiac metabolism in real-time for the early assessment of cardiac diseases, the principle metabolic pathways which contribute to the production of energy necessary for the contraction of the heart in physiological and pathophysiological conditions are described in Section 1.4.

An overview of the most commonly used imaging modalities in cardiology is introduced in Section 1.5. Many imaging modalities are able to produce dynamic data representing the evolution of the measured variable over the time. In order to derive quantitative or semi-quantitative information on the phenomena observed dynamic data can be analysed using several different approaches. An overview of the most common methods used for the analysis of cardiac dynamic data is presented in Section 1.6. In Section 1.7 the objectives of this thesis are introduced and the structure of this thesis is presented in Section 1.8.

1.2 Cardiac perfusion

1.2.1 Physiological Perfusion

The heart together with the complex system of arteries and veins plays a fundamental role in the distribution of blood and nutrients to the rest of the body. During the cardiac cycle, poorly oxygenated blood from the systemic circulation

is delivered to the right atrium through the inferior and superior vena cava. The contraction of the right atrium facilitates the flow of the blood into the right ventricle that once filled pumps the blood into the pulmonary artery that delivers the blood to the lungs, where it is oxygenated. Blood returns to the left atrium by the pulmonary veins and enters the left ventricle by passing through the mitral valve. The left ventricle ejects the oxygenated blood into the aorta that delivers it to the rest of the body. The cardiac muscle receives the oxygen and nutrients necessary for its survival, through the coronary arteries which arise from the coronary ostia at the base of the aorta (Figure 1.1).

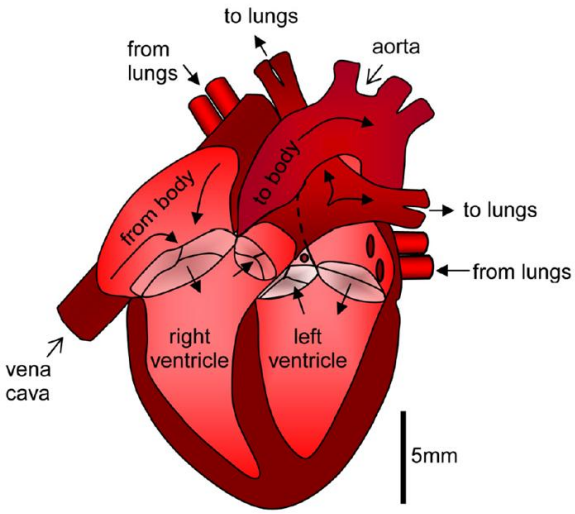

Figure 1.1: Schematic representation of the physiological perfusion of the heart. Deoxygenated blood is delivered to right atrium through the inferior and superior vena cava. The contraction of the right atrium facilitates the passage of the blood to the right ventricle that once filled pumps the blood into the pulmonary artery that delivers the blood to the lungs where it is oxygenated. The blood returns to the left atrium via the pulmonary veins and once in the left ventricle is ejected into the aorta that delivers it to the rest of the body. The cardiac muscle receives the oxygen and nutrients necessary for its survival, through the coronary arteries which arise from the coronary ostia at the base of the aorta. Adapted from reference (Hillman et al. 2007).

1.2.2 Langendorff Perfusion

The Langendorff perfusion method supplies nutrients to an isolated heart exploiting the same principles of its physiological perfusion. After removing the heart from the animal carefully cutting the major blood vessels, a cannula is inserted into the aorta and a buffer is perfused into the heart under physiological pressure (Figure 1.2). The pressure generated by the buffer in the aorta forces the aortic valve to remain closed and the myocardium is perfused through the coronary arteries as it would be physiologically.

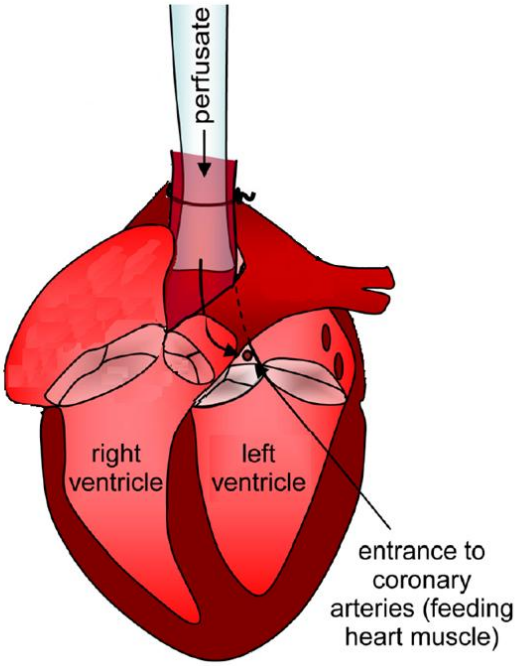

Figure 1.2: Schematic representation of a Langendorff perfusion. The isolated heart is perfused with a Krebs-Henseleit buffer that contains all the electrolytes and nutrients that the heart needs to survive. The Langendorff heart is perfused exclusively through the coronary arteries. Adapted from reference (Hillman et al. 2007).

The heart rate of an isolated rat heart is normally lower than that *in vivo*. For rat hearts, for example, it is 250-320beats/min rather than 350-400beats/min (Skrzypiec-Spring et al. 2007). Since it is empty, and not performing active work, the Langendorff perfused heart is a beating but not pumping heart and therefore it is a biologically relevant model for studying cardiac metabolism, but not cardiac mechanics.

1.3 Cardiac Hypoxia and Ischemia

Myocardial hypoxia is a pathophysiological condition defined as an imbalance between the myocardial oxygen demand and the amount of oxygen supplied to the heart. Similarly, myocardial ischemia is characterised by a disparity between the amount of blood delivered to the myocardium through the coronary arteries and that required for an efficient contraction of the heart. Ischemia not only causes hypoxia but also reduces the hydrostatic pressure and nutrient delivery. Nevertheless the reduction in blood flow causes an accumulation of the wastes from the cardiac metabolism that eventually damage myocytes.

Coronary artery disease (CAD) is the most common cause of hypoxia and/or ischemia. It is characterised by a reduction or cut off in the amount of blood normally delivered to the myocardium associated with the formation of atherosclerotic plaques within the wall of one or more coronary arteries. The prognosis associated with this type of cardiovascular disease is inversely proportional to the duration of the ischemic events. For this reason, diagnostic

tools for early detection of ischemic/hypoxic myocardium would extremely improve the mortality associated with CAD.

1.4 Cardiac Metabolism

Many if not all cardiac pathologies involve modulation or malfunction of key signalling pathways, leading to downstream changes in cellular metabolism and to physiological and mechanical dysfunction.

The heart is the only restless muscle in the human body. Its contraction requires energy in the form of adenosine triphosphate (ATP) which in normal conditions is continuously generated by glycolysis and fatty acid metabolism.

The production of energy in the heart can be divided in three key processes: (i) utilisation of a substrate such as free fatty acids and glucose from the diet, (ii) production of energy in the form of ATP by the mitochondrial respiratory chain and (iii) ATP transfer and utilisation (Neubauer 2007).

1.4.1 Fatty Acid Metabolism

The unbound fatty acids that cross the membrane of cardiac myocytes via specific membrane proteins originate primarily from plasma fatty acids bound to albumin or from fatty acids stored in the form of lipoproteins. In the cytosol free fatty acids are transformed to long chain fatty acyl-CoA by the action of fatty acid synthase (FAC S). Acyl-CoA is converted by carnitine palmitoyltransferase 1 (CPT1), located in the outer mitochondrial membrane, to long chain

acylcarnitine transported within the mitochondria by carnitine translocase (CAT) which exchange one molecule of acylcarnitine with one molecule of carnitine. Once within the mitochondrial space, acylcarnitine is transformed back to acyl-CoA by the enzyme CPT2 located in the inner mitochondrial membrane. At this point the long chain acyl-CoA enters the fatty acid β-oxidation pathway where in a cyclic process is broken down to generate acetyl-CoA which enters the citric acid cycle or tricarboxylic acid cycle (TCA). The NADH and $FADH_2$ produced during the fatty acid β-oxidation are transferred to the electron transport chain (ETC) where, in the presence of oxygen, are used to produce ATP (Figure 1.3).

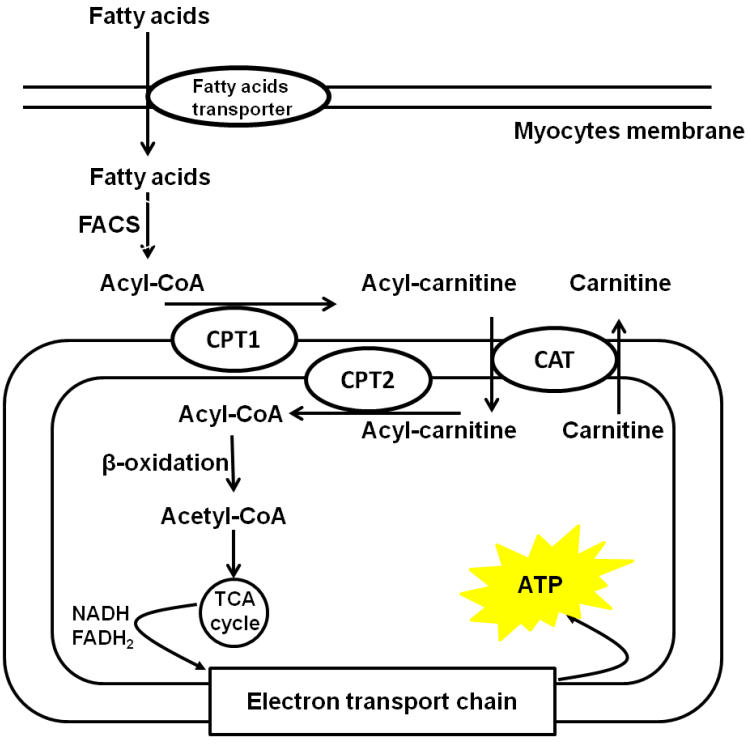

Figure 1.3: Schematic representation of the fatty acid metabolism. Adapted from reference (Lopaschuk et al. 2010).

1.4.2 Glucose Metabolism

Glucose is transported into the cell by specific glucose transporters (GLUTs) where through a cascade of ten enzyme-catalysed reactions (glycolysis), which take place in the cytosol, it is transformed to pyruvate whose fate depends on the level of myocardial oxygenation. When myocardial cells receive sufficient oxygen, pyruvate is transported into the mitochondria where it is converted by pyruvate dehydrogenase (PDH) to acetyl-CoA which subsequently enters the TCA cycle (aerobic glycolysis). During the metabolic conversion of glucose to pyruvate two molecules of ATP and one of NADH are produced. NADH is recycled back to NAD^+ by oxidation through the ETC with oxygen as the terminal electron acceptor (Figure 1.4).

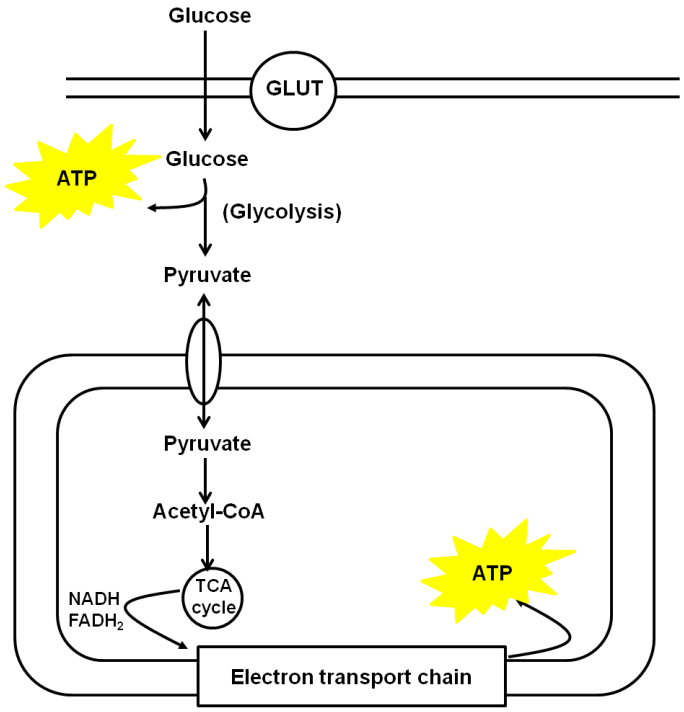

Figure 1.4: Schematic representation of glucose metabolism in presence of oxygen (aerobic glycolysis). Adapted from reference (Lopaschuk et al. 2010).

1.4.3 Tricarboxylic Acid Cycle

The acetyl-CoA produced through fatty acid metabolism or aerobic glycolysis enters the TCA cycle where through a series of chemical reactions is used to produce three molecules of NADH and one molecule of $FADH_2$ which are transferred to the ETC where in the presence of oxygen are used to produce ATP (Figure 1.5).

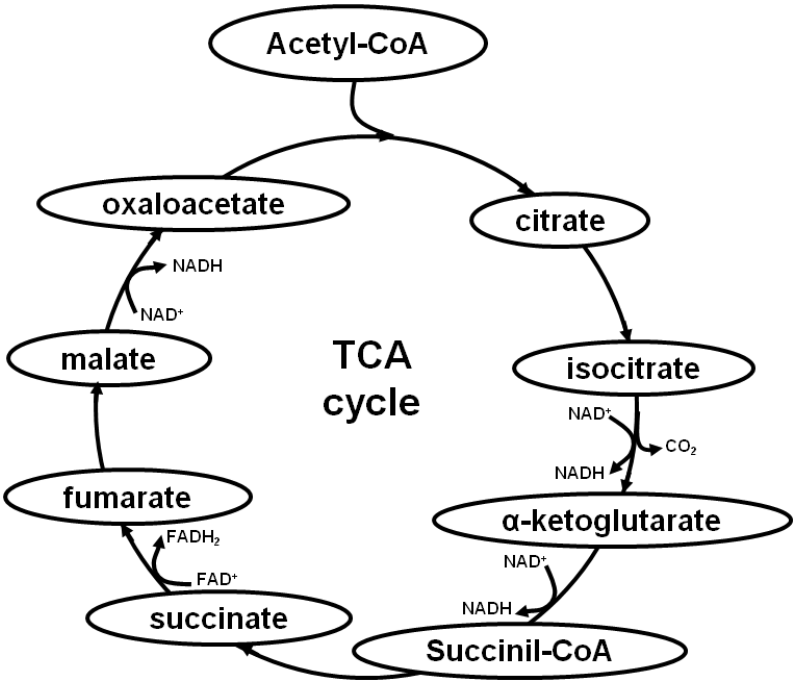

Figure 1.5: Schematic representation of the tricarboxylic acid (TCA) cycle. The acetyl-CoA produce through aerobic glycolysis and fatty acid metabolism is used through a series of chemical reaction to produce three molecules of NADH and one molecule of $FADH_2$ which are transferred to the ETC.

1.4.4 Electron Transport Chain

The ETC is formed by four inner membrane-associated enzyme complexes that are able to receive and transfer among them the electrons donated from the

NADH produced in both aerobic glycolysis and TCA cycle and from $FADH_2$ derived from the TCA cycle. The transfer of electrons between one complex of the ETC to another generates a proton gradient that drives ATP synthase which converts adenosine diphosphate (ADP) and inorganic phosphate to ATP. The process of electron transport is entirely dependent on molecular oxygen which acts as the terminal electron acceptor (Figure 1.6).

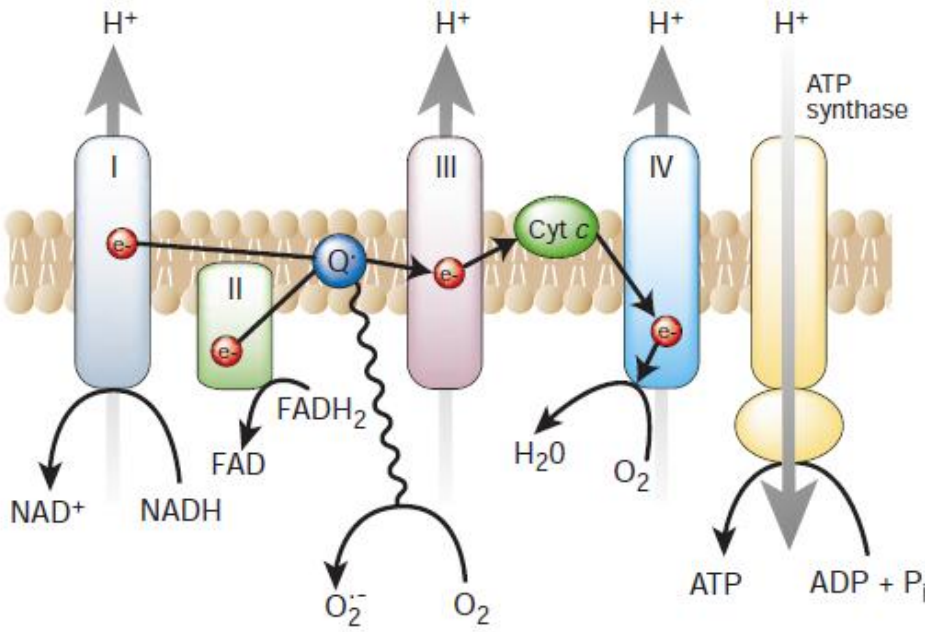

Figure 1.6: Representative scheme of the electron transport chain (ETC) where the electrons donated by NADH, produced during both aerobic glycolysis and fatty acid metabolism, and by $FADH_2$, derived from the fatty acid metabolism, are used to produce a proton gradients that drives the production of ATP through ATP synthase. Adapted from reference (Brownlee 2001).

1.4.5 Creatine Kinase Energy Shuttle

The creatine kinase energy shuttle has two main functions: (i) facilitate the transport of ATP produced in the mitochondria to the myofibrils where it is used for myocardial contraction and (ii) energy buffering. Creatine kinase (CK) is able to convert creatine (Cr) and ATP to phosphocreatine (PCr) and ADP. The creatine kinase energy shuttle therefore facilitates energy transfer by providing a parallel pathway to ATP diffusion. At the same time CK is able to maintain the cellular level of ATP constant by controlling the creatine-phosphocreatine exchange (Opie 1991).

1.4.6 Myocardial Metabolism in Hypoxia/Ischemia

In a healthy, well perfused and oxygenated heart approximately 50-70% of the ATP needed for the heart contraction is produced by fatty acid metabolism with only 30-50% of the ATP generated via glucose metabolism (Lopaschuk et al. 2010). The aerobic glycolysis is regulated by the citrate released by the TCA cycle, with the majority of glucose being converted to glycogen for storage. In this condition, the creatinine kinase energy shuttle maintains the cellular level of ATP constant by controlling the creatine-phosphocreatine exchange (Opie 1991).

As explained in Section 1.4.4, the ETC is able to produce ATP using the electrons donated by NADH and $FADH_2$ only in presence of O_2 that is the terminal electron acceptor. In conditions in which the level of oxygen is low due, for example, to the appearance of pathophysiological conditions such as

hypoxia or ischemia the production of ATP through the ETC is inhibited. The accumulation of intermediates of cardiac metabolism inhibits both aerobic glycolysis and fatty acid metabolism. In this condition the NADH produced during the conversion of glucose to pyruvate that is not transferred to the inactive ETC is used to convert pyruvate to lactate via lactate dehydrogenase (LDH) (anaerobic glycolysis)(Heather and Clarke 2011). The two molecules of ATP produced during the conversion of glucose to pyruvate are however not enough to meet the energy required to maintain cardiac contraction. In this condition of reduced availability of ATP, the creatinine kinase shuttle is initially able to maintain the level of ATP constant by converting PCr to Cr. When the oxygen deprivation is prolonged the reservoir of Cr are eventually depleted and the creatinine kinase shuttle is not longer able to maintain the level of ATP necessary for the contraction of the heart. The myocardial damage is therefore proportional to the length of the period of energy starvation.

1.5 Cardiovascular Imaging Techniques

1.5.1 Ultrasound

Ultrasound systems exploit acoustic energy characterised by a frequency between 1MHz and 20 MHz in order to form two-dimensional images of the plane scanned. Ultrasound can be used to obtain information on the anatomy and perfusion of the heart. Anatomical information is usually displayed on greyscale images where the intensity of the signal is proportional to the distance

of the structure detected to the source of ultrasound waves. Colour images (RGB, red-green-blue) are instead used to display the perfusion of the organ studied. Typically, positive (red) and negative (blue) values represent areas in which the detected structure is moving towards or away from the source of ultrasound waves, respectively. These two types of ultrasound images are called B-mode (brightness modulated) and colour Doppler images, respectively (Liang and Blomley 2003).

Ultrasound has been used by cardiologists for more than 50 years as a first screening test for the detection of many cardiac diseases mainly due to the fact that it is portable and relatively cheap (Wells 2001). It is able to acquire cardiac information in real time with a very high temporal resolution, typically in the order of milliseconds. The depth of penetration of the ultrasound waves as well as the contrast between different anatomical structures is however often limited due to the energy attenuation by the body tissue.

In order to improve contrast, in the last ten years many studies have been aimed at the development of ultrasound contrast agents (e.g. microbubbles) usually injected intravenously and targeted to specific biological structures of interest (Blomley et al. 2001).To date, the use of this technique is still limited to research studies but the possibility of using this approach in clinical routine for improving tissue contrast in ultrasounds images represent a concrete possibility in the near future.

1.5.2 Nuclear Imaging Techniques

SPECT and PET are able to image the distribution of a probe molecule labelled with γ-emitting or positron-emitting isotopes, respectively, in a region of interest (ROI) or in the whole body. A radioactive nuclide is characterised by an unstable nucleus that undergoes radioactive decay during which it emits γ-rays or subatomic particles such as protons.

In order to form SPECT images the γ-rays emitted during the radioactive decay of γ-emitting isotopes attached to specific biological molecules are detected using a rotating gamma camera. All emitted γ-rays are counted and therefore to evaluate the location of the radioactive decay a parallel-hole collimator fitted to the γ-camera is needed.

The radioisotopes used in PET imaging emit a positron during their radioactive decay. After travelling a few millimetres the emitted positron combines with a free electron forming a positronium. This system is unstable and the two particles annihilate each other to produce two gamma-ray photons which travel in nearly opposite direction with energy of 511 KeV each. The location of the photon emission in PET does not need a collimator but is performed electronically using pairs of collinearly aligned detectors arranged to form a ring and only simultaneous events are used for image reconstruction. In both imaging modalities angular information is used to form 2D images from which 3D views of the ROI can be reconstructed.

The most used γ-radionuclides in SPECT cardiac imaging are technetium (^{99m}Tc, half-life = 6.01h) and thallium (^{201}Tl, half-life = 73h), whereas fluorine

(^{18}F, half-life = 109.7min), carbon (^{11}C, half-life=20.3min), nitrogen (^{13}N, half-life = 9.9min) and oxygen (^{15}O, half-life = 122.2s) are commonly exploited in PET.

The radioisotopes used in SPECT are characterised by half-lives in general much longer than those of positron-emitting isotopes. This means that SPECT imaging does not required a cyclotron close to the scanner and that a biological process can be observed over many hours after the administration of the tracer while the time window in which it is possible to detect signal from PET radionuclides requires the installation of a cyclotron in the same hospital or in a nearby institute strongly limiting the applicability of this imaging modality.

SPECT tracers such as ^{99m}Tc -sestamibi, ^{99m}Tc-tetrofosmin are mainly used for the assessment of myocardial perfusion providing both diagnostic and prognostic information (Plesniak 2011). PET tracers such as ^{18}F-fluorodeoxyglucose (FDG), an analogue of glucose, and ^{13}N-ammonia ($^{13}NH_3$) are commonly used to assess myocardial glucose metabolism or perfusion, respectively.

Due to the importance of an early detection of CAD, in the last ten-fifteen years many research studies have been aimed at the development of novel imaging agents able to identify and characterise hypoxic myocardium. Two different classes of molecules have been proposed: the nitroimidazoles (e.g. [^{18}F]-FMISO) and the copper bis (thiosemicarbazone) complexes (e.g. ^{64}Cu-ATSM). These imaging agents are characterised by the common feature of being cleared rapidly from blood and non-target tissues and retained in hypoxic tissues (Handley et al. 2011; Handley et al. 2014).

Previous studies have also shown that using ^{11}C-labelled probes it is possible to measure a number of different metabolic pathways in the heart (Paans et al. 1985).

SPECT is characterised by a better spatial resolution (0.5mm – 2.0mm) than PET (1.0mm – 2.0mm) however due to the low geometric efficiencies (defined as the percentage of detected to emitted photon) of the collimator, PET is superior to SPECT with respect to sensitivity (two to three orders of magnitude). Additionally, due to the presence of a rotating γ-camera SPECT is characterised by a lower temporal resolution than PET (Rahmim and Zaidi 2008; Dobrucki and Sinusas 2010).

1.5.3 Magnetic Resonance Imaging and Spectroscopy

MR is an imaging modality based on the detection of the signal of nuclei possessing a non-zero spin, after the application of a radiofrequency (RF) pulse in presence of an external magnetic field. The basic physical principles of MR are presented in Chapter 2 in details.

In clinical practice MR imaging (MRI) is most often used to image the distribution of ^{1}H nuclei contained in water and fat which form approximately 60% of the human body weight. This imaging modality can provide a wide variety of anatomical and functional information. Cardiac CINE imaging, for example, is commonly used to derive functional information by assessing the motion of the heart in real time and detecting changes in the anatomical configuration over the cardiac cycle. From the analysis of such dynamic images

it is possible to quantitatively estimate the volume of the cardiac chambers, myocardial mass as well as ejection fraction which have a prognostic value for many cardiac diseases (Pennell et al. 2011). MRI contrast agents (e.g. gadolinium) are used to enhance the contrast between the different biological structures in the body. In late contrast enhancement (LCE) MRI the signal from ^{1}H is detected approximately 15min after an intravenous injection of a gadolinium solution (0.1mmol/kg body mass). The contrast agent is completely washed out from well perfused areas of the myocardium while it is retained in the interstitial space in fibrotic regions. Gadolinium makes the characteristic relaxation time of ^{1}H nuclei shorter and therefore it allows the localisation of scar tissue. In order to obtain a map of myocardial perfusion dynamic contrast enhancement (DCE) MR is used. In this case the ^{1}H MR signal is acquired soon after the injection of the gadolinium dose and complete or partial occlusions of the coronary artery tree can be detected.

CINE, LCE and DCE MRI give complementary information and they are for example used to establish the stage of the infracted heart in patients. A reduced perfusion (DCE), the formation of scar tissue (LCE) and a reduction in the injection fraction (CINE) are the pathological signs that appear with the progression of heart failure. Before the formation of fibrous tissue, a reduction of blood and nutrients supply due, for example, to the formation of atherosclerotic plaques in one or more coronary arteries causes pathophysiological alteration in the cardiac metabolism. Information on molecular processes at the cellular and subcellular level can be obtained by using MR spectroscopy (MRS). The detection of ^{31}P is for example used to characterise high energy phosphate

metabolism where Cr is phosphorylated to PCr by CK (Neubauer 2007). As explained in Section 1.4 many other metabolite pools participate in giving the heart the amount of energy it needs. Fatty acid and glucose metabolism, for example, play a very important rule in supplying energy to the heart. Many molecules involved in these metabolic pathways contain ^{12}C nuclei and it could therefore be possible to enrich these molecules with ^{13}C nuclei and detect cardiac metabolism in real time using MRS. From the practical point of view the real time assessment of cardiac metabolism using traditional ^{13}C MR spectroscopic is prohibited by the low natural abundance, sensitivity and concentration of ^{13}C nuclei.

1.5.4 Hyperpolarised Magnetic Resonance

As explained in more details in Chapter 2, for nuclei with spin I = ½ (e.g. ^{1}H, ^{13}C, ^{15}N) the MR signal is proportional to the difference in population between the two energy levels corresponding to the two configurations (parallel and antiparallel) that these nuclear spins can assume in the presence of an external magnetic field B_0. At room temperature, the difference in population between the two energy states is very small and a MR signal can be detected only if the concentration of the nucleus assessed is high. This is the case for ^{1}H contained in water but not of ^{13}C nuclei.

In order to increase the detectable MR signal of low natural abundance and concentration nuclei, such as ^{13}C, a number of different approaches able to temporally increase the difference in population between the two energy levels

that the spins can occupy in the presence of an external magnetic field have been proposed. *Spin exchange optical pumping*, *para-hydrogen induced polarisation* (PHIP) and *dynamic nuclear polarisation* (DNP) are able to enhance the characteristic polarisation of a specific nucleus by transferring the polarisation from the high polarised electrons or parahydrogen to the nucleus of interest. *Spin exchange optical pumping* has been used for enhancing the signal from noble gases such as ^{3}He and ^{129}Xe for the real time assessment of lung ventilation and perfusion (Fain et al. 2007). PHIP and DNP have both been used to enhance the MRS signal of nuclei such as ^{15}N and ^{13}C within metabolically relevant molecules by the order of tens of thousands (Ardenkjaer-Larsen et al. 2003) to facilitate the measurement of the kinetics of cardiac metabolic processes in healthy or diseased tissue previously inaccessible to MR.

Previous studies have shown that using hyperpolarised [1-$^{13}C_1$] pyruvate allows measurement of the activity of PDH *ex vivo* in the perfused rat heart (Merritt et al. 2007; Merritt et al. 2008) and *in vivo* under pathophysiological conditions such as diabetes and hypertrophy (Schroeder et al. 2008; Atherton et al. 2011). The TCA cycle has been assessed using hyperpolarised [2-$^{13}C_1$] pyruvate and a decrease of its intermediates, such as ^{13}C citrate and ^{13}C glutamate, has been detected in response to myocardial ischemia (Schroeder et al. 2010). PDH activity and TCA cycle have been also assessed simultaneously using hyperpolarised [1,2-$^{13}C_2$] pyruvate (Chen et al. 2012). Fatty acid metabolism has also been probed through the buffering of hyperpolarised [1-$^{13}C_1$] acetate with [1-$^{13}C_1$] acetylcarnitine in response to reperfusion after ischemia (Jensen et

al. 2009) or through the addition of water soluble fatty acids such as octanoate (Merritt et al. 2007).

While information from non-selective MRS is sufficient for estimating metabolic changes and pathologies with global effects, spatially resolved spectroscopy is needed to study local effects in the heart. MR spectroscopic imaging (MRSI) potentially provides the capacity to study local effects in the heart, allowing the characterisation of heterogeneous metabolic changes and pathologies such as found in ischemic heart disease (Southworth et al. 2002; Golman et al. 2008; Arai 2011). Experiments in both rodents and pigs have demonstrated that it is possible to image metabolic maps of the spatial distribution of $H^{13}CO_3^-$, [1-$^{13}C_1$] lactate and [1-$^{13}C_1$] alanine produced from the metabolic conversion of hyperpolarised [1-$^{13}C_1$] pyruvate via PDH, LDH and alanine transaminase (ALT), respectively (Rider and Tyler 2013).

MRSI of hyperpolarised probes poses additional challenges compared to that of more traditional thermally polarised ^1H MRSI. The rapidly decaying nature of hyperpolarisation to thermal equilibrium and the metabolic conversion by enzymatic reactions require fast spectroscopic imaging techniques. The hyperpolarised magnetisation needs to be traded between individual images and the number of dynamics in the imaging series. To preserve the magnetisation for all dynamics, a low number of signal excitations in combination with small flip angles are desired. At the same time sufficient SNR needs to be assured. A number of fast pulse sequences able to preserve the hyperpolarised for a sufficient duration have been proposed (Cunningham et al.

2007; Cunningham et al. 2008) and validated *in vivo* in pig hearts (Lau et al. 2010).

1.6 Analysis Methods for Dynamic Data

The dynamic data acquired using SPECT, PET and hyperpolarised MR have the common feature of containing information of the interaction between a detected probe and the biological system of interest. Quantitative and semi-quantitative parameters which describe biological phenomena can be derived using several analysis methods. A detailed description of the analysis methods exploited in this thesis is presented in Chapter 4.

The most common approach to the quantitative analysis of dynamic data is compartmental modelling (Godfrey 1982). Using this method the interaction of the injected probes with the tissue of interest is described with a number of compartments that interconvert at characteristic rates. Compartmental modelling has been, used to describe the dynamics of the PET tracer [^{18}F]-FDG in the human heart (Bertoldo et al. 1998), to quantify myocardial perfusion and capillary permeability after the injection of a bolus of gadolinium using DCE-MRI (Sourbron and Buckley 2012) as well as to characterise cardiac metabolism using hyperpolarised ^{13}C MR (Menichetti et al. 2012). Compartmental modelling requires *a priori* knowledge of the number of compartments involved in probe uptake and redistribution, and for this reason it is inadequate when new radiotracers or metabolic pathways are studied. In PET, linear and nonlinear spectral analysis (SA and NLSA) (Cunningham and Jones 1993; Turkheimer et

al. 1994; Bertoldo et al. 1998) are commonly used to derive the kinetic components which describe the dynamic data with only few *a priori* assumption on the type of interaction between the tracer and the biological system studied. Quantitative information is also derived from dynamic PET data using graphical methods (Sokoloff et al. 1977; Logan et al. 1990). This approach is easy to implement and does not require any *a priori* assumption on the number of compartments involved in the tracer uptake and redistribution. Only the nature of the tracer retention (reversible or irreversible) has to be known. Using graphical methods however it is not possible to fully describe the tracer kinetics as only one macroparameter (e.g. the tracer net trapping uptake for Patlak and the tracer distribution volume for Logan) is estimated. An alternative approach is represented by semi-quantitative analysis methods. In PET the Standard Uptake Value (SUV) and the tissue-to-plasma ratio (RATIO) are commonly used to characterise the tracer uptake (Kubota et al. 1985; Lehtio et al. 2003; Mitkovski et al. 2005). The most used semi-quantitative index in MR is the area under the signal intensity vs. time curve (AUC). In DCE-MRI the AUC is commonly exploited as a semi-quantitative measurement of myocardial perfusion (Jerosch-Herold 2010) whereas the ratio of AUC of the injected hyperpolarised probe (e.g. [1-$^{13}C_1$] pyruvate) and product metabolite (e.g. [1-$^{13}C_1$] lactate) has been shown to be proportional to the rate of the enzymatic conversion observed (Hill et al. 2013).

1.7 Objectives of the Research

The research presented in this thesis aimed to develop new approaches for the assessment of cardiac metabolism using molecular imaging techniques combined with quantitative and semi-quantitative analysis methods. An experimental protocol for the polarisation of metabolically active ^{13}C probes was developed using DNP. To this end, different ^{13}C molecules have been hyperpolarised and the polarisation enhancement as well as the longitudinal time constant of these molecules was measured in solution. An MR acquisition protocol was developed for the real-time assessment of the conversion of hyperpolarised [1-$^{13}C_1$] pyruvate to its downstream metabolites *in vitro* in whole blood cells and *ex vivo* in Langendorff perfused rat hearts. Global information on the metabolic state of isolated hearts was obtained using ^{13}C MRS whereas the spatial distributions of these ^{13}C metabolite signals was measured using ^{13}C MRSI. A number of analysis methods were developed in order to derive quantitative and semi-quantitative parameters representing the metabolic state of the heart. They were applied to hyperpolarised ^{13}C MR dynamic data to quantify the rates of metabolic conversion of hyperpolarised [1-$^{13}C_1$] pyruvate to its downstream metabolites *in vitro* in whole blood cells and *ex vivo* in Langendorff perfused hearts. Analysis methods were also used to derive kinetic information from time-activity curves of two PET tracers, [^{18}F]-FDG and [^{18}F]-FMISO, acquired from Langendorff perfused rat hearts in physiological and hypoxic conditions.

1.8 Structure of the Thesis

The Chapters of this thesis are organised as follow:

Chapter 1 introduces the Langendorff perfusion and the main metabolic pathways through which the energy required for the contraction of the heart is produced both in physiological and pathophysiological conditions. This chapter also presents an overview on the most used imaging modalities for the characterisation of the anatomy, physiology and metabolism of the heart as well as the approaches commonly exploited for the quantitative and semi-quantitative analysis of dynamic cardiac data.

Chapter 2 presents the physical principles of MRI and MRS as well as of hyperpolarised MR.

Chapter 3 describes the experimental protocols developed and validated in this thesis. A number of metabolically active ^{13}C molecules were hyperpolarised using DNP and their relaxivity properties as well polarisation enhancement were measured in solution. An experimental protocol was developed for detecting the conversion of [1-$^{13}C_1$] pyruvate to its downstream metabolites *in vitro* in whole blood cells as well as *ex vivo* in Langendorff perfused rat hearts. Isolated hearts were also used to characterise the kinetics of two PET tracers, namely [^{18}F]-FDG and [^{18}F]-FMISO.

Chapter 4 introduces the quantitative and semi-quantitative approaches used in this thesis for the analysis of cardiac dynamic data acquired using hyperpolarised ^{13}C MR probes and PET tracers.

Chapter 5 presents the dynamic data acquired *in vitro* in whole blood cells and *ex vivo* in Langendorff perfused rat hearts using hyperpolarised ^{13}C MRS and the results obtained from their quantitative and semi-quantitative analysis.

Chapter 6 presents the dynamic data acquired *ex vivo* in Langendorff perfused rat hearts using two PET tracers, namely [^{18}F]-FDG and [^{18}F]-FMISO, and the results obtained from their quantitative and semi-quantitative analysis.

Chapter 7 presents the dynamic data acquired *ex vivo* in Langendorff perfused rat hearts using hyperpolarised ^{13}C MRSI. Monte Carlo simulations aimed at exploring the detection limits of cardiac ischemia using dynamic MRSI of hyperpolarised ^{13}C pyruvate combined with compartmental modelling *in vivo* in small rodents are also presented.

Chapter 8 summarises the main findings of this thesis, its final conclusions and suggestions for future development of this work

Chapter 2 : Magnetic Resonance

MR is a physical phenomenon according to which in presence of an external magnetic field (B_0) atomic nuclei are able to absorb and re-emit the electromagnetic (EM) energy following the application of a radiofrequency (RF) pulse. This property of nuclei with non-zero spin was first observed in molecular beams in 1938 by Isidor Isaac Rabi who received the Nobel Prize in Physics in 1944 *"for his resonance method for recording the magnetic resonance of atomic nuclei"* (Rabi et al. 1938). In 1946 Felix Bloch and Edward Mills Purcell independently extended the work of Rabi to liquid and solid, respectively. They were jointly awarded the Nobel Prize in Physics in 1952 "*for their development of new ways and methods for nuclear magnetic precision measurements"* (Bloch 1946; Purcell et al. 1946). The possibility of using the MR principle to form images using magnetic field gradients was proposed by Peter Mansfield and Paul Lauterbur (Lauterbur 2003; Mansfield 2003) who were jointly awarded the Nobel Prize in Physiology or Medicine in 2003 *"for their discoveries concerning magnetic resonance imaging".*

For around 20 years since its discovery the phenomena of MR was exclusively developed and used for physical and molecular analysis, largely in chemistry. The first evidence that MR could be used in the field of the diagnostic medicine

was provided in 1971 by Raymond Vahan Damadian who demonstrated that the characteristic time with which atomic nuclei re-emit the EM energy absorbed after the application of a RF pulse in a malignant lesion differs from that of nuclei in healthy tissues (Damadian 1971). He showed for the first time the possibility of discerning tumours from healthy tissues based on their MR properties. After this extraordinary discovery numerous studies were focused at the development of new technologies able to produce an image exploiting the MR phenomenon. The first MR image was obtained from a tube filled with water in 1973 and only in 1977 the first full human body image was acquired (Damadian et al. 1977).

Compared to other imaging modalities, MR offers high soft-tissue contrast with the capability of investigating both anatomic and functional parameters and has the advantage to not requiring ionising radiation.

The physical principles behind MR are described in the following sections.

2.1 Aim

This Chapter presents the basic physical principles behind MR imaging and spectroscopy as well as hyperpolarised MR.

MR is based on the detection of an EM sinusoidal signal generated by a nuclear spin-system placed in an external magnetic field after its perturbation. This physical phenomenon is macroscopically described by the Bloch equations presented in Section 2.2. After its perturbation, the system of nuclear spins relaxes back to its thermal equilibrium through a series of processes called

relaxation introduced in Section 2.3. The methods used in this thesis to measure the relaxation processes are presented in Section 2.4. In Section 2.5 the basic principles used in MRI to produce images of the ROI are introduced.

The intensity of the MR signal detected depends on the concentration, natural isotope abundance and electromagnetic properties of the nucleus assessed. For nuclei characterised by high natural abundance and high concentration in the biological tissues such as ^{1}H in H_2O, the intensity of the MR signal generated is adequate to detect and image real-time changes in the biological system assessed. However, for atomic nuclei characterised by low natural abundance and concentration such as ^{13}C new technologies have been developed to artificially enhanced their detectable MR signal. A brief introduction of the DNP technique used in this thesis to enhance the polarisation of ^{13}C nuclei within metabolically active molecules is presented in Section 2.7.

2.2 Basic Principles of Magnetic Resonance

Some atomic nuclei possess an intrinsic physical property called spin. The spin angular momentum is a vector that is related to the spin quantum number $\vec{I}$ of a nucleus as follows:

$$\vec{\mathrm{L}} = \hbar\vec{\mathrm{I}} \qquad 2.1$$

where $\hbar$ is the reduced Planck constant. The amplitude *L* and direction *m* of the spin angular momentum $\vec{\mathrm{L}}$ are given by Equations 2.3 and 2.4, respectively.

$$\mathrm{L} = \hbar\sqrt{\mathrm{I}(\mathrm{I}+1)} \qquad 2.2$$

$$\mathrm{m} = -\mathrm{I}, -\mathrm{I}+1, -\mathrm{I}+2, \ldots, \mathrm{I} \qquad 2.3$$

In absence of an external magnetic field 2I+1 energy levels are degenerate

The characteristic magnetic moment generated by the rotation of the nuclear spin angular momentum vector is given by:

$$\vec{\mu} = \gamma\vec{\mathrm{J}} = \gamma\hbar\vec{\mathrm{I}} \qquad 2.4$$

where γ is the gyromagnetic ratio, a proportionality constant intrinsic of each nucleus. The net magnetisation is given by the sum of the magnetic moments of the nuclei that form the sample (Equation 2.5).

$$\vec{\mathrm{M}} = \sum \vec{\mu} \qquad 2.5$$

In absence of an external magnetic field, the magnetic moments are randomly distributed and the net magnetisation is equal to zero.

2.2.1 Zeeman Effect

When an external magnetic field (B_0) is applied, the magnetic moments of the nuclei within the sample align parallel or antiparallel to B_0 generating a non-zero net magnetisation (Figure 2.1 A). In this condition the degenerate spin-states are split into 2I+1 levels characterised by different energies. For example, for an atomic nucleus with spin ½ two different energy levels are generated (Figure 2.1 B). This phenomenon is called *Zeeman Effect*.

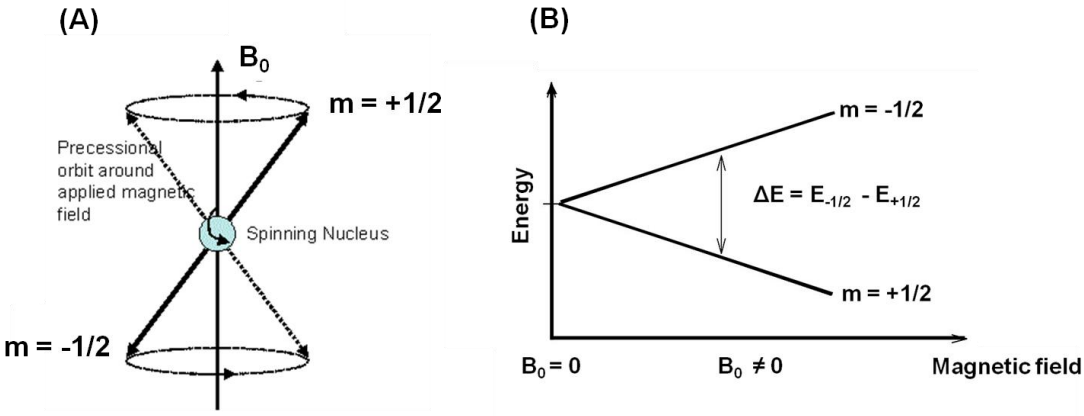

Figure 2.1: (A) The magnetic moments of atomic nuclei with spin 1/2 align parallel or antiparallel to the external magnetic field applied (B_0). The magnetic moments are not perfectly aligned with B_0 but they precess about the external magnetic field B_0. (B) Possible energy levels for a nucleus with spin 1/2.

The energy associated with each level depends on the magnetic moment $\vec{\mu}$ and external magnetic field B_0 as presented in Equation 2.6.

$$E = -\vec{\mu} \cdot \overrightarrow{B_0} \qquad 2.6$$

The spins with the magnetic moments aligned parallel to B_0 occupy the lowest energy level (m = +1/2) also named α, whereas spins with magnetic moment aligned antiparallel to B_0 are located in the higher energy level (m = -1/2) also named β (Figure 2.1 B). The number of nuclei in each spin-state is given by the *Boltzmann distribution* as follow:

$$\frac{N_\beta}{N_\alpha} = e^{\frac{-\Delta E}{k_B T}} \qquad 2.7$$

where N_α and N_β represent the population of nuclei in the α and β energy level, respectively. ΔE is the difference in energy between α and β, T is the temperature of the system and k_B is the Boltzmann constant.

The magnetic moments of the atomic nuclei do not orient exactly parallel (or anti-parallel) with the direction of the applied field B_0 but precess around this field at a characteristic angular velocity ω_0 named *Larmor frequency* (Equation 2.8) (Figure 2.1 A).

$$\omega_0 = \gamma B_0 \qquad 2.8$$

2.2.2 Bloch Equations

In MR the external magnetic field B_0 is conventionally directed along the z-axis and therefore after the insertion of the sample into the field, the net magnetic moment of the nuclei will be aligned along +z or –z direction. In order to generate a detectable MR signal the spin-system is perturbed by applying a RF

pulse at the Larmor frequency of the type of nuclei studied. The RF pulse generates an electric current in the transmit coil that produces a magnetic field B_1 perpendicular to B_0 that tilts the net magnetisation vector from the z-axis to the x-y plane. The flip angle θ is proportional to B_1, γ and to the length of the RF pulse (t_p) as follow:

$$\theta = \gamma B_1 t_p \qquad 2.9$$

When the RF pulse is switched off, the magnetization along the z-axis (M_z) recovers its initial value (M_0) according to a time constant T_1 (longitudinal relaxation time), whereas the magnetization in the x-y plane (M_{xy}) precesses about the z-axis with characteristic frequency equal to ω_0 and decays to zero with a time constant T_2 (transversal relaxation time). Relaxation processes will be described in more details in Section 2.3.

The motion of the net magnetisation M in these conditions is macroscopically described by the Bloch equations which can be written in the “laboratory frame” as follows:

$$\frac{dM_x}{dt} = \gamma\left(M_y(t)B_z(t) - M_z(t)B_y(t)\right) - \frac{M_x(t)}{T_2} \qquad 2.10$$

$$\frac{dM_y}{dt} = \gamma\left(M_z(t)B_x(t) - M_x(t)B_z(t)\right) - \frac{M_y(t)}{T_2} \qquad 2.11$$

$$\frac{dM_z}{dt} = \gamma\left(M_x(t)B_y(t) - M_y(t)B_x(t)\right) - \frac{M_z(t) - M_0}{T_1} \qquad 2.12$$

In the “laboratory frame” the magnetisation in the x-y plane rotates at the Larmor frequency about the z-axis. In many applications it is more convenient to deal with a stationary M_{xy} and this can be obtained by using a “rotating frame” in which the x-y plane rotates about the z-axis at the frequency $-\omega_0$. Equations 2.10-2.12 can be written in the “rotating frame” by considering each $B_z = B_0 = -\omega_0/\gamma$ (derived from Equation 2.8). The Bloch equations in the “rotating frame” are:

$$\frac{dM_x}{dt} = -M_y(t)\omega_0 - \gamma M_z(t)B_y^r(t) - \frac{M_x(t)}{T_2} \quad 2.13$$

$$\frac{dM_y}{dt} = \gamma M_z(t)B_x^r(t) + \omega_0 M_x(t) - \frac{M_y(t)}{T_2} \quad 2.14$$

$$\frac{dM_z}{dt} = \gamma\left(M_x(t)B_y^r(t) - M_y(t)B_x^r(t)\right) - \frac{M_z(t) - M_0}{T_1} \quad 2.15$$

where $B_{x,y}^r$ indicates the magnetic field in the “rotating frame”. The longitudinal component of the magnetisation is M_z, whereas the transverse component is equal to:

$$M_{xy} = M_x + iM_y \quad 2.16$$

2.2.3 Magnetic Resonance Spectrum

The magnetisation on the x-y axis precesses about the z-axis and decays to zero with the characteristic time constant T_2 generating a current in the receiver

coil that oscillates at the Larmor frequency ω_0 called free induction decay (FID) (Figure 2.2).

This decaying oscillating signal is described mathematically as:

$$M_{xy}(t) = M_0 e^{-\frac{t}{T_2^*}}(\cos(\omega_0 t) + i\sin(\omega_0 t)) \quad 2.17$$

The time constant T2* depends on the relaxation rate of the tissue T_2 and the magnetic field inhomogeneity of B_0.

The Fourier transform of the FID gives the frequency domain signal or *spectrum* which is composed by a real and an imaginary part representing the absorption and the dispersion of the nuclei at the characteristic frequency ω_0, respectively (Figure 2.3).

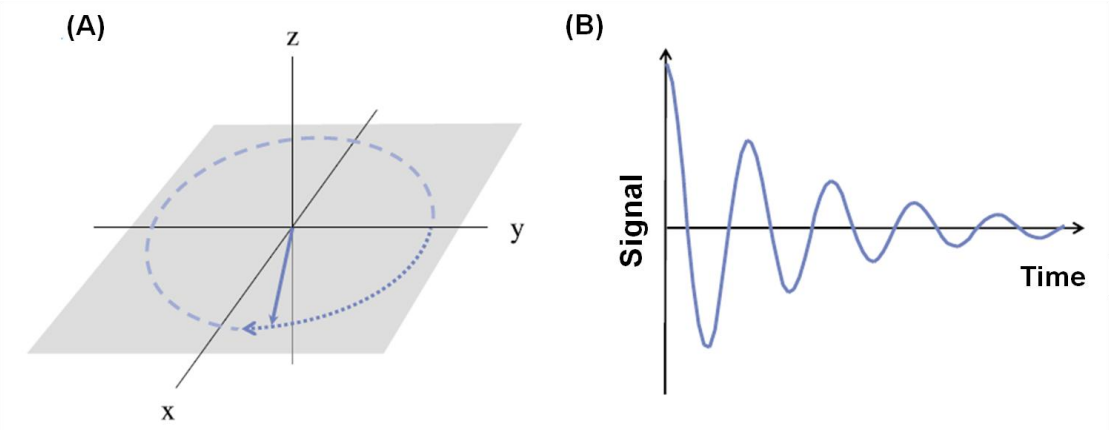

Figure 2.2: (A) Precession of the transverse component of the magnetisation M_{xy} about the z-axis after the application of a RF pulse. This precession generates an electric current in the receiver coil producing a complex MR signal named free induction decay (FID). (B) Representative FID. Adapted from reference (McRobbie D. W. 2006).

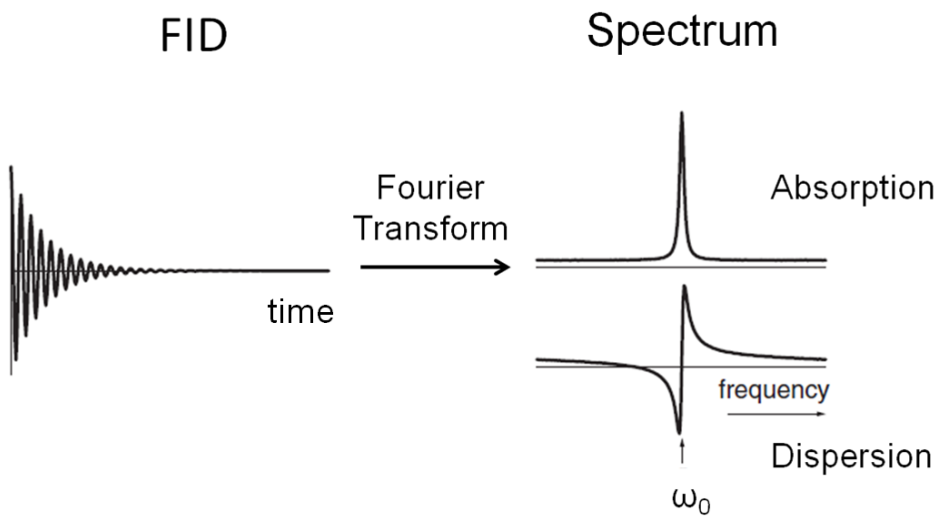

Figure 2.3: Representative FID and MR spectrum obtained by Fourier transforming the FID. The real and the imaginary part of the MR spectrum represent the absorption and dispersion of the nuclear spin-system at the characteristic frequency ω_0, respectively. Adapted from reference (www.keeler.ch.cam.ac.uk/)

2.2.4 Chemical Shift

The electrons surrounding a nucleus also possess angular momentum and generate a magnetic field B_e opposed to B_0. The local magnetic field experienced by the atomic nuclei is given by:

$$B_{eff} = B_0 - B_e \qquad 2.18$$

The nuclei therefore precess about the z-axis at characterised by a Larmor frequency equal to:

$$\omega_0 = \gamma B_{eff} \qquad 2.19$$

This shift in the Larmor frequency of the nuclei depends on the type of nucleus and on the electrons motion in the nearby atoms within a molecule and is named *chemical shift*. The chemical shift is usually expressed in parts per million (ppm) and defined in terms of a standard reference as follows:

$$\delta = \frac{(\omega_N - \omega_R)}{\nu_S} * 10^6 \qquad 2.20$$

where ω_N and ω_R are the resonance frequencies of the nucleus observed and that of a reference, respectively. ν_S represents the operating frequency of the spectrometer.

For nuclei such as ^{1}H and ^{13}C trimethylsilyl propionate (TSP) is commonly used as standard reference, whereas 85% phosphoric acid is preferred for ^{31}P.

Even if the Larmor frequency of a nucleus depends on the strength of the magnetic field in which the nucleus is placed, the chemical shift in ppm is independent from it.

2.3 Relaxation

Relaxation consists of a series of processes that operates simultaneously by which the system of nuclear spins returns to its equilibrium after being perturbed (e.g. application of a RF pulse). In this section the main relaxation mechanism are presented.

2.3.1 Spin-Lattice Relaxation

The spin-lattice relaxation is the mechanism by which the component of the magnetisation along the z-axis (M_z) returns to its thermal equilibrium value (M_0). In this process nuclear spins dissipate the energy acquired after the application of a RF pulse by transferring energy to the neighbouring molecules (lattice). The spin-lattice relaxation can be described by the simplified Bloch equation (Equation 2.21).

$$\frac{dM_z}{dt} = \frac{M_0 - M_z}{T_1} \qquad 2.21$$

The recovery of the magnetisation along the z-axis after the application of a RF pulse is therefore described by a mono-exponential function with the characteristic time constant T_1 (Equation 2.22).

$$M_z(t) = M_0(1 - e^{-\frac{t}{T_1}}) \qquad 2.22$$

The spin-lattice (or longitudinal) relaxation time constant T_1 represents the length of time required for the perturbed system to return 63% of the way toward thermal equilibrium. It depends on the gyromagnetic ratio of the nucleus assessed and on the rotational motion of the molecule in the lattice.

2.3.2 Spin-Spin Relaxation

The spin-spin relaxation is the mechanism by which the component of the magnetisation in the x-y plane returns to its equilibrium value of zero after a perturbation. In this type of relaxation the energy the nuclear spins acquired after the application of an RF pulse is not exchanged with the lattice but between neighbouring spins. The spin-spin relaxation can be described by the simply Bloch equation for the transverse magnetisation as follow:

$$\frac{dM_{xy}}{dt} = -\frac{M_{xy}}{T_2} \qquad 2.23$$

The relaxation of the transverse component of the magnetisation is therefore described by a mono-exponential decay with the characteristic time constant T_2 (Equation 2.24).

$$M_{xy}(t) = M_{xy}(0)e^{-\frac{t}{T_2}} \qquad 2.24$$

where $M_{xy}(0)$ is the value of the transverse magnetisation at the time point in which the spin-spin relaxation starts that corresponds to the time point in which the RF pulse is switched off.

As mentioned in Section 2.2.3 the linewidth of the real part of the MR spectrum is given by the transverse relaxation time constant T_2 and the magnetic field inhomogeneity. The latter makes T_2 shorter and T_2^* is used to represent the

effective transverse relaxation time that is related to the linewidth of the MR spectrum as follows:

$$\Delta\nu_{1/2} = \frac{1}{\pi T_2^*} \tag{2.25}$$

where $\Delta\nu_{1/2}$ represents the full width at half maximum (FWHM) of the MR spectrum.

2.3.3 Dipole-Dipole Interaction

The relaxation processes described in Sections 2.3.1 and 2.3.2 occur mainly by interaction of the nuclear spins with the magnetic fields produced by the molecular motion of the neighbouring nuclei (spin-spin relaxation) or of nuclei located in the lattice (spin-lattice relaxation). The relationship between the relaxation time constants and the molecular motion is presented in Equations 2.26 and 2.27 and plotted in Figure 2.4.

$$\frac{1}{T_1} = \gamma^2\overline{H^2}\frac{\tau_C}{1 + (2\pi\nu_0\tau_C)^2} \tag{2.26}$$

$$\frac{1}{T_2} = \gamma^2\overline{H^2}\left(\tau_C + \frac{\tau_C}{1 + (2\pi\nu_0\tau_C)^2}\right) \tag{2.27}$$

$\overline{H^2}$ is the mean-square average of the local magnetic fields and is a measure of the strength of the interaction between the nuclear spin and the fluctuating

magnetic fields. τ_C is the correlation time which is a quantitative measure of the rate of a molecular motion or rotation. As shown in Figure 2.4 both relaxation rates are related to the operating frequency of the spectrometer ν_s and therefore the T_1 and T_2 of a sample depend on the strength of the external magnetic field B_0.

The magnetic field created by an unpaired electron is much larger than that of a nucleus. An unpaired electron is half a million times more effective in promoting relaxation than a proton at the same distance from a relaxing nucleus. This is the essential basis for development of paramagnetic contrast agents such as gadolinium in MR (James 1998).

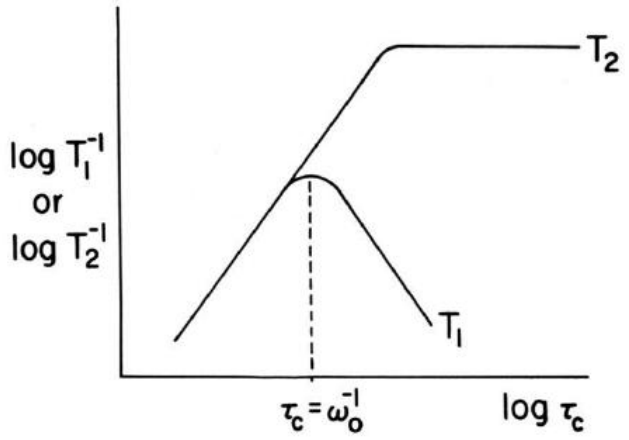

Figure 2.4: The relaxation rates $1/T_1$ and $1/T_2$ are plotted as function of the correlation time τ_C. $\omega_o = 2\pi\nu_s$ where ν_s is the spectrometer frequency. Adapted from reference (James 1998).

2.4 Measurement of Relaxation Time Constants

In this Section the methodologies used in this thesis for the measurement of the T_1 of ^{13}C nuclei are presented. The T_2 estimation was not addressed in this thesis.

The T_1 of samples at thermal equilibrium were measured using an inversion recovery method, whereas the T_1 of hyperpolarised samples were measured by fitting the experimental curves obtained by plotting the area under the ^{13}C hyperpolarised MR spectrum (real part) (Figure 2.3 B) as function of time with Equation 2.28.

$$M_z(t) = M_0 \cos\theta^n e^{-\frac{t}{T_1}} \qquad 2.28$$

θ is the small flip angle used for the acquisition of the hyperpolarised spectra and *n* is the number of RF pulses applied

2.4.1 Inversion Recovery Method

Inversion recovery is a method commonly used in MR for measuring the spin-lattice relaxation time constant T_1 of different types of nuclei. The sequence used in this type of experiment is presented in Figure 2.5.

A 180° RF pulse is applied at the Larmor frequency characteristic of the type of nuclei of which the T_1 is to be measured. Before the application of the RF pulse the magnetisation is aligned with the external magnetic field B_0 along +z-axis and its value is equal to M_0, whereas the M_{xy} magnetisation is null.

Following the application of the RF pulse the longitudinal and the transverse magnetisation are:

$$M_z = M_0 \cos\theta_{inv} \quad 2.29$$

$$M_{xy} = M_0 \sin\theta_{inv} \quad 2.30$$

where θ_{inv} is the flip angle chosen for the RF pulse.

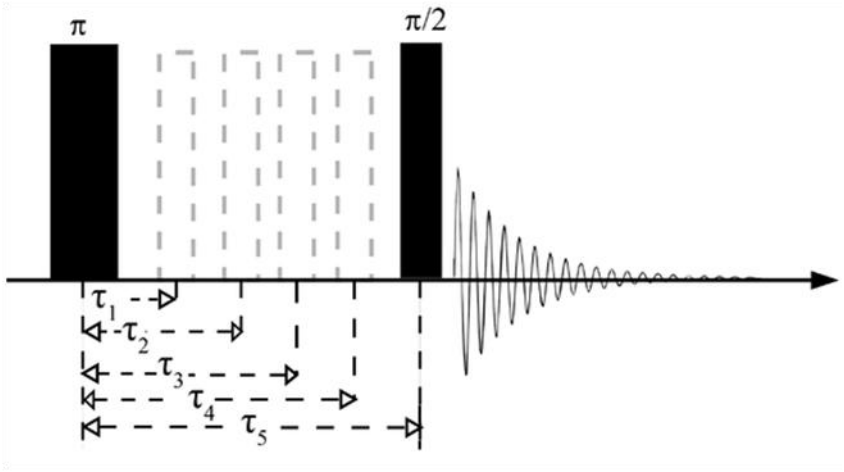

Figure 2.5: Inversion recovery pulse sequence. A 180º RF pulse is applied to invert the net magnetisation from z to –z axis. After a time $\tau < T_1$ a 90º RF pulse is applied and the FID produced by the magnetisation in the x-y plane recorded. The transverse component of the net magnetisation is measured at different time point during its relaxation by repeating for a certain number of times the inversion recovery sequence. The time delay τ between the application of the two RF pulses is increased each time.

At this point the longitudinal magnetisation M_z starts to relax back towards its equilibrium value M_0 following the simplify Bloch equation presented in Equation

2.21. Using Equation 2.29 as initial condition the time-dependent longitudinal magnetisation is equal to:

$$M_z(t) = M_0[1 - (1 - \cos\theta_{inv})]e^{-\frac{t}{T_1}} \qquad 2.31$$

After a short amount of time ($\tau < T_1$) a 90° RF pulse is applied. The net magnetisation is tilted on the x-y plane, a FID is generated and the value of the area under the MR spectrum measured (Figure 2.6).

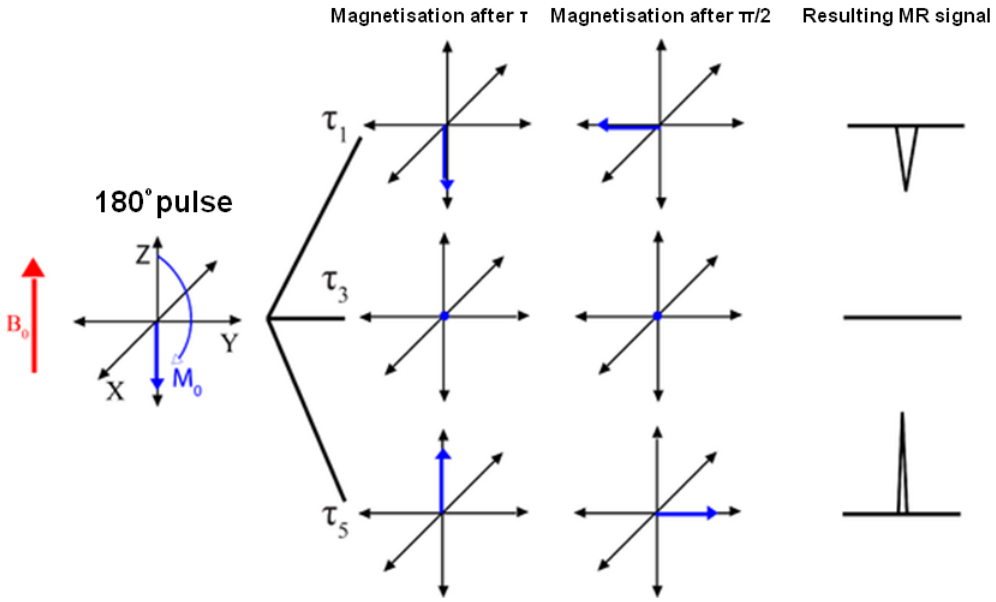

Figure 2.6: Evolution of the longitudinal magnetisation M_z after the application of the 180° and 90° pulses. The MR signal corresponding to the real part of the Fourier transform of the FID is shown in the last column on left.

This sequence of RF pulses is repeated after a period of time long enough to allow the magnetisation along the z-axis to fully recover its thermal equilibrium value M_0. At each repetition the delay time τ is increased ($\tau_1 < \tau_2 < ... < \tau_n$) and the values of M_z is measured at different relaxation time points (Figure 2.7).

By fitting the experimental data representing the area under the MR spectrum acquired at different point of the spin-lattice relaxation plotted as function of τ using Equation 2.31 (with $t = \tau$ and $\theta_{inv} = 180^o$) it is possible to derive the characteristic T_1 of the nucleus assessed. Due to the dipole-dipole interaction the same nucleus is characterised by different T_1 depending on the surrounding chemical environment.

When the T_1 of ^{13}C was measured a proton decoupling during the acquisition was used.

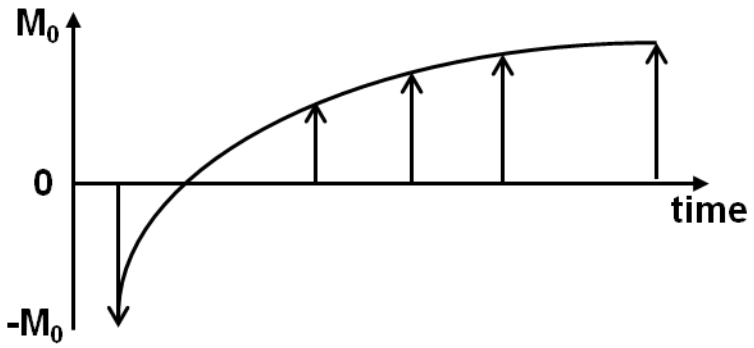

Figure 2.7: Representative inversion recovery measurement. The longitudinal magnetisation is sampled at different time points and the experimental data are fitted with Equation 2.31 to derive the characteristic T_1 of the nucleus assessed.

2.5 Basic principles of Magnetic Resonance Imaging

As introduced in Section 2.2, after the application of a RF pulse the transverse component of the net magnetisation creates a current in the receiver coil that oscillates at the Larmor frequency ω_0 that represent the MR signal named FID. In order to form an image the system must locate the signal spatially in three dimensions. In MRI the localisation of the region in the body from which the signal was emitted is performed using linear magnetic gradients. Commonly the signal is first located within a slice (slice selection) and subsequently along both axes of the selected slice (phase and frequency encoding).

In the MR scan the external magnetic field B_0 is always present, whereas the magnetic field gradients are switched on and off during the image acquisition. The application of a linear magnetic field gradient modifies the magnitude B_0. In particular, the local magnetic field experienced by the nuclear spins will be bigger or smaller than B_0 depending on their location. Spins located in regions in which the local magnetic field is smaller than B_0 precess at a frequency slower than the Larmor frequency, whereas those nuclei located in regions in which the local magnetic field is bigger than B_0 precess at a frequency faster than ω_0 (Figure 2.8). The spins precessing at different frequency produces FIDs which are characterised by different frequencies and therefore the application of linear magnetic gradients can be used to localise the region from which the signal was generated. Magnetic field gradients can be applied in any direction and orientation.

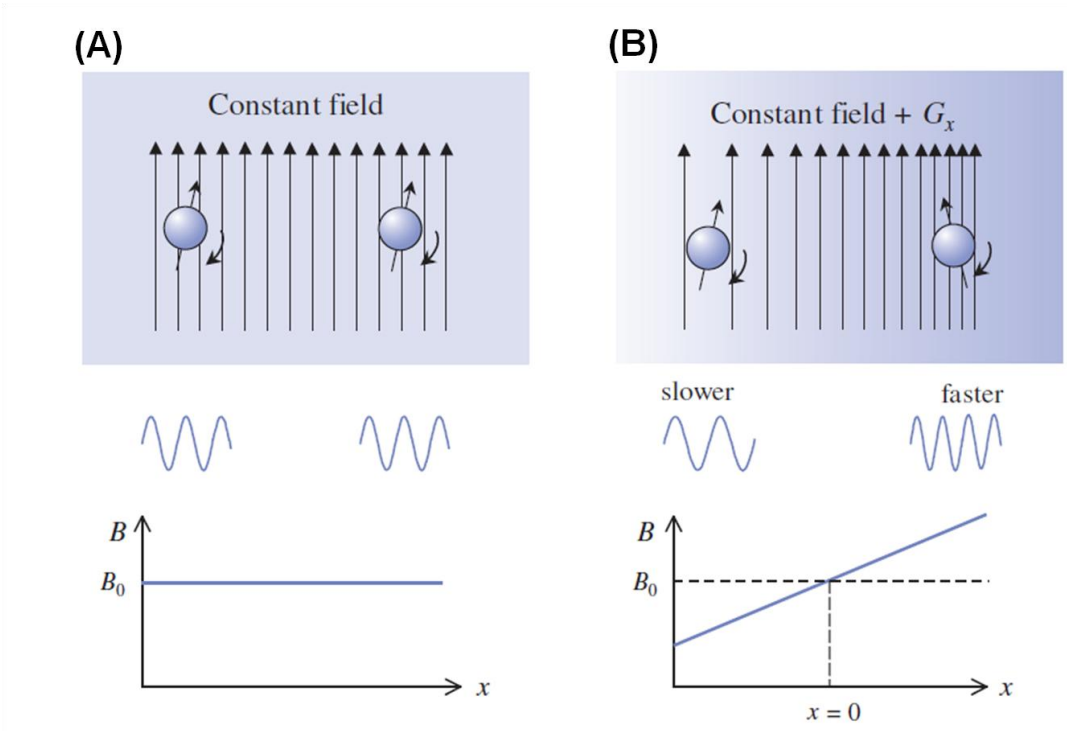

Figure 2.8: (A) In presence of a constant magnetic field B_0 all nuclear spins in the ROI process at the Larmor frequency. (B) The application of a linear magnetic gradient modifies the magnitude of B_0. Spins located in regions in which the local magnetic field is smaller than B_0 precess at a frequency slower than the Larmor frequency, whereas those nuclei located in regions in which the local magnetic field is bigger than B_0 precess at a frequency faster than ω_0. In this example the magnetic gradient is applied along the x-axis but magnetic gradients can be applied in any direction or orientation. Adapted from reference (McRobbie D. W. 2006).

2.5.1 Slice Selection

In order to localise the MR signal within a slice the appropriate gradient coil is switched on. As seen in the previous section, the presence of gradient field will induce the nuclear spin to process at different frequencies depending on their spatial location. At this point an RF pulse is applied. As shown in Figure 2.9 only

the nuclei that precess at the frequencies within the bandwidth of the RF pulse are excited and produce a detectable MR signal. The range of frequencies contained in the RF pulse is called bandwidth. The selected slice is always perpendicular to the direction of the magnetic gradients applied.

In Figure 2.9 the gradient for the slice selection is applied along the z-axis and therefore an axial slice is selected. The position of the selected slice can be change, for example, by changing the central frequency (carrier frequency) of the RF pulse and maintaining the same magnetic gradients. The thickness of the slice can be adjusted by changing the RF bandwidth or changing the slope of the magnetic gradient applied.

Once an image slice is selected the MR signals coming from it must be spatially located (encoded) along both axes of the image. This is performed using phase and frequency encoding.

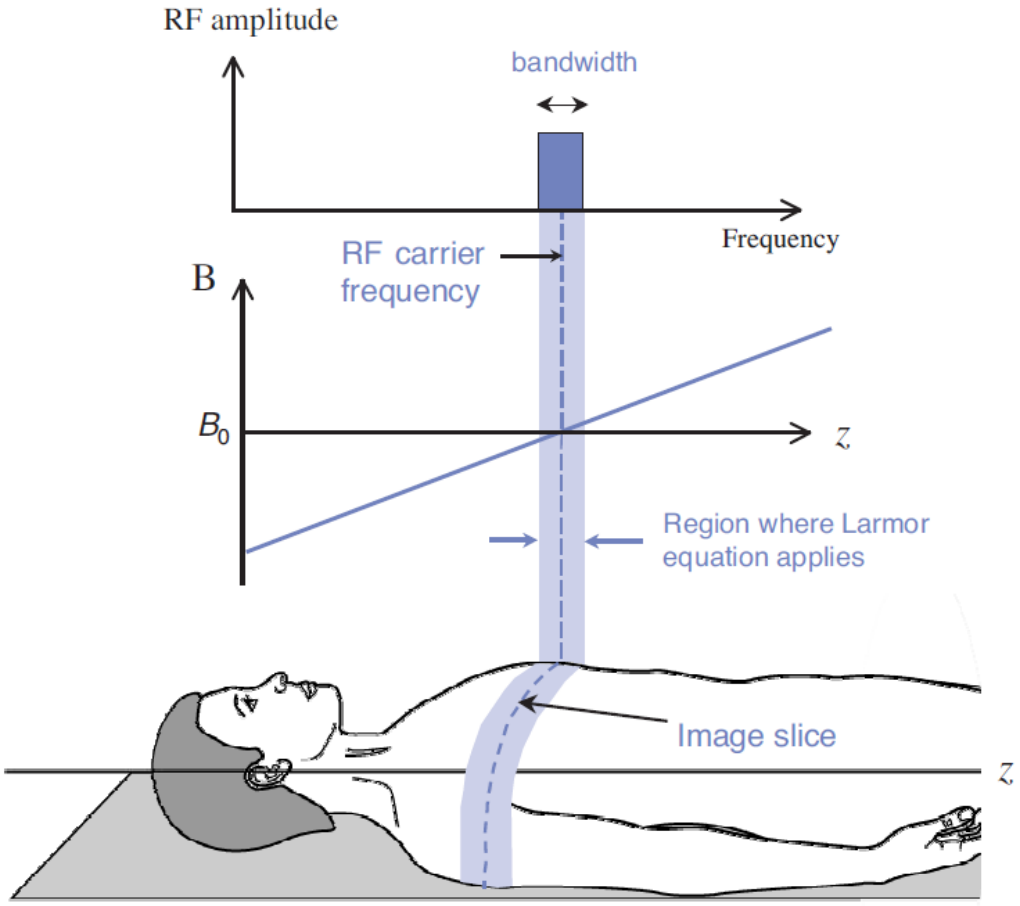

Figure 2.9: In the slice selection precess a linear magnetic gradient is used in order to change the precession frequency of the nuclear spins depending on their position. A RF pulse is applied at the same time and only the nuclei characterised by the range of frequencies contained in the RF pulse (bandwidth) are excited and therefore produce a detectable MR signal. Adapted from reference (McRobbie D. W. 2006).

2.5.2 Phase Encoding

Phase encoding is usually performed by applying a linear magnetic gradient along the short axis of the anatomy. The presence of a gradient modifies the frequency of precession as well as the accumulated phase of the nuclear spins depending on their position. When the phase encoding gradient is switched off,

the magnetic field strength returns to B_0 and the precessional frequency of all the nuclei returns to the Larmor frequency. However the phase difference between nuclei remains. This difference in phase between the nuclei is used to determine their position along the axis of the phase encoding gradient.

2.5.3 Frequency Encoding

Frequency encoding is usually performed by applying a linear magnetic gradient along the long axis of the anatomy. The precessional frequency of signal along the axis is therefore altered in a linear fashion and the signal can be located along the axis of the gradient according to its frequency. The frequency encoding gradient is usually switched on during the collection of the signal.

2.5.4 k-space

In order to form a MR images the slice selection, phase and frequency encoding have to be repeated a number of times. The time between one acquisition and another is called repetition time (TR). During this acquisition process the MR signals acquired are digitalised and stored in temporary image space named k-space (Figure 2.10). In order to fill out different lines of the k-space, the slope of the phase encoding gradient must be altered after each TR. Once filled the k-space, the data stored in it are converted into an image mathematically using the Fourier transform.

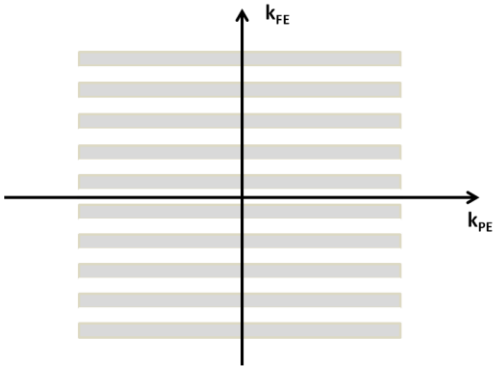

Figure 2.10: Schematic representation of k-space. In order to fill every line the slope of the phase encoding gradient has to be changed after each TR. Once filled the k-space, the MR signals store in the k-space in their digitalised form are converted to an image using the Fourier transform.

2.6 MR Sensitivity

As mentioned in Section 2.2.1, for nuclei with spin ½ (e.g. ^{1}H, ^{13}C, ^{15}N) the MR signal is proportional to the difference in population between the two energy levels in the presence of an external magnetic field B_0 (Figure 2.11 A).

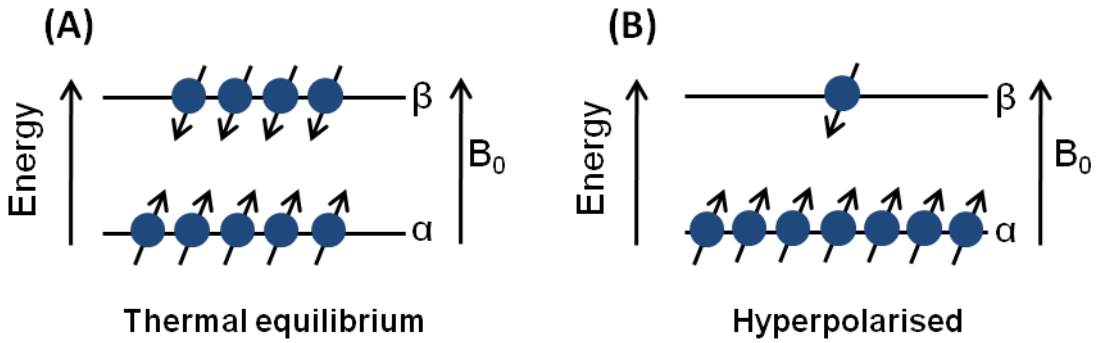

Figure 2.11: Schematic representation of the (A) thermal equilibrium and (B) hyperpolarised population distribution.

The detectable MR signal S is proportional to the spin-system polarisation which can be derived from the Boltzmann distribution (Equation 2.7) and is equal to:

$$S \propto M_z \propto P = \left|\frac{N_\alpha - N_\beta}{N_\alpha + N_\beta}\right| = \tanh\left(\frac{\gamma\hbar B_0}{2k_B T}\right) \quad 2.32$$

where T is temperature of the sample. At body temperature, the difference in population between the two spin-states is very low (e.g. P = 9.88*10^{-6} for ^{1}H and P = 2.48 * 10^{-6} for ^{13}C at 9.4T and 310K). It is therefore possible to detect a significant signal only if the nucleus of interest is characterised by a very high natural abundance and concentration. This is the case for hydrogen ^{1}H in water (100% natural abundance and molar concentrations), but not for nuclei such as ^{13}C and ^{15}N which have a millimolar (mM) endogenous concentration and natural abundance equal to 1.1% and 0.3% natural abundance, respectively.

According to Equation 2.32, the polarisation of a spin-system can be enhanced by increasing the strength of the external magnetic field, decreasing the temperature or both. Since these two possibilities are physically limited, other non-equilibrium techniques able to artificially increase the difference in population of the two spin states, creating a so called “hyperpolarised” configuration, have been developed (Figure 2.11 B).

As mention in Section 1.5.4 different methodologies such as spin exchange optical pumping, PHIP and DNP have been developed to enhance the polarisation of a number of nuclei. In the following Section the physical

principles of hyperpolarisation by DNP used in this thesis for increasing the detectable MR signal from ^{13}C nuclei are presented.

2.7 Basic Principles of Dynamic Nuclear Polarisation

DNP is able to enhance the MR signal of a variety of nuclei such as ^{13}C, ^{15}N and ^{1}H by greater than a factor 10,000 times (Ardenkjar-Larsen et al. 2003) such that metabolites previously invisible to MR can be quantified and imaged.

At very low temperature free electrons are almost completely polarised while atoms such as ^{1}H, ^{13}C and ^{15}N are characterised by a low polarisation (<10%) (Figure 2.12). The dominant mechanism of solid state DNP can be described by the *solid effect* through which the high polarisation of unpaired electrons is transferred to the nuclei of interest.

In this thesis the only ^{13}C was hyperpolarised, for this reason in this Section the basic principles of DNP are presented with particular reference to this nucleus.

In DNP experiments a sample containing ^{13}C nuclei of which the polarisation is to be enhancing is doped with free electrons in the form of free radicals. In presence of an external magnetic field the degenerate ground state of the two-spin-system are spitted in four possible energy states due to the Zeeman Effect (Section 2.2.1) (Figure 2.13 A).

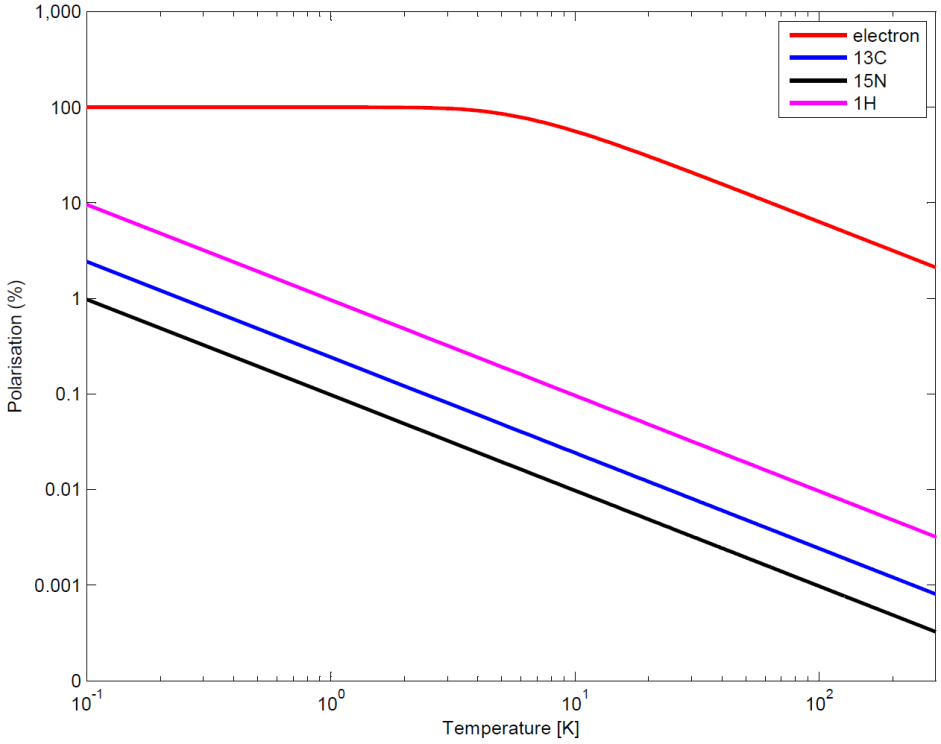

Figure 2.12: (A) Polarisation of free electrons, ^{13}C, ^{15}N and ^{1}H atomic nuclei plotted as function of temperature at 9.4T calculated from the Equation 2.32.

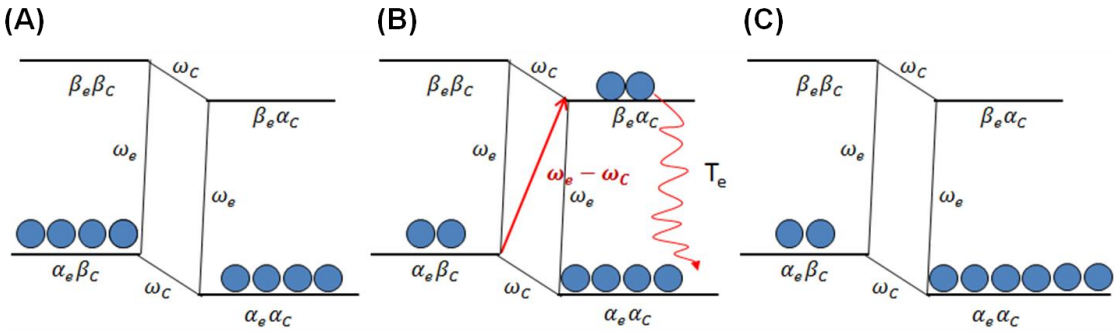

Figure 2.13: Solid effect in a two-spin-system, electron/^{13}C (zero-quantum transition). (A) Schematic thermal equilibrium Boltzmann distribution for the electron-^{13}C coupled spin-system. ω_e is the electron-spin resonance (ESR) frequency while ω_C is the ^{13}C Larmor frequency. (B) The application of a microwave pulse at ω_e-ω_C (zero-quantum transition) equalises the population between $\alpha_e\beta_C$ and $\beta_e\alpha_C$ energy states. Electron relaxation at the frequency ω_e is showed by wavy lines. (C) Terminated the electron relaxation, the difference in population between $\alpha_e\alpha_C$ and $\alpha_e\beta_C$ is greatly enhanced generating a positive polarisation.

At thermal equilibrium, the difference in population between the two carbon transitions, $\alpha_e\alpha_C \rightarrow \alpha_e\beta_C$ and $\beta_e\alpha_C \rightarrow \beta_e\beta_C$, is very small, while the difference in population between the two electrons transitions $\alpha_e\alpha_C \rightarrow \beta_e\alpha_C$ and $\alpha_e\beta_C \rightarrow \beta_e\beta_C$ is large at low temperature. The thermal equilibrium population can be artificially changed by applying a microwave field with frequency equal to $\omega_e - \omega_C$ (zero-quantum transition) or $\omega_e + \omega_C$ (double-quantum transition) (Figure 2.13 and Figure 2.14).

The irradiation of the zero-quantum transition equalises the population between $\alpha_e\beta_C$ and $\beta_e\alpha_C$ energy states (Figure 2.13 B). This new distribution is unstable and both electrons and ^{13}C nuclei relax back to their thermal equilibrium configuration. At the operating temperature of DNP (~ 1.4K) the relaxation rate of electrons is fast (10^3 s^{-1}) whilst that of ^{13}C is very slow (10^{-3} s^{-1}). As result of the electron relaxation from $\beta_e\alpha_C$ to $\alpha_e\alpha_C$, the difference in population between the energy states $\alpha_e\alpha_C$ and $\alpha_e\beta_C$ is greatly enhanced generating a positive polarisation (Figure 2.13 C).

The difference in polarisation of the two-spin-system can also be enhanced by applying a microwave pulse with frequency $\omega_e + \omega_C$ (double-quantum transition) (Figure 2.14 B). In this case the difference in population between $\alpha_e\alpha_C$ and $\alpha_e\beta_C$ is enhanced and a negative polarization is generated (Figure 2.14 C).

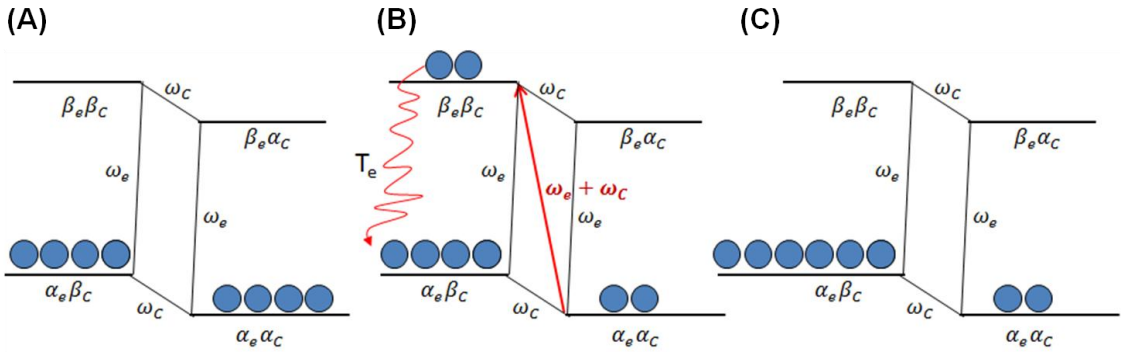

Figure 2.14: Solid effect in a two-spin-system, electron/^{13}C (double-quantum transition). (A) Schematic thermal equilibrium Boltzmann distribution for the electron-^{13}C coupled spin-system. ω_e is the electron-spin resonance (ESR) frequency while ω_C is the ^{13}C Larmor frequency. (B) The application of a microwave pulse at $\omega_e+\omega_C$ (double-quantum transition) equalises the population between $\alpha_e\alpha_C$ and $\beta_e\beta_C$ energy states. Electron relaxation at the frequency ω_e is showed by wavy lines. (C) Terminated the electron relaxation, the difference in population between $\alpha_e\alpha_C$ and $\alpha_e\beta_C$ is greatly enhanced generating a negative polarisation.

The hyperpolarised population distribution in the solid state is retained at low temperature through a continuous microwave irradiation of the sample. In this condition the spin-lattice relaxation constant T_1 of ^{13}C nuclei is much slower of that of electrons and the hyperpolarised configuration is maintained. However in the absence the microwave field or during the sample dissolution (Section 3.2) the relaxation of ^{13}C prevails and the system returns to its thermal equilibrium configuration with decay time T_{1C} that varies from one chemical compound to another.

Chapter 3 : Experimental Methodology

3.1 Aims

The experimental aim of this thesis was to detect cardiac metabolism in the perfused rat heart using hyperpolarised ^{13}C MR probes and PET tracers. The first step consisted in installing (autumn 2010) the HyperSense DNP polariser (Oxford Instruments®) in the pre-clinical laboratory of the Imaging Chemistry and Biology Department at St. Thomas's hospital in London. The performance of HyperSense was validated by hyperpolarising several ^{13}C molecules and measuring the polarisation enhancement achieved as well as the longitudinal relaxation time constants of the hyperpolarised molecules in the liquid state (Section 3.2). Further validation of the DNP methodology was performed *in vitro* mixing hyperpolarised ^{13}C pyruvate with whole blood cells in order to determine whether the signal enhancement achieved was adequate to detect the conversion of pyruvate into its metabolites in a cell system in real-time (Section 3.3). MR spectroscopic protocols for *in vitro* experiments were developed and optimised at the same time. Finally, a system for the Langendorff perfused rat heart was developed and validated in order to allow detecting cardiac metabolism using hyperpolarised ^{13}C MR probes and PET tracers (Section 3.4 and 3.5).

3.2 Hyperpolarised ^{13}C Magnetic Resonance

3.2.1 HyperSense DNP Polariser

To hyperpolarise ^{13}C labelled molecules a HyperSense DNP polariser was used in this thesis. All experiments were carried out at St. Thomas' Hospital in London where the polariser is placed next to a vertical wide bore Bruker 9.4T Avance III spectrometer (Figure 3.1).

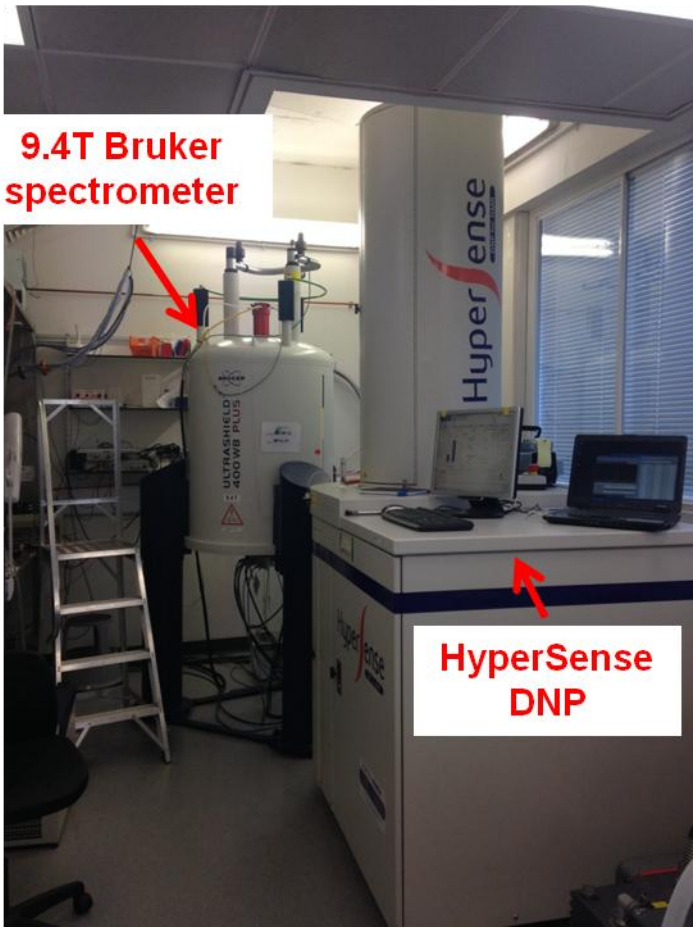

Figure 3.1: Experimental set up at St. Thomas' Hospital in London. The HyperSense DNP polariser is located next to a vertical wide bore Bruker 9.4T Avance III spectrometer.

The DNP polariser is composed by a DNP insert allocated in the centre of a 3.35T superconductive magnet (Figure 3.2). The DNP insert includes a cryogenic chamber, also named Variable Temperature Insert (VTI), positioned in a liquid helium bath whose temperature is maintained below 4K by an external vacuum pump that modulates the temperature by controlling the pressure inside the VTI.

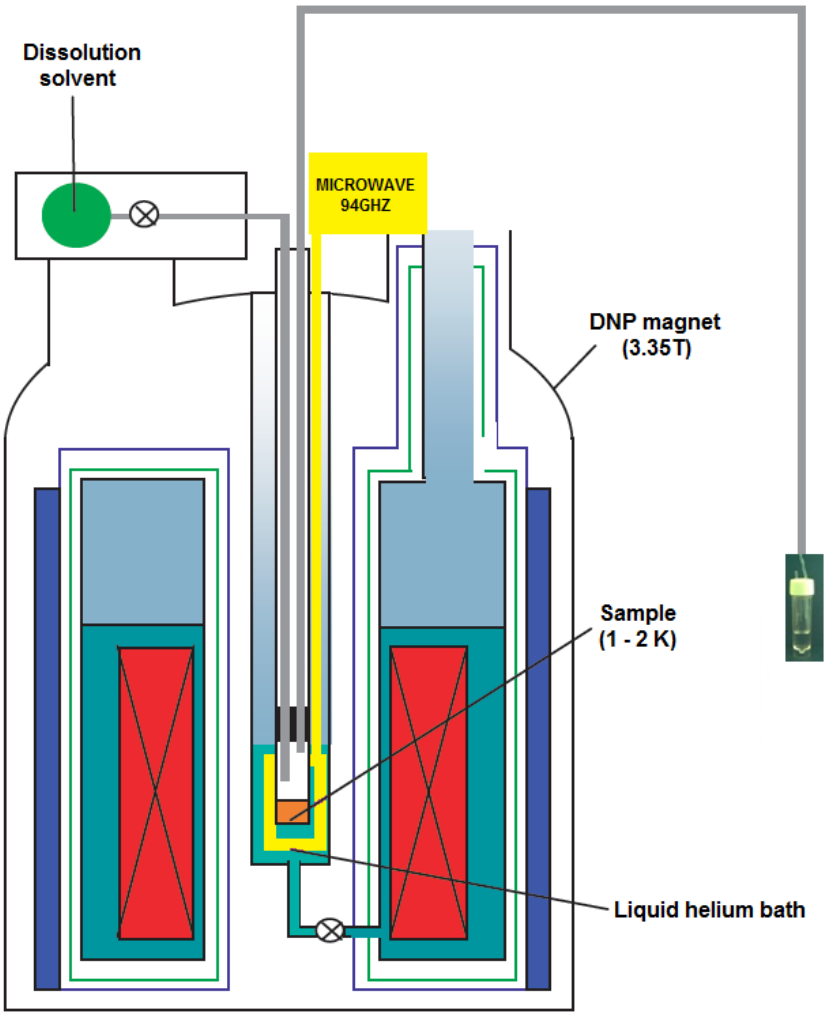

Figure 3.2: Scheme of the HyperSense DNP polariser. Adapted from reference (Frydman and Blazina 2007).

During the polarisation of the sample the temperature inside the VTI is normally lowered and maintained at 1.4K. The VTI is connected to a microwave generator through a microwave guide tube that irradiates the sample at 94GHz. The sample is surrounded by a saddle coil tuned to the ^{13}C frequency and able to measure the MR signal in the solid-state. Once the sample is fully polarised, a dissolution process is performed by an automatic pneumatic system that heats an aqueous buffered solution to at high temperature and pressure. The dissolved hyperpolarised solution is ejected from the machine, collected in a plastic tube and immediately placed into a 5mm MR tube for *in vitro* experiments or injected into a perfusion line for *ex vivo* and *in vivo* experiments (Figure 3.2).

3.2.2 Sample Preparation

The samples are normally prepared by dissolving a polarising agent into a solution containing the molecule to be polarised. Previous studies have shown that the polarisation of molecules that form a glass when frozen yields to a much higher DNP signal enhancement than that of molecules characterised by a frozen crystal structure (Barnes et al. 2008). For this reason, the latter are mixed with a co-solvent (DMSO or glycerol) before inserting the sample in the DNP polariser to enable the formation of a glass at low temperature.

In this thesis three different ^{13}C metabolically active molecules were hyperpolarised:

- [1-$^{13}C_1$] pyruvic acid
- [2-$^{13}C_1$] pyruvic acid
- [1,4-$^{13}C_2$] fumaric acid

Figure 3.3 shows a scheme of the chemical structure of these molecules.

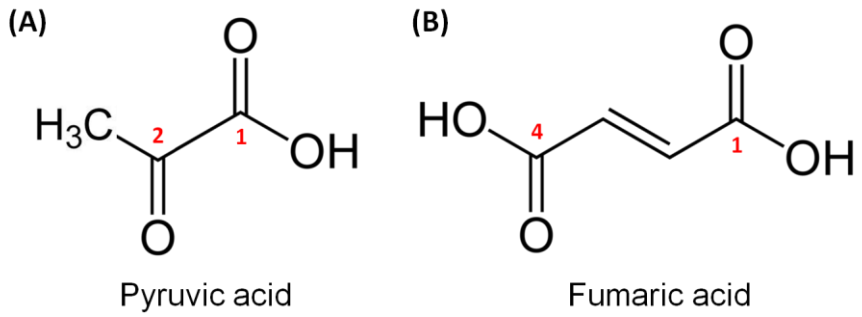

Figure 3.3: Scheme of the chemical structure of (A) pyruvic acid, (B) fumaric acid. The number in red indicates the carbon atoms that were labelled with ^{13}C and hyperpolarised.

Pyruvic acid is composed by three carbon atoms each of which can be labelled with ^{13}C. Different metabolic pathways can be studied in real-time depending on the carbon atom labelled. [1-$^{13}C_1$] pyruvic acid, for example, has been used to investigate the metabolic conversion of pyruvate to lactate (via LDH), to alanine (via ALT) or to CO_2 and bicarbonate (via PDH) (Merritt et al. 2007; Schroeder et al. 2008). On the other hand [2-$^{13}C_1$] pyruvic acid has been previously exploited to assess the TCA cycle metabolism (Schroeder et al. 2009). Pyruvic acid can also be labelled in C1 and C2 position at the same time allowing the

simultaneous investigation of LDH, ALT, PDH activity and TCA cycle metabolism (Chen et al. 2012). The characteristic T_1 of [3-$^{13}C_1$] pyruvic acid is very short, due to the presence of the methyl protons, which makes this molecule isotope position not particularly attractive for *ex vivo* and *in vivo* experiments (Rider and Tyler 2013). In this thesis [1,2-$^{13}C_2$] pyruvic acid as well as [3-$^{13}C_1$] pyruvic acid were not hyperpolarised.

Fumaric acid is a symmetric molecule formed by four carbon atoms each of which can be labelled with a ^{13}C atom. In this thesis only [1,4-$^{13}C_2$] fumaric acid was hyperpolarised. The signal obtained by hyperpolarising [1,4-$^{13}C_2$] fumaric acid therefore arises from two ^{13}C labels. Fumarase (FUM) converts [1,4-$^{13}C_2$] fumarate to [1,4-$^{13}C_2$] malate that is characterised by two non-equivalent carbons. [1,4-^{13}C] fumaric acid has been used in previous studies as an imaging agent of tumour cell death (Shan 2004).

The standard samples of [1-$^{13}C_1$] pyruvate, [2-$^{13}C_1$] pyruvate and [1,4-$^{13}C_2$] fumarate used in all the experiments reported in this Section to validate the performance of the HyperSense polariser were prepared as described below. The same standard sample of [1-$^{13}C_1$] pyruvate was also used to assess the conversion of hyperpolarised pyruvate to its metabolites *in vitro* in whole blood cells (Section 3.3) and *ex vivo* in perfused rat hearts (Section 3.4).

The hydrophilic trityl free-radical OX63 (MW = 1427g/mol) (Oxford Instruments®,UK) was used as a polarising agent for the hyperpolarisation of [1-$^{13}C_1$] pyruvate, [2-$^{13}C_1$] pyruvate and [1,4-$^{13}C_2$] fumarate.

Regardless of the carbon atom labelled with ^{13}C, pyruvic acid (MW = 89.05g/mol) is a liquid at room temperature and forms a glass when frozen. It

was therefore polarised directly without the need of a co-solvent. The standard sample (14µl) used in this thesis contained 14M of [1-$^{13}C_1$] or [2-$^{13}C_1$] pyruvic acid and 15mM free-radical. Where specified, a low concentration of gadolinium paramagnetic metal ions was added in the form of Dotarem (~1.5mM).

Fumaric acid (MW = 118.06g/mol) is solid at room temperature and was therefore dissolved in a glassing mixture with addition of a co-solvent (DMSO and water) containing the free-radicals. The final concentration of the standard sample (80µl) to polarise was approximately 2.5M [1,4-$^{13}C_2$] fumaric acid, 15mM free-radical and 1.5mM gadolinium.

3.2.3 Solid-State MR Spectrum

The sample was placed in a small plastic cup and inserted into the cryogenic chamber of the VTI using a stainless steel stick. In this position the sample cup is surrounded by a saddle coil tuned at the ^{13}C frequency (35MHz) that enables the measurement of the MR signal in the solid-state. This measurement is used mainly for calibrating the optimal microwave frequency for the sample irradiation and for monitoring the build-up of the polarisation. In Figure 3.4 a representative solid-state ^{13}C MR spectrum is shown for the pyruvic acid (labelled in C1 or C2 position) and [1,4-$^{13}C_2$] fumaric acid samples.

3.2.4 Microwave Sweep

In order to maximise the polarisation transfer from the free electrons to the ^{13}C atoms, it is necessary to induce either zero-quantum or double-quantum transition of the couple electron-nuclear system by applying a microwave pulse, as described in Section 2.7. The optimal frequency is chosen by carrying out a microwave sweep where the sample is sequentially irradiated with microwave pulses over a range of frequencies for 2min. A solid-state ^{13}C MR spectrum is acquired at the end of each irradiation by applying a 90° pulse. After the acquisition of the ^{13}C signal and before the next irradiation the residual magnetisation is destroyed by applying a spoiling pulse.

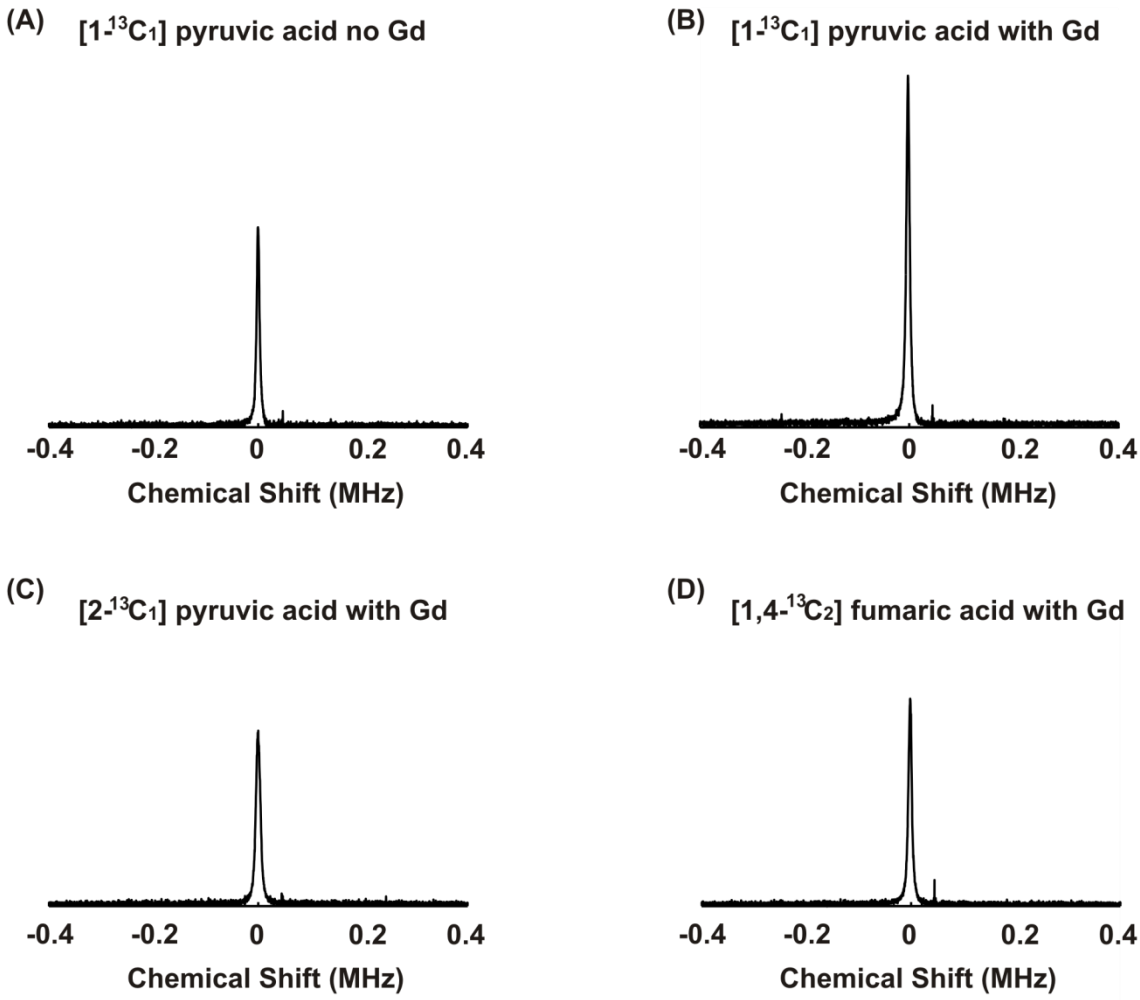

Figure 3.4: Representative solid-state ^{13}C MR spectrum measured using a pair of saddle coils placed around the sample cup in the VTI. (A) 14M [1-$^{13}C_1$] pyruvic acid and 15 mM free-radicals sample. (B) 14M [1-$^{13}C_1$] pyruvic acid, 15 mM free-radicals and 1.5 mM gadolinium sample. (C) 14M [2-$^{13}C_1$] pyruvic acid, 15mM free-radicals and 1.5mM gadolinium sample. (D) 2.5M [1,4-$^{13}C_2$] fumaric acid, 15mM free-radicals and 1.5mM gadolinium sample. The y-axis represents the ^{13}C signal intensity (a.u.). All spectra are plotted on the same scale intensity.

A representative microwave sweep is shown in Figure 3.5 where the concentration of the sample polarised was 14M [1-$^{13}C_1$] pyruvic acid, 15mM OX63 free-radical and 1.5mM gadolinium. Two peaks were found at $\Omega = \omega_e - \omega_C$ = 94.102GHz and $\Omega' = \omega_e + \omega_C$ = 94.161GHz corresponding to the

frequency that induces zero-quantum or double-quantum transition, respectively. The microwave sweep was repeated periodically to account for possible magnetic field drifts.

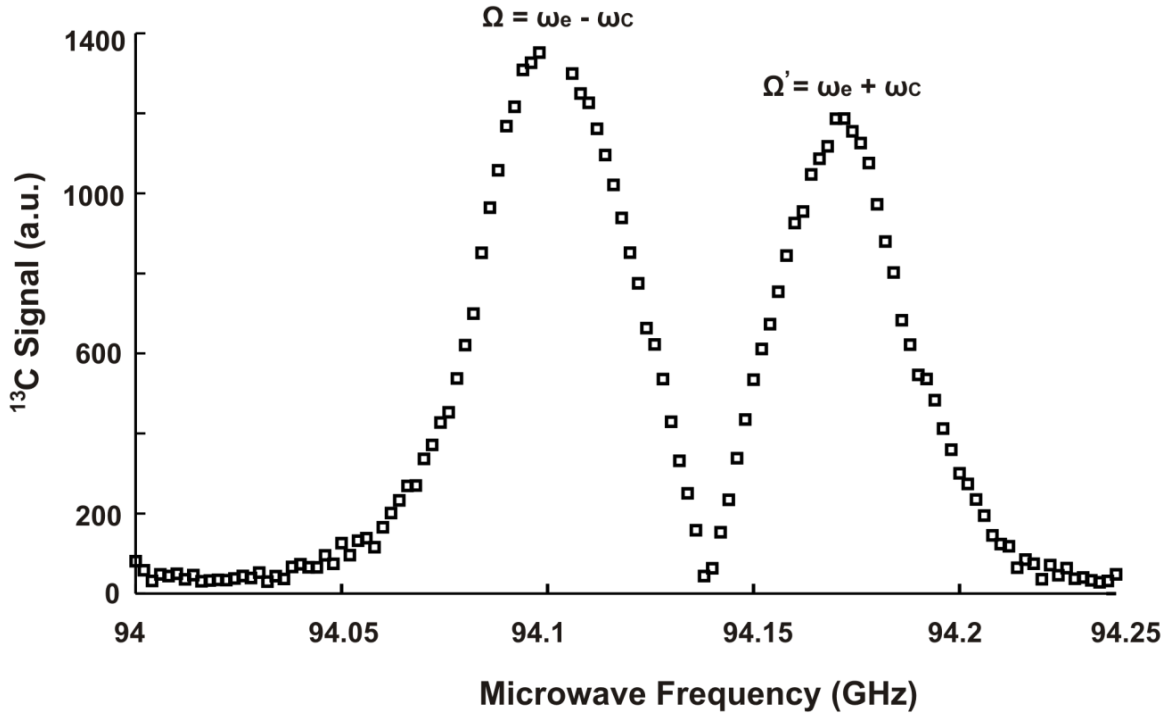

Figure 3.5: A representative microwave sweep for a 14M [1-$^{13}C_1$] pyruvic acid, 15mM OX63 free-radical and 1.5mM gadolinium sample. A solid-state ^{13}C MR spectrum was measured using a 90° flip-angle after irradiating the sample with a microwave pulse over a range of frequencies. The increment in frequency used is 2MHz.

3.2.5 Polarisation Build up

Once the irradiation frequency was optimised the sample was polarised using a microwave pulse with a characteristic frequency $\Omega = \omega_e - \omega_C$ or $\Omega' = \omega_e + \omega_C$.

The build-up of the polarisation was monitored in the solid-state by acquiring a ^{13}C MR spectrum with a small flip-angle θ applied every 5min. It is possible to quantify the time constant of the solid-state build-up T_{ss} by fitting the signal intensity curve to the mono-exponential build-up in Equation 3.1

$$M(t) = M(\infty)\left(1 - e^{-\frac{t}{Tss}}\right) \qquad 3.1$$

M(t) is the magnetisation as a function of time . M (∞) is the magnetisation at saturation (maximum polarisation achievable) and T_{ss} depends on sample conditions such as the type of molecule, free-radical concentration, microwave frequency, concentration of the paramagnetic agent and temperature. Figure 3.6 shows the characteristic build-up of a 14M [1-$^{13}C_1$] pyruvic acid, 15mM OX63 free-radicals sample irradiated at $\Omega = \omega_e - \omega_C$ and $\Omega' = \omega_e + \omega_C$. The maximum polarisation achieved using a microwave pulse at $\Omega = \omega_e - \omega_C$ is higher than that obtained when the same sample is irradiated at $\Omega' = \omega_e + \omega_C$ in agreement with the results from the microwave sweep (Figure 3.1).

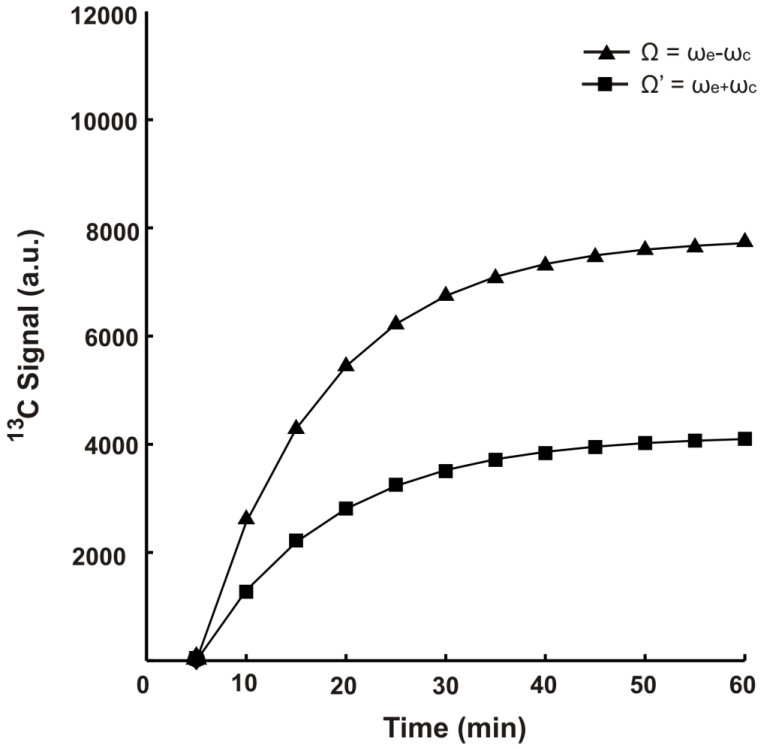

Figure 3.6: A representative polarisation build-up of a sample 14M [1-$^{13}C_1$] pyruvic acid, 15mM OX63 free-radicals without gadolinium. The maximum polarisation level was higher when the sample was irradiated at $\Omega = \omega_e - \omega_C$ than at $\Omega' = \omega_e + \omega_C$.

Figure 3.7 shows a representative polarisation build-up in the solid-state for a 14M [1-$^{13}C_1$] pyruvic acid, 15mM OX63 free-radical solution with and without 1.5mM gadolinium irradiated at $\Omega = \omega_e - \omega_C$. The maximum polarisation achieved for [1-$^{13}C_1$] pyruvic acid sample with gadolinium is higher than that obtained when the same sample without the paramagnetic agent is polarised. Previous studies have suggested that the ability of gadolinium of shorten the T_1 of electrons results in a greater final polarisation (Gordon et al. 2012).

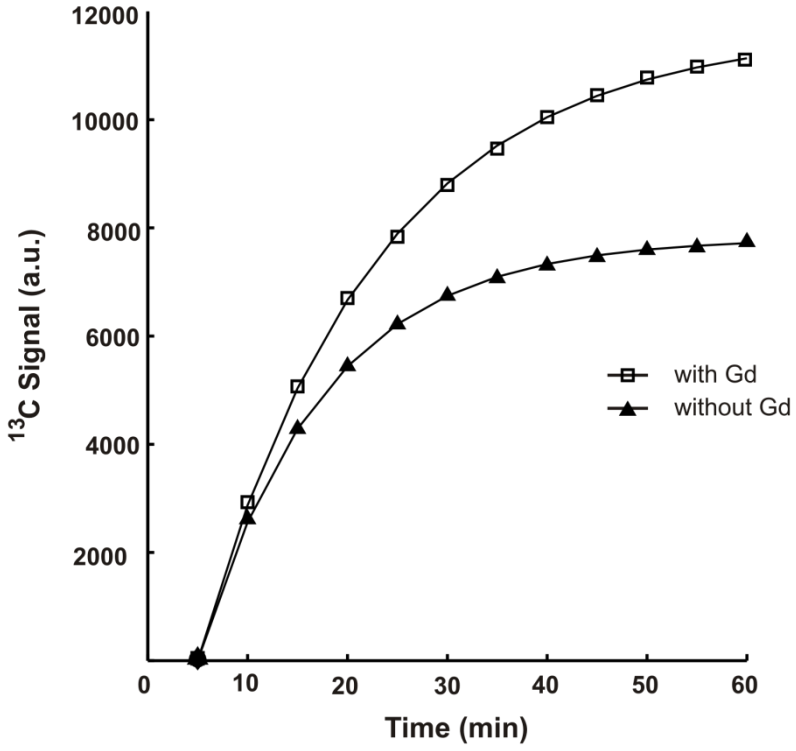

Figure 3.7: Representative solid-state polarisation built-up for a 14M [1-$^{13}C_1$] pyruvic acid, 15mM OX63 free-radical solution with and without 1 mM gadolinium.

The build-up time constant and the maximum polarisation depend also on the type of molecule. In Figure 3.8 an example of solid-state build-up is presented for three different samples: 14M [1-$^{13}C_1$] pyruvic acid, 14M [2-$^{13}C_1$] pyruvic acid and 2.5M [1,4-$^{13}C_2$] fumaric acid. All solution are characterised by the same concentration of free-radical (15mM) and gadolinium (1.5mM).

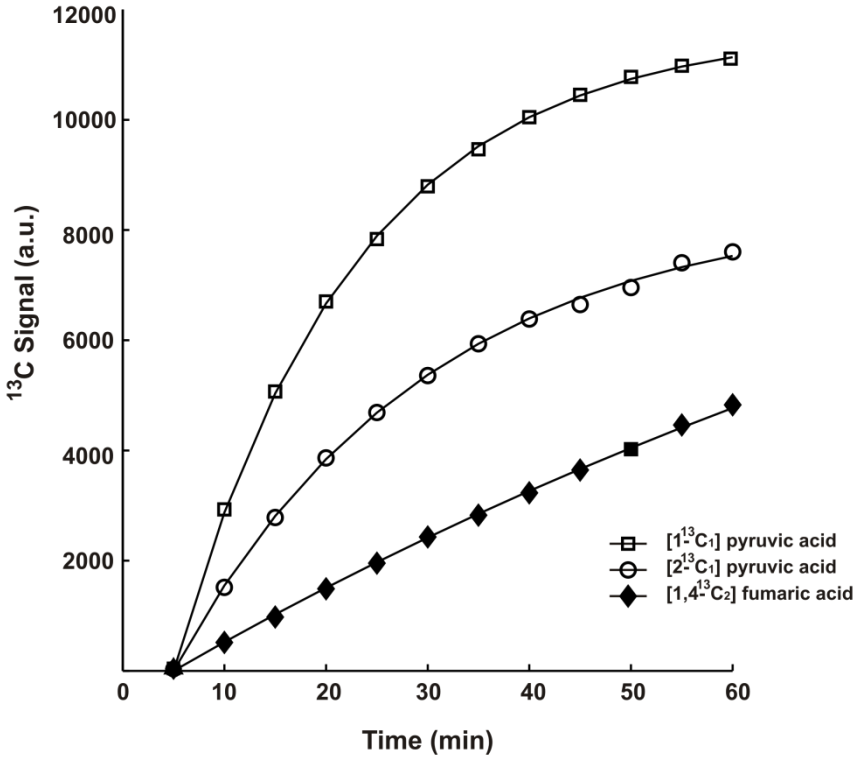

Figure 3.8: A representative solid-state build up for three different samples: 14M [1-$^{13}C_1$] pyruvic acid, 14M [2-$^{13}C_1$] pyruvic acid and 2.5M [1,4-$^{13}C_2$] fumaric acid. All three samples were characterised by the same concentration of free-radical (15mM) and gadolinium (1.5mM).

In Table 3.1 the values reported for M(∞) and T_{ss} fitting the solid-state build-up curves shown in Figure 3.6, Figure 3.7 and Figure 3.8 to Equation 3.1.

Table 3.1: Values reported for M(∞) and T_{ss} for the samples whose solid-state build-up is shown in Figure 3.6, Figure 3.7 and Figure 3.8.

	[Free-radical] (mM)	[Gadolinium] (mM)	Microwave frequency	M(∞) (a.u.)	T_{ss} (min)
14M [1-$^{13}C_1$] pyruvic acid	15	0	$\Omega = \omega_e + \omega_C$	4130	14
14M [1-$^{13}C_1$] pyruvic acid	15	0	$\Omega = \omega_e - \omega_C$.	7758	13
14M [1-$^{13}C_1$] pyruvic acid	15	1.5	$\Omega = \omega_e - \omega_C$.	11266	18
14M [2-$^{13}C_1$] pyruvic acid	15	1.5	$\Omega = \omega_e - \omega_C$.	7781	25
2.5M [1,4-$^{13}C_2$] fumaric acid	15	1.5	$\Omega = \omega_e - \omega_C$.	5133	130

3.2.6 Hyperpolarised Solution-State MR Spectrum

Once the maximum polarisation was achieved, the samples were dissolved using 4ml of 40mM TRIS buffer and 1mM EDTA. The buffer was inserted at the top of the HyperSense and heated to a high temperature (180°C or equivalently 453.15K) and high pressure (10bar). It is then injected into the sample positioned within the cryostat via an automatic pneumatic system. Both pyruvic acid and fumaric acid were neutralised by adding to the collection vessel a number of moles of NaOH equal to that of the acid contained in the sample. After dissolution the pyruvate solution was 50mM ^{13}C pyruvate (labelled in C1 or C2 position), 52µM OX63 free-radical and 5.2µM gadolinium when present. The concentration of the fumarate sample was 50mM [1,4-$^{13}C_2$] fumarate, 0.3mM OX63 free-radical and 30µM gadolinium.

600µl of the resulting hyperpolarised solutions were placed in a 5mm MR tube and quickly inserted within the 9.4T Bruker scanner next to the HyperSense where a series of ^{13}C-MRS spectra was acquired for each molecule hyperpolarised using a small flip-angle.

Figure 3.9 A shows a series of hyperpolarised ^{13}C spectra (number of spectra, ns = 128) of a 50mM [1-$^{13}C_1$] pyruvate, 52µM OX63 free-radical solution acquired with $\theta = 10^{\circ}$ and TR = 2s (total experimental time 4.26min). Figure 3.9 B shows the thermal equilibrium ^{13}C MR spectrum of the solution used in the hyperpolarised experiment and acquired using the same acquisition parameters (θ, TR, etc.) exploited for the hyperpolarised signal sampling. This ^{13}C MR spectrum was obtained by adding 32 spectra (total experimental time = 1.06min).

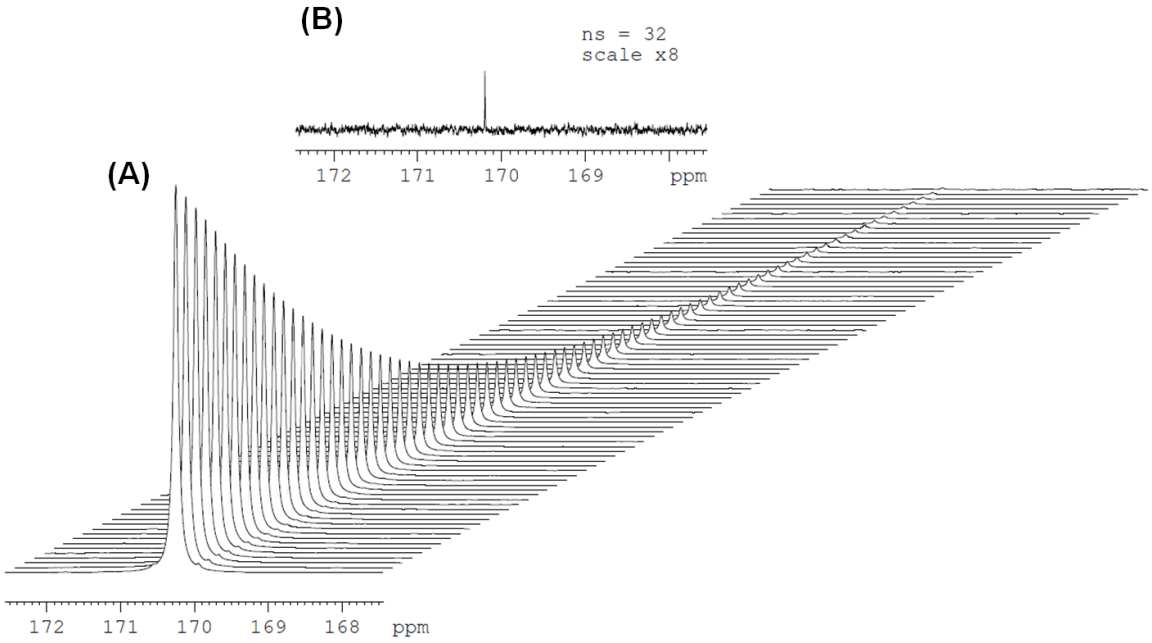

Figure 3.9: (A) Representative series of hyperpolarised ^{13}C spectra from a sample of 50mM [1-$^{13}C_1$] pyruvate, 52µM OX63 free-radical acquired with θ = 10° and TR = 2s. (B) Equilibrium ^{13}C MR spectrum of the same sample used in (A) obtained by adding 32 scans and using the acquisition parameters exploited in (A).

In Figure 3.10 A a series of hyperpolarised ^{13}C spectra (ns = 256) of 50mM [1,4-$^{13}C_2$] fumarate, 0.3mM OX63 free-radical and 30µM gadolinium solution acquired with θ = 1° and TR = 1s (total experimental time = 4.26min) is shown. In Figure 3.10 B shows the thermal equilibrium ^{13}C MR signal of the solution used in the hyperpolarised experiment and acquired using the same acquisition parameters (θ, TR, etc.) exploited for the hyperpolarised signal sampling. This ^{13}C MR spectrum was obtained by adding 128 spectra (total experimental time = 2.13min).

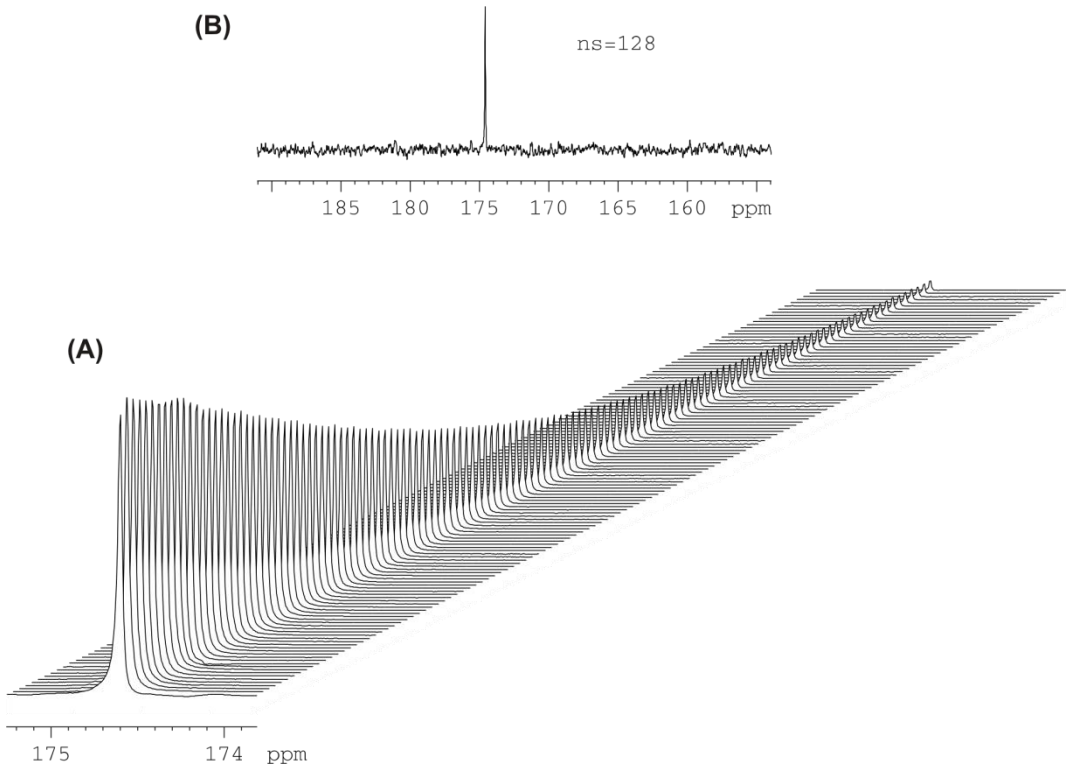

Figure 3.10: (A) Representative series of hyperpolarised ^{13}C spectra from a sample of 50mM [1,4-$^{13}C2$] pyruvate, 0.3mM OX63 free-radical and 30μM gadolinium acquired with a θ = 1º and TR = 1s. (B) Equilibrium ^{13}C MR spectrum of the same sample in (A) obtained by adding 128 scans and using the same acquisition parameters used in (A).

3.2.7 Polarisation Measurement

In this thesis the enhancement factor ξ was calculated as the ratio of the maximum intensity of the hyperpolarised signal and the signal at thermal equilibrium acquired with the same sample and experimental protocol (e.g. θ, TR, etc). The polarisation P of the hyperpolarised solution was calculated by multiplying the enhancement factor ξ by the polarisation at thermal equilibrium calculated for the same nucleus, B_0 and T. The values of ξ and P obtained for the ^{13}C molecules hyperpolarised in this thesis are presented in Table 3.2.

Table 3.2: Values of signal enhancement ξ and polarisation P obtained for the ^{13}C molecules hyperpolarised in this thesis.

	[Free-radical] (mM)	[Gadolinium] (mM)	Microwave frequency	ξ (a.u.)	P (%)
14M [1-$^{13}C_1$] pyruvic acid	15	--	$\Omega = \omega_e + \omega_C$	6947	6.7
14M [1-$^{13}C_1$] pyruvic acid	15	--	$\Omega = \omega_e - \omega_C$.	7619	10.4
14M [1-$^{13}C_1$] pyruvic acid	15	1.5	$\Omega = \omega_e - \omega_C$.	27839	22
14M [2-$^{13}C_1$] pyruvic acid	15	1.5	$\Omega = \omega_e - \omega_C$.	11429	9.3
2.5M [1,4-$^{13}C_2$] fumarate	15	1.5	$\Omega = \omega_e - \omega_C$.	4324	3.5

3.2.8 Measurement T_1 of Hyperpolarised Molecules in Solution

The hyperpolarised signal relaxes to the equilibrium signal with a characteristic decay time T_1 that depends on the type of ^{13}C molecule, sample concentration, θ, T, B_0. T_1 can be quantified in solution fitting a time-series given by the peak area of the dynamic ^{13}C MR spectra of each molecule as a function of time to Equation 2.28. $\cos^n(\theta)$ in Equation 2.28 is a correction factor for the loss of magnetisation due to the application of *n* RF pulse. When $\theta < 5^{\circ}$, $\cos^n(\theta) \approx 1$ and the correction factor can be omitted. In Figure 3.11 the characteristic relaxation curves of the hyperpolarised signal of a 50mM [1-$^{13}C_1$] pyruvate, 52mM OX63 free-radical and 50mM [1,4-$^{13}C_2$] fumarate, 0.3mM OX63 free-radical and 30μM gadolinium solutions acquired using θ = 1°, TR = 1s and ns = 256 (total experimental time = 4.26min) are plotted with overlaid fits as function of time. Table 3.3: presents the values of T_1 reported for all molecules hyperpolarised in this thesis estimated without taking in account the loss of magnetisation due to the application on *n* RF pulse as the flip-angles used were small.

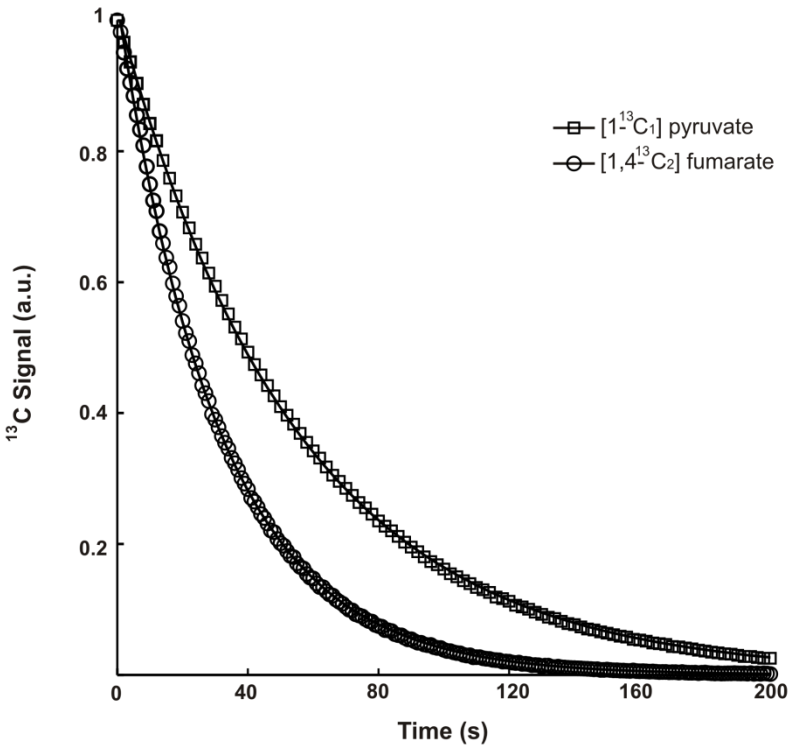

Figure 3.11: Time-series with fit overlaid of two hyperpolarised ^{13}C solutions: 50mM [1-$^{13}C_1$] pyruvate, 52µM OX63 free-radical and 50mM [1,4-$^{13}C_2$] fumarate, 0.3mM OX63 free-radical and 30µM gadolinium. The ^{13}C MR spectra of both molecules from which was derived the time-series curves were acquired θ = 1° and TR = 1s.

Table 3.3: Values of the relaxation time constant T_1 estimated without taking in account the loss of magnetisation due to the application of *n* pulse characterised by flip-angle α.

	[Free-radical] (mM)	[Gadolinium] (mM)	Microwave frequency	T_1 (s)
14M [1-$^{13}C_1$] pyruvic acid	15	--	$\Omega = \omega_e + \omega_C$	49.2
14M [1-$^{13}C_1$] pyruvic acid	15	--	$\Omega = \omega_e - \omega_C$.	52.7
14M [1-$^{13}C_1$] pyruvic acid	15	1.5	$\Omega = \omega_e - \omega_C$.	25
14M [2-$^{13}C_1$] pyruvic acid	15	1.5	$\Omega = \omega_e - \omega_C$.	38
2.5M [1,4-$^{13}C_2$] fumarate	15	1.5	$\Omega = \omega_e - \omega_C$.	31

3.3 *In vitro* MR Experimental Protocol

After demonstrating that it was possible to enhance the ^{13}C MR signal of metabolically active molecules, such as pyruvate and fumarate, further *in vitro* experiments were carried out in order to determine whether the polarisation achieved after dissolution was adequate to detect the conversion of pyruvate to its downstream metabolites in a biological system in real-time. This involved the design and validation of an *in vitro* experimental protocol described in the following sections.

3.3.1 Whole Blood Cell Preparation

All procedures involving animals were carried out in accordance with the Home Office Guidance on the Operation of Animals (Scientific Procedures) Act 1986, HMSO (London).

Blood samples from male Wistar rats were collected in heparinised MR tubes from male Wistar rats (250-300g, n = 4) under terminal anaesthesia at the same time of the excision of the heart for a separate experiment. 100µl of a hyperpolarised 50mM [1-$^{13}C_1$] pyruvate, 52µM OX63 free-radical and 5.2µM gadolinium solution was vigorously mixed with 500µl of whole blood in a 5mm MR tube before being inserted into the bore of the Bruker 9.4T Avance III spectrometer. For this type of experiment it was assumed an instantaneous mixing of the hyperpolarised solution and the blood cells to be instantaneous.

3.3.2 MR Protocol

Choosing the flip-angle θ of the RF pulse is a crucial point in the optimisation of the acquisition protocol for hyperpolarised MR signals. As mentioned in Section 3.2.8, small flip-angles are preferable to reduce the loss of signal associated with the application of a series of RF pulses (Equation 2.28). It is therefore a good experimental practice to regularly calibrate the RF pulse to account for any drift in the magnetic field of the spectrometer.

The flip-angle θ is proportional to the length of the RF pulse t_1 as shown in Equation 2.9. The calibration of the RF pulse is performed by applying RF pulses over a range of durations and measuring the generated magnetisation on the x-y axis by measuring the spectrum at each pulse. In Figure 3.12 shows a representative RF pulse calibration performed for the Broad Band Observe (BBO) coil used for the *in vitro* experiments presented in this Section.

The sample used for the calibration was 0.5M $H^{13}CO_3^-$, 1mM EDTA and 3.5mM gadolinium. The gadolinium was added to shorten the T_1 of $H^{13}CO_3^-$ and make the acquisition process faster. The length of the first RF pulse and the increment were both chosen equal to 0.5μs and the pulse power was set to 0dB. A signal intensity equal to zero is generated by a 180° RF pulse that tips the magnetisation on the –z-axis. In the example presented in Figure 3.12 the length reported for a 180° pulse was 19.5μs from which it is possible to calculate the characteristic length of a 90º pulse of 9.75μs etc.

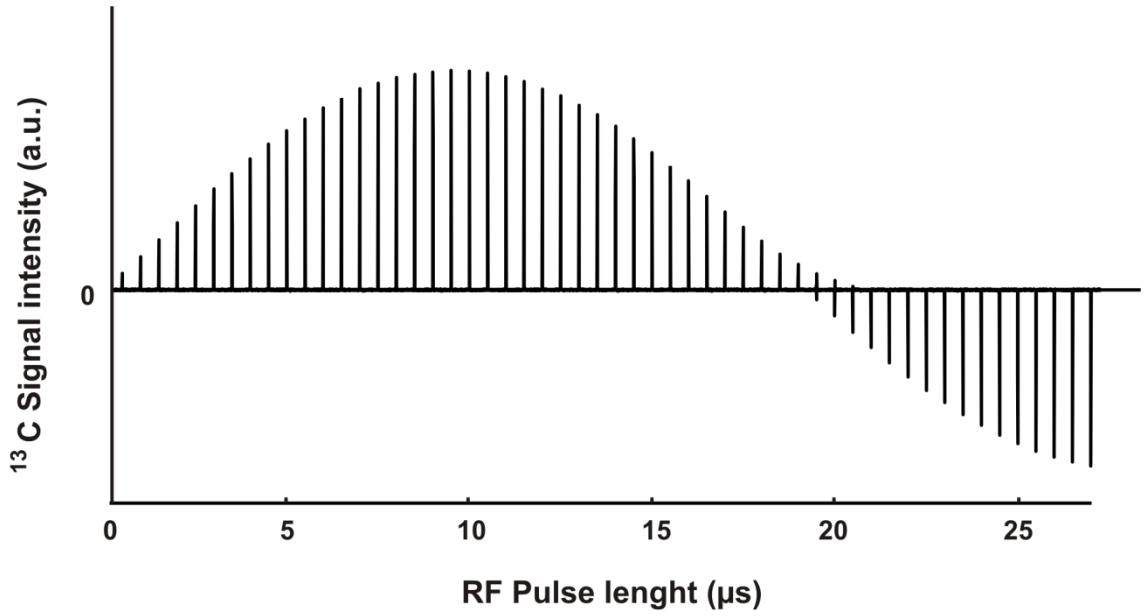

Figure 3.12: Representative calibration of the RF pulse for a BBO coil. For the acquisition of a 0.5M $H^{13}CO_3^-$, 1mM EDTA and 3.5mM gadolinium solution was used.

The relationship between the signal-loss due to the application of an RF pulse and the chosen flip-angle θ is clearly shown in Figure 3.13 A where the characteristic relaxation curves of the hyperpolarised signal of a 50mM [1-$^{13}C_1$] pyruvate, 52mM OX63 free-radical solution acquired using five different flip-angle θ (θ = 1°, 5°, 10°, 20°, 30°), TR = 2s and ns = 128 (total experimental time = 4.26min) are plotted as function of time. The larger the flip-angle, the greater the signal loss.

In agreement with the Bloch equations, the decay of the hyperpolarised signal should be mono-exponential with time constant T_1. However, Figure 3.13 B shows that only for very small values of flip-angle the decay of [1-$^{13}C_1$] pyruvate is mono-exponential (straight line). For values of θ greater than 10° the log of

the hyperpolarised signal plotted as a function of time is characterised by more complex dynamics.

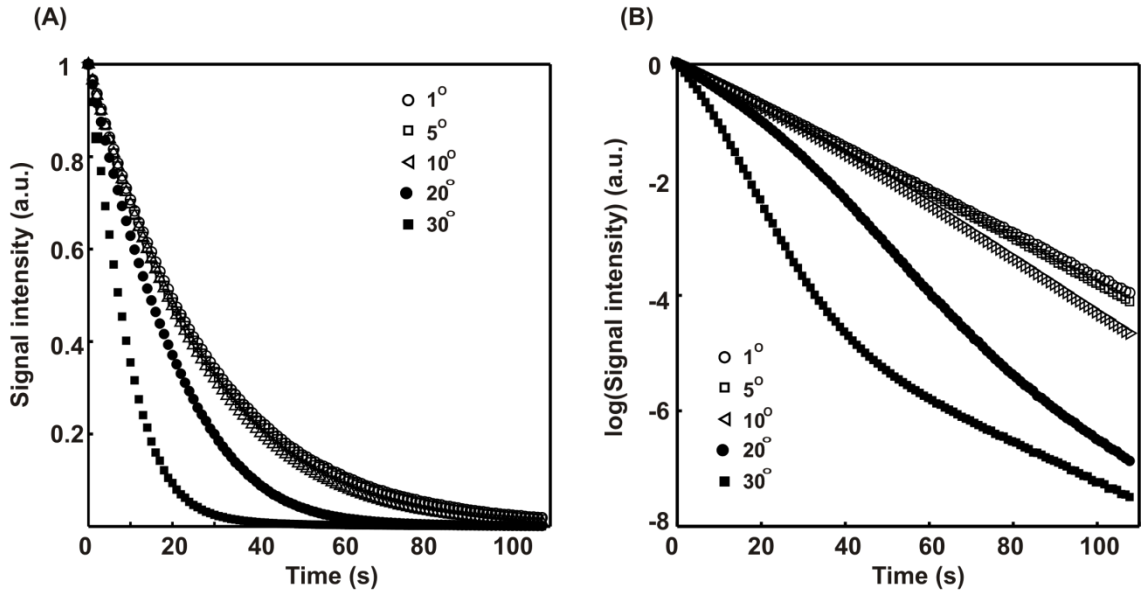

Figure 3.13: (A) Characteristic relaxation curves of the hyperpolarised signal of a 50mM [1-$^{13}C_1$] pyruvate, 52mM OX63 free-radical solution acquired for five different flip-angle θ. (B) The relaxation curves presented in (A) are plotted on logarithmic scale.

This is due to the presence of B_1 that tends to flip the magnetisation back towards the +z-axis acting against B_0. This phenomenon is commonly named "radiation damping". The greater the flip-angle, the greater the magnitude of the magnetisation and the stronger is the strength of the induced magnetic field B_1 in the receiver coil. The radiation damping effect depends also on the concentration of the hyperpolarised solution. In Figure 3.14 A the decay of the hyperpolarised signal of a 5mM [1-$^{13}C_1$] pyruvate, 52µM OX63 free-radical

solution acquired using five different flip-angle θ (θ = 1°, 5°, 10°, 20°, 30°), TR = 2s and ns= 128 (total experimental time = 4.26min) is plotted as function of time.

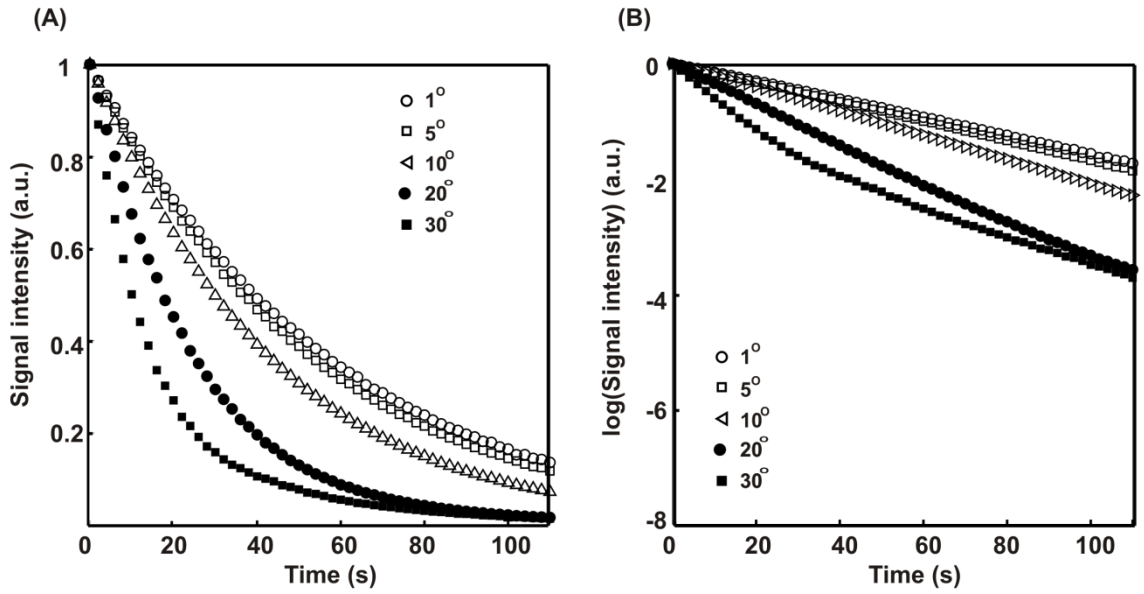

Figure 3.14: (A) Characteristic relaxation curves of the hyperpolarised signal of a 5mM [1-$^{13}C_1$] pyruvate, 52mM OX63 free-radical solution acquired for five different flip-angle θ. (B) The relaxation curves presented in (A) are plotted on logarithmic scale.

The diluted sample is characterised by a slower relaxation time constant T_1 and the radiation damping effect is less pronounced than in 50mM [1-^{13}C] pyruvate sample (Figure 3.14 B).

In order to minimise the "radiation damping" effect just described, ^{13}C MR dynamic spectra of the hyperpolarised 50mM [1-$^{13}C_1$] pyruvate, 52µM OX63 free-radical and 5.2µM gadolinium solution mixed with whole blood were

acquired using a flip angle equal θ = 10°, TR = 2s, ns = 128 (total experimental time 4.26min).

3.4 *Ex vivo* MR Experimental Protocol

The ultimate experimental challenge consisted in detecting cardiac metabolism in real-time *ex vivo* in perfused rat hearts using hyperpolarised ^{13}C MR. In order to achieve this aim an *ex vivo* MR protocol was designed and validated for perfused rat hearts. Due to the necessity of designing and optimising an MR protocol from scratch, different acquisition parameters were chosen at different stages of this thesis.

3.4.1 Langendorff Perfused Rat Heart Protocol

Male Wistar rats (250-300g) underwent terminal anaesthesia by intraperitoneal injection of sodium pentobarbitone (100mg/kg) and heparin (200IU) to avoid the formation of blood clots during the excision of the heart. After checking the absence of any reflex in the animal, a transabdominal incision was made, cutting through the diaphragm and ribs, in order to expose the thoracic cavity. The heart was gently held between fingers and the major vessels were cut taking care that sufficient length of aorta was retained. The isolated heart was temporarily arrested in cold Krebs-Henseleit buffer in order to minimise ischemic injuries (Skrzypiec-Spring et al. 2007).

A plastic cannula (ø = 3mm) was inserted into the aorta and the heart was perfused, using a peristaltic pump, with Krebs-Henseleit buffer at a constant flow of 14ml/min to achieve a perfusion pressure of 76mmHg at the coronary arteries comparable to the arterial pressure *in vivo* (Bessho and Chambers 2001). The standard composition of the Krebs-Henseleit buffer used in this thesis was: NaCl 118mM, $NaHCO_3$ 25mM, $MgSO_4$ 1.2mM, KCl 5.9mM, Na_2EDTA 0.6mM, $CaCl_2$ 2.5mM and glucose 11.1mM. When specified 2.5mM of unlabeled sodium pyruvate was added to the standard buffer. These two buffers were chosen because both commonly used in perfused rat hearts experiments (Garlick et al. 2000; Schroeder et al. 2009). The final buffer pH was adjusted to 7.4 at 37 °C. The temperature of the buffer was regulated using a thermostatically controlled water-jacketed system in which the perfusate glass reservoir and the delivery lines are surrounded by recirculating hot water (Sutherland and Hearse 2000). Finally to assure a good oxygenation of the buffer, 95% O_2 - 5% CO_2 was bubbled throughout the experiment into the Krebs reservoir.

3.4.2 Cardiac Function Measurement

Assessing the contractile function of Langendorff hearts is crucial in order to assess the consistency of the perfusion protocol as well as to confirm the contractile impairment induced by hypoxia or ischemia.

In the experiments carried out in the early stages of this thesis cardiac function was not recorded due to lack of a MR compatible system able to measure

cardiac function of a perfused heart within the magnet. In the later stages of this project, a MR compatible system able to monitor the contractile function of the perfused heart inside the magnet was developed and validated.

The pressure in the left ventricle was monitored with a water-filled balloon inserted into the left ventricular lumen connected to a pressure transducer and recording apparatus. Perfusion pressure was measured by a further pressure transducer inserted into the arterial line. Figure 3.15 shows the experimental set up developed for the hyperpolarised ^{13}C MR experiments carried out in this thesis.

Another crucial point in the development of a consistent and efficient Langendorff heart is electronic pacing. The number of full myocardial contraction per minutes decreases with the time of the perfusion because the quality of the preparation declines with time. The ability of the perfused heart to contract is also challenged by the induction of pathophysiological conditions such as hypoxia or ischemia induced during the experimental protocol. This is due to the attempt of the perfused heart to save fuel in an unfavourable energetic condition. *In vivo*, the cardiac impairment induced by the presence of hypoxia or ischemia is initially compensated by the neurohumoral system that maintains the heart rate constant straining the cardiac muscle. In order to replicate the *in vivo* situation a MR compatible pacing system was developed and used in the perfused rat hearts experiments performed in the later stage of this thesis.

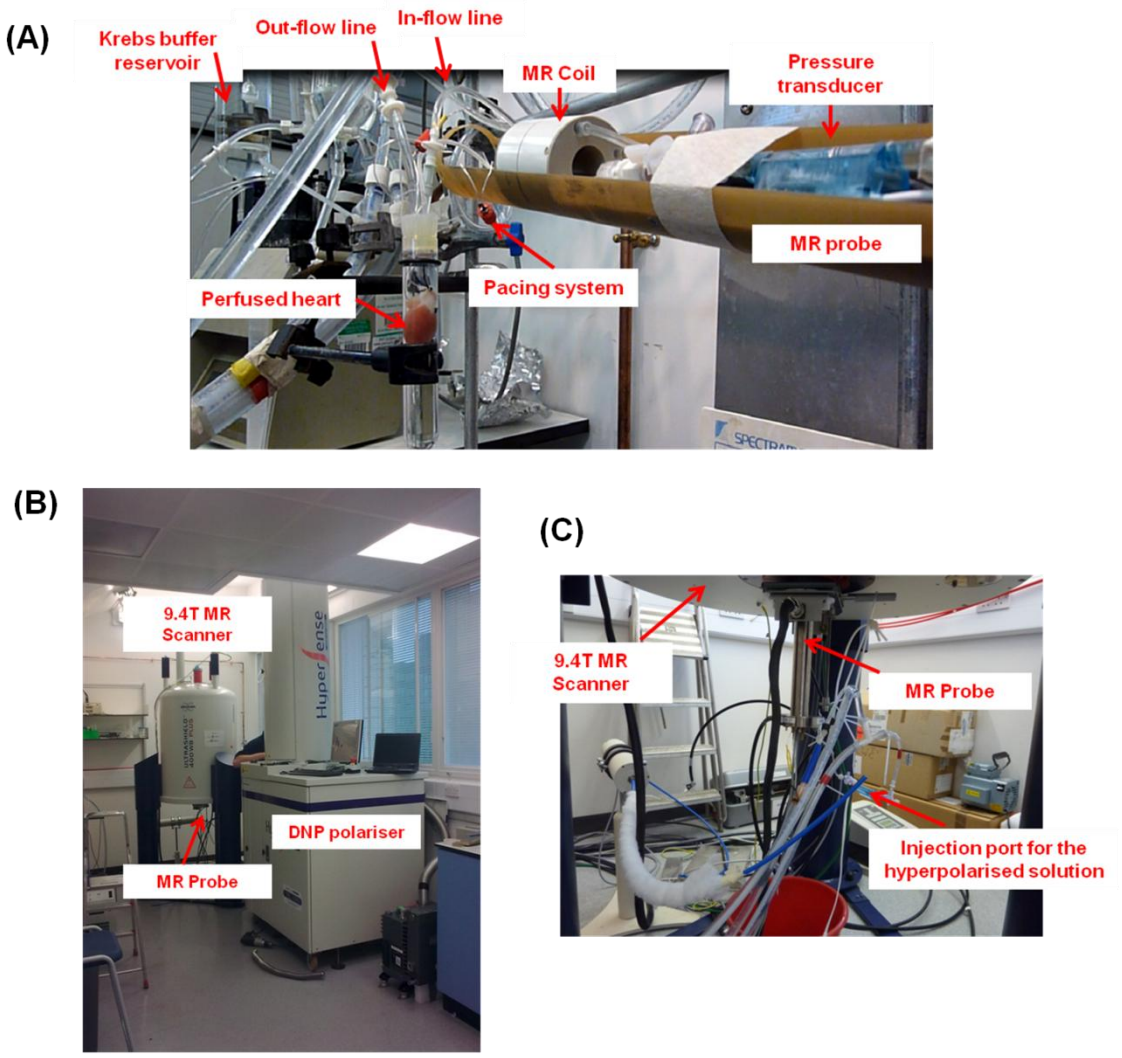

Figure 3.15: Experimental setup developed and validated at St. Thomas' hospital for hyperpolarised ^{13}C MR Langendorff perfused rat hearts experiments. (A) The perfused rat heart is cannulated, placed in a glass tube and perfused with Krebs-Henseleit buffer. Once stabilised the cardiac function the tube containing the perfused heart is inserted within the MR coil placed in the MR probe. (B) The MR probe is subsequently inserted into the 9.4T MR Bruker scanner, from the bottom, placed next to the DNP polariser. Once the hyperpolarised solution is ready it is expelled by the DNP polariser and quickly injected into the perfusion line of the perfused rat heart though the injection port shown in (C).

This system consists of a signal generator (DC) and a pair of silver wires used to deliver the electric current to the perfused heart while at the same time minimising induced currents within the MR scanner that would degrade the quality of the MR signal. The beats/min of the Langendorff perfused rat hearts were controlled by regulating the frequency of the DC current emitted by the generator.

3.4.3 MR Protocol

All experiments were carried out on a vertical wide bore Bruker 9.4T Avance III spectrometer with the bore maintained 37 °C at St. Thomas' Hospital. The perfused heart was inserted in a glass tube (ø = 15mm, sealed with a silicone bung) filled with Krebs-Henseleit buffer. Coronary perfusate was aspirated from the top by a gravity-fed siphon.

3.4.4 ^{31}P MR Spectroscopy

The experimental protocol presented in this section was developed with the help of Dr. Rodolfo Medina.

In order to validate the system used to monitor the cardiac contractility the relationship between the cardiac energy level and cardiac function was assessed using ^{31}P MRS. The detection of ^{31}P is commonly used to characterise the creatine-kinase energy shuttle described in Section 1.4.5 where under basal metabolic conditions CK converts Cr and ATP to PCr and

ADP. Under high-energy demand, PCr is rapidly re-converted to Cr and ATP is released.

In this experiment Langendorff hearts were initially perfused with a well oxygenated buffer for a period long enough to ensure their stabilisation (12min). In order to assess if the system developed for the measurement of the cardiac function was sensitive enough to detect changes associated with an external insult perfused hearts were made ischemic by stopping the flow of Krebs-Henseileit buffer (12min) and then reperfused (16min). Cardiac contractility was monitored throughout the experiment and ^{31}P MR spectra were acquired to obtain information of the metabolic state of the heart. Perfused hearts were paced at a constant frequency of 300beats/min.

^{31}P spectra were acquired using a dual-tuned $^{1}H/^{31}P$ birdcage coil (ø=15mm), flip-angle $\theta = 60^{\circ}$, TR = 3.8s and 64 scans to give a total experiment time of 4min per spectrum. In normoxia and ischemia ns = 3 (total experimental time = 12min), whereas in during the reperfusion of the isolated heart ns = 4 (total experimental time = 16min).

In Figure 3.16 the series of ^{31}P spectra acquired following the protocol described above is presented.

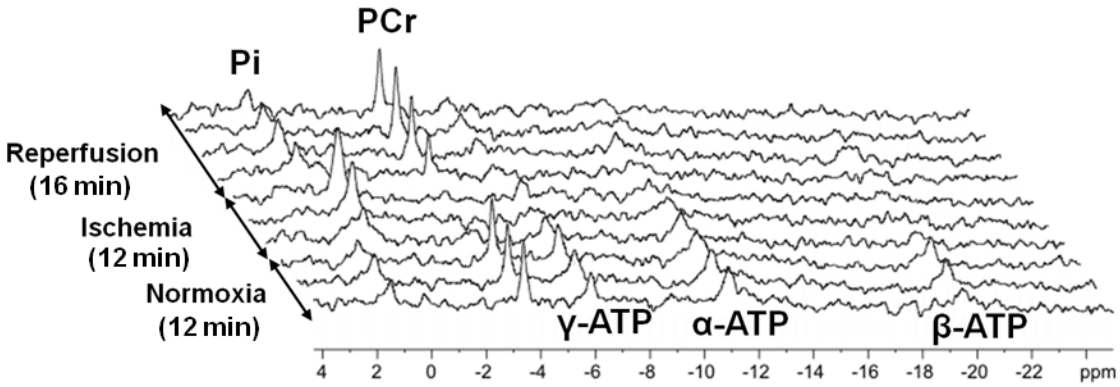

Figure 3.16: A series of ^{31}P spectra acquired from a perfused rat heart in normoxia, ischemia and during repefusion.

The perfusion pressure, heart rate, left ventricular developed pressure (LVDP) and end diastolic pressure (LVDEP) measured during the acquisition of the ^{31}P MR spectra shown in Figure 3.16 are presented in Figure 3.17.

The ^{31}P spectrum of a normoxic perfused heart yields one peak corresponding to PCr (~ -3.5ppm) and one to inorganic phosphate (Pi) (~ 1.5ppm) as well as to three peaks characteristic of the phosphates in the ATP molecule (γ-ATP, α-ATP and β-ATP). During normoxia the perfusion pressure, heart rate, LVDP and LVEP are stable (Figure 3.17). After stopping the flow of oxygenated buffer to the heart the perfusion pressure drops and the heart becomes arrhythmic (Figure 3.17 B) resulting in a significant reduction of the LVDP and LVEDP (Figure 3.17 A, C and D). In this condition, the intensity of the PCr peak in the ^{31}P spectrum diminishes together with the ATP peaks, while the P_i peak intensity increases. This is justified by the fact that during ischemia the total amount of ATP available diminishes and CK converts PCr to Cr in order to maintain the level of ATP constant (Section 1.4.6). At the same time ATP

hydrolysis leads to the production of P_i. This reaction is pH dependent and the characteristic resonance frequency of the P_i peak during ischemia is shifted towards lower frequencies (Stewart et al. 1986; Raftos et al. 1990). After reperfusion the total amount of ATP available increased as well as the PCr produced by the conversion of ATP via CK, while P_i decreased. The heart quickly recovers the rate of pacing (300beats/min), while both LVDP and LVEDP require longer time before returning to the basal value.

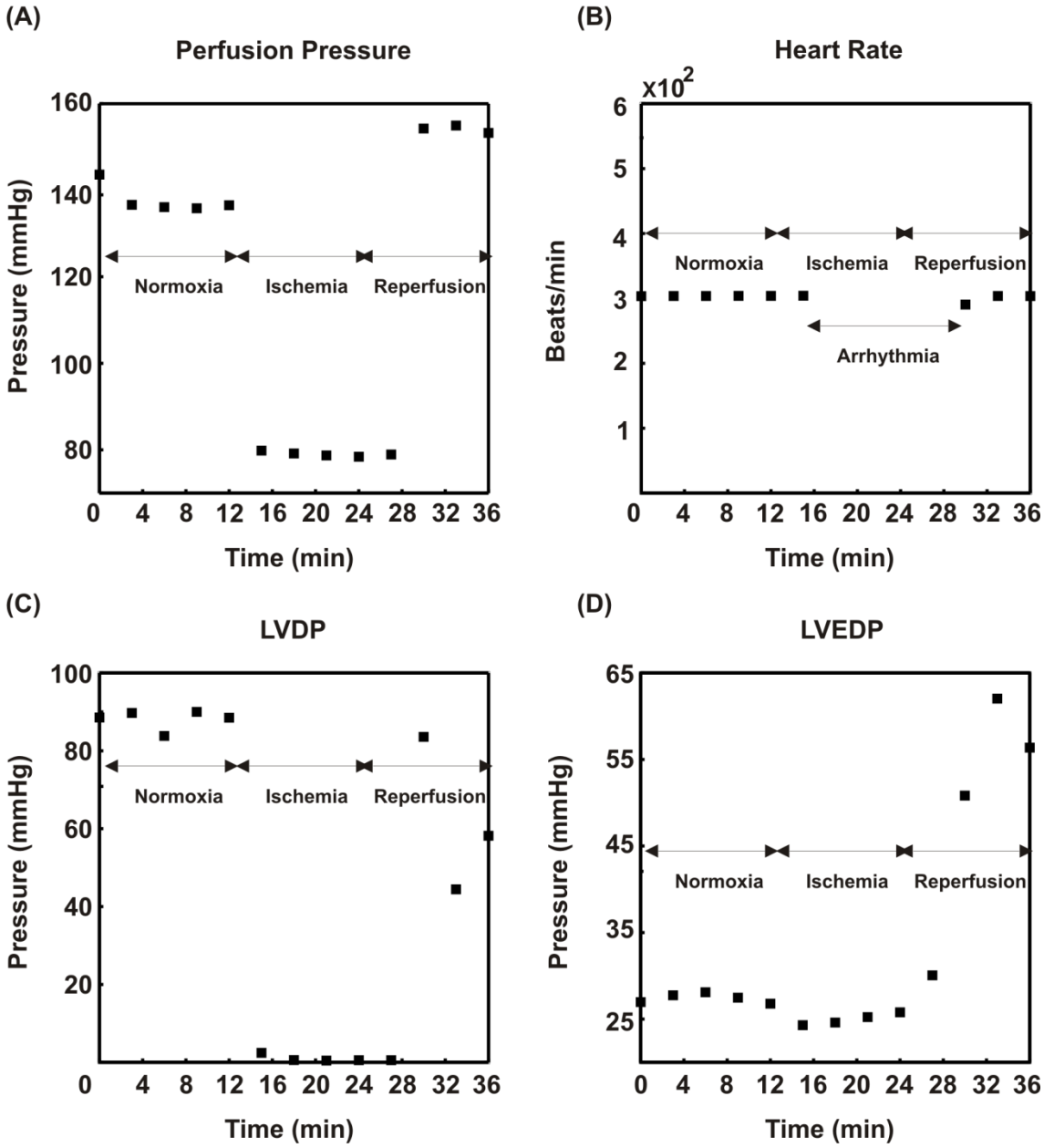

Figure 3.17: Parameters measured to monitor the cardiac contractility during the acquisition of the ^{31}P spectra presented in Figure 3.16 are presented as a function of time. (A) Perfusion pressure, (B) Heart rate, (C) LVDP and (D) LVDEP.

3.4.5 ^{13}C MR Spectroscopy

In the early stages of this thesis, the tube containing the perfused heart was placed within the isocenter of a custom-built ^{23}Na/^{13}C saddle coil (ø=15mm), and inserted into the spectrometer. Shimming was carried out using the ^{23}Na signal (FWHM 13Hz), and then re-tuned to ^{13}C. In studies carried out at a later point a ^{1}H/^{13}C birdcage coil (ø = 15mm) was used for the acquisition of the^{13}C MR spectra. Shimming was performed on the water signal using the ^{1}H channel of the coil (FWHM 35Hz). Although characterised by the same internal diameter, the two coils have a different geometry. Additionally the shimming was performed using the signal from two different nuclei characterised by a different concentration within the tube containing the perfused heart and its perfusion solution. The sensitivity of the two coils was not measured in this thesis and therefore it is not possible to exclude a priori that the ^{23}Na/^{13}C saddle coil and the ^{1}H/^{13}C birdcage coil are characterised by a different sensitivity. This factor has to be taken into account when the acquired hyperpolarised ^{13}C MR spectra are interpreted.

Regardless the type of coil used the acquisition of the MR data was commenced at the end of the dissolution. In all the experiments presented in this Section a 50mM [1-$^{13}C_1$] pyruvate, 52µM OX63 free-radical and 5.2µM gadolinium hyperpolarised solution was injected into the perfused heart through an injection pump. A time-series of ^{13}C-MR spectra (ns = 128) was acquired using a single acquisition per spectrum, θ = 10°, TR = 2s (total experimental time = 4.26 min). ^{13}C MRS data were processed and analysed using TopSpin

(Bruker). All spectra were baseline corrected and integrals of each peak extracted as a function of time.

Two groups of Langendorff hearts (n=5 for each group) were used. The first group was perfused with the standard Krebs-Henseleit buffer containing 11.1mM glucose while the buffer used to perfuse the second group contained 11.1mM glucose and 2.5 mM sodium pyruvate. Details on the type of experimental protocol used for the acquisition of the dynamic ^{13}C spectra for each heart are reported in Table 3.4.

Table 3.4: Experimental protocol used to acquire hyperpolarised ^{13}C MR time-series from Langendorff rat hearts.

	Buffer	Cardiac Function	Pacing	Coil
Heart 1	Glucose	NO	NO	$^{23}Na/^{13}C$
Heart 2	Glucose	NO	NO	$^{23}Na/^{13}C$
Heart 3	Glucose	NO	NO	$^{23}Na/^{13}C$
Heart 4	Glucose	NO	NO	$^{23}Na/^{13}C$
Heart 5	Glucose	YES	YES	$^{1}H/^{13}C$
Heart 6	Glucose + Pyruvate	NO	NO	$^{1}H/^{13}C$
Heart 7	Glucose + Pyruvate	NO	NO	$^{1}H/^{13}C$
Heart 8	Glucose + Pyruvate	NO	NO	$^{1}H/^{13}C$
Heart 9	Glucose + Pyruvate	YES	YES	$^{1}H/^{13}C$
Heart 10	Glucose + Pyruvate	YES	YES	$^{1}H/^{13}C$

3.4.6 Metabolite Peak Assignment

Natural abundance ^{13}C MR spectra of a range of metabolites were acquired to assign relevant metabolite peaks detected in the hyperpolarised spectra. Each sample was prepared by mixing 600µl of PBS, 60µl of deuterium and the metabolite (150mM, pH = 7.4). 128 spectra were acquired for each compound using a flip-angle $\theta = 30°$, TR = 21s (total experimental time = 45min) and then added together (Appendix A). The final spectrum of each compound was

compared with the ^{13}C hyperpolarised spectrum acquired for each heart and matches were found.

3.4.7 ^{13}C MR Spectroscopic Imaging

All the images presented in this Section were acquired in collaboration with Dr. Kilian Weiss (PhD student at the Institute for Biomedical Engineering at the University and ETH, Zurich).

In the MRSI experiments the tube containing the Langendorff heart (n=2, perfused with Krebs- Henseleit buffer containing 11.1mM glucose only) was placed within the isocenter of a dual-tuned $^{1}H/^{13}C$ birdcage coil with (ø = 20mm). A hyperpolarised 50mM [1-$^{13}C_1$] pyruvate, 52µM OX63 free-radical and 5.2µM gadolinium solution was injected in both hearts. Shimming was performed on the water signal using the ^{1}H channel of the coil (FWHM 35Hz). Cardiac contractility was not recorded in these experiments and perfused hearts were left beating spontaneously.

In order to check the position of the heart within the coil, standard ^{1}H cine images were acquired in short axis and four chamber view using a self-gated gradient echo sequence (Heijman et al. 2007) with the following parameters; TE: 2.9ms, TR: 8ms, acquisition matrix: 128 x 128, field of view: 32 x 32 mm^2, spatial resolution: 250 x 250 μm^2, slice thickness: 5mm, $\theta = 20°$, 10 cardiac frames.

Hyperpolarised ^{13}C spectroscopic images of [1-$^{13}C_1$] pyruvate and its metabolites [1-$^{13}C_1$] lactate and $H^{13}CO_3^-$ were acquired using an echo planar

spectroscopic imaging (EPSI) sequence as shown in Figure 3.18. The acquisition parameters were as follows; TE: 1.315ms, TR: 89ms, time between dynamic images Δt = 5s, acquisition matrix: 16 x 16, field of view: 32 x 32 mm^2, θ = 20°, spatial resolution: 2 x 2 mm^2, slice thickness: 5mm, spectral bandwidth during acquisition: 6250Hz, spectral resolution 12.2Hz. For each experiment 64 images were acquired in a total time of 320s starting with the dissolution of the sample. MRSI data were reconstructed using Matlab (Mathworks Inc., Natick, MA). To avoid spectral N/2 ghosts, even and odd echoes of the echo planar readout were combined after linear phase correction of the even echoes, resulting in a spectral bandwidth of 3125Hz.

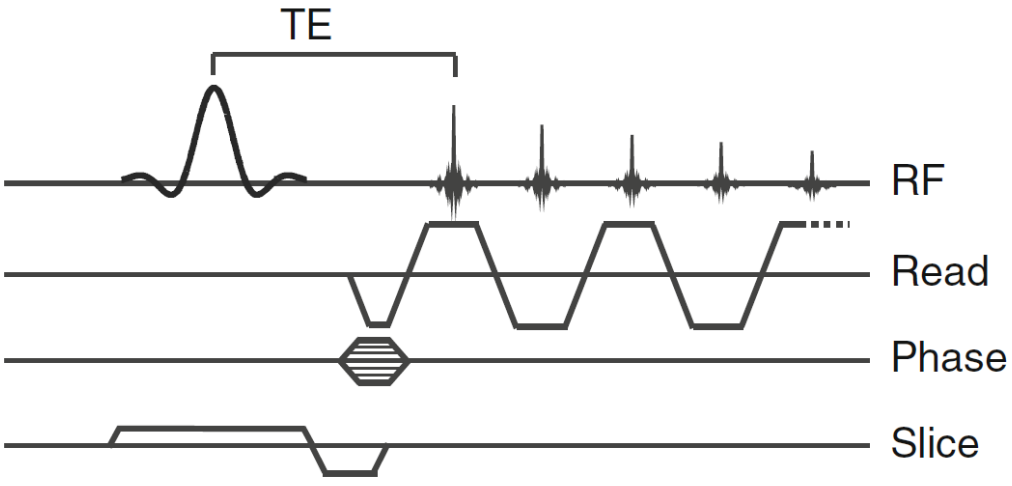

Figure 3.18: Schematic diagram of the echo planar spectroscopic imaging (EPSI) sequence. Slice selective excitation is followed by phase encoding. The signal is acquired during an alternating gradient train. Adapted from reference (Weiss and Mariotti et al. 2012).

3.5 *Ex vivo* PET Experimental Protocol

All the experiments presented in this Section were carried out by Dr. Richard Southworth and Dr. Rodolfo Medina in order to quantify the uptake of two PET tracers [^{18}F]-FDG and [^{18}F]-FMISO in normoxic and hypoxic perfused rat hearts. [^{18}F]-FDG was provided by the clinical PET Centre, St. Thomas' Hospital, whereas [^{18}F]-FMISO was prepared following a previously reported method (Oh et al. 2005).

Langendorff rat hearts (n = 4 for [^{18}F]-FDG and n=3 for [^{18}F]-FMISO) were perfused with a Krebs-Henseleit buffer containing 11.1mM glucose only. Cardiac contractile function was monitored with a water-filled balloon inserted into the left ventricular lumen as explained in Section 3.4.2. A bolus of each radiotracer (1MBq in 100µl KHB) was administered via an in-line injection port, and its transit through the perfusion apparatus was monitored by NaI detectors (i) in the arterial line above the heart cannula, and (ii) directly opposite the heart (to quantify the tracer accumulation in the heart) connected to a GinaSTAR TM ITLC unit (Figure 3.19). All datasets were acquired with a time resolution Δt = 0.0033min.

After a stabilisation period, where KHB perfusate was gassed with 95% O_2-5% CO_2, the first bolus of either [^{18}F]-FDG or [^{18}F]-FMISO was injected into the perfusion line, and their passage through the system under "normoxic" conditions was recorded. After 5 min, hypoxia was induced by switching to a second reservoir (KHB gassed with 95% N_2 - 5% CO_2). Further boli of each tracer were injected into the system after 5min and 15min of hypoxic buffer perfusion respectively, and the kinetics of cardiac retention monitored.

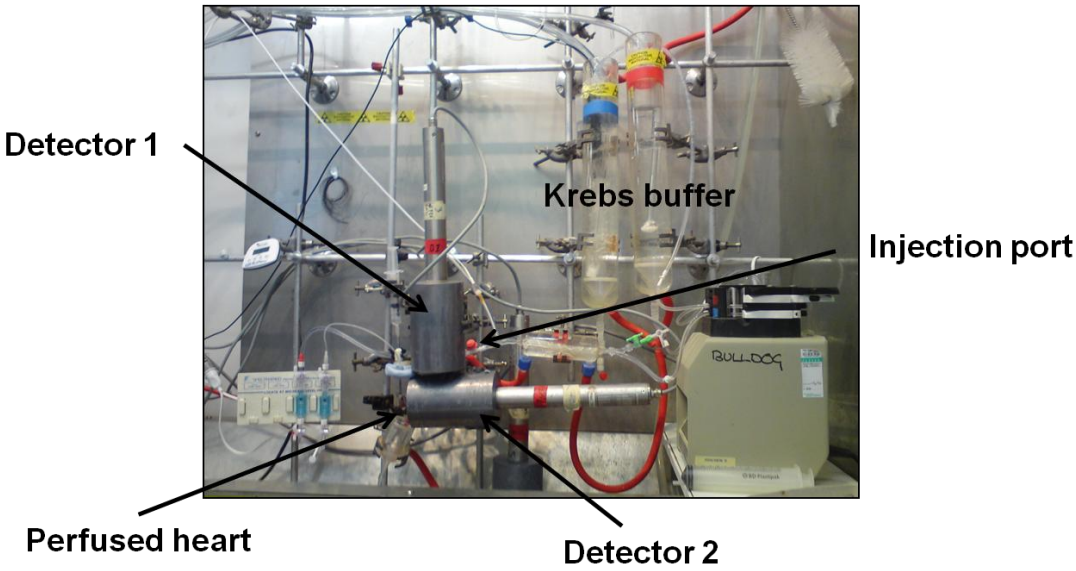

Figure 3.19: Experimental set up. In each experiment, a bolus of [^{18}F]-FDG or [^{18}F]-FMISO was injected through the injection port and its passage through the perfusion line was recorded using two NaI γ-detectors able to measure the input (detector 1) and the tissue (detector 2) time-activity curves. Adapted from (Mariotti et al. 2013).

Chapter 4 : Kinetic Modelling

4.1 Introduction

Imaging modalities are able to detect the distribution of endogenous probes. While MRI informs on structure, function and perfusion, MRS and hyperpolarised technologies allow the distinction and imaging of an injected molecule from its downstream metabolites to uncover biochemical changes in the myocardium. PET and SPECT are characterised by a significantly higher sensitivity than MR, but the signals from injected tracers and their metabolites are indistinguishable. 1D dynamic time-series containing information on the interaction between the injected imaging agent and the underlying biological system are directly acquired *in vitro* or *ex vivo*, or can be obtained from 2D or 3D *in vivo* images by plotting the signal over the time for either a ROI, or pixel by pixel. Regardless the technique used the dynamics of the imaging agents is typically described by differential equations whose solution to an impulse input is multi-exponential. Kinetic information on the observed phenomenon can be derived by fitting the time-series with mathematical models.

The available analysis methods can be divided in two groups:

- Quantitative

- Semi-quantitative

The gold standard quantitative analysis technique is represented by compartmental modelling (Godfrey 1982). This approach allows a complete characterisation of the imaging agent kinetics by deriving micro (e.g. rates of conversion) and macro (net uptake) parameters. It however requires *a priori* assumptions of the number of compartments involved in the tracer kinetics, information not always available especially when new biological systems or imaging agents are studied. The hybrid Maximum Entropy/Nonlinear Least Squares method (MEM/NLS) (Steinbach et al. 2002) and Spectral-based Algorithms (SA) (Cunningham and Jones 1993; Bertoldo et al. 1998) are quantitative analysis techniques that allow the full characterisation of the tracers dynamics and require little *a priori* knowledge of the system studied. They therefore represent a valid alternative to compartmental modelling when there is a certain degree of uncertainty on the metabolic pathway or on the system assessed. An alternative approach is represented by graphical methods (Patlak et al. 1983) that allow estimating macro parameters from the dynamic curves, but do not fully describe the tracer kinetics. Together with the quantitative analysis techniques mentioned above, semi-quantitative indices are routinely used in the characterisation of tracer kinetics (Huang 2000; Lehtio et al. 2003; Hill et al. 2013). They are simple to apply, but less informative and more sensitive to experimental conditions than quantitative methods.

4.2 Aims

This Chapter introduces the quantitative and semi-quantitative techniques used in this thesis for the analysis of time-activity curves of PET tracers acquired *ex vivo* from perfused rat hearts and hyperpolarised MR dynamic data whose acquisition is presented in Chapter 3.

Compartmental modelling is the gold standard analysis methods for both PET and hyperpolarised MR dynamic data. In Section 4.3.1 the most commonly used compartmental models in PET are presented with particular reference to the irreversible radiotracers used in this thesis: [^{18}F]-FDG and [^{18}F]-FMISO. The application of this analysis technique to the kinetic analysis of hyperpolarised data is described in Section 4.3.2.

The biological systems studied using hyperpolarised MR probes or PET tracers are not always well characterised. In this case analysis methods that require a minimum *a priori* knowledge of the biological mechanisms involved in the dynamics observed are desirable. A general introduction on the implementation of the MEM/NLS algorithm is presented in Sections 4.4 with particular reference to hyperpolarised time-series acquired *in vitro* (Section 4.4.1). Spectral-based algorithms and graphical methods applied to *ex vivo* PET data are introduced in Section 4.5 and 4.6, respectively. Section 4.7 introduces the semi-quantitative techniques exploited for the analysis of *ex vivo* PET time-activity curves and hyperpolarised dynamic data. Finally, the Monte Carlo method used in this thesis to assess the accuracy and reproducibility of the proposed analysis methods is introduced in Section 4.8.

4.3 Compartmental Modelling

In compartmental modelling, a system is approximated by a number of compartments that interact with each other at characteristic rates. This approach requires some general assumptions such as an instantaneous mixing of the imaging agent within each compartment and that the amount of tracer added does not perturb the system under study (Gunn et al. 2001). Depending on the type of imaging technique used, different compartmental models are used in order to account for the characteristic interaction of the imaging agent with the underlying biological system and the experimental protocol.

4.3.1 PET Dynamic Data

A three compartment, three rates model (3K model) (Figure 4.1) (Sokoloff et al. 1977) is the most commonly used compartmental model for the kinetic analysis of time-activity curves of irreversible tracers such as [^{18}F]-FDG and [^{18}F]-FMISO (Bertoldo et al. 1998; Wang et al. 2009). According to this model, the radiotracers can move back and forward between the plasma/blood (C_p) and a reversible tissue compartment (C_e), but once it enters the irreversible compartment C_m it cannot return into the plasma.

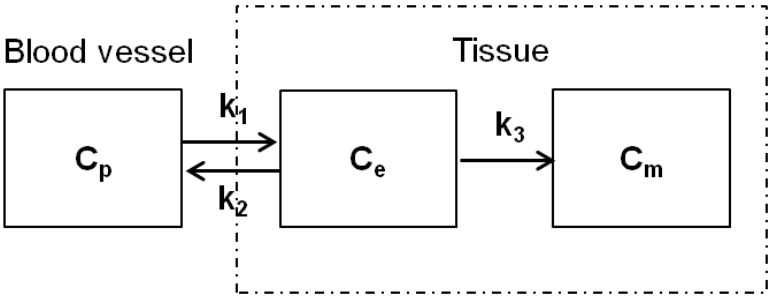

Figure 4.1: Block diagram for a 3K compartmental model used for PET tracer that are irreversibly trapped such as [^{18}F]-FDG and [^{18}F]-FMISO.

The evolution in time of the tissue compartments in Figure 4.1 is described by a system of linear differential equations as follow:

$$\frac{dC_e(t)}{dt} = k_1 C_p(t) - (k_2 + k_3) C_e(t) \quad 4.1$$

$$\frac{dC_m(t)}{dt} = k_3 C_e(t) \quad 4.2$$

$$C_e(0) = 0 \quad 4.3$$

$$C_m(0) = 0 \quad 4.4$$

where k_1 and k_2 are unknown kinetic rates that characterise the movement of the tracers from the blood stream to the tissue (influx) and vice versa (efflux), while k_3 is the rate at which the tracer moves from the reversible to the irreversible tissue compartment. In PET experiments $C_p(t)$, which represents the delivery of the radiotracer to the tissue of interest, is assumed to be known and can be measured through blood sampling *in vivo* or using a γ-detector coupled with the inflow line *ex vivo*. The solution of Equations 4.1- 4.4 is given by:

$$C_e(t) = k_1 e^{-(k_2+k_3)t} \otimes C_p(t) \quad 4.5$$

$$C_m(t) = \frac{k_1 k_3}{k_2 + k_3}\left(1 - e^{-(k_2+k_3)t}\right) \otimes C_p(t) \quad 4.6$$

where ⊗ indicates the mathematical operator convolution. The total amount of signal in the ROI (e.g. voxel or field of view of the detector) that includes the tissue and the vascular space is given by:

$$C_{ROI}(t) = (1 - V_b)(C_e(t) + C_m(t)) + V_b C_b(t) \quad 4.7$$

V_b and C_p representing the fraction of vascular space in the tissue of interest and the tracer concentration in whole blood, respectively (Lammertsma et al. 1992). By fitting the experimental data to Equation 4.7 the unknown parameters k_1, k_2, k_3 and V_b can be derived.

Approximating the delivery input function $C_p(t)$ by a sum of exponentials and assuming that the whole blood curve is approximated by the plasma curve Equation 4.7 can be re-written as follow:

$$C_{ROI}(t) = V_b C_b(t) + (1 - V_b)(C_{reversible}(t) + C_{irreversible}(t)) \quad 4.8$$

$$C_b(t) = C_p(t) \quad 4.9$$

$$C_{reversible}(t) = \frac{k_1 k_2}{k_2 + k_3} e^{-(k_2+k_3)t} * C_p(t) \quad 4.10$$

$$C_{irreversible}(t) = \frac{k_1 k_3}{k_2 + k_3} * C_p(t) \quad 4.11$$

For $t \to \infty$ the reversible component decreases, while the irreversible component increases. The net uptake rate for this type of model is given by:

$$K_i = \frac{k_1 k_3}{k_2 + k_3} \qquad 4.12$$

For example for [^{18}F]-FDG this index can be used *in vivo* to calculate glucose metabolic rate (MR_{gluc}) as the product of K_i and the steady-state concentration of glucose (C_{gluc}) in the blood (Equation 4.13).

$$MR_{gluc} = \frac{C_{gluc}}{LC} \cdot K_i \qquad 4.13$$

The “lumped constant” (LC) in Equation 4.13 is used to relate the measured uptake of [^{18}F]-FDG to that of glucose. This correction factor assumes that the transport and the phosphorylation rates of glucose and its tracer do not change with respect to each other (Sokoloff et al. 1977). Langendorff hearts are usually perfused with a constant glucose concentration (11.1 mM) and therefore MR_{gluc} should be directly proportional to K_i. However, previous studies have identified a mismatch between glucose and [^{18}F]-FDG uptakes under a number of pathophysiological conditions such as ischemia (Southworth 2009). In these conditions the LC is not constant and the accuracy of the estimation of the glucose uptake using [^{18}F]-FDG is limited.

The approach just introduced assumes that each compartment is homogenous. When time-series reflect the distribution of the tracers within heterogeneous systems, the most appropriate approach is given by the compartmental model shown in Figure 4.2 A. It considers one compartment for the plasma and *n* 3K models representing the heterogeneity of the tissue studied. This is equivalent to a 3K model shown in Figure 4.2 B and is described by the following system of differential equations:

$$\frac{dC_e(t)}{dt} = k_1' C_p(t) - (k_2(t) + k_3(t)) C_e(t) \quad 4.14$$

$$\frac{dC_m(t)}{dt} = k_3(t) C_e(t) \quad 4.15$$

$$C_e(0) = 0 \quad 4.16$$

$$C_m(0) = 0 \quad 4.17$$

Using the exponential approximation for $k_2(t)$ and $k_3(t)$ (Equations 4.18 and 4.19) the number of unknown parameters to estimate by fitting the experimental data is five: k_1' is the rate constant of the influx of the tracer from the plasma to the heterogeneous tissue, k_2' and k_3' the mass-weighted rate constants for efflux of the tracer from the heterogeneous tissue to the plasma and for the transport in the irreversible compartment, respectively. C_1 and C_2 are parameters that describe the time varying nature of $k_2(t)$ and $k_3(t)$ (Schmidt et al. 1991).

$$k_2(t) = k_2'\left(1 - C_1 e^{-C_2 t}\right) \quad 4.18$$

$$k_3(t) = k_3'\left(1 - C_1 e^{-C_2 t}\right) \quad 4.19$$

The net uptake rate for this type of model is given by:

$$K_i' = \frac{k_1' k_3'}{k_2' + k_3'} \quad 4.20$$

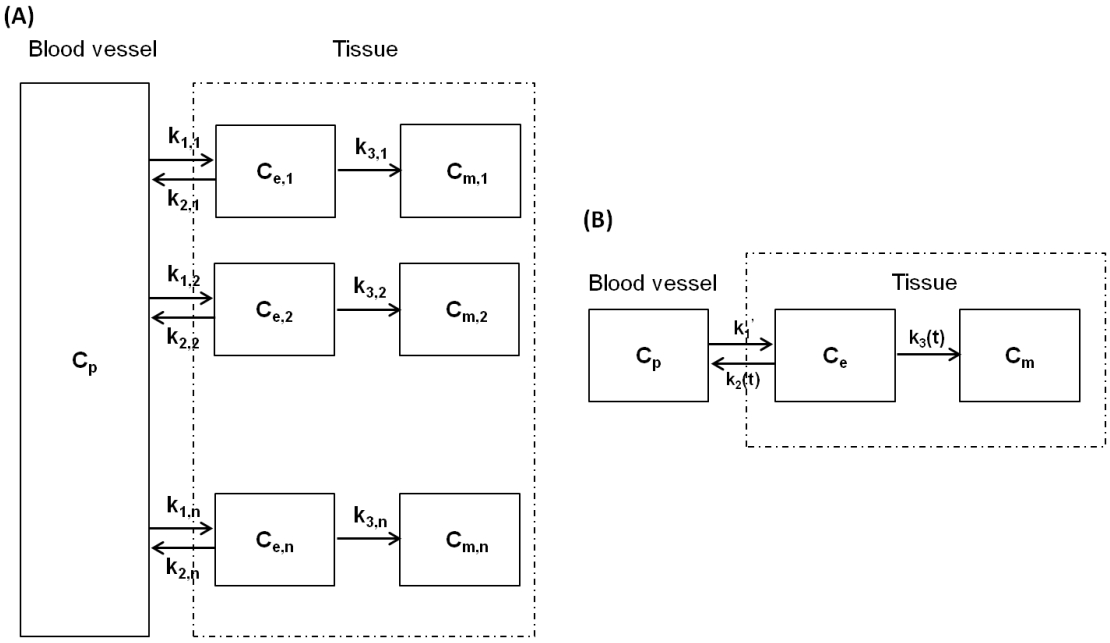

Figure 4.2: (A) Block diagram for a heterogeneous system where *n* 3K compartmental models are considered to represent the heterogeneity of the tissue. (B) Simplification of the system shown in (A). k_1' is the rate constant of the influx of the tracer from the plasma to the heterogeneous tissue. $k_2(t)$ and $k_3(t)$ are given by Equations 4.3 and 4.4.

4.3.2 Hyperpolarised Dynamic Data

Hyperpolarised MR allows the metabolically active molecule injected into the system of study to be distinguished from its downstream metabolites in a time

window given by approximately $5*T_1$, with T_1 indicating the longitudinal relaxation time of the hyperpolarised signal. The evolution in time of this type of system is described by the Bloch-McConnell equations obtained combining the traditional Bloch equations with those describing the chemical reaction as explained below.

The chemical exchange between two molecules A and B can be modelled with a two-compartment kinetic model as shown in Figure 4.3.

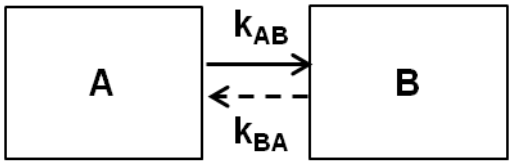

Figure 4.3: Block diagram for the chemical exchange of two molecules.

k_{AB} and k_{BA} are the characteristic rates of conversion between A and B. This system is described by a system of linear differential equations as follows:

$$\frac{dA(t)}{dt} = -k_{AB}A(t) + k_{BA}B(t) \quad 4.21$$

$$\frac{dB(t)}{dt} = k_{AB}A(t) - k_{BA}B(t) \quad 4.22$$

Equations 4.21 and 4.22 can be also written in matrix form:

$$\frac{d}{dt}\begin{bmatrix}A(t)\\B(t)\end{bmatrix}=\begin{bmatrix}-k_{AB} & k_{BA}\\ k_{AB} & -k_{BA}\end{bmatrix}\begin{bmatrix}A(t)\\B(t)\end{bmatrix} \quad 4.23$$

The Bloch equations that describe the evolution of the net magnetisation of a spin-system in the presence of an external magnetic field and relaxation processes can be written in the rotational frame as:

$$\frac{d}{dt}\begin{bmatrix}M_x(t)\\M_y(t)\\M_z(t)\end{bmatrix}=\begin{bmatrix}-\frac{1}{T_2} & -\omega_0 & 0\\ \omega_0 & -\frac{1}{T_2} & 0\\ 0 & 0 & -\frac{1-M_0}{T_1}\end{bmatrix}\begin{bmatrix}M_x(t)\\M_y(t)\\M_z(t)\end{bmatrix} \quad 4.24$$

where ω_0 is the Larmor frequency of the nucleus observed and M_0 represents the steady-state nuclear longitudinal magnetisation (Section 2.2.2).

The evolution in time of longitudinal component of the net magnetisation of nuclear spin-systems in chemical exchange is described by the Bloch-McConnell equations obtained by combining Equation 4.23 with the Bloch equations (Equation 4.24) as follows:

$$\frac{d}{dt}\begin{bmatrix}M_{z,A}(t)\\M_{z,B}(t)\end{bmatrix}=\begin{bmatrix}\frac{M_{0,A}-1}{T_{1,A}}-k_{AB} & k_{BA}\\ k_{AB} & \frac{M_{0,B}-1}{T_{1,B}}-k_{BA}\end{bmatrix}\begin{bmatrix}M_{z,A}(t)\\M_{z,B}(t)\end{bmatrix} \quad 4.25$$

where $M_{z,(A,B)}$ and $M_{0,(A,B)}$ are the longitudinal and the steady-state nuclear magnetisations of the two species, respectively. The compartmental model

described by Equation 4.25 is presented in Figure 4.4 where $r_{1A} = T_{1A}^{-1}$ and $r_{1B} = T_{1B}^{-1}$ are the relaxation rates of the hyperpolarised signal of compartment A and B, respectively.

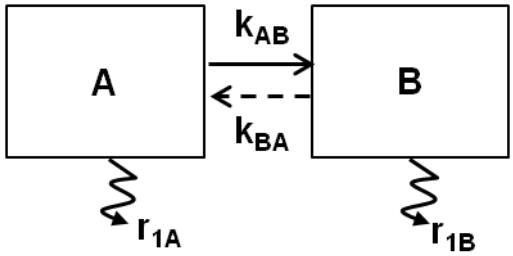

Figure 4.4: Block diagram for the chemical exchange between the hyperpolarised molecules A and B

The hyperpolarised magnetisation is several orders of magnitude more intense than that at thermal equilibrium ($M_z >> M_0$). For this reason in this case it is possible to consider $M_0 \approx 0$. Under this assumption the kinetics of $M_z(t)$ of the two chemical species A and B is obtained by solving System 4.25 with $M_{0,A} = C$ and $M_{0,B} = 0$ (Equations 4.26- 4.28).

$$M_{z,A}(t) = \frac{C \cdot \left[(k_{AB} + r_{1A} - \lambda_2)e^{-t\lambda_1} + (k_{BA} + r_{1B} - \lambda_2)e^{-t\lambda_2}\right]}{\lambda_1 - \lambda_2} \quad 4.26$$

$$M_{z,B}(t) = \frac{C \cdot k_{AB}(e^{-t\lambda_2} - e^{-t\lambda_1})}{\lambda_1 - \lambda_2} \quad 4.27$$

$$\lambda_{1,2} = (r_{1B} + r_{1A} + k_{AB} + k_{BA}) \mp \sqrt{((r_{1B} + k_{BA}) - (r_{1A} + k_{AB}))^2 + 4k_{AB}k_{BA}} \quad 4.28$$

$$r_{1,(A,B)} = T_{1(A,B)}^{-1} - TR^{-1}\ln(\cos\theta) \quad 4.29$$

The term $TR^{-1}\ln(\cos\theta)$ takes in account the loss of hyperpolarised signal due to the application of a RF excitation pulse characterised by a flip angle θ.

Depending on the experimental protocol, it may be necessary to consider the delivery of the hyperpolarised probe to the tissue of interest (see Figure 4.5).

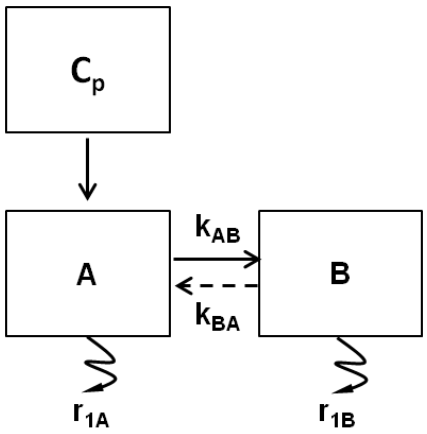

Figure 4.5 : Bloch diagram that describe the conversion of a hyperpolarised molecule A into to its metabolic product B through a single first order enzymatic conversion.

In this thesis the delivery of the hyperpolarised solution to the assessed system $C_p(t)$ (input function) was not detected experimentally. $C_p(t)$ was approximated to a delta function for *in vitro* experiments where the mixing of the hyperpolarised probe with the cell solution is considered instantaneous (Section 5.2.1), while for *ex vivo* perfused rat hearts experiments $C_p(t)$ was modelled as a γ-variate function (Section 5.3.1).

The equations that describe M_z of A and B as a function of time are given by the convolution of Equations 4.26 and 4.27 with $C_p(t)$:

$$M_{z,A}(t) = \frac{C \cdot \left[(k_{AB} + r_{1A} - \lambda_2)e^{-t\lambda_1} + (k_{BA} + r_{1B} - \lambda_2)e^{-t\lambda_2}\right]}{\lambda_1 - \lambda_2} \otimes C_p(t) \quad 4.30$$

$$M_{z,B}(t) = \frac{C \cdot k_{AB}(e^{-t\lambda_2} - e^{-t\lambda_1})}{\lambda_1 - \lambda_2} \otimes C_p(t) \quad 4.31$$

where $\lambda_{1,2}$ is presented in Equation 4.28. The unknown parameters to estimate are C, k_{AB}, k_{BA}, r_{1a} and r_{1b}. They can be derived by fitting the experimental data to the mathematical function that describe the kinetics of the longitudinal magnetisation $M_z(t)$ of the two metabolites. All the equations derived above are valid if the two metabolites A and B are exchangeable. If the enzymatic reaction is unidirectional all the equations introduced above are still valid assuming k_{BA} = 0.

Enzymatic conversions of metabolites depend on the availability of one or more cofactors (e.g. ATP is the cofactor for the conversion of Cr to PCr via CK). Hyperpolarised probes are injected into the system at super physiological concentrations, potentially inducing a rapid depletion of the cofactors involved in the enzymatic reaction studied. In systems able to rapidly regenerate the cofactor through other metabolic pathways the conversion of metabolite A into B can be considered independent from the availability of the cofactors and modelled as explained above. When the system is not able to compensate for the loss of cofactor, the enzymatic reaction observed after the injection of the hyperpolarised metabolite does depend on the availability of cofactor and it

follows a second order kinetics. In this condition, the chemical conversion of molecule A to molecule B can be modelled using a three-compartment second-order kinetic model as shown in Figure 4.6.

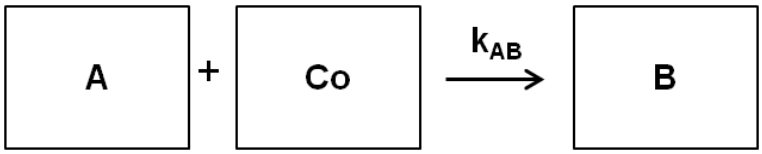

Figure 4.6: Block diagram for a second-order chemical conversion of molecule A to molecule B including the depletion of the cofactor Co.

Co rappresents the cofactor compartment. This system is described by a system of non-linear differential equations as follows:

$$\frac{\mathrm{d}}{\mathrm{dt}}\begin{bmatrix}\mathrm{A(t)}\\ \mathrm{B(t)}\\ \mathrm{Co(t)}\end{bmatrix} = \begin{bmatrix}-\mathrm{k_{AB}Co(t)} & 0 & 0\\ \mathrm{k_{AB}Co(t)} & 0 & 0\\ -\mathrm{k_{AB}Co(t)} & 0 & 0\end{bmatrix}\begin{bmatrix}\mathrm{A(t)}\\ \mathrm{B(t)}\\ \mathrm{Co(t)}\end{bmatrix} \qquad 4.32$$

The Bloch-McConnell equations that the described the evolution in time of the longitudinal component of the net magnetisation of the system shown in Figure 4.6 are obtained by combining Equation 4.30 with the Bloch equation (Equation 4.25) as follows:

$$\frac{d}{dt}\begin{bmatrix} M_{z,A}(t) \\ M_{z,B}(t) \\ M_{z,CO}(t) \end{bmatrix} = \begin{bmatrix} -(k'_{AB} + r_{1A}) & 0 & 0 \\ (k'_{AB} + r_{1A}) & -r_{1B} & 0 \\ -(k'_{AB} + r_{1A}) & 0 & -r_{1CO} \end{bmatrix} \begin{bmatrix} M_{z,A}(t) \\ M_{z,B}(t \\ M_{z,CO}(t) \end{bmatrix} \quad 4.33$$

r_{1CO} is the relaxation rate of the hyperpolarised magnetisation associated with Co and r_{1A} and r_{1B} are described by Equation 4.29.

Depending on the experimental protocol, it may be necessary to consider the delivery of the hyperpolarised probe to the tissue of interest (Figure 4.7).

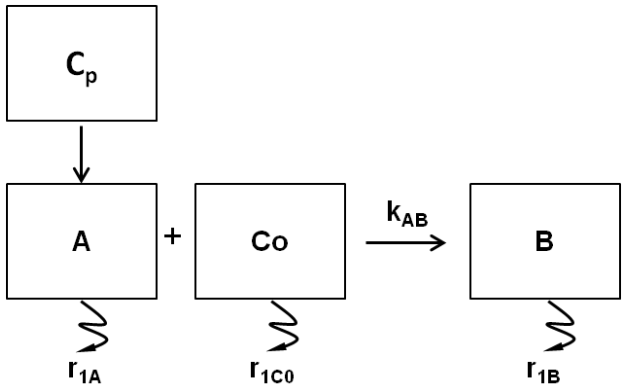

Figure 4.7: Bloch diagram that describe the conversion of a hyperpolarised molecule A into to its metabolic product B through a single second order enzymatic conversion.

This type of system is described by a system of differential equations as follow:

$$\frac{d}{dt}\begin{bmatrix} M_{z,A}(t) \\ M_{z,B}(t) \\ M_{z,CO}(t) \end{bmatrix} = \begin{bmatrix} -(k'_{AB} + r_{1A}) & 0 & 0 \\ (k'_{AB} + r_{1A}) & -r_{1B} & 0 \\ -(k'_{AB} + r_{1A}) & 0 & -r_{1CO} \end{bmatrix} \begin{bmatrix} M_{z,A}(t) \\ M_{z,B}(t \\ M_{z,CO}(t) \end{bmatrix} + C_p(t) \quad 4.34$$

By fitting the data to the solution of Equations 4.34, assuming for example $M_{z,(A,B)}(0) = 0$ and $M_{z,CO}(0) = C_0$, it is possible to derive the values of the unknown parameters C_0, k_{AB}, $k_{BA,}$ r_{1A} and r_{1B}.

The measurement of the optimal input function for hyperpolarised *in vivo* and *ex vivo* experiments is still an unsolved problem. The dynamics of the injected hyperpolarised molecule does not represent the input function because this not only contains information on the delivery of the injected probe but also on its metabolic conversion. Recent studies have proposed methods to obtain an accurate measure of the *in vivo* input function directly by measuring the hyperpolarised metabolite signal in the arterial blood or indirectly by detecting the hyperpolarised signal of urea, a non metabolically active compound, injected into the system at the same time of the molecule of interest (von Morze et al. 2012; Kazan et al. 2013). Alternatively, the delivery of the hyperpolarised probe to the tissue of interest can be modelled as a sum of exponentials (Menichetti et al. 2012). *In vitro* it is reasonable to assume that the mixing between the hyperpolarised solution and the cells suspension or enzyme is instantaneous, and therefore $C_p(t)$ can be approximated to a delta function.

4.4 Maximum Entropy/Nonlinear Least Squares Method

In order to derive kinetic information on the underlying physiological or biochemical processes, multi-exponential time-series can be fitted to a function given by the discrete sum of exponentials as follows:

$$x(t) = \sum_{i=1}^{n_c} A_i \exp(-r_i t) \qquad 4.35$$

where A_i is the characteristic amplitude of the rate r_i and n_c is the total number of kinetic components contained in the data. The problem of finding the optimal value for the unknown parameters A_i, r_i and n_c is often formulated as an optimisation problem and a nonlinear least squares (NLS) algorithm is commonly used.

This approach requires *a priori* knowledge of the nature of the tracer kinetics and it is likely to be hampered by the "multiple minimum problem". NLS, through an iterative process, choose the optimal value for the unknown parameters by minimising the sum of squares of the vertical distances of the fitting curve and the data (Motulsky and Christopoulos 2004). This corresponds to find the global minimum of the surface formed by the curves generated by all possible combinations of values of the unknown parameters. When the number of kinetic rates to derive is high, this surface is characterised by multiple minima and in this condition it is likely that the NLS fails in discerning the global minimum from the surrounding local minima which do not minimise the sum of square. The ability of the NLS to find the global minimum avoiding the local minima also

depends on the initial values of the unknown parameters chosen that correspond to the point on the multidimensional curve where the algorithm starts to find the global minimum.

Experimental time-series can alternatively be fitted to a continuous function defined in Equation 4.36.

$$x(t) = \int_{-\infty}^{\infty} g(\log\tau)\exp(-t/\tau)\,d\log\tau \qquad 4.36$$

This formulation corresponds to the Laplace transform where the integral over the rate constant $r = 1/\tau$ is replaced by an integral over $\log\tau$. Experimental dynamic curves can be characterised by kinetic rates that differ by several orders of magnitude and therefore a logarithmic space is more appropriate for their derivation than a linear one. The distributions that best describe the data are obtained by applying the inverse Laplace transform to x(t) without any assumption on the nature of the metabolic conversion. The Laplace inversion of experimental data characterised by random noise is an ill-posed problem (e.g. an infinite number of solutions is available) and a regularisation strategy is required to find the optimal distribution $g(\log\tau)$. The maximum entropy method (MEM) finds the unique optimum distribution $g(\log\tau)$ maximising the following function (Mohammad-Djafari et al. 2002):

$$Q = S - \alpha\,\chi^2 \qquad 4.37$$

where the S is the entropy term and χ^2 is the normalised mean square error given by Equations 4.38 and 4.39 respectively (Steinbach et al. 2002).

$$S(\vec{f},\vec{F}) = \sum_{j=1}^{M}\left[f_j - F_j - f_j \ln\left(\frac{f_j}{F_j}\right)\right] \qquad 4.38$$

$$X^2 = \frac{1}{N}\sum_{i=1}^{N}\left(\frac{Fit_i - Data_i}{\sigma_i}\right) \qquad 4.39$$

where M in Equation 4.38 is the number of points in which the fitting function is estimated, whereas N in Equation 4.39 is the number of point in which the experimental measure is available. $\vec{f}$ is a vector containing the values of the MEM distribution that best approximates the experimental data at each time point. $\vec{F}$ is used during the optimisation process to filter artefacts from $\vec{f}$ (Steinbach et al. 2002). This approach guarantees a unique solution independent on the initial guess of the model parameters. MEM, however, intrinsically forces $\vec{f}$ to follow $\vec{F}$ leading to biased results and non-random residuals (Steinbach et al. 2002).

Steinbach and colleagues have proposed a new analysis method based on a hybrid Maximum Entropy/Nonlinear Least Squares method (MEM/NLS) that allows combining the advantages of NLS with those of MEM. Using MEM/NLS, the distribution of rates that best describes the experimental data is derived without any *a priori* assumption of the number of the kinetic processes described in the time-series; it is unique and not biased.

The MEM/NLS algorithm is based on an iterative process that exploits a continuous distribution derived from the experimental data through MEM to insert one exponential at time in the NLS fit.

In more details, as the first iteration of the MEM optimisation starts $\vec{f}$ is set equal to $\vec{F}$. A Newton-Raphson optimisation of Q at fixed values of λ is followed by automatic adjustments of this Lagrange multiplier. During the optimisation of *Q*, S and χ^2 are progressively adapted to maximise Q. When the value of χ^2 stops changing appreciably (<1%) the optimisation of Q is terminated. At this point, the first NLS fit is performed with a number of exponentials equal to the total number of peaks in the MEM distribution. The initial values for the amplitude and the initial values of the discrete rates are set equal to the area under the curve and the mean of the peaks in the continuous solutions, respectively. The large and well resolved peaks in $\vec{f}$ are include in $\vec{F}$ unchanged, while the smaller and less resolved features are blurred before being added to $\vec{F}$. Once the new $\vec{F}$ is defined, the optimisation of Q is started afresh with $\vec{f} = \vec{F}$. Every time the MEM algorithm converges the number of peaks *n* in the continuous distribution is characterised and the NLS fit is performed with one exponential more than those used at the previous iteration. If the number of peaks in the continuous distribution is increased by more than one from the previous iteration, only the *n+1* peaks with the largest AUC are considered for the NLS fit in an iterative process until all the peaks that appear in the continuous distribution are accounted for in the discrete fit. The MEM optimisation is terminated when the number of peaks is not changed from the previous iteration. The optimal

distributions are chosen according to the values of X^2 and the correlation length of the residuals τ_{corr} given by the sum of the autocorrelation function $|C_j|$ (Equation 4.40) over the first three quarters of the time interval:

$$C_j = \frac{\langle (R_i - \langle R \rangle)(R_{i+j} - \langle R \rangle) \rangle}{\langle R^2 \rangle - \langle R \rangle^2} \qquad 4.40$$

$\langle \_ \rangle$ indicates the mean over *i*. τ_{corr} is a measure of the systematic deviation of the derived distribution from the data and therefore this index is very helpful in deciding which is the optimal fit among all those generated.

The chosen optimal MEM distribution is the last one for which both X^2 and τ_{corr} have decreased by more than 1% from the previous MEM optimisation. While the chosen optimal NLS fit will be that characterised by the maximum number of exponentials, *n*, for which both X^2 and τ_{corr} have decreased by more than 1% from those reported for the discrete distribution characterised by *n-1* kinetic rates.

4.4.1 Hyperpolarised Dynamic Data

As previously mentioned, hyperpolarised time-series of the injected molecule and its metabolites are characterised by a multi-exponential dynamics and therefore the MEM/NLS algorithm can be used to extract kinetic information of the metabolic conversion observed.

Assuming to have as input to the MEM/NLS algorithm two time-series corresponding to the evolution in time of the MR signal of the hyperpolarised molecule A and its metabolite B observed *in vitro* (impulse input function) then a possible MEM/NLS solution is:

$$A_{MEM_{NLS}}(t) = A_1 e^{-t\lambda_{1A}} + A_2 e^{-t\lambda_{2A}} \quad 4.41$$

$$B_{MEM_{NLS}}(t) = B_1 e^{-t\lambda_{1B}} + B_2 e^{-t\lambda_{2B}} \quad 4.42$$

where A_i and B_i are amplitudes and λ_{ij} are kinetic rates.

After deriving the number of kinetic rates that characterised the dynamic of hyperpolarised time-series, it is possible to associate a compartmental model to the metabolic pathway under certain hypotheses. It is however not possible to unequivocally associate a model to the data. A compartmental model that is compatible with this the MEM/NLS solution in Equations 4.41 and 4.42 is that shown in Figure 4.5 with $C_p \approx$ delta function. Under this hypothesis the amplitudes and the rates in Equations 4.41 and 4.42, derived without any assumption on the system studied, are related to the characteristic rates and amplitudes of a two-compartment, bidirectional kinetic model described by Equations 4.30 and 4.31 as follows:

$$A_1 = C(k_{AB} + r_{1A} - \lambda_2)/(\lambda_1 - \lambda_2) \quad 4.43$$

$$A_2 = C(k_{BA} + r_{1B} - \lambda_2)/(\lambda_1 - \lambda_2) \quad 4.44$$

$$\lambda_{1A} = \lambda_{1B} = \lambda_1 \quad 4.45$$

$$\lambda_{2A} = \lambda_{2B} = \lambda_2 \quad 4.46$$

$$B_1 = Ck_{AB}/(\lambda_1 - \lambda_2) \quad 4.47$$

$$B_2 = -Ck_{AB}/(\lambda_1 - \lambda_2) \quad 4.48$$

Another possible solution that can be obtained by fitting the two time-series corresponding to the hyperpolarised molecule A and its metabolite B with the MEM/NLS algorithm is:

$$A_{MEM_{NLS}}(t) = A_1 e^{-t\lambda_{1A}} \quad 4.49$$

$$B_{MEM_{NLS}}(t) = B_1 e^{-t\lambda_{1B}} + B_2 e^{-t\lambda_{2B}} \quad 4.50$$

In this case a two-compartment, unidirectional (k_{AB} = 0) compartmental model is compatible with the MEM/NLS solution. The relationship between the rates and the amplitudes derived with MEM/NLS and those characteristics of a two compartment, one-way reaction system (Equations 4.30 and 4.31 with k_{BA} = 0) is:

$$A_1 = C \quad 4.51$$

$$\lambda_{1A} = k_{AB} + r_{1A} \quad 4.52$$

$$B_1 = Ck_{AB}/(k_{AB} + r_{1A} - r_{1B}) \quad 4.53$$

$$B_2 = -Ck_{AB}/(k_{AB} + r_{1A} - r_{1B}) \quad 4.54$$

$$\lambda_{1B} = r_{1B} \quad 4.55$$

$$\lambda_{2B} = k_{AB} + r_{1A} \quad 4.56$$

By solving the system of linear algebraic equations (Equations 4.43-4.48 and 4.51-4.56), it is possible to derive the unknown parameters C, r_{1A}, r_{1B}, k_{AB} and k_{BA}.

4.5 Spectral-based Algorithm

A different approach to derive information on the kinetic process contains in dynamic data is represented by SA (Cunningham and Jones 1993), originally proposed for the analysis of clinical PET data. This method does not need *a priori* assumptions about the structure of the system but it is applicable only to single input/output noncyclic systems (Schmidt 1999). In SA the concentration of the activity at time t, $C_{tiss}(t)$, is modelled as a convolution of the plasma time-activity curve, $C_p(t)$, with the sum of M+1 distinct exponential terms as in Equation 4.57.

$$C_{tiss}(t) = \sum_{j=0}^{M} C_p(t) \otimes \alpha_j e^{-\beta_j t} \quad 4.57$$

where α_j and β_j are assumed to be real and non-negative. The upper limit, M, represents the maximum numbers of terms to be included in the model and is usually set equal to a large number (M = 100). The values of β_j are

predetermined and fixed in order to cover a range of all possible kinetic components measurable from the data. Commonly, the grid of values of the rates β_j ($\beta_1 < \beta_2 < \ldots < \beta_M$) is defined as a logarithmic distribution with lower limit $\beta_1 = 1/(3T_{end})$, where T_{end} is the end time of the experiment, and upper limit $\beta_M = 3/T_{in}$ (DiStefano 1981). T_{in} is the duration of the first time frame of the experiment. A component for $\beta = 0$ is included in the model corresponding to a fully trapped component. The M+1 values of α_j are estimated using non-negative least square (NNLS) estimator and normally only few components with $\alpha_j > 0$ are detected.

It is possible that the value of β_j that gives the best fit to the experimental data is not present in the predefined discrete grid. In this case the algorithm will choose two consecutive values of β that include the optimal value. Under the hypothesis that consecutive components in the SA solution are due to the effect just described, the components j and j+1 are replaced with a single new component with amplitudes and exponents calculated as follows (Veronese et al. 2010):

$$\beta_{\mathrm{NEW}} = \frac{\beta_j \alpha_j + \beta_{j+1} \alpha_{j+1}}{\alpha_j + \alpha_{j+1}} \qquad 4.58$$

$$\alpha_{NEW} = \alpha_j + \alpha_{j+1} \qquad 4.59$$

Using this approach the kinetic processes contained in the experimental data are derived without any *a priori* knowledge of the system studied. A disadvantage of SA similar to that of the MEM/NLS method is that it is not

possible to determine an unequivocal correspondence between the spectrum of kinetic components derived through SA and a compartmental model (Gunn et al. 2001). When the purpose of SA is to find the number of kinetic components of the system, an alternative approach is to estimate the number of exponentials (M in Equation 4.57) necessary for the SA model to give a good fit to the data by using models of increasing order. This approach firstly presented by *Bertoldo and colleagues* (Bertoldo et al. 1998) is also called NLSA.

For the implementation of NLSA, it is not necessary to specify a grid of values of β_j and the M+1 unknown values of β_j and α_j are estimated through nonlinear fitting. The standard model parsimony criteria techniques, such as the Akaike information criterion (AIC) (Akaike 1971) or the Bayesian information criterion (BIC) (Schwarz 1978), can be used to choose the best model. The AIC or BIC index for a given model is written in the form:

$$\mathrm{index} = -2\log \mathrm{L} + \mathrm{kP} \qquad 4.60$$

where L is the likelihood function, P is the number of unknown parameters in the model, and k is 2 for AIC and $\log(n_p)$ for BIC, with n_p number of points in the dataset. BIC therefore penalises a model characterised by a larger number of unknown parameters more than AIC does.

4.6 Graphical Method: Patlak Plot

Time-series describing the distribution of a given imaging agent can be alternatively fitted using graphical analysis techniques. This approach does not require any a priori assumption of the number of compartments involved in the distribution and uptake of the tracer but only the reversible or irreversible nature of the tracer. Graphical methods are based on the assumption that after a certain time from the intravenous injection into the system the movement of the tracer from and to the reversible compartment reaches equilibrium. Based on this hypothesis it is possible to calculate the tracer distribution volume (reversible tracers) or the tracer uptake (irreversible tracers) using Logan (Logan et al. 1990) or Patlak (Patlak et al. 1983) graphical methods, respectively.

This type of analysis, however, does not allow the complete characterisation of the tracer kinetics and only macro-parameters can be derived.

In this thesis only time-activity of irreversible PET tracers such as [^{18}F]-FDG and [^{18}F]-FMISO were analysed and therefore the graphical method of choice was Patlak.

Patlak and colleagues showed that the evolution in time of the amount of tracer in the region of tissue of interest, $C_{tiss}(t)$, is given by:

$$C_{tiss(t)} = K_i \int_0^t C_p(\tau)d\tau + (V_0 + V_b)C_p(t) \qquad 4.61$$

K_i represents the net uptake rate of the tracer, V_0 and V_b are the distribution volume in the reversible compartment and the fractional blood volume, respectively. Dividing Equation 4.61 by $C_p(t)$:

$$\frac{C_{tiss}(t)}{C_p(t)} = K_i \frac{\int_0^t C_{in}(\tau)d\tau}{C_p(t)} + (V_0 + V_b) \qquad 4.62$$

For tracers characterised by an irreversible trapping, the Patlak plot will result in a straight line, after sufficient equilibration time, with slope K_i and intercept $V = V_0 + V_b$. The unknown macro-parameters K_i and V are obtained by linear regression from a graph of $C_{tiss}(t)/C\ \ (t)$ against $\int_0^t C_p(\tau)d\tau/C_p(t)$.

4.7 Semi-quantitative Indices

Semi-quantitative indices are common alternatives to the quantitative analysis methods introduced in the previous sections. They are easy and fast to calculate, but very sensitive to the experimental conditions.

4.7.1 PET Dynamic Data

SUV is a semi-quantitative analysis routinely used for the analysis of clinical PET data (Kubota et al. 1985; Huang 2000). This index is calculated as the

ratio of tissue radioactivity concentration ($C_{tiss}(t)$, MBq/Kg) at a specific time and the injected dose (e.g. MBq) divided by the body weight (e.g. Kg).

$$SUV = \frac{C_{tissue}(t)}{\text{injected dose/body weight}} \qquad 4.63$$

In *ex vivo* experiments the input function is delivered as an impulse with no re-circulation and therefore the plasma radioactivity rapidly decays to zero. Additionally, the experimental set up used for the acquisition of time-activity curves of PET tracers (Section 3.5) *ex vivo* does not allow relating directly the measured activity to the concentration of the radioactive tracer injected. This is due to the fact that the time-activity curves are acquired from the arterial line above the heart cannula (input function) and from the heart using two different γ-detectors. As explained in Section 3.5, one γ-detector is placed perpendicular to the inflow line (input function), while the other is positioned in front of the Langendorff perfused rat heart (Figure 3.19). Due to this geometry, the amount of radioactivity detected by the due γ-detectors may differ and a unique calibration between the two is not guaranteed. For this reasons when *ex vivo* data are analysed the semi-quantitative index SUV cannot be computed as defined for *in vivo* experiments.

In this thesis the normalised activity (NA) was defined as a surrogate of the traditional SUV. NA was calculated as a ratio of the mean tissue activity ($C_{tiss}(t)$) (CPS) over a small interval at the end of the experiment and the maximum value of $C_{tiss}(t)$ (CPS) that replaced the normalised injected dose of the tracer normally used in SUV (Equation 4.64) (Mariotti et al. 2013).

$$NA = \frac{\text{mean}\langle C_{tiss}(t_{end-0.075min}, t_{end})\rangle}{\max\left(C_{tiss}(t)\right)} \quad 4.64$$

4.7.2 Hyperpolarised Dynamic Data

Different semi-quantitative approaches have been proposed for deriving information on the enzymatic conversion of a molecule A to its metabolite B from hyperpolarised ^{13}C MR spectra. The conversion of hyperpolarised pyruvate to bicarbonate was, for example, estimated using the ratio of the maximum intensity of the bicarbonate time-series to that of pyruvate in rat hearts (Schroeder et al. 2008) . This approach was shown to be sensitive enough to detect changed in the enzymatic activity. It is however not possible to relate mathematically this semi-quantitative index to the rate of enzymatic conversion k_{AB}. In this thesis the ratio between AUC of metabolite A and B was used as semi-quantitative index for the characterisation of the enzymatic conversion of a molecule A into its metabolite B. This index was chosen not only because it was shown to be sensitive to changes in the rate of metabolic conversion but also because it is possible to mathematically relate this index to the forward rate of enzymatic conversion k_{AB} (Hill et al. 2013). The relation between the AUC ratio and k_{AB} can be derived from the Bloch-McConnell equations that describe the system studied. For example for the system shown in Figure 4.5 the Bloch-McConnell equations are:

$$\frac{dM_{z,A}(t)}{dt} = -(k_{AB} - r_{1A})M_{z,A}(t) + k_{BA}M_{z,B}(t) + M_{z,Cp}(t) \quad 4.65$$

$$\frac{dM_{z,B}(t)}{dt} = k_{AB}M_{z,A}(t) - (r_{1B} + k_{BA})M_{z,B}(t) \quad 4.66$$

The Laplace transform of Equation 4.66 is:

$$sM_{z,B}(s) - M_{z,B}(0) = k_{AB}M_{z,A}(s) - r_{1B}M_{z,B} \quad 4.67$$

By re-arranging the member in Equation 4.67 becomes:

$$\frac{M_{z,B}(s)}{M_{z,A}(s)} = \frac{k_{AB}}{s + r_{1B} + k_{AB}} \quad 4.68$$

The general definition of Laplace transform for function X(t) is given by:

$$X(s) = \int_0^\infty e^{-st}X(t)dt \quad 4.69$$

$$X(0) = \int_0^\infty X(t)dt = AUC \quad 4.70$$

Since the hyperpolarised signal of both metabolite A and B decays to the thermal equilibrium value within the experimental time window, it is possible to write:

$$\frac{M_{z,B}(0)}{M_{z,A}(0)} = \frac{AUC(B)}{AUC(A)} = \frac{k_{AB}}{r_{1B} + k_{AB}} = AUC \qquad 4.71$$

The ratio between the area under the curve of metabolite B and A can be therefore used as a semi-quantitative index of the rate of forward conversion k_{AB}. This method is easy to apply and does not require any knowledge of the delivery input function $C_p(t)$.

4.8 Monte Carlo Method

The Monte Carlo method was firstly introduced in 1946 by Stanislaw Ulam a Polish-American mathematician who worked on the nuclear weapons project during the World War II. This approach includes a large number of computational algorithms which rely on running simulations many times in order to obtain the distribution of an unknown probabilistic entity.

Monte Carlo simulations are especially useful for simulating phenomena characterised by a large uncertainty in inputs and system with many degrees of freedom. This method is commonly used in many different fields such as computational biology, computer graphics, applied statistics, finance and business.

In this thesis Monte Carlo simulations were used to assess the performance of the analysis methods proposed. In particular, simulations were carried out in order to investigate the effect of the presence of the random noise normally exhibited by experimental data on the accuracy and reproducibility of MEM/NLS

algorithm, SA, NLSA in the estimation of the number of the kinetic processes described in the time-series and their values.

Chapter 5 : Hyperpolarised ^{13}C Dynamic Data

5.1 Aims

In this Chapter the results obtained from the hyperpolarised ^{13}C dynamic experiments described in Chapter 3 are presented with particular reference to the [1-$^{13}C_1$] pyruvate-lactate exchange detected *in vitro* in whole blood cells (Section 5.2) and to the metabolic conversion of [1-$^{13}C_1$] pyruvate to its downstream metabolites observed *ex vivo* in perfused rat hearts (Section 5.3). The characteristic rates of the ^{13}C pyruvate-lactate exchange were derived using three different approaches: (i) compartmental modelling (Section 5.2.1), (ii) MEM/NLS algorithm (Section 5.2.2) and (iii) semi-quantitative index AUC (Section 5.2.3). Compartmental modelling and AUC were also used to measure the rate of conversion of [1-$^{13}C_1$] pyruvate to $H^{13}CO_3^-$ via PDH *ex vivo* in perfused rat hearts (Section 4.3 and Section 5.3.3, respectively).

5.2 *In vitro* Systems: Hyperpolarised [1-$^{13}C_1$] Pyruvate-Lactate Exchange in Whole Blood Cells

The datasets presented in this Section were acquired as described in Section 3.3 using a flip-angle θ = 10° to avoid the radiation damping effect described in Section 3.3.2. Figure 5.1 A shows a representative hyperpolarised MR ^{13}C time-series of three molecules, namely [1-$^{13}C_1$] pyruvate (~170.5ppm), [1-$^{13}C_1$] pyruvate hydrate (~179ppm) and [1-$^{13}C_1$] lactate (~183ppm), detected in whole blood cells at 9.4T. [1-$^{13}C_1$] pyruvate hydrate is a not metabolically active molecule formed when [1-$^{13}C_1$] pyruvate is placed in an aqueous solution, whereas [1-$^{13}C_1$] lactate is produced from [1-$^{13}C_1$] pyruvate through LDH. In Figure 5.1 B a detail of the evolution in time of the [1-$^{13}C_1$] lactate hyperpolarised peak is shown. Two factors contribute to the dynamics of the hyperpolarised signal of [1-$^{13}C_1$] pyruvate: (i) the loss of signal due to metabolic conversion of pyruvate to lactate and (ii) the relaxation of the hyperpolarised pyruvate signal to thermal equilibrium. Similarly, the build up of the [1-$^{13}C_1$] lactate hyperpolarised signal is due to the production of the molecule from [1-$^{13}C_1$] pyruvate, while the decay is due to the relaxation of the hyperpolarised lactate signal to thermal equilibrium.

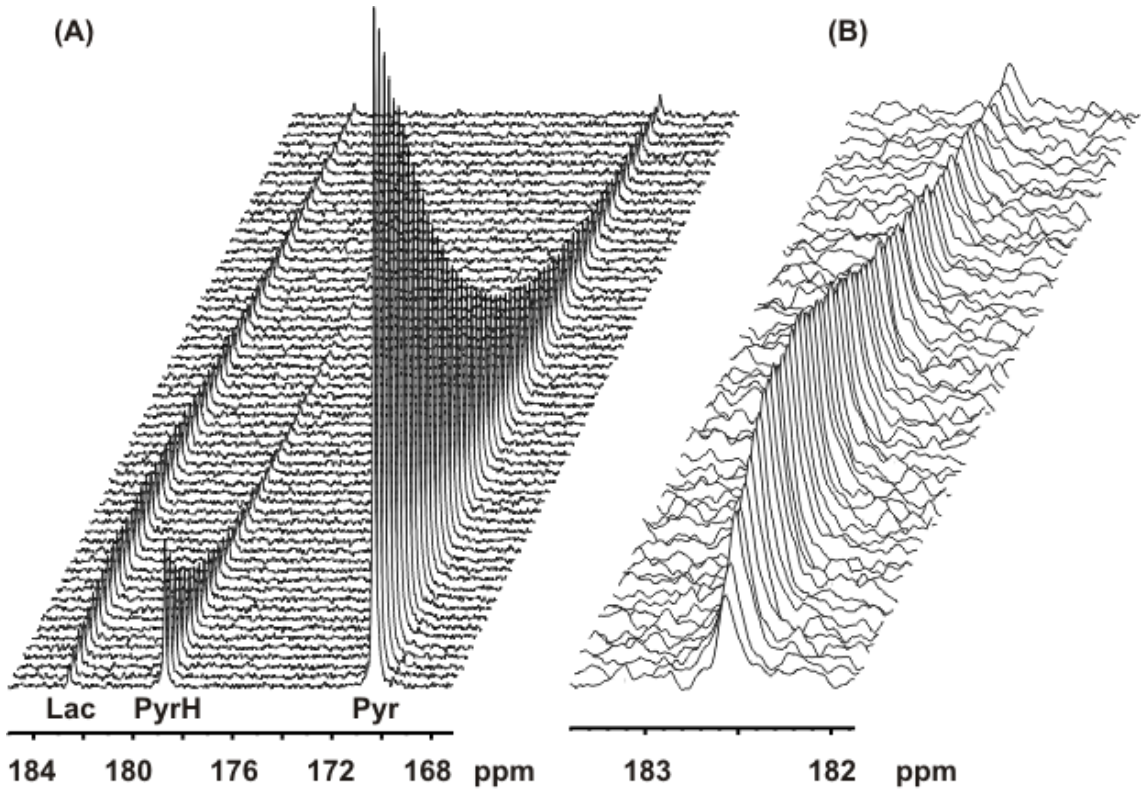

Figure 5.1: (A) Hyperpolarised ^{13}C MR time-series of [1-$^{13}C_1$] pyruvate (~170.5ppm), [1-$^{13}C_1$] pyruvate hydrate (~179ppm) and [1-$^{13}C_1$] lactate (~183ppm) acquired in real time in whole blood cells. (B) Details of the [1-$^{13}C_1$] lactate hyperpolarised peak.

5.2.1 Compartmental Modelling

The metabolic conversion of hyperpolarised [1-$^{13}C_1$] pyruvate to [1-$^{13}C_1$] lactate *in vitro* is an exchange reaction that is close to equilibrium and therefore it commonly approximated by a two-compartment, first-order, bidirectional model shown in Figure 4.4 where pyruvate and lactate are represented by compartment A and B, respectively. The input function $C_p(t)$ is usually not considered in the modelling of this type of experiments as the hyperpolarised solution in mixed with the cell suspension before the sample is inserted into the MR scan and instantaneous mixing is assumed. As explained in Chapter 4, this

type of model is described by a system of differential equations whose solution is presented in Equations 4.26 and 4.27. The characteristic rates of the exchange (k_{AB} and k_{BA}) as well as the effective relaxation rates of the hyperpolarised signal of the two molecules (r_{1A} and r_{1B}) can be derive by fitting the experimental data with Equations 4.26 and 4.27. In Figure 5.2 A the representative peak integrals of pyruvate (blue) and lactate (black) with overlaid fits (red) are plotted as function of time. In this thesis all residuals obtained from different fits are plotted normalised to the pyruvate peak value in agreement with previous hyperpolarised studies(Hill et al. 2013). Residuals obtained from the compartmental fit are presented in Figure 5.2 B in blue for pyruvate and in black for lactate. Their values were found to be in agreement with previous *in vitro* studies. The values obtained for the unknown parameters obtained by fitting the experimental datasets (n = 4) with a two-compartment, bidirectional kinetic model were: C = 1.01 ± 0.025 (a.u.), r_{1A} = 0.028s^{-1} ± 0.005s^{-1}, r_{1B} = 0.034s^{-1} ± 0.011s^{-1}, k_{AB} = 0.006s^{-1} ± 0.002s^{-1}. The algorithm failed in estimating the values of k_{BA} always returning the value of the lowest boundary condition set. The coefficient of variation in percentage (%CV_p) was estimated as index of the accuracy in the estimation of the unknown parameter p. The values reported were: %CV_C = 0.45% ± 0.15%, %CVr_{1A} = 2.61% ± 1.35%, %CV r_{1B} = 12.15% ± 9.51%, %CV_{KAB} = 7.32% ± 3.4%.

The quality of the fit did not change appreciably when the experimental datasets were fitted with a two-compartment, first-order, unidirectional model (Figure 4.4 with k_{BA} = 0). The values estimated for the four unknown parameters were almost identical to those found using a bidirectional compartmental model: C =

1.01 ± 0.025 (a.u.), r_{1A} = 0.027s^{-1} ± 0.004s^{-1}, r_{1B} = 0.038s^{-1} ± 0.0051s^{-1}, k_{AB} = 0.006s^{-1} ± 0.002s^{-1}. The %CV calculated for each parameter was: $\%CV_C$ = 0.37% ± 0.12%, $\%CVr_{1A}$ = 1.8% ± 0.97%, $\%CVr_{1A}$= 6.46% ± 2.94%, $\%CV_{KAB}$ = 7.32% ± 3.5%.

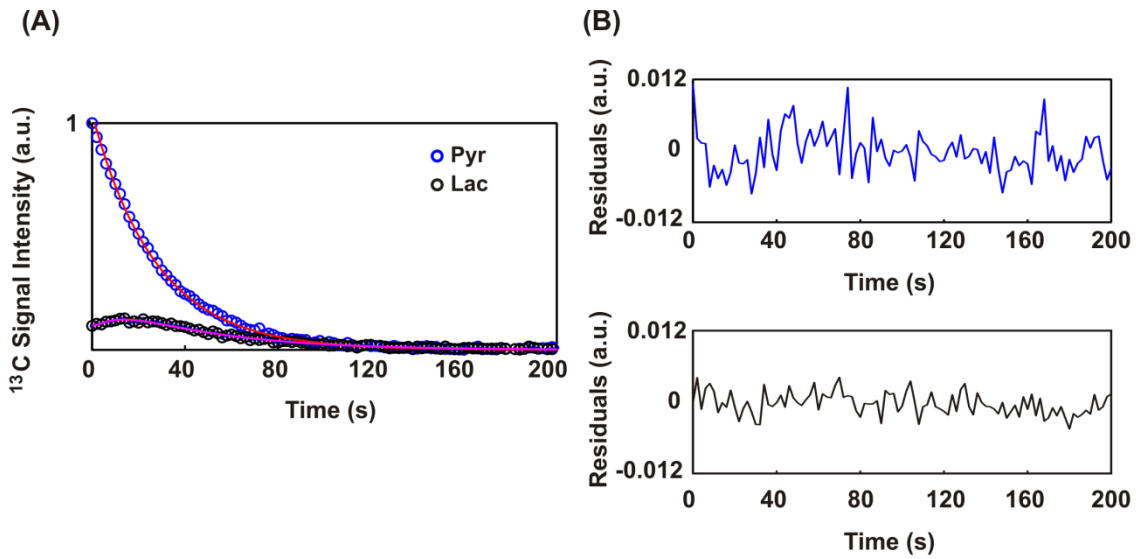

Figure 5.2: (A) Peaks integrals of [1-$^{13}C_1$] pyruvate (blue) and [1-$^{13}C_1$] lactate (black) with overlaid fits plotted as a function of time. (B) Residuals normalised to the peak value of the pyruvate time-series and plotted as a function of time for pyruvate (blue) and lactate (black).

5.2.2 MEM/NLS Method

The MEM/NLS method, presented in Section 4.4, was originally proposed by *Steinbach and colleagues* for the analysis of protein folding (Steinbach et al. 2002). In this thesis the feasibility of using this approach for the kinetic analysis of hyperpolarised data was studied for the first time using Monte Carlo

simulations over a range of known kinetics. After its validation the MEM/NLS algorithm was applied to the characteristic time-series of hyperpolarised ^{13}C pyruvate-lactate exchange acquired *in vitro* in whole blood cells.

5.2.2.1 Monte Carlo Simulations

Two groups of Monte Carlo simulations were used in this thesis to assess the accuracy and reproducibility of the hybrid MEM/NLS algorithm for the kinetic characterisation of *in vitro* hyperpolarised data. Time-series representing the hyperpolarised peak integrals of uni- and bi-directional *in vitro* systems were simulated using the solution of the Bloch-McConnell equations written for a two-compartment, first-order system (Equations **4.30** and **4.31**, Figure 4.5Figure 4.4). In this thesis the mixing of the hyperpolarized solution and the *in vitro* system was considered to be instantaneous and therefore $C_p(t)$ was modelled as a delta function.

In the first group of Monte Carlo simulations *in vitro* systems were simulated for four different values of k_{AB} ($k_{AB} = 0.002s^{-1}$, $k_{AB} = 0.004s^{-1}$, $k_{AB} = 0.006s^{-1}$ and $k_{AB} = 0.008s^{-1}$), while the rates of decay of the hyperpolarised signals of compartment A and B were maintained constant in all systems simulated ($r_{1A} = 0.0267s^{-1}$ and $r_{1B} = 0.045s^{-1}$). Bidirectional systems were simulated considering $k_{BA} = k_{AB}$, while in unidirectional systems $k_{BA} = 0$.

The values of k_{AB} and k_{BA} used in the second group of Monte Carlo simulations are reported in Table 5.1. In this case, r_{1A} and r_{1B} were randomly generated within a chosen interval ($0.022s^{-1} < r_{1A} < 0.04s^{-1}$ and $0.03s^{-1} < r_{1B} < 0.05s^{-1}$) for both uni- and bi-directional systems.

Table 5.1: Values chosen for the rates of conversion k_{AB} and k_{BA} in the second group of Monte Carlo simulations where r_{1A} and r_{1B} were randomly generated within a chosen interval ($0.022s^{-1} < r_{1A} < 0.04s^{-1}$ and $0.03s^{-1} < r_{1B} < 0.05s^{-1}$).

	Bidirectional		**Unidirectional**	
	k_{AB}	**k_{BA}**	**k_{AB}**	**k_{BA}**
system 1	0.02	0.002	0.002	0
system 2	0.04	0.004	0.004	0
system 3	0.06	0.006	0.006	0
system 4	0.08	0.008	0.008	0

Units are in s^{-1}.

The rate values used in both groups of simulations were chosen within a physiological range characteristic of the *in vitro* conversion of pyruvate to lactate and in agreement with previous studies (Harris et al. 2009; Hill et al. 2013; Hill et al. 2013). In each dataset the time-series of both compartments were normalised to the maximum value of the time-series of compartment A and therefore the unknown parameter C in Equations **4.30** and **4.31** was always equal to 1. To assess the influence of random noise in the data, each dataset was simulated for a low and a high signal-to-noise ratio (SNR) (SNR = 20 and SNR=90) in the range of those found in our experimental data. Usually the lowest SNR detected *in vitro* is associated with the hyperpolarised time-series of the product of the metabolic conversion in this case represented by

compartment B. In this study the SNR was calculated as the ratio between the maximum value of the time-signal intensity curve of compartment B and the standard deviation of the thermal equilibrium signal (noise) of the same curve (SNR_B) (Santarelli et al. 2012). Datasets were simulated with Δt = 2s equal to the experimental TR used for the *in vitro* hyperpolarised experiments carried out in this thesis and repeated N = 100 times at each set of parameters.

The ability of the MEM/NLS algorithm to derive the correct number of known kinetic components in the simulated data was firstly assessed. The values of C, r_{1A}, $r_{1B,}$ k_{AB} and k_{BA} were subsequently derived by associating a compatible compartmental model to the MEM/NLS solution and solving the system of algebraic equations shown in Equations 4.43-4.48 and Equations 4.51-4.56 for bi- and uni-directional systems, respectively. These values were compared to the simulated reference values as well as to the estimates derived using conventional compartmental modelling. The percent bias (%BIAS) for the kinetic rates k_{AB} and k_{BA} was calculated as a performance index:

$$\%\mathrm{BIAS}_{\mathrm{p}} = 100 * \sum_{\mathrm{j}=1}^{\mathrm{k}} \frac{(\mathrm{p_j} - \mathrm{p_{TRUE}})}{\mathrm{p_{TRUE}}} \qquad 5.1$$

where p_j and p_{TRUE} are the estimated and true value of the indices p.

Monte Carlo simulations and the fit using compartmental models were performed using a custom-made Matlab (MathWorks®) code, whereas the fitting was performed with MeMExp software available online (http://cmm.cit.nih.gov/memexp/download.cgi) (Steinbach et al. 2002).

The results from Monte Carlo simulations showed that the hybrid MEM/NLS algorithm is able to discern between uni- and bi-directional *in vitro* systems by identifying the number of exponentials that describe the data. Figure 5.3 A and B show a representative simulated time-series for compartment A (blue) and B (black) with overlaid the MEM/NLS fits (red) for bi- and uni-directional systems, respectively. The random residuals obtained from the data fit, normalised to the peak value of the pyruvate time-series are shown in Figure 5.3 C and D in blue for compartment A and black for compartment B. Values were found in agreement with previous hyperpolarised *in vitro* studies. In both group of Monte Carlo simulations, the hybrid algorithm was able to derive two rates for compartment B from the time-series of both systems (black lines in Figure 5.3 E and F), while two and one exponentials are identified from the dynamic curve of compartment A of a bi- and uni-directional system, respectively (blue lines in Figure 5.3 E and F). This is in agreement with the solution of the Bloch-McConnell equations written for bi- and uni-directional *in vitro* systems (Equations 4.30 and 4.31 with C_p = delta function) in which the hyperpolarised time-series of compartment A is characterised by a bi- and mono-exponential dynamics, respectively.

The percentage errors in identifying the number of components using the MEM/NLS algorithm from bi- and uni-directional systems are presented in Table 5.2 and Table 5.3 for first and the second group of Monte Carlo simulations, respectively.

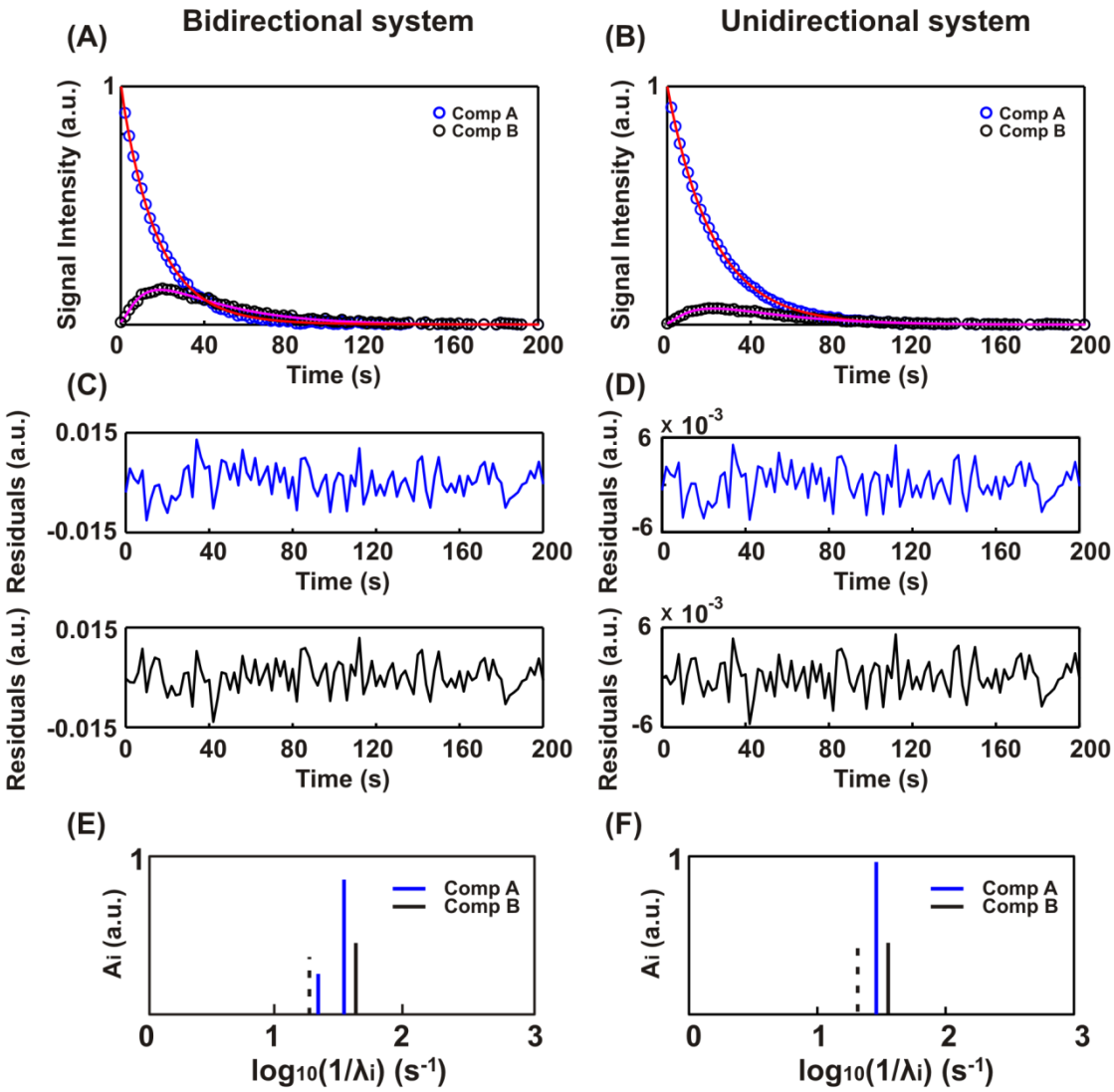

Figure 5.3: Representative results from the hybrid MEM/NLS fit for bidirectional reaction kinetics, left panel, and unidirectional reaction kinetics systems, right panel.) and (B) show simulated datasets (coloured dots) and overlaid fits (coloured lines) plotted for compartments A (blue) and B (black). (C) and (D) Residuals, normalised to the peak value of the pyruvate time-series, from the fits shown in (A) and (B) are plotted in blue and black for compartment A and B, respectively. (E) and (F) show the kinetic rates resulted from the MEM/NLS analysis of the datasets shown in (A) and (B), respectively. Solid and dashed lines indicate rates with positive and negative amplitudes, respectively.

The ability of the hybrid method in deriving the correct number of rates from the time-series of compartment A in general does not dependent on the SNR_B in the range of noise values simulated as well as on the simulated value of k_{AB} and $k_{BA.}$ For both groups of simulations and regardless the type (uni- or bi-directional) system simulated, the percentage of correctness (CE) is > 90%, with the only exception of the bidirectional system in the second group of simulations simulated with the smallest k_{AB} and the highest noise (CE = 64%) (Table 5.2 and Table 5.3).Results also suggested that the capability of the algorithm in deriving the correct number of exponentials from compartment B decreases with increasing values of k_{AB} for all simulated systems. Similarly to compartment A, also in compartment B, SNR_B played a minor role in the correct identification of the simulated components.

The values of the apparent kinetic rates k_{AB} and k_{BA} were derived in both groups of simulation by associating a compatible compartmental model to the MEM/NLS solution as detailed in Section 4.4.1. The values calculated for k_{AB} and k_{BA} using the MEM/NLS algorithm and those obtained by fitting the data with a corresponding compartmental modelling are plotted against the values used as input to the Monte Carlo simulations in Figure 5.4. The values of k_{AB} estimated for bidirectional systems using the hybrid algorithm for both group of simulations are in excellent agreement with those derived through compartmental modelling (reference) and the real values (Figure 5.4 A-C and D-F) regardless the SNR_B and the value of k_{AB}. In the first group of simulation where $k_{BA} = k_{AB}$, the MEM/NLS algorithm was not able to derive the correct value of k_{BA} regardless the type of system (uni- or bi-directional), the value of

k_{BA} and SNR_B simulated (Figure 5.4 B). In the second group of simulations results show that the MEM/NLS algorithm is less accurate than traditional compartmental modelling in the estimation of the rate at lower values of k_{BA}, nevertheless the values of k_{BA} reported using the hybrid method are in a linear relationship with the real input values, regardless the SNR_B studied (Figure 5.4 E).

Table 5.2: Performance of MEM/NLS algorithm in identifying the number of kinetic components from simulated datasets. In this set of Monte Carlo simulations $r_{1A} = 0.0267s^{-1}$ and $r_{1B} = 0.045s^{-1}$.

BIDIRECTIONAL SYSTEMS

	Compartment A						Compartment B					
	SNR_B=20			SNR_B=90			SNR_B=20			SNR_B=90		
Simulated scenario	**UE**	**OE**	**CE**	**UE**	**OE**	**CE**	**UE**	**OE**	**CE**	**UE**	**OE**	**CE**
k_{AB} = 0.002/k_{BA}=0.002	8%	--	92%	1%	--	99%	1%	2%	97%	--	--	100%
k_{AB} = 0.004/ k_{BA} =0.004	6%	--	94%	1%	--	99%	3%	4%	93%	--	--	100%
k_{AB} = 0.006/ k_{BA} =0.006	5%	--	95%	--	--	100%	2%	7%	91%	9%	7%	84%
k_{AB} = 0.008/ k_{BA} =0.008	2%	--	98%	3%	--	97%	10%	5%	85%	7%	8%	85%

UNIDIRECTIONAL SYSTEMS

	Compartment A						Compartment B					
	SNR_B=20			SNR_B=90			SNR_B=20			SNR_B=90		
Simulated scenario	**UE**	**OE**	**CE**	**UE**	**OE**	**CE**	**UE**	**OE**	**CE**	**UE**	**OE**	**CE**
k_{AB} = 0.002	--	4%	96%	--	1%	99%	1%	4%	95%	--	4%	96%
k_{AB} = 0.004	--	9%	91%	--	5%	95%	--	6%	94%	--	1%	99%
k_{AB} = 0.006	--	10%	90%	--	7%	93%	3%	4%	93%	--	4%	96%
k_{AB} = 0.008	--	8%	92%	2%	8%	90%	2%	8%	90%	--	2%	98%

k_{AB} and k_{AB} indicate the apparent rates of enzymatic conversion. Units are in s^{-1}. UE = Underestimated number of components; OE = overestimated number of components; CE = correctly estimated.

Table 5.3: Performance of MEM/NLS algorithm in identifying the number of kinetic components from simulated datasets. In this set of Monte Carlo simulations r_{1A} and r_{1B} were randomly generated within a chosen interval (0.022s-1 < r_{1A} < 0.04s-1 and 0.03s-1 < r_{1B} < 0.05s-1).

BIDIRECTIONAL SYSTEMS												
	Compartment A						Compartment B					
	SNR_B=20			SNR_B=90			SNR_B=20			SNR_B=90		
Simulated scenario	**UE**	**OE**	**CE**	**UE**	**OE**	**CE**	**UE**	**OE**	**CE**	**UE**	**OE**	**CE**
k_{AB} = 0.02/k_{BA}=0.002	36%	--	64%	--	2%	98%	2%	4%	94%	--	5%	95%
k_{AB} = 0.04/ k_{BA} =0.004	4%	--	96%	5%	--	95%	4%	8%	88%	1%	13%	86%
k_{AB} = 0.06/ k_{BA} =0.006	5%	--	95%	5%	--	95%	1%	22%	77%	1%	23%	76%
k_{AB} = 0.08/ k_{BA} =0.008	2%	--	98%	1%	--	99%	11%	19%	70%	9%	21%	70%

UNIDIRECTIONAL SYSTEMS												
	Compartment A						Compartment B					
	SNR_B=20			SNR_B=90			SNR_B=20			SNR_B=90		
Simulated scenario	**UE**	**OE**	**CE**	**UE**	**OE**	**CE**	**UE**	**OE**	**CE**	**UE**	**OE**	**CE**
k_{AB} = 0.002	--	--	100%	--	--	100%	1%	5%	94%	--	5%	95%
k_{AB} = 0.004	--	2%	98%	--	--	100%	2%	4%	94%	--	2%	98%
k_{AB} = 0.006	--	--	100%	--	--	100%	3%	4%	93%	--	2%	97%
k_{AB} = 0.008	--	--	100%	--	--	100%	5%	6%	89%	--	3%	97%

k_{AB} and k_{AB} indicate the apparent rates of enzymatic conversion. Units are in s^{-1}. UE = Underestimated number of components; OE = overestimated number of components; CE = correctly estimated.

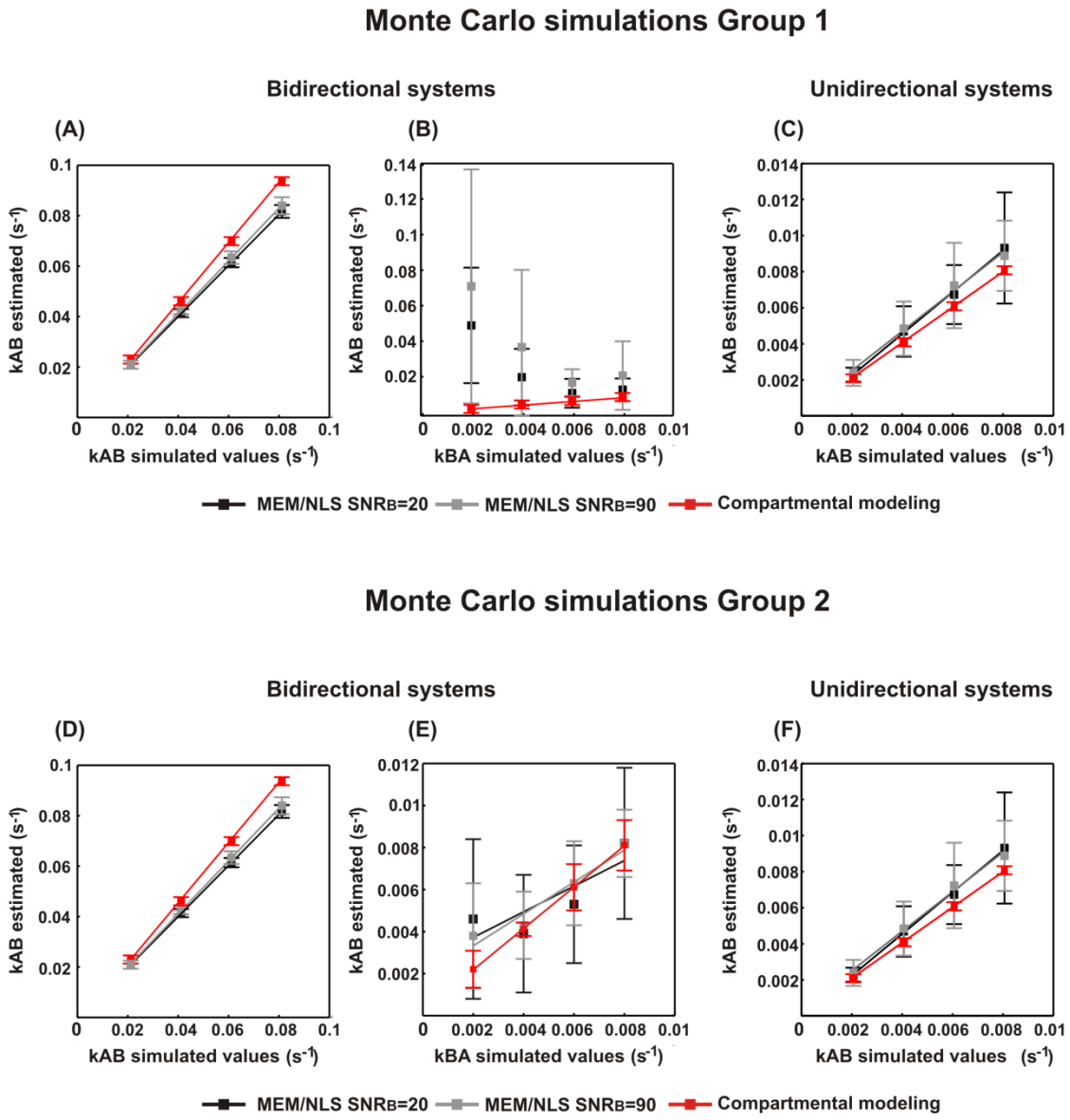

Figure 5.4: Bidirectional *in vitro* systems: (A)-(B) and (D)-(E) show the values of k_{AB} and k_{BA}, respectively, derived using the MEM/NLS algorithm plotted for SNR_B = 20 (black) and SNR_B = 90 (gray) against the real values used as input to the two groups of Monte Carlo simulations. The values estimated for the same rates using a conventional two-compartment, bidirectional kinetic model are plotted in the same figure in red. Unidirectional *in vitro* systems: (C) and (F) show the relationship between the values of k_{AB} estimated through the MEM/NLS method and the real values for SNR_B = 20 (black) and SNR_B = 90 (gray) for the first and the second group of Monte Carlo simulations, respectively. The values estimated through a two-compartment, unidirectional kinetic model are plotted against the input values in red.

This disagreement in the results is due to the different values chosen for k_{AB} and k_{BA} in the two groups of Monte Carlo simulations. In the first group of simulations k_{AB} was chosen equal to k_{BA}. In this particular case the values of the simulated rates $\lambda_{1(A,B)}$ and $\lambda_{2(A,B)}$ are much closer that those generated in the second group of Monte Carlo simulations where $k_{AB} >> k_{BA}$. Nevertheless, the MEM/NLS algorithm was able to discern the two rates equally well in the two groups of simulations (Table 5.2 and Table 5.3). The accuracy in the estimation of the values of $\lambda_{1(A,B)}$ and $\lambda_{2(A,B)}$was however effected by the proximity of the two unknown rates to derive.

The maximum and the minimum values of $\%Bias_{KAB}$ and $\%Bias_{KBA}$ estimated using the MEM//NLS algorithm are reported in Table 5.4 for both groups of Monte Carlo simulations.

In light of the results obtained from the two groups of Monte Carlo simulations it possible to conclude that the MEM/NLs algorithm is adequate to characterise the kinetic of *in vitro* hyperpolarised time-series by identifying the number of kinetic rates that best describe the data. Additionally MEM/NLS algorithm is as accurate as compartmental modelling in the estimation of the values of k_{AB} derived by associate a compatible compartmental model to the MEM/NLS solution. However the ability of the proposed approach in estimating the values of k_{BA} depends on the values of k_{AB} and k_{BA}.

Table 5.4: Maximum and the minimum values of $\%Bias_{KAB}$ and $\%Bias_{KBA}$ estimated using the MEM//NLS algorithm for both groups of Monte Carlo simulations.

	BIDIRECTIONAL SYSTEMS				UNIDIRECTIONAL SYSTEMS	
	$\%Bias_{KAB}$		$\%Bias_{KBA}$		$\%Bias_{KAB}$	
	Min $SNR_b=90$ $k_{AB}=0.002s^{-1}$	**Max** $SNR_b=20$ $k_{AB}=0.008s^{-1}$	**Min** $SNR_b=90$ $K_{BA}=0.008s^{-1}$	**Max** $SNR_b=20$ $K_{BA}=0.002s^{-1}$	**Min** $SNR_b=90$ $k_{AB}=0.002s^{-1}$	**Max** $SNR_b=20$ $k_{AB}=0.008s^{-1}$
Simulations Group 1 ($k_{AB}=k_{BA}$)	2.1%±3.1%	4.9%±4.1%	158.1%±241.1%	$2.34*10^3$%±$1.62*10^3$%	5.3%±4.1%	8.7%±19.4%
Simulations Group 2 ($k_{AB}>>k_{BA}$)	-0.3%±2%	1.1%±6.1%	22.14%±20%	-17.6%±57.3%	3.6%±2.7%	7.2%±18.2%

5.2.2.2 Experimental Data

The hyperpolarised time-series in whole blood of pyruvate (blue) and lactate (black) with overlaid MEM/NLS fits (red) are plotted as function of time in Figure 5.5 A. Fitting residuals are presented in Figure 5.5 B for both pyruvate (blue) and lactate (black). Figure 5.5 C shows the results of the MEM/NLS fits to the hyperpolarised ^{13}C data. One discrete rate was derived through the hybrid algorithm from the pyruvate curve (blue line), whereas two rates were obtained from the lactate time-series (black lines). This solution is compatible with a two-compartment, first-order, unidirectional compartmental model and therefore Equations 4.51-4.56 were used to derive the characteristic kinetic rates of the pyruvate (compartment A) to lactate (compartment B) conversion.

The linear relationship between the values estimated for k_{AB} ($k_{AB} = 0.0058s^{-1} \pm 0.0020s^{-1}$, n=4) using the MEM/NLS approach and those derived using a two-compartment, unidirectional kinetic model ($k_{AB} = 0.0059s^{-1} \pm 0.0022s^{-1}$, n=4) is plotted in Figure 5.5 D. The values reported for r_{1A} and r_{1B} were equal to $0.02s^{-1} \pm 0.002s^{-1}$ and $0.05s^{-1} \pm 0.01s^{-1}$, respectively. The SNR_B estimated for these datasets was 35 ± 10 (a.u.) in agreement with the values used in the Monte Carlo simulations.

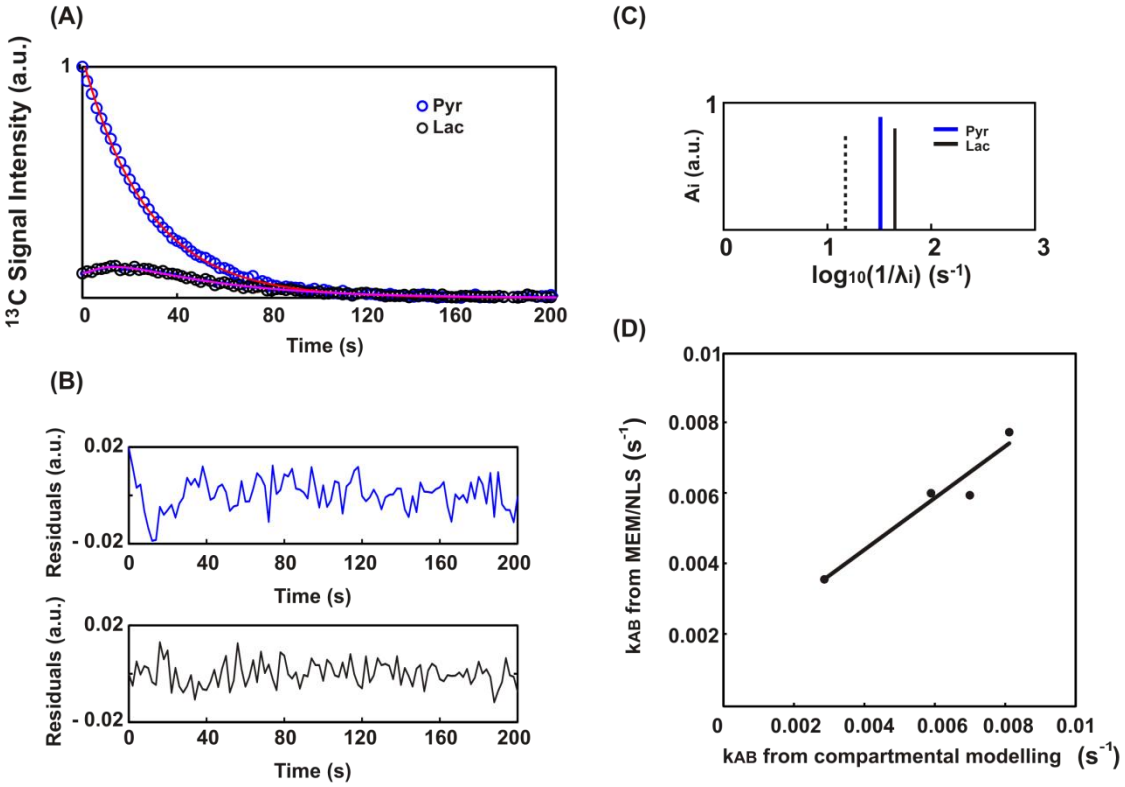

Figure 5.5: (A) Peaks integrals of [1-$^{13}C_1$] pyruvate (blue) and [1-$^{13}C_1$] lactate (black) with overlaid fits plotted as a function of time. (B) Residuals normalised to the peak value of the pyruvate time-series and plotted as a function of time for pyruvate (blue) and lactate (black). (C) Representative kinetic rates derived through the MEM/NLS analysis. Solid and dashed lines correspond to rates with positive and negative amplitude, respectively. (D) The values of k_{AB}, representing the rate of conversion of pyruvate to lactate via LDH, derived using the MEM/NLS approach are plotted against those obtained fitting the experimental data with a two compartments, first-order, unidirectional kinetic model.

5.2.3 Semi-quantitative Index: AUC

The AUC index for the ^{13}C pyruvate-lactate exchange datasets was calculated as detailed in 0. In Figure 5.6, the results are plotted against the values of k_{AB} estimated by fitting the same datasets with a two-compartment, first-order, unidirectional compartmental model.

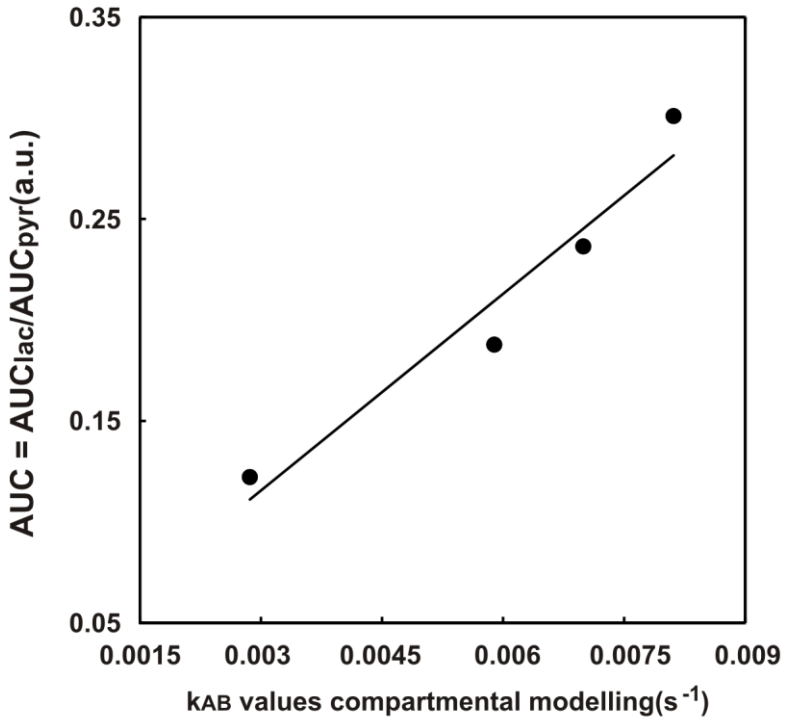

Figure 5.6: AUC ratio values calculated for the ^{13}C time-series acquired for the pyruvate-lactate exchange are plotted against the k_{AB} values obtained by fitting the same datasets with a two-compartment, first-order, unidirectional compartmental model.

5.3 *Ex vivo* Systems: Metabolism of Hyperpolarised [1-$^{13}C_1$] Pyruvate Detected in Langendorff Perfused Rat Hearts

^{13}C MR dynamic spectra were acquired after the injection of the injection of 50mM [1-$^{13}C_1$] pyruvate and 5.2µM gadolinium into two different groups of Langendorff rats hearts. The first group of isolated hearts (n = 5) was perfused using a Krebs-Henseleit buffer containing 11.1mM glucose, whereas the second group (n = 5) using a Krebs-Henseleit buffer containing 11.1mM glucose and 2.5mM unlabelled pyruvate (Section 3.4.1). Hyperpolarised ^{13}C spectra (ns = 128) were acquired using a single acquisition per spectrum, flip-angle θ = 10°

and a time resolution Δt = 2s (Section 3.4.5). Details of the type of Krebs-Henseleit buffer and of the type of coil used in each experiment are reported in Table 3.4. Peaks were assigned by comparing the chemical shift of the ^{13}C metabolites in the hyperpolarised spectra with the natural abundance ^{13}C MR spectra of several common metabolites as detailed in Section 3.4.6. Figure 5.9 A and B show a representative ^{13}C hyperpolarised spectrum acquired from a perfused rat heart and the natural abundance ^{13}C MR spectrum of lactate, aspartate, alanine, pyruvate and bicarbonate obtained by adding together the spectra of the different amino acids (Appendix A), respectively.

A schematic diagram of the metabolic pathways observed after the injection of hyperpolarised [1-$^{13}C_1$] pyruvate into Langendorff perfused rat hearts is shown in Figure 5.10. The metabolic conversion of hyperpolarised [1-$^{13}C_1$] pyruvate to lactate catalysed by LDH, to alanine catalysed by alanine transaminase (ALT), to bicarbonate catalysed by PDH, and interconversion of bicarbonate and CO_2 catalysed by carbonic anhydrase (CA) were observed for both groups of perfused rat hearts. The conversion of hyperpolarised [1-$^{13}C_1$] pyruvate to aspartate C1 and C4 by transamination via oxaloacetate was detected only for the group of Langendorff hearts perfused with a Krebs-Henseleit buffer containing 11.1mM glucose only. This is attributed to anaplerotic metabolism via the action of pyruvate carboxylase (PC). The C1 label appears from direct conversion of pyruvate via oxaloacetate. It has been suggested that the C4 signal in aspartate arises from TCA cycle conversion of oxaloacetate to malate and fumarate where the position of the hyperpolarised signal is scrambled in this symmetric molecule (Merritt et al. 2011).

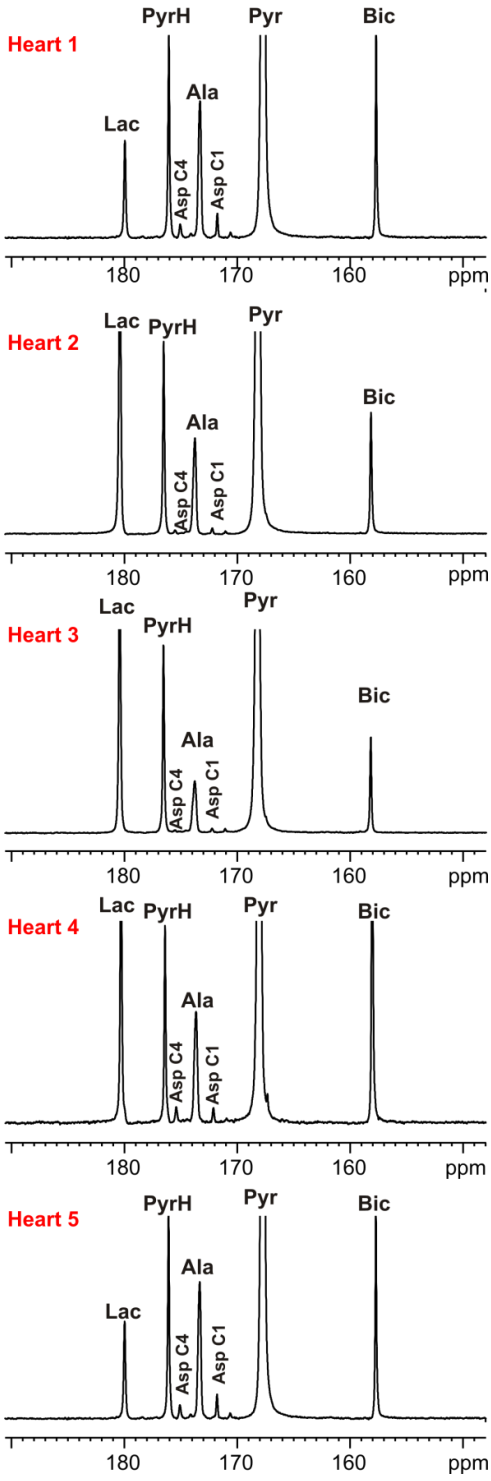

Figure 5.7: ^{13}C MR spectrum obtained by summing the entire hyperpolarised (ns=128) ^{13}C time-series acquired after the injection of a solution of [1-$^{13}C_1$] pyruvate and gadolinium into Langendorff rat hearts perfused with a Krebs-Henseleit buffer containing 11.1mM glucose only. *Lac = lactate, PyrH = pyruvate hydrate, Asp = aspartate, Ala = alanine, Pyr = pyruvate, Bic = bicarbonate.*

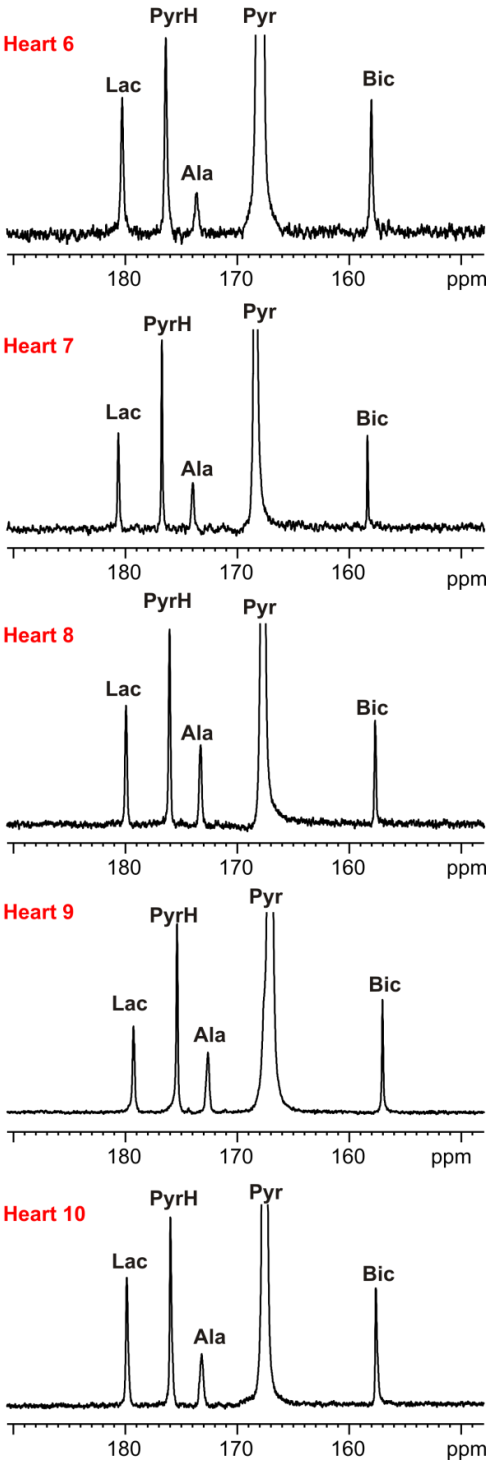

Figure 5.8: ^{13}C MR spectrum obtained by summing the entire hyperpolarised (ns=128) ^{13}C time-series acquired after the injection of a solution of [1-$^{13}C_1$] pyruvate and gadolinium is shown for each heart perfused with a Krebs-Henseleit buffer containing 11.1mM glucose and 2.5mM pyruvate. *Lac = lactate, PyrH = pyruvate hydrate, Asp = aspartate, Ala = alanine, Pyr = pyruvate, Bic = bicarbonate.*

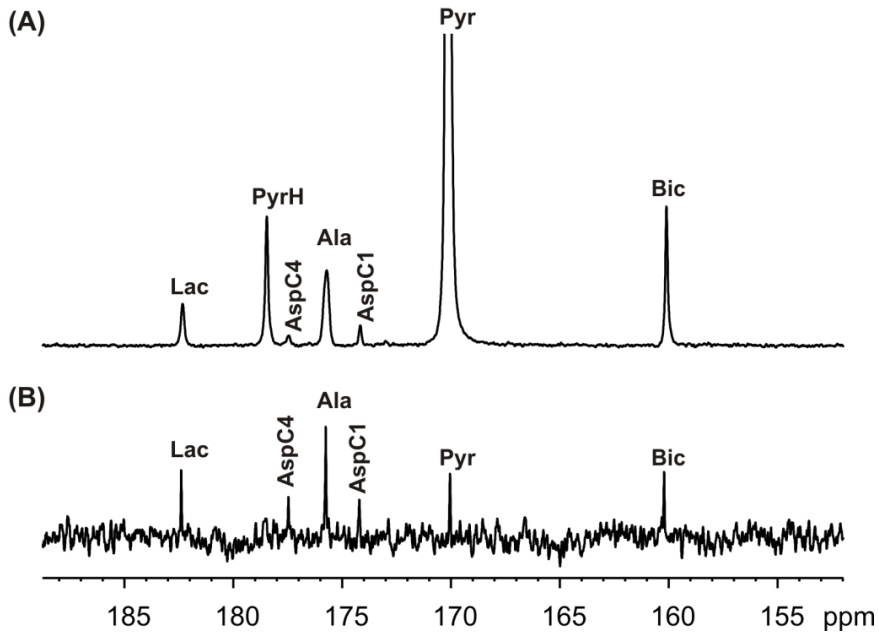

Figure 5.9: (A) Representative ^{13}C MR spectrum obtained by summing the entire hyperpolarised ^{13}C time-series acquired after the injection of a solution of [1-$^{13}C_1$] pyruvate and gadolinium into Langendorff rat hearts perfused with a Krebs-Henseleit buffer containing 11.1mM glucose only. (B) Natural abundance ^{13}C MR spectrum of lactate, aspartate, alanine, pyruvate and bicarbonate obtained by adding together the spectra of the different amino acid spectra shown in the Appendix A. *Lac = lactate, PyrH = pyruvate hydrate, Asp = aspartate, Ala = alanine, Pyr = pyruvate, Bic = bicarbonate.*

The aspartate C4 signal was less intense than the aspartate C1 signal. However, oxaloacetate, malate or fumarate where not observed and therefore it was not possible to distinguish between this process and a possible direct carboxylation of pyruvate by hyperpolarised CO_2.

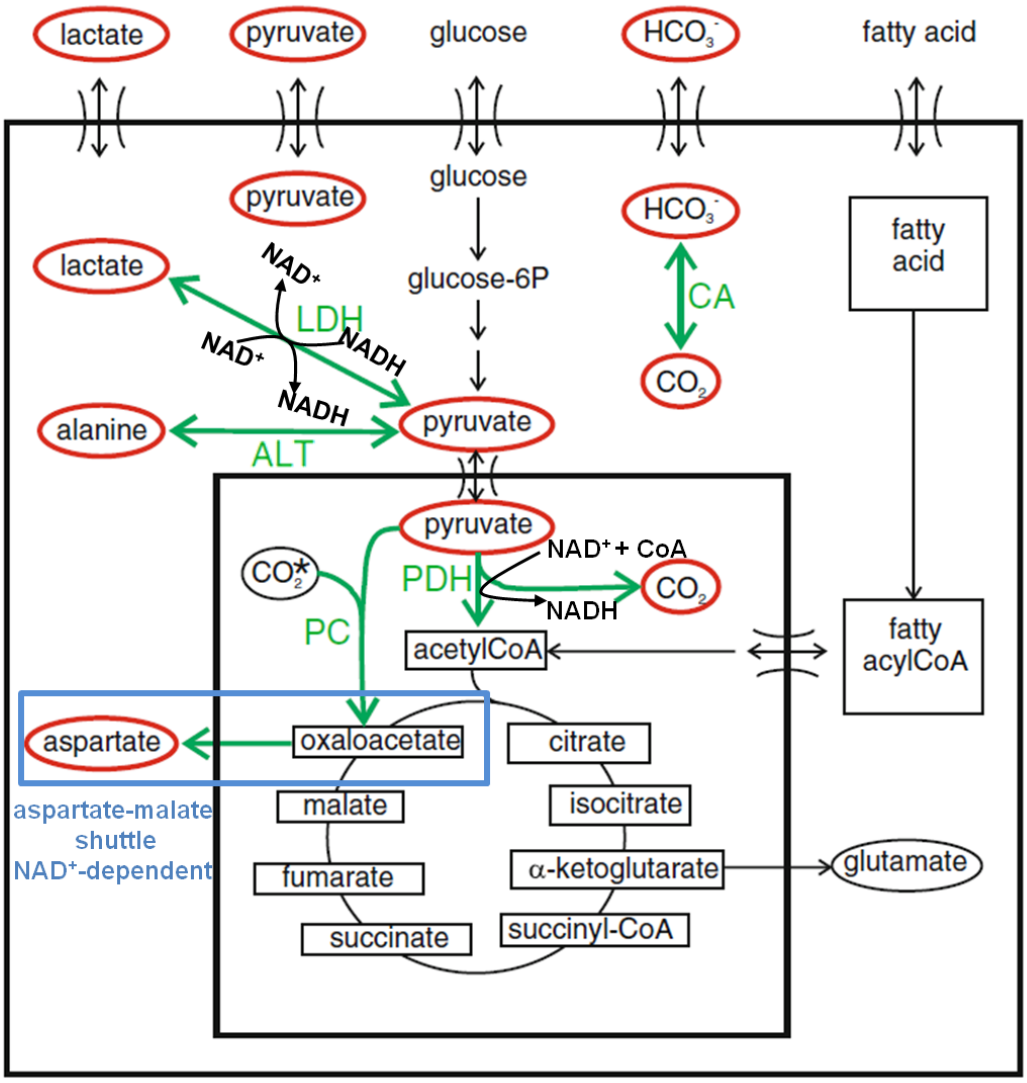

Figure 5.10: Schematic representation of pyruvate metabolism with the metabolites observed in the Langendorff perfused heart experiments shown in red. The conversion of hyperpolarised [1-$^{13}C_1$] pyruvate to [1-$^{13}C_1$] lactate, [1-$^{13}C_1$] alanine, $H^{13}CO_3^-$ under the action of LDH, ALT, PDH, respectively, was detected for both groups of hearts. The conversion of [1-$^{13}C_1$] to oxalocetate through pyruvate carboxylase (PC) and the transamination of oxaloacetate to aspartate were detected only in the group of heart perfused with a buffer containing 11.1mM glucose. The outer box corresponds to the plasma membrane whilst the inner box is the mitochondrial membrane. Figure adapted from reference (Weiss and Mariotti et al. 2012).

Figure 5.11 A and B show a representative ^{13}C time-series of pyruvate, lactate, alanine and $H^{13}CO_3^-$ acquired from isolated rat hearts perfused with 11.1mM glucose only and 11.1mM glucose plus 2.5mM pyruvate, respectively.

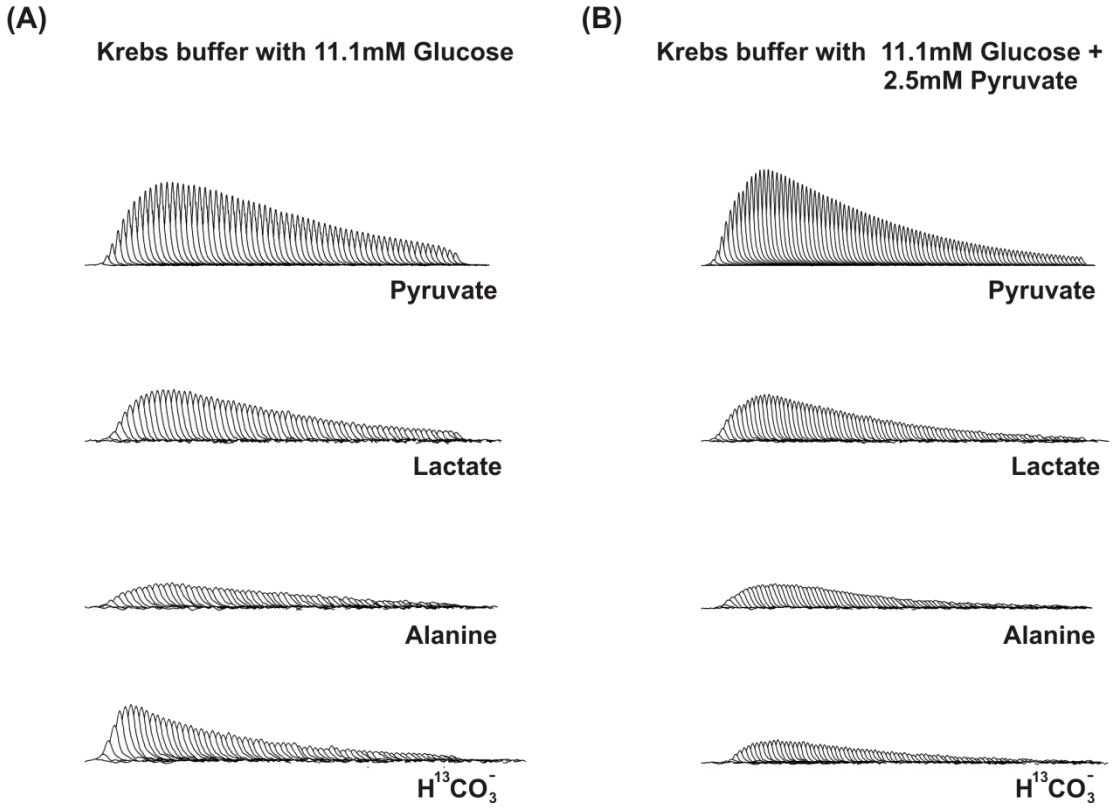

Figure 5.11: Representative ^{13}MR time-series of [1-$^{13}C_1$] pyruvate, lactate, alanine and $H^{13}CO_3^-$ for Langendorff rat hearts perfused with a Krebs- Henseleit buffer containing (A) 11.1mM glucose and (B) 11.1mM glucose plus 2.5mM pyruvate.

The two groups of hearts mainly differed in the $H^{13}CO_3^-$ time-series dynamics. In those acquired from isolated heart perfused with only glucose the build up of the $H^{13}CO_3^-$ time-series was extremely fast reaching a maximum value 15.8s ±

9.28s before the peak value of the pyruvate curve. $H^{13}CO_3^-$ time-series acquired from Langendorff hearts perfused with glucose and pyruvate were characterised by a slower build up reaching a maximum value at the same time or soon after that of the pyruvate peak value. The dynamics of the $H^{13}CO_3^-$ curves of the two groups of hearts will be investigated in more details in the following Sections.

5.3.1 Compartmental Modelling

The metabolic pathway that has been most assessed in the heart using hyperpolarised ^{13}C MR is that characterised by the conversion of pyruvate to Acetyl-CoA via PDH (Figure 5.12). In this reaction the mitochondrial cofactors NAD^+ and Co-A are necessary to convert pyruvate to Acetyl-CoA. The resultant CO_2 is rapidly converted to HCO_3^- by carbonic anhydrase (CA).

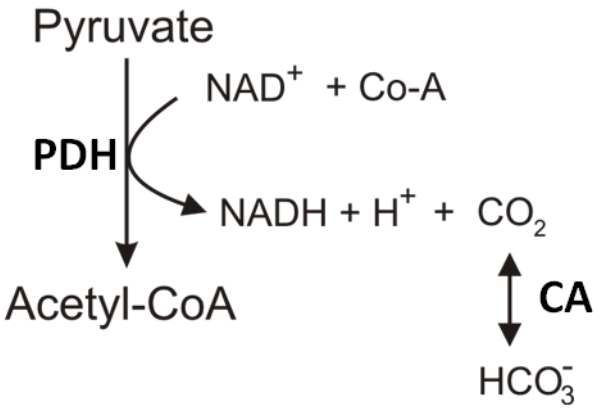

Figure 5.12: Schematic representation of the metabolic conversion catalysed by PDH that converts [1-$^{13}C_1$] pyruvate to Acetyl-CoA utilising the mitochondrial cofactors NAD^+ and CoA. The resultant CO_2 is rapidly converted to HCO_3^- by carbonic anhydrase (CA).

Previous studies have shown that it is possible to derive the apparent rate of the metabolic conversion of PDH fitting the experimental hyperpolarised time-series of [1-$^{13}C_1$] pyruvate and $H^{13}CO_3^-$ (Schroeder et al. 2010; Schroeder et al. 2011). It has been commonly assumed that the metabolic conversion of pyruvate to $H^{13}CO_3^-$ follows first-order kinetics and therefore in order to derive the characteristic rates of the system experimental time-series have been fitted using a two-compartment, first-order, unidirectional kinetic model (Figure 4.5). This approach has been shown to be adequate for the analysis of data acquired *in vivo* where it is possible to assume that the enzyme cofactors are regenerated faster than they are consumed. The validity of first-order kinetics however has not been demonstrated for data acquired *ex vivo* where the metabolism of the heart and its ability to regenerate the enzyme cofactors greatly depends on the substrate contained in the Krebs-Henseleit buffer. In the following sections the time-series of pyruvate and $H^{13}CO_3^-$ acquired for the two groups of Langendorff perfused hearts are fitted using two different compartmental models and the results are compared.

5.3.1.1 First-order Kinetics

Experimental time-series of [1-$^{13}C_1$] pyruvate and $H^{13}CO_3^-$ acquired from the two groups of perfused rat hearts were fitted using a two-compartment, first-order, unidirectional model (Figure 4.5). The input function (C_p) was modelled as a γ-variate function (Equation 5.2).

$$A(t - t_{arrival})^{alpha} * e^{\frac{(t-t_{arrival})}{beta}} \quad 5.2$$

Where A, alpha and beta are parameters that characterised the shape of the input function, whereas $t_{arrival}$ is the time point in which the hyperpolarised signal of pyruvate is first detected. In this case k_{AB} corresponds to the rate of conversion of hyperpolarised [1-$^{13}C_1$] pyruvate to $H^{13}CO_3^-$ via PDH. Figure 5.13 (A) and (B) show a representative peak integrals of [1-$^{13}C_1$] pyruvate (blue) and $H^{13}CO_3^-$ (black) with overlaid fits (red) acquired from Langendorff rat hearts perfused with a Krebs-Henseleit buffer containing 11.1mM glucose only and 11.1mM glucose plus 2.5mM pyruvate, respectively.

Regardless, the initial condition chosen for the NLS fitting, the chosen compartmental model was not able to fit correctly the $H^{13}CO_3^-$ time-series characterised by a fast build up and corresponding to those acquired from isolated hearts perfused with glucose only (Figure 5.13 A). However, the $H^{13}CO_3^-$ time-series acquired from the group of hearts perfused with glucose and pyruvate were well fitted using first-order, two-compartment, unidirectional model. The value of k_{AB} estimated for this last group of hearts was $0.014s^{-1} \pm 0.002s^{-1}$ with a corresponding $\%CV_{kAB}$ equal to 188% ± 62.4%.

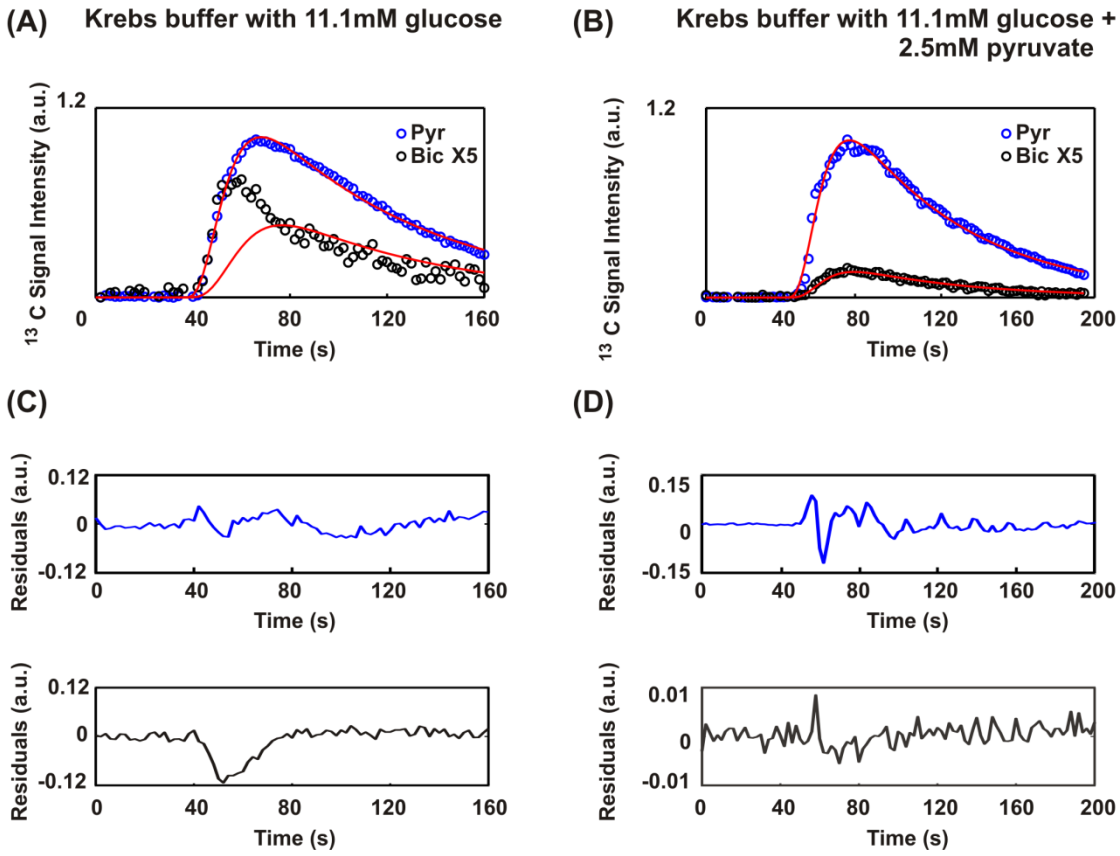

Figure 5.13: Peaks integrals of [1-$^{13}C_1$] pyruvate (blue) and $H^{13}CO_3^-$ (black) with overlaid fits (red) for the group of Langendorff hearts perfused using a Krebs-Henseleit buffer containing (A) 11.1mM glucose only and (B) 11.1mM glucose plus 2.5mM pyruvate. (C) and (D) show the residuals normalised to the peak value of the pyruvate time-series and for pyruvate (blue) and $H^{13}CO_3^-$ (black) to the fits in (A) and (B), respectively.

5.3.1.2 Second-order Kinetics

The results presented in the previous section suggested that the conversion of hyperpolarised [1-$^{13}C_1$] pyruvate to $H^{13}CO_3^-$ does not follow simple first-order kinetics in Langendorff rat hearts perfused with a Krebs-Henseleit buffer containing 11.1mM glucose only. As mentioned before the assumption that the metabolic conversion catalysed by PDH follows first-order kinetics is true only if

the enzyme cofactors are in abundance or are regenerated faster than they are consumed.

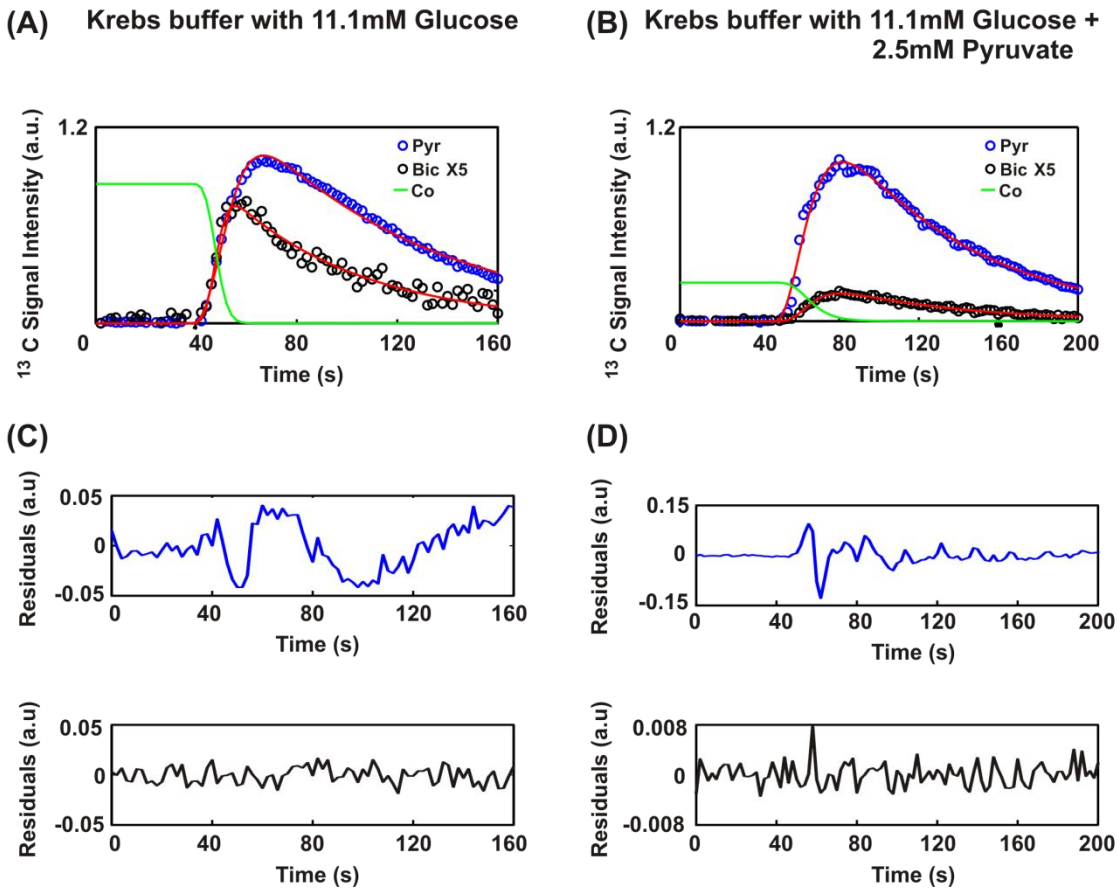

Figure 5.14: Peaks integrals of [1-$^{13}C_1$] pyruvate (blue) and $H^{13}CO_3^-$ (black) with overlaid fits (red) for the group of Langendorff hearts perfused using a Krebs-Henseleit buffer containing (A) 11.1mM glucose only and (B) 11.1mM glucose plus 2.5 mM pyruvate. The cofactor dynamics is represented in (A) and (B) in green on the same arbitrary scale. (C) and (D) show the residuals normalised to the peak value of the pyruvate time-series and for pyruvate (blue) and $H^{13}CO_3^-$ (black) to the fits in (A) and (B), respectively.

To investigate whether the enzymatic reaction assessed was limited by the availability of the enzyme cofactors a three-compartment, second-order,

unidirectional model (Figure 4.7) was used to fit the experimental data. The time-series of pyruvate and $H^{13}CO_3^-$ presented in Figure 5.13 A are plotted with overlaid the fit derived from the second-order model in Figure 5.14 A. Residuals are presented in Figure 5.14 B. Using this approach the experimental curves of both metabolites are well fitted suggesting that the metabolic conversion catalysed by PDH in isolated hearts perfused with only 11.1mM glucose most probably follows second-order rather than first-order kinetics. The value of k_{AB} derived was $0.006s^{-1} \pm 0.0009s^{-1}$ with a corresponding $\%CV_{KAB}$ equal to 35.2% ± 34.9%.

Even if well fitted with first-order compartmental model, the datasets acquired from the group of hearts perfused with 11.1mM glucose plus 2.5mM pyruvate were also analysed using a two-compartment, second-order, unidirectional model. The value of k_{AB} derived in this case was $0.0015s^{-1} \pm 0.0002s^{-1}$. The value estimated for $\%CV_{KAB}$ for the second group of hearts using second-order kinetics was equal to 51% ± 42.5%, significantly lower that reported for the same group of dataset using first-order kinetic model ($p < 0.05$). This result suggests that also the group of isolated hearts perfused with glucose plus pyruvate is better characterised by second-order rather that first-order kinetics. The values of mean ± SD reported for k_{AB} fitting the experimental datasets using a two-compartment, second-order, unidirectional model are presented in Figure 5.15 for both groups of perfused hearts assessed. Statistical analysis was performed in Matlab (MathWorks®) using a two sample t-test.

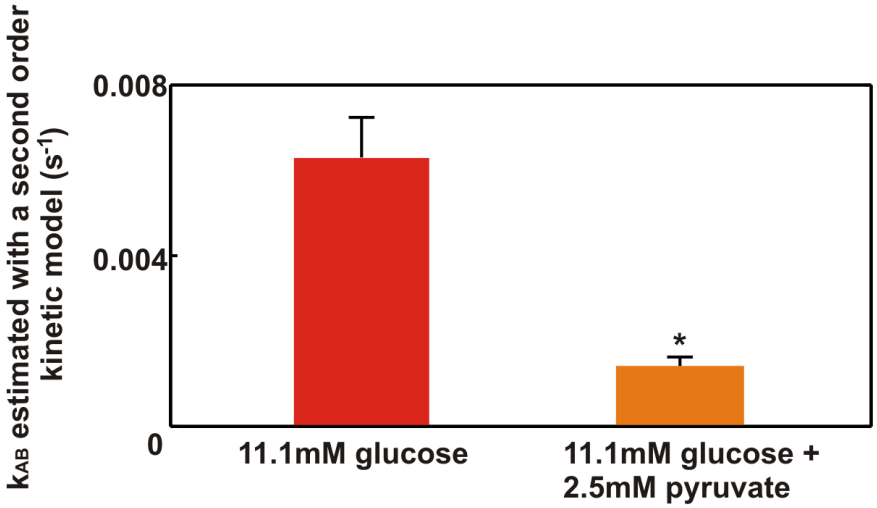

Figure 5.15: Mean ± SD reported for k_{AB} fitting the experimental time-series of [1-$^{13}C_1$] pyruvate and $H^{13}CO_3^-$ using a two-compartment, second-order, unidirectional kinetic model for isolated hearts perfused with Krebs buffer containing 11.1mM glucose only (red) and 11.1mM glucose plus 2.5 mM pyruvate (orange). * indicates $p < 0.05$.

The values of k_{AB} estimated for the group of Langendorff rat hearts perfused with only 11.1mM glucose were significantly higher than those reported for the group of hearts perfused with 11.1mM glucose and 2.5mM pyruvate ($p < 0.05$).

5.3.2 NADH Surface Fluorescence

The results from the kinetic analysis of experimental hyperpolarised ^{13}C time-series acquired from Langendorff rat hearts perfused with two different Krebs-Henseleit buffers suggested that the metabolic conversion of hyperpolarised [1-$^{13}C_1$] pyruvate to $H^{13}CO_3^-$ via PDH likely follows second-order rather than first-order kinetics. In other words the PDH activity in perfused rat hearts depends on the availability of the enzyme cofactors. PDH catalyses the enzymatic

conversion of pyruvate to acetyl-CoA using the mitochondrial cofactors NAD^+ and CoA (Figure 5.12). In order to relate the results obtained from the kinetic analysis to the underlying biology a real time measurement of the enzymatic cofactors is desirable. In this Section a preliminary study aimed at the real time measurement of NAD^+ cofactor concentration in perfused rat hearts during the injection of a 50mM pyruvate solution is presented. NAD^+ accepts electrons during the metabolic conversion (oxidation) of pyruvate to Acetyl-CoA (Figure 5.12). This coenzyme is, therefore, found in two forms in cells: NAD^+ that accepts electrons from pyruvate and becomes reduced to NADH. Previous studies have shown the possibility of using surface fluorescence imaging to measure the characteristic fluorescence intensity of the cofactors that is proportional to fluorophore concentration. Using this imaging modality it is only possible to detect the signal from NADH as NAD^+ does not fluoresce.

In this thesis a preliminary NADH surface fluorescence imaging experiment of perfused hearts was performed by Dr. Coert Zuurbier at the University of Amsterdam. A Langendorff rat heart was perfused with a Krebs-Henseleit buffer identical to that used for the hearts perfused at St. Thomas' hospital and containing 11.1mM glucose only. Fluorescence imaging of NADH was carried out during the injection of a 50mM pyruvate solution (to mimic the hyperpolarised experimental protocol) by digital video recording with a temporal resolution $\Delta t = 1s$. The fluorescence intensity of NADH averaged over the whole heart is plotted as a function of time in Figure 5.16 where $t = 0$ corresponds to the point in which the infusion of 50mM pyruvate solution was started. It is notable how the NADH fluorescence signal, and therefore the concentration of

this coenzyme, increased throughout the experimental protocol. Assuming that [NAD^+] + [NADH] is constant during the experimental time, the increase in NADH concentration corresponds to a decrease in NAD^+ availability. This is in agreement with results of the kinetic modelling presented in Section 5.3.1.2.

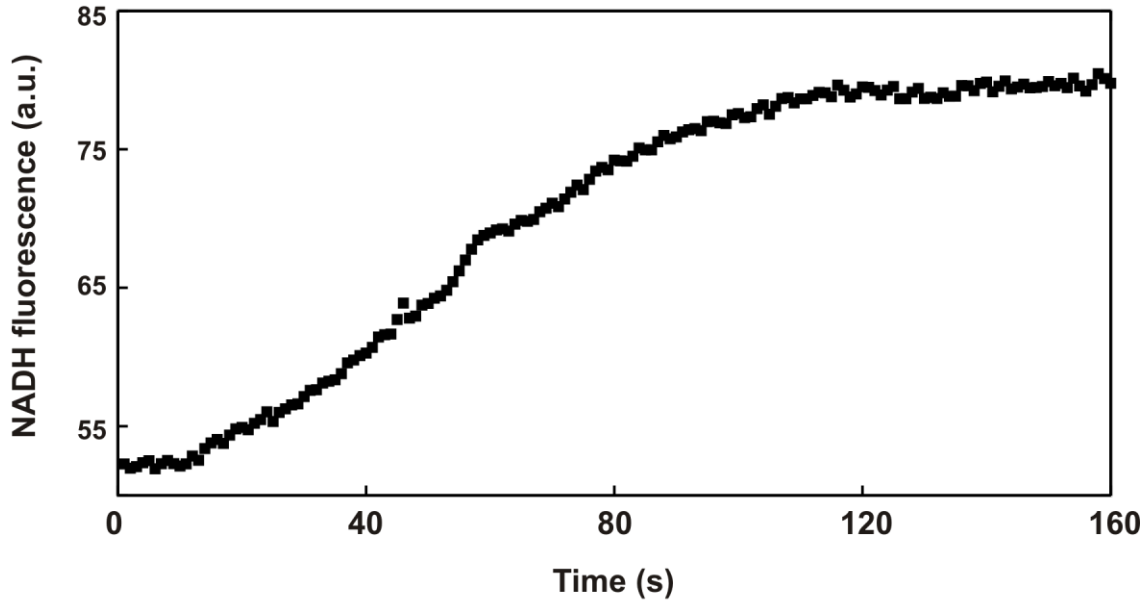

Figure 5.16: A representative NADH fluorescence signal acquired from a Langendorff rat heart perfused with a Krebs-Henseleit buffer containing 11.1mM glucose in which a bolus of 50mM pyruvate is injected though an injection pump. t = 0 represents the time point in which the infusion of the pyruvate was started.

5.3.3 Semi-quantitative Index: AUC

Figure 5.17 shows the AUC ratio values calculated for the conversion of hyperpolarised [1-$^{13}C_1$] pyruvate to $H^{13}CO_3^-$ estimated from the experimental time-series acquired from Langendorff rat hearts perfused with a Krebs-

Henseleit buffer containing 11.1mM glucose only (blue) and 11.1mM glucose plus 2.5mM pyruvate (red) plotted against k_{AB} values obtained by fitting the same datasets with a two-compartment, second-order, unidirectional compartmental model. For this set of datasets the AUC ratio was found not to be proportional to the values of k_{AB} regardless the compartmental model chosen to fit the data.

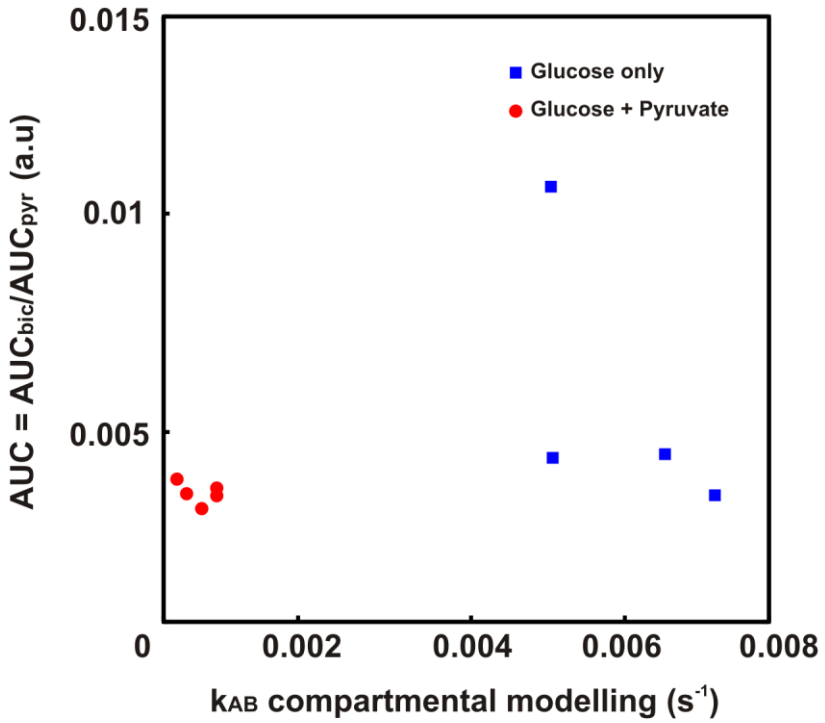

Figure 5.17: AUC ratio values calculated for the conversion of hyperpolarised [1-$^{13}C_1$] pyruvate to $H^{13}CO_3^-$ estimated from experimental time-series acquired from Langendorff rat hearts perfused with a Krebs-Henseleit buffer containing 11.1mM glucose only (blue) and 11.1mM glucose plus 2.5mM pyruvate (red) plotted against k_{AB} values obtained by fitting the same datasets with a two-compartment, second-order, unidirectional compartmental model.

5.4 Discussion

The conversion of hyperpolarised [1-$^{13}C_1$] pyruvate to [1-$^{13}C_1$] lactate and [1-$^{13}C_1$] pyruvate hydrate was detected *in vitro* in whole blood cells. Lactate is produced from pyruvate via LDH, whereas the pyruvate hydrate is formed when pyruvate is placed in aqueous solution. In order to quantify the characteristic rates of pyruvate-lactate exchange the hyperpolarised ^{13}C time-series of the two molecules were fitted using two quantitative and one semi-quantitative analysis methods. If compartmental modelling is the standard analysis method for hyperpolarised data, MEM/NLS algorithm has been previously proposed for the kinetic analysis of protein folding and has never been applied to hyperpolarised data. In this thesis the feasibility of using the MEM/NLS algorithm for the analysis of hyperpolarised data was assessed using Monte Carlo simulations. After its validation, the proposed method was used to derive the characteristic kinetic rates of the pyruvate-lactate exchange and the results were compared with those obtained from the analysis of the experimental data with compartmental modelling. The results from Monte Carlo simulations showed the MEM/NLS algorithm is able to discern between uni- and bi-directional systems by identifying a different number of rates from the hyperpolarised time-series of compartment A. Additionally it was shown that under certain hypothesis it is possible to associate a compatible compartmental model to the MEM/NLS solution. Solving a system of algebraic equations shown in Equations 4.43-4.48and 4.51-4.56 for bi- and uni-directional systems, respectively, it is also possible to derive the value of the kinetic rates (C, r_{1A}, r_{1B}, k_{AB} and k_{BA}) characteristic of the system studied. The accuracy of the MEM/NLS algorithm in

estimating the value of k_{AB} with the MEM/NLS algorithm was comparable with that of conventional compartmental modelling for both types of systems. However the ability of the hybrid method in estimating the values of k_{BA} depends on the values of k_{AB} and k_{BA}. When applied to *in vitro* hyperpolarised ^{13}C time-series of pyruvate-lactate exchange in whole blood cells the MEM/NLS algorithm identified one rate from the pyruvate time-series, whereas two rates were detected from the lactate time-series. The conversion of pyruvate to lactate catalysed by LDH is an exchange reaction that is close to equilibrium. In the absence of other information, it would be therefore reasonable to fit the experimental data with a two compartment, bidirectional kinetic model as presented in Section 5.2.1. MEM/NLS however identifies only a single rate for the pyruvate curve suggesting that the experimental data reflect a unidirectional enzymatic conversion rather than exchange reaction as known from the biology. We speculate that in this experiment, carried out in a suspension of blood cells, the concentrations are compartmentalised according to the intracellular and extracellular volume fractions. The signal from hyperpolarised pyruvate would therefore be dominated by the large extracellular pool which is not in exchange and the decay of the hyperpolarised signal is then characterized by the T_1 relaxation time of this compartment with only the smaller cytosolic pool being in exchange with intracellular lactate. This information is lost when the data are analysed with a compartment model assuming a priori a bidirectional reaction. The value of k_{AB} for the conversion of pyruvate to lactate derived using the MEM/NLS algorithm were found to be in very good agreement with those estimated using conventional compartmental modelling and with those

previously published (Hill et al. 2013). The semi-quantitative index AUC calculated for the pyruvate-lactate exchange was found to be linearly proportional to the values of k_{AB} estimated using a two- compartment, unidirectional model (Figure 5.6) in agreement with previous studies (Hill et al. 2013).

Hyperpolarised ^{13}C spectra of pyruvate and its metabolites were acquired from two different groups of perfused rat hearts. Peaks corresponding to [1-$^{13}C_1$] pyruvate, [1-$^{13}C_1$] lactate, [1-$^{13}C_1$] alanine and $H^{13}CO_3^-$ were detected for both groups of hearts, whereas those attributed to aspartate C1 and C4 were identified in the group of Langendorff hearts perfused with a Krebs-Henseleit buffer containing 11.1mM glucose only but not in those perfused with 11.1mM glucose plus 2.5mM pyruvate. The aspartate C1 and C4 peaks observed in the isolated hearts perfused with only glucose were previously described in the liver, where AcetylCoA is produced via anaplerosis (Merritt et al. 2011) but never in the heart. Anaplerotic reactions are also essential in the heart to maintain the intermediates of the TCA cycle (e.g. oxaloacetate, malate, α-ketoglutarate) constant under different metabolic conditions. It has previously been reported under similar perfusion conditions that 80% of the acetyl-CoA generated in the heart arises from pyruvate metabolism whilst only 8-10% is attributed to anaplerosis. To verify that the hearts perfused in this thesis were characterised by an energetic state similar to those reported in previous studies, the PC and PDH activity were estimated dividing the maximum intensity of the aspartate C1 and $H^{13}CO_3^-$ peak, respectively, to the maximum intensity of the pyruvate peak. It was found that the PC activity representing the anaplerotic

metabolism was approximately 7% the total metabolism (anaplerotic + pyruvate metabolism) and therefore in good agreement with that reported previously (Moreno et al. 2010). To date, anaplerosis has only been studied using ^{13}C-isotopomer analysis by MR (Malloy et al. 1988; Chatham et al. 2003; Merritt et al. 2007; Moreno et al. 2010), but no real-time estimation of this important metabolic pathway has been carried out.

The difference in the number of metabolites identified in the characteristic hyperpolarised ^{13}C MR spectra acquired from the two groups of Langendorff perfused rat heart could also be due to the different sensitivity of the two coils ($^{23}Na/^{13}C$ saddle coil and $^{1}H/^{13}C$ birdcage coil) used in this thesis. In the tube containing the perfused heart and its perfusion solution the concentration of ^{1}H was higher than that of ^{23}Na. It is therefore likely that the shimming performed using the signal from the first type of nucleus was more efficient than that performed on the second type of nucleus. The spectra acquired using the $^{1}H/^{13}C$ birdcage coil would therefore be characterised by a narrow bandwidth than those acquired using the $^{23}Na/^{13}C$ saddle coil. Narrower the bandwidth, better metabolites characterised by adjacent frequencies of resonance can be discern in the hyperpolarised ^{13}C MR spectrum. However, as detailed in Table 3.4 most all the hyperpolarised ^{13}C MR spectra acquired from the Langendorff hearts perfused with glucose plus pyruvate, and for which the aspC1 and aspC4 peaks were not observed, were acquired with the $^{1}H/^{13}C$ birdcage coil which, for what mentioned above, is likely to be characterised by a higher sensitivity than the $^{23}Na/^{13}C$ saddle coil. Additionally, the spectra acquired from the Langendorff hearts perfused with glucose only, for which the aspartate peaks were detected,

were acquired using both types of coils and the aspartate peaks were always detected regardless the type of coil used.

The most widely explored application of hyperpolarised ^{13}C MR in the heart is the measurement of the characteristic rate constant of PDH. Previous studies have shown that it is possible to derive this rate by fitting the hyperpolarised time-series of [1-$^{13}C_1$] pyruvate and $H^{13}CO_3^-$ with a two compartments, first-order, unidirectional compartmental model. This assumes that the PDH activity is not limited by the enzyme cofactors availability and therefore that the cofactors are regenerated quicker than consumed. This condition may be true *in vitro* where often the coenzymes are added in stoichiometric amount or *in vivo* where the heart metabolic substrates are regenerated via a number of competitive metabolic pathways. Langendorff hearts for hyperpolarised experiments are commonly perfused with Krebs-Henseleit buffers containing glucose (or glucose plus pyruvate) but not fatty acids because the physiological long-chain fatty acids bound to albumin shortening the characteristic T_1 making more difficult the real time detection of the hyperpolarised molecules involved in the metabolic pathway assessed (Moreno et al. 2010). Due to the uniqueness of the experimental protocol exploited for the hyperpolarised experiments in perfused hearts it was necessary to verify if the metabolic conversion catalysed by PDH does not depend on the availability of the enzyme cofactor as previously reported for *in vitro* and *in vivo* experiments. With this aim the hyperpolarised time-series of pyruvate and $H^{13}CO_3^-$ acquired for both groups of perfused hearts were fitted with both a first and second-order compartmental model. Results suggested that, regardless the Krebs-Henseleit buffer used to

perfuse the isolated hearts the conversion of pyruvate to $H^{13}CO_3^-$ appears to follow second-order rather than first-order kinetics as previously suggested for *in vivo* and *in vitro* experiments. Two co-factors are involved in the metabolic conversion catalysed by PDH: NAD^+ and CoA. In this thesis a study was carried out in collaboration with the University of Amsterdam in order to assess the dynamic of cofactor NAD^+ in perfused rat hearts during the injection of a 50mM pyruvate solution using fluorescence imaging. Although at very preliminary stage, results showed that NAD^+ is depleted during the injection of pyruvate suggesting the possibility that the PDH activity is limited by the availability of this cofactor in perfused hearts.

The value of the apparent rate of conversion of pyruvate to $H^{13}CO_3^-$ (k_{AB}) estimated using a two-compartment, second-order, unidirectional kinetic model was significantly lower for the group of isolated hearts perfused with a Krebs-Henseleit buffer containing 11.1mM glucose plus 2.5mM pyruvate than that reported for the group of hearts perfused with only 11.1mM glucose (Figure 5.15). It is possible that perfusing the isolated hearts with a Krebs buffer containing 11.1mM glucose plus 2.5 mM pyruvate results in a baseline value of the cofactors NAD^+ at the moment of the injection of hyperpolarised pyruvate significantly lower than that characteristic of isolated rat hearts perfused with Krebs buffer containing only 11.1mM glucose. As a result, in the pyruvate perfused hearts the PDH activity is significantly lower due to the reduced amount of NAD^+ available. It is also possible that the lack of the metabolic peaks corresponding to aspartate C1 and C4 in the ^{13}C MRS spectrum of isolated hearts perfused with 11.1mM glucose and 2.5mM pyruvate is related to

the lower availability of NAD^+ in the mitochondria. The conversion of malate to oxaloacetate, part of the TCA, as well as the aspartate-malate shuttle depends on the availability of NAD^+. Therefore, it is plausible that the production aspartate C1 and C4 is stopped or drastically reduced when the availability of the cofactor NAD^+ is low.

The semi-quantitative index AUC was also estimated for the conversion of hyperpolarised [1-$^{13}C_1$] pyruvate to $H^{13}CO_3^-$. In contrast to what is reported for the pyruvate-lactate exchange detected *in vitro* in whole blood cells, AUC was found not to be directly proportional to the PDH enzymatic rate regardless the compartmental model used for the determination of k_{AB}. This is probably due to the fact that the conversion of pyruvate to $H^{13}CO_3^-$ does not follow first-order kinetics for which has been shown the proportionality of the AUC ratio to the rate of metabolic conversion k_{AB} estimated using compartmental modelling.

All analysis methods used in this thesis to characterise the metabolic conversion of hyperpolarised ^{13}C pyruvate to its metabolites both *in vitro* and *ex vivo* do not account for the measurement error. In the experimental MR protocols used in these types of studies each point of the hyperpolarised time-series is acquired using the same experimental time. The error associated with the measurement can be therefore considered equal at each time point. For this reason un-weighted estimators has been commonly used in previous studies for the analysis of hyperpolarised time-series (Menichetti et al. 2012; Hill et al. 2013) .

The results presented in this Chapter show that the experimental protocol developed was adequate to detect in real time to metabolic conversion of

hyperpolarised [1-$^{13}C_1$] pyruvate to its downstream metabolites both *in vitro* in whole blood cells and *ex vivo* in Langendorff rat hearts. There are, however, some limitations in the methodologies used in this thesis that have to be considered. All experiments presented in this Chapter were carried out during the optimisation of the experimental protocol for the hyperpolarisation of metabolically active molecules, heart perfusion, and MR acquisition. The datasets are therefore characterised by some variability in the intensity of the metabolite peaks (Figure 5.7 and Figure 5.8). Additionally, in the experiments carried out in the early stage of this thesis the cardiac function was not monitored due to the lack of an MR compatible system, meaning that it was not possible to assess the consistency of the heart perfusion protocol after it was inserted into the spectrometer. In future studies, hyperpolarised time-series of [1-$^{13}C_1$] pyruvate and its downstream metabolites will be acquired using the same optimised experimental protocol and cardiac contractility will be monitored throughout each experiment.

The kinetic analysis of the hyperpolarised time-series of [1-$^{13}C_1$] pyruvate and $H^{13}CO_3$- suggested that the metabolic conversion catalysed by PDH follows second-order kinetics rather than first-order kinetics as speculated for *in vitro* and *in vivo* data. A preliminary study suggested that availability of NAD^+ may be reduced during the injection of a 50mM pyruvate solution in Langendorff rat hearts perfused with a Krebs buffer containing 11.1mM glucose only. Further studies are however needed to confirm this hypothesis. In future studies, the dynamics of the cofactor NAD^+ during the injection of a 50mM pyruvate solution will be measure using fluorescence imaging in two groups of Langendorff rat

hearts; one group will be perfused with a Krebs-Henseleit buffer containing only 11.1mM glucose while the buffer used to perfuse the second group will contain 11.1mM glucose plus 2.5mM.

Compartmental modelling suggests that the hyperpolarised signal from the cofactor is characterised by sigmoidal dynamics starting to decay as soon as the hyperpolarised pyruvate arrives to the perfused heart and reaches a minimum after ten-twenty seconds (Figure 5.14). A more complete compartmental model that will be developed in the future will not model hyperpolarised signals but concentrations. In order to do so it is necessary to add three additional compartments representing the thermal equilibrium signal of pyruvate, $H^{13}CO_3^-$ and cofactor to the compartmental model presented in Figure 4.7.

In the compartmental models developed in this thesis the rate of uptake across the mitochondria membrane of the hyperpolarised pyruvate was not included assuming that the formation of the pyruvate products is limited by the rate of the enzymatic conversion rather than by the uptake of the hyperpolarised solution. Pyruvate is transported within mitochondria through specific proteins. The rates of uptake of this molecule can therefore limit the formation of pyruvate metabolites such as bicarbonate. The transport of hyperpolarised pyruvate across the mitochondria membrane will be included in future compartmental models.

Additional details on the dependency of the PDH activity on the enzyme cofactor concentration may be derived using the hybrid MEM/NLS algorithm for the kinetic analysis of *ex vivo* hyperpolarised time-series. In this Chapter it was

shown that the MEM/NLS algorithm is an adequate tool for the kinetic analysis of *in vitro* hyperpolarised dynamic data however the extension of this analysis method to *ex vivo* data needs further considerations. In this thesis the proposed algorithm was tested for the sensitivity to noise of the hybrid method only for a range of SNR_Bs typical of *in vitro* experiments ($20 < SNR_B < 90$). Hyperpolarised time-series acquired *ex vivo* exhibit higher noise levels than those detected *in vitro*. The performance of the MEM/NLS algorithm at lower SNR_Bs should be therefore accurately assessed before extending this method to the analysis of *ex vivo* data. Extending this method to the analysis of *ex vivo* data also requires further consideration on the input function. The measurement of the optimal input function during hyperpolarised *ex vivo* experiments is still an unsolved problem. The hyperpolarised signal of the injected molecule cannot be used as an input function because it contains information on the delivery of the molecule but also on its metabolic conversion. Recent studies have proposed methods to obtain an accurate measure of the delivery input function directly by measuring the hyperpolarised signal of the injected molecule in the tube used to perfused the heart or indirectly by detecting the hyperpolarised signal of urea, a non metabolically active compound, injected into the system at the same time of the metabolite of interest (von Morze et al. 2012; Kazan et al. 2013). With an accurate knowledge of the delivery input function, the hyperpolarised time-series of detected metabolites can be deconvoluted before applying the MEM/NLS algorithm.

5.5 Conclusion

This Chapter presented the results of the *in vitro* and *ex vivo* hyperpolarised experiments whose acquisition protocols are detailed in Chapter 3. The metabolic conversion of hyperpolarised [1-$^{13}C_1$] pyruvate to its downstream metabolites was detected *in vitro* in whole blood cells and *ex vivo* in Langendorff rat hearts. In order to quantify the rate of the metabolic conversions observed using hyperpolarised ^{13}C MR, experimental time-series were fitted using the analysis methods presented in Chapter 4. For *in vitro* data the results from the Monte Carlo simulations showed that the MEM/NLS algorithm is able to identify the number of exponentials that describe the time-series of hyperpolarised data. It is then possible under certain hypothesis to associate a compatible compartmental model to the MEM/NLS solution and derive the characteristic kinetic rates of the system assessed. In this Chapter the combination of the hybrid MEM/NLS algorithm was shown to be able to derive information on the enzymatic conversions that would otherwise be ignored if the experimental data were analysed with the traditional compartmental models only where the type of reaction is assumed *a priori*.

The extension of this approach to the analysis of *ex vivo* hyperpolarised data requires further considerations and has not been addressed in this thesis. In this Chapter the hyperpolarised time-series of [1-$^{13}C_1$] pyruvate and $H^{13}CO_3^-$ were fitted using compartmental modelling in order to derive the characteristic rate of the PDH activity. Preliminary results suggested that *ex vivo* the metabolic conversion of pyruvate to $H^{13}CO_3^-$ does not follow first-order kinetics as speculated for *in vitro* and *in vivo* experiments and that the PDH activity is

limited by the enzyme cofactor NAD^+ availability. Further studies are needed in this direction but the experiments carried out in this thesis pointed out the possibility that the injection of a non-tracer amount (50mM) of hyperpolarised pyruvate solution into a perfused heart may change the biological system and therefore the kinetics of the enzymatic reaction assessed before measuring it. In light of the results presented in this thesis, a new study aimed at investigating the effect of different concentrations of hyperpolarised pyruvate on the kinetics of the metabolic conversions observed using ^{13}C MR should be perform.

Chapter 6 : Analysis Methods for Time-Activity Curves of PET Tracers Acquired *Ex vivo* from Langendorff Rat Hearts

6.1 Introduction

The Langendorff perfused heart has been often used for the early evaluation of novel radiotracer pharmacokinetics. It is a biologically relevant model, with an intact vasculature, which provides insight into tracer uptake and retention in a metabolically active beating heart, without the potential complications of systemic metabolism and recirculation. This experimental protocol is versatile in terms of allowing direct drug or tracer administration, control of perfusion, workload, and energy substrate supply, simple induction of hypoxia or ischemia, and the capacity to monitor the effects of such interventions upon cardiac contractile function and biochemistry (Southworth et al. 2007; Southworth 2009). Perfused hearts were, for example, used to assess the possibility of using copper bis(thiosemicarbazonato) (BTSC) complexes (Fujibayashi et al. 1997; Handley et al. 2014), [^{18}F]- FMISO (Shelton et al. 1989) and [^{99m}Tc]-Nitroimidazole (Ng et al. 1995) as hypoxia imaging agents.

In order to derive information on tracer kinetics, *ex vivo* time-activity curves have to be fitted with accurate and reliable analysis methods.

To date there is not a gold standard analysis technique for the kinetic characterisation of time-activity curves of PET tracers acquired *ex vivo* from perfused hearts. Previous studies have fitted this type of data to exponential functions characterized by an pre-specified number of rates and quantified the tracer retention by averaging the activity measured in a chosen time interval at the end of the acquisition window (Ng et al. 1995). This approach requires *a priori* assumption of the number of kinetic processes described in the data, information not always available especially when new biological systems or imaging agents are studied.

A number of quantitative and semi-quantitative analysis methods that do not require any *a priori* assumption on tracer kinetics are available for the evaluation of PET tracer kinetics *in vivo*, but to date there is a lack of studies that investigate their performance for the kinetic characterisation of *ex vivo* time-activity curves. Due to the differences between the two experimental set up it is not possible to assume that the techniques validated for the analysis of *in vivo* PET data are appropriate for the kinetic characterisation of *ex vivo* time-activity curves of PET tracer. The delivery of the tracer ($C_p(t)$) to a Langendorff perfused heart can be measured with a γ-detector coupled to the inflow line while the time-activity curve in the heart ($C_{tiss}(t)$) can be acquired using a single γ-detector interrogating the entire isolated perfused heart. As tracer uptake is heterogeneous across the myocardium (from endocardium to epicardium, for example (Southworth et al. 2002)), time-activity curves from perfused hearts

likely represent a more heterogeneous range of kinetics than spatially resolved imaging data. *Ex vivo* time-activity curves further differ from those acquired *in vivo* in terms of SNR and lack of recirculation leading to an input function that decays rapidly to zero.

6.2 Aims

In this Chapter the possibility of using a number of methods for the kinetic characterisation of time-activity curves of PET tracers acquired from perfused rat heart was assessed using Monte Carlo simulations and experimental time-activity curves of two hypoxia-sensitive PET tracers: [^{18}F]-FDG and [^{18}F]-FMISO acquired as described in Section 3.5. In particular this study aimed at investigating the performance of spectral-based algorithms (SA and NLSA), introduced in Chapter 4, in (1) identifying the presence of irreversible trapping, (2) deriving the number of kinetic components and (3) quantifying the irreversible trapped component (α_0) from *ex vivo* time-activity curves. The accuracy and reproducibility of SA and NLSA in quantifying α_0 were compared to those of the Patlak graphical method and the semi-quantitative index NA also presented in Chapter 4.

The analysis methods used in this Chapter were chosen because they can be applied to homogenous as well as heterogeneous systems with only few hypotheses on the number of compartments necessary to describe the data. All Monte Carlo simulations and kinetic analysis were performed through a custom-

made Matlab (MathWorks®) code. SA was implemented in collaboration with Dr. Mattia Veronese.

6.3 Monte Carlo Simulations

Datasets were simulated reproducing the characteristics of *ex vivo* time-activity curves from isolated hearts in normoxia and at different levels of hypoxia. Bi- and tri-exponential *ex vivo* time-activity curves with known kinetics were simulated using Equation 4.57. The values of β_j were fixed (for tri-exponentials $\beta_1 = 0.5\text{min}^{-1}$, $\beta_2 = 5\text{min}^{-1}$ and $\beta_3 = 15\text{min}^{-1}$, and for bi-exponentials $\beta_1 = 0.5\text{min}^{-1}$ and $\beta_2 = 15\text{min}^{-1}$), whereas α_j were randomly generated within a chosen interval (for tri-exponentials $0.011\text{min}^{-1} < \alpha_1 < 0.11\text{min}^{-1}$, $0.12\text{min}^{-1} < \alpha_2 < 0.2\text{min}^{-1}$, $5\text{min}^{-1} < \alpha_3 < 8\text{min}^{-1}$, and for bi-exponentials $0.011\text{min}^{-1} < \alpha_1 < 0.11\text{min}^{-1}$, $5\text{min}^{-1} < \alpha_2 < 8\text{min}^{-1}$). Bi- and tri-exponential curves were simulated with and without a trapped component α_0 (for $\beta_0 = 0$). Four different values of irreversible trapping were simulated ($\alpha_{0,1} = 0.006\text{min}^{-1}$, $\alpha_{0,2} = 0.06\text{min}^{-1}$, $\alpha_{0,3} = 0.2\text{min}^{-1}$ and $\alpha_{0,4} = 0.6\text{min}^{-1}$) (Figure 6.1). The values used in the simulations were chosen within a physiological range and in agreement with previous studies (Bertoldo et al. 1998). To obviate further sources of variability between one dataset and another, the same $C_p(t)$, taken from an experimental dataset and representative of these experiments, was used for all simulations. Each dataset was simulated for a low and a high SNR (SNR = 60 and SNR = 120), consistent with the experimental data. N=100 and a time resolution $\Delta t = 0.0033\text{min}$ were chosen. The SNR of PET images is commonly estimated as the ratio between the

standard deviation and the mean value of the radioactive signal detected in the ROI (Dahlbom 2002). In this thesis the SNR was estimated from *ex vivo* time-activity curves and not from *in vivo* images. To take into account the differences between the *in vivo* and the *ex vivo* PET experimental protocol, a new definition of SNR, similar to that exploited for *ex vivo* MR ^{13}C time-series, was used in this thesis. In particular the SNR of the time-activity curves of PET data acquired *ex vivo* from Langendorff rat hearts was calculated as the ratio of the maximum value of the time-activity curve and the standard deviation of the signal in the last minute of each experiment.

The percent bias (%BIAS) of quantitative and semi-quantitative indices (α_0, Patlak and NA) was calculated as a performance index (Equation 6.1).

$$\%\mathrm{BIAS}_p = 100 * \sum_{j=1}^{k} \frac{(p_j - p_{TRUE})}{p_{TRUE}} \qquad 6.1$$

where p_j and p_{TRUE} are the estimated and true value of the indices p, respectively.

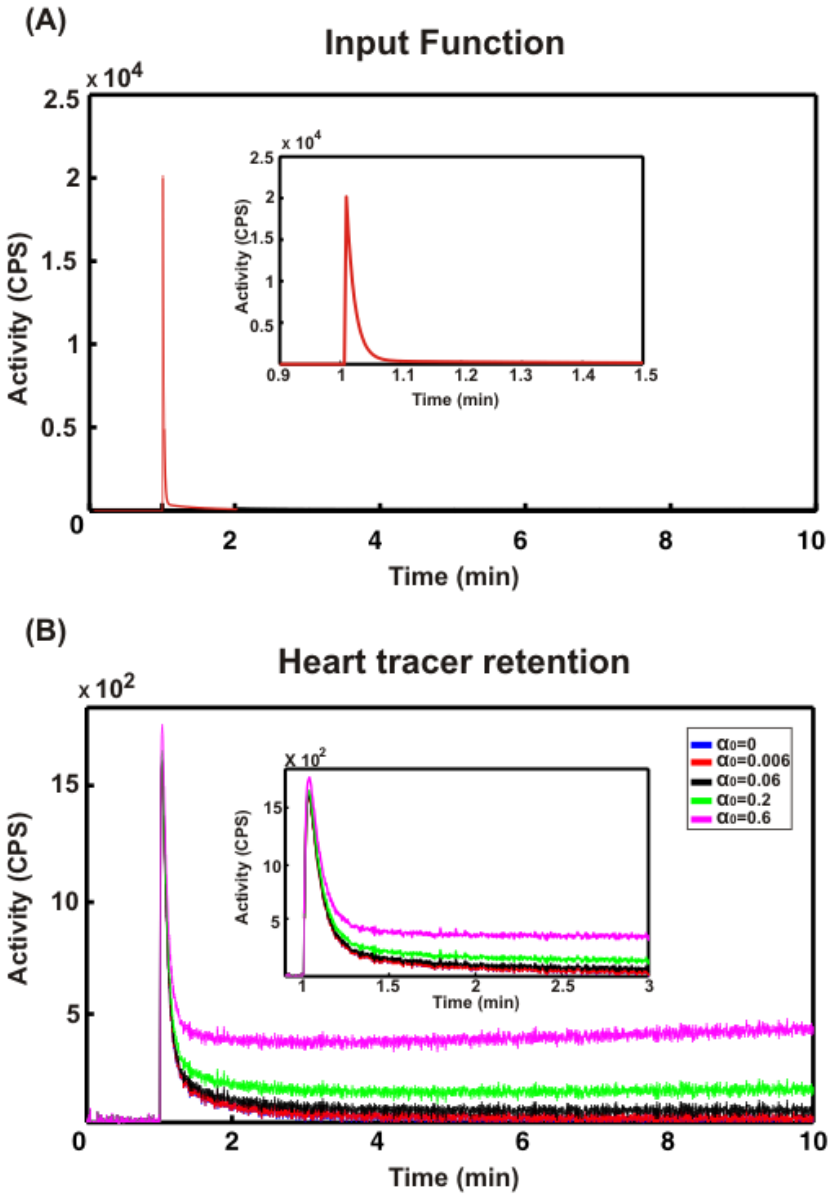

Figure 6.1: Simulated datasets. (A) Representative input function used in the simulations. (B) Representative simulated heart time-activity curves for different values of irreversible trapped components (α_0) (units are in min^{-1}). The dynamics simulated were chosen to mimic the tissue time-activity curves of hypoxia sensitive tracers characterised by an increase in tracer uptake when the perfused heart is made hypoxic compared to that measure in normoxia.

6.4 Experimental E*x vivo* Time-Activity Curves of PET Tracers

Time activity curves of two hypoxia sensitive PET tracers ([^{18}F]-FDG and [^{18}F]-FMISO) were acquired *ex vivo* in Langendorff perfused rat hearts as described in Section 3.5. Representative [^{18}F]-FDG input and tissue time-activity curves are shown in Figure 6.2 B, while the experimental protocol used for their acquisition in Figure 6.2 A.

6.5 Data Analysis

Simulated and experimental time-activity curves were analysed using (1) spectral-based algorithms (SA and NLSA), (2) the Patlak graphical plot and (3) the semi-quantitative index NA. All datasets were corrected for radioactive decay.

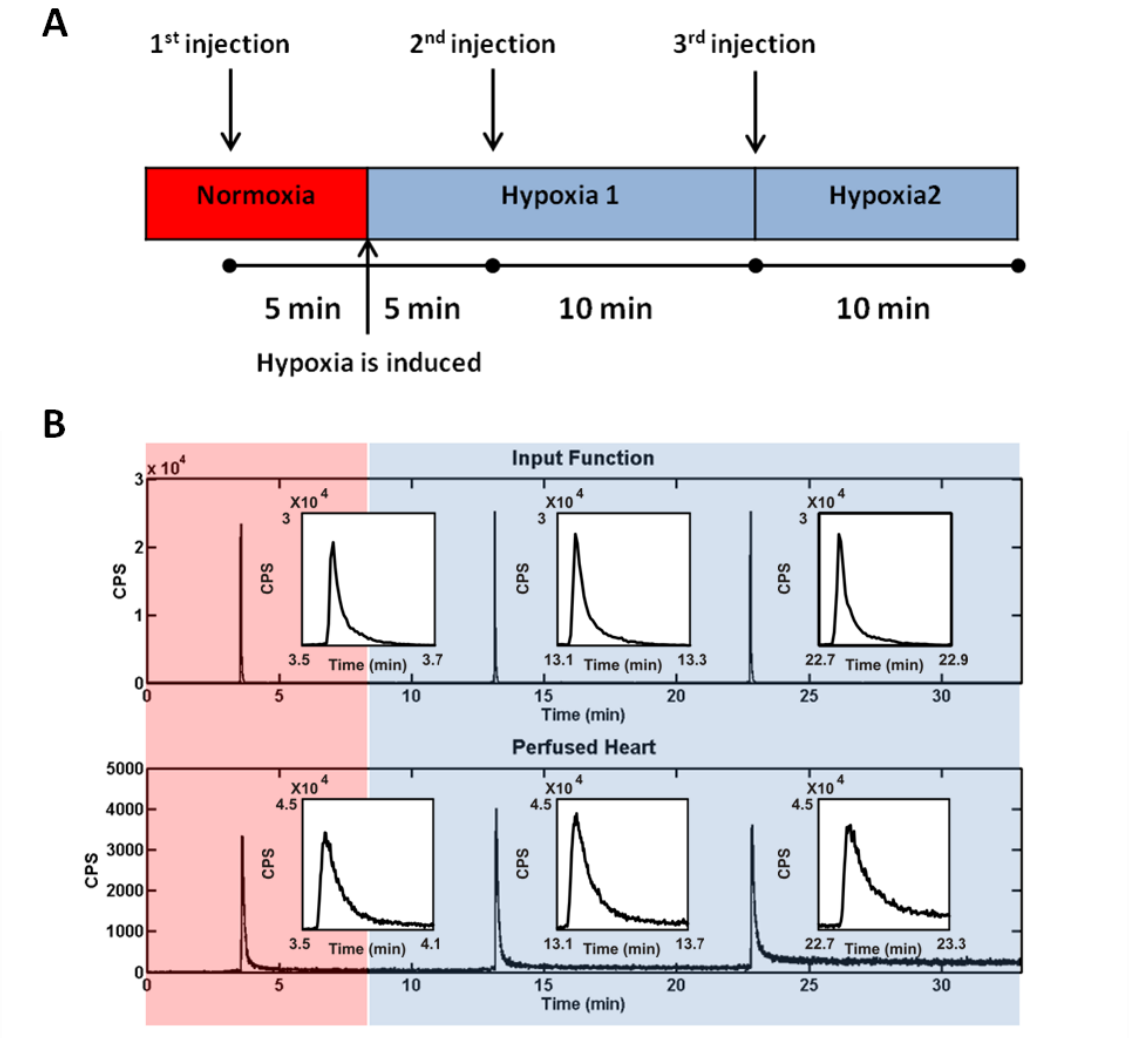

Figure 6.2: (A) Schematic representation of the experimental protocol used to acquire [^{18}F]-FDG and [^{18}F]-FMISO *ex vivo* time-activity curves from perfused rat hearts. (B) Representative [^{18}F]-FDG input and tissue time-activity curves acquired *ex vivo* using the protocol described in (A) (y-axis units are counts per second).

To adjust the experimental data for residual activity due to prior injections in the same heart, a model prediction correction was used. The time-activity curve acquired in normoxia was fitted with the algorithm assessed (SA or NLSA) and the result was extrapolated in the time interval relative to the second injection.

The contribution of the activity from the first injection to the second was therefore calculated and subtracted. After the background correction the curve relative to the second injection was fitted and its contribution subtracted to the third injection. Statistical analysis was performed using GraphPad Prism® (GraphPad Software Inc, USA). All values are expressed as the mean ± SD. Data were analysed using a one way ANOVA with Dunnett's test to compare each group of datasets acquired in hypoxia with the corresponding control group measured in normoxia (Dunnett 1955).

6.6 Results

6.6.1 Monte Carlo Simulations

The results of simulations showed that NLSA is more accurate than SA in identifying the absence of irreversible trapping ($\alpha_0 = 0 min^{-1}$) for the dynamics and SNRs considered. For the lowest value of the trapping simulated ($\alpha_0 = 0.006 min^{-1}$) with tri-exponential kinetics a similar degree of accuracy was found for SA and NLSA whereas for bi-exponential kinetics SA was found to be superior. For higher values of trapping, the accuracy in estimating the presence of the trapping of the two algorithms was equal to 100% (Table 6.1).

Table 6.1: Proportion of simulations that had α0 = 0 or α0 ≠ 0 identified by NLSA and SA.

Simulated scenario	NLSA performance						SA performance					
	SNR = 60			SNR = 120			SNR = 60			SNR = 120		
	$\alpha_0 = 0$ (%)	$\alpha_0 \neq 0$ (%)	**Accuracy** (%)	$\alpha_0 = 0$ (%)	$\alpha_0 \neq 0$ (%)	**Accuracy** (%)	$\alpha_0 = 0$ (%)	$\alpha_0 \neq 0$ (%)	**Accuracy** (%)	$\alpha_0 = 0$ (%)	$\alpha_0 \neq 0$ (%)	**Accuracy** (%)
Tri-exponential												
No trapping ($\alpha_0 = 0$)	100	-	*100*	100	-	*100*	21	79	*21*	14	86	*14*
Trapping 1 ($\alpha_0 = 0.006$)	10	90	*90*	6	94	*94*	6	94	*94*	10	90	*90*
Trapping 2 ($\alpha_0 = 0.06$)	-	100	*100*	-	100	*100*	-	100	*100*	-	100	*100*
Trapping 3 ($\alpha_0 = 0.2$)	-	100	*100*	-	100	*100*	-	100	*100*	-	100	*100*
Trapping 4 ($\alpha_0 = 0.6$)	-	100	*100*	-	100	*100*	-	100	*100*	-	100	*100*
Bi-exponential												
No trapping ($\alpha_0 = 0$)	100	-	*100*	100	-	*100*	14	86	*14*	2	98	*2*
Trapping 1 ($\alpha_0 = 0.006$)	23	77	*77*	13	87	*87*	4	96	*96*	-	100	*100*
Trapping 2 ($\alpha_0 = 0.06$)	6	94	*94*	2	98	*98*	-	100	*100*	-	100	*100*
Trapping 3 ($\alpha_0 = 0.2$)	-	100	*100*	-	100	*100*	-	100	*100*	-	100	*100*
Trapping 4 ($\alpha_0 = 0.6$)	-	100	*100*	-	100	*100*	-	100	*100*	-	100	*100*

α_0 indicates the tracer trapping. Units are in min^{-1}.Hyphens indicate 0.

The values of $\%BIAS\alpha_0$ (Equation 6.1) reported with NLSA and SA for both bi- and tri-exponential curves and high and low SNRs are shown in Figure 6.3. For tri-exponential kinetics (Figure 6.3 A and C), NLSA displayed a lower bias than SA for the quantification of small α_0 values with a $\%BIAS\alpha_0$ equal to 38.30% ± 4.92% and 176.15% ± 114.65% at $\alpha_{0,1} = 0.006min^{-1}$ and SNR = 60 for NLSA and SA, respectively. For higher values of trapping ($\alpha_{0,3} = 0.2min^{-1}$ and $\alpha_{0,4} = 0.6min^{-1}$), SA and NLSA were of similar accuracy, with a $\%BIAS\alpha_0$ equal to 0.17% ± 0.03% for SA and to 1.55% ± 0.34% for NLSA at $\alpha_{0,4} = 0.6\ min^{-1}$ and SNR = 120. The same trend was found for bi-exponential curves (Figure 6.3 B and D), where $\%BIAS\alpha_0$ was 16.41% ± 4.71% for NLSA and 228.39% ± 117.70% for SA at $\alpha_{0,1} = 0.006\ min^{-1}$ and SNR = 60. The values estimated for $\%BIAS_{\alpha 0}$ at higher trapping were similar to those found for tri-exponential kinetics. The accuracy in quantification of α_0 for both NLSA and SA algorithms improved with increasing values of trapping and SNR. Additionally, the %BIAS reported for both algorithms were generally lower for bi-exponential curves than those estimated for tri-exponential kinetics.

In Figure 6.4 A and B the mean and the standard deviation of the %BIAS reported for Patlak and NA are presented for simulated tri-exponential curves. In the absence of noise, Patlak returns the exact value of α_0, whereas NA is a surrogate measurement of the trapped component proportional to α_0.

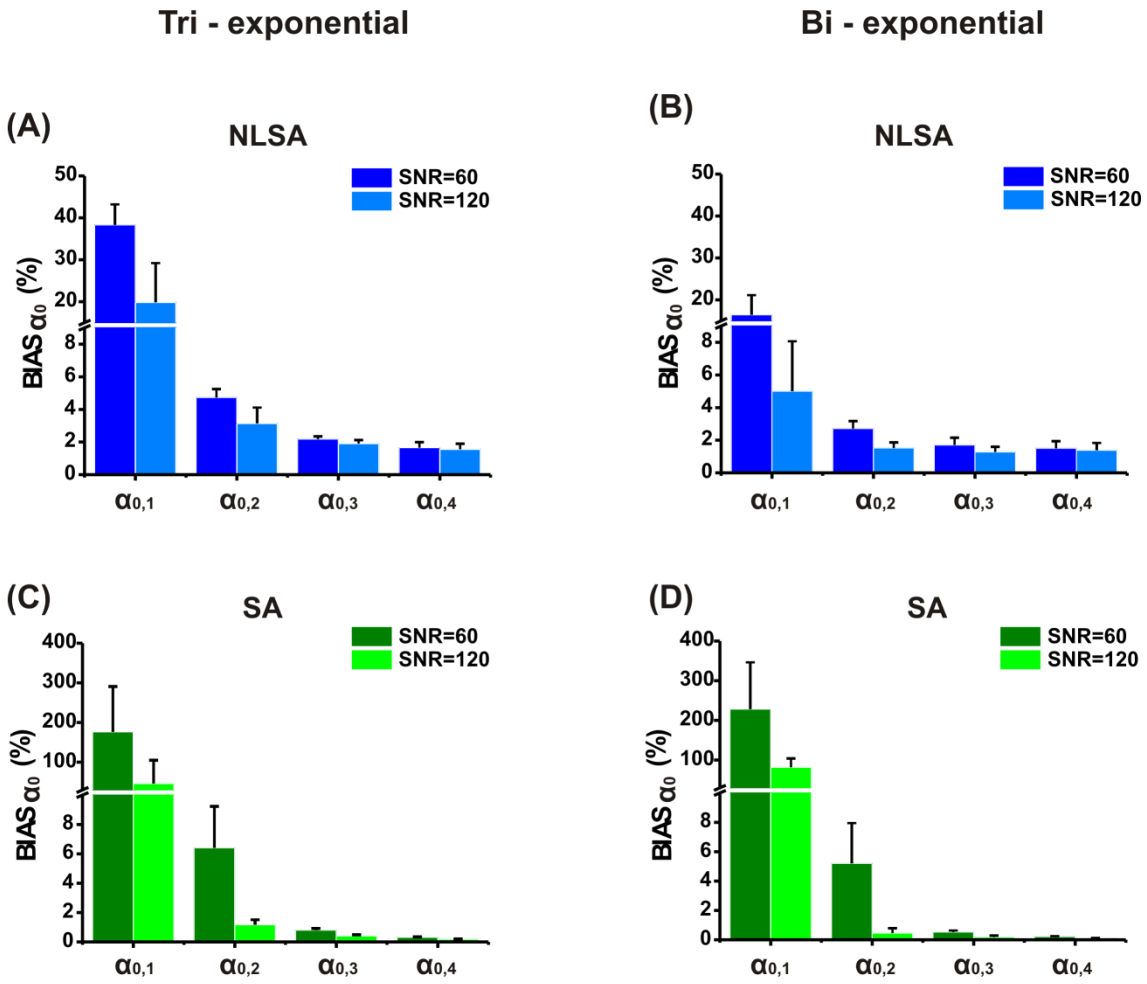

Figure 6.3: %Bias in estimated trapping (α_0) of the NLSA and SA algorithm applied to simulated tri-exponential (A-B) and bi-exponential (C-D) models. $\alpha_{0,i}$ indicates the trapping of the tracer with the values reported in Table 6.1. Units are in min^{-1}.

The accuracy in quantifying the trapped component from the simulated data using Patlak increased with the value of trapping and SNR with a maximum %BIAS equal to -1662% ± 1053.8% at SNR = 60 and -507% ± 230% at SNR = 120 and a minimum value equal to -20.2% ± 3% at SNR = 60 and -12.2% ± 2.5% at SNR = 120. The maximum %BIAS reported for NA is 5.3% ± 10% at SNR = 60 and 3.2% ± 10% at SNR = 120 while the minimum value was equal to

0.8% ± 12.4% at SNR = 60 and 0.6% ± 12.4% at SNR = 120. The %BIAS reported for both Patlak and NA estimated from bi-exponential curves were not significantly different from those calculated for tri-exponential curves (data not reported).

Table 6.2 shows the performance of the NLSA and SA algorithm in estimating the number of non-trapped components from simulated bi- and tri-exponential curves. Results showed the percentage of datasets where the number of components was under estimated (UE), over estimated (OE) or correctly estimated (CE). For tri-exponential time-activity curves, the accuracy in determining the number of components was better for NLSA when $\alpha_0 = 0 min^{-1}$, whilst SA was more accurate at all other values of α_0 simulated. For bi-exponential kinetics the accuracy in determining the number of components was significantly better than for tri-exponential time-activity curves. NLSA was more accurate when $\alpha_0 = 0 min^{-1}$, whereas SA was better than NLSA for all non zero values of trapping simulated.

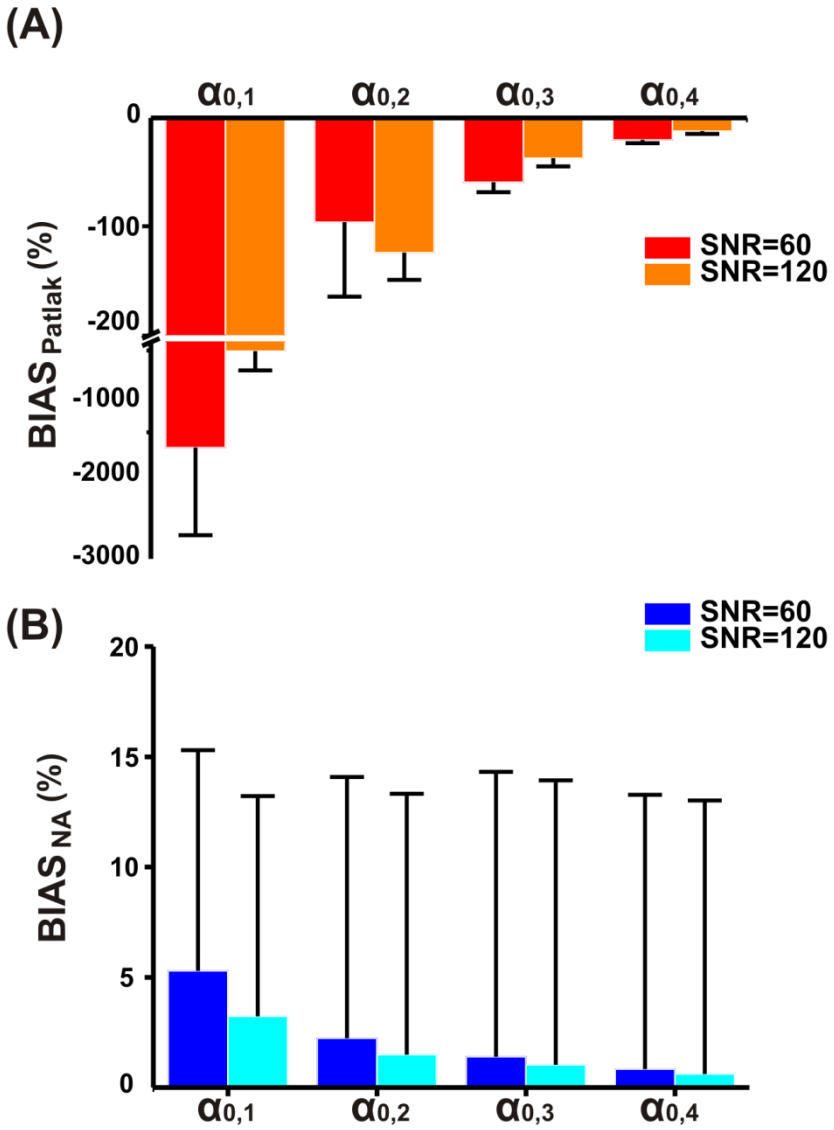

Figure 6.4: %Bias reported for (A) Patlak and (B) NA applied to simulated tri-exponential time-activity curves.

Table 6.2: Proportion of simulations that had the number of components underestimated, overestimated or correctly estimated by NLSA and SA

Simulated scenario	NLSA performance						SA performance					
	SNR = 60			SNR = 120			SNR = 60			SNR = 120		
	UE (%)	OE (%)	**CE** (%)	UE (%)	OE (%)	**CE** (%)	UE (%)	OE (%)	**CE** (%)	UE (%)	OE (%)	**CE** (%)
Tri-exponential												
No trapping (α_0 = 0)	85	-	*15*	-	-	*100*	-	81[a]	*19*[a]	-	100[a]	-[a]
Trapping 1 (α_0 = 0.006)	100	-	-	46	-	*54*	18	-	*82*	-	-	*100*
Trapping 2 (α_0 = 0.06)	100	-	-	60	-	*40*	18	-	*82*	-	-	*100*
Trapping 3 (α_0 = 0.2)	100	-	-	95	-	*5*	46	-	*54*	-	-	*100*
Trapping 4 (α_0 = 0.6)	100	-	-	100	-	-	53	-	*47*	1	-	*99*
Bi-exponential												
No trapping (α_0 = 0)	-	-	*100*	-	-	*100*	-	86[a]	*14*[a]	-	-	*100*[a]
Trapping 1 (α_0 = 0.006)	1	-	*99*	-	-	*100*	17	18	*65*	-	-	*100*
Trapping 2 (α_0 = 0.06)	1	-	*99*	-	-	*100*	-	-	*100*	-	-	*100*
Trapping 3 (α_0 = 0.2)	11	-	*89*	5	-	*95*	-	-	*100*	-	-	*100*
Trapping 4 (α_0 = 0.6)	34	-	*66*	32	-	*68*	-	-	*100*	-	-	*100*

α_0 indicates the tracer trapping. Units are in min^{-1}; *UE,* underestimated number of components; *OE*, overestimated number of components; *CE*, correctly estimated. Results are shown only for the percentage of datasets where the presence of baseline was correctly estimated (Table 6.1). [a]An accuracy in baseline identification was <25%. Hyphens indicate 0.

6.6.2 Experimental Datasets

Two time-activity curves were acquired for each experiment: one representative of the delivery input function and a second reflecting the tracer accumulation in the heart. Both curves were included in the SA and NLSA fitting. In Figure 6.5 a representative normoxic dataset after decay and background correction (coloured dots) is shown with overlaid fits (coloured lines). The SNRs estimated for the [^{18}F]-FDG time-activity curves were 165 ± 40 (a.u) in normoxia, 129 ± 35 (a.u.) at 5min hypoxia and 103 ± 32 (a.u.) at 15min hypoxia. The SNRs estimated for the [^{18}F]-FMISO time-activity curves were 253 ± 117 (a.u.) in normoxia, 182± 20 (a.u.) at 5min hypoxia and 151 ± 17 (a.u.) at 15min hypoxia. Results from the NLSA and SA quantification of [^{18}F]-FDG datasets (n = 4) are shown in Table 6.3. The NLSA algorithm always identified a trapped component α_0 (with the exception of one dataset run 4, Hypoxia1), whereas SA determined a null trapped component for 5 datasets out of 12. NLSA identified 4 kinetic components different from α_0 while SA identified between 3 and 5 components.

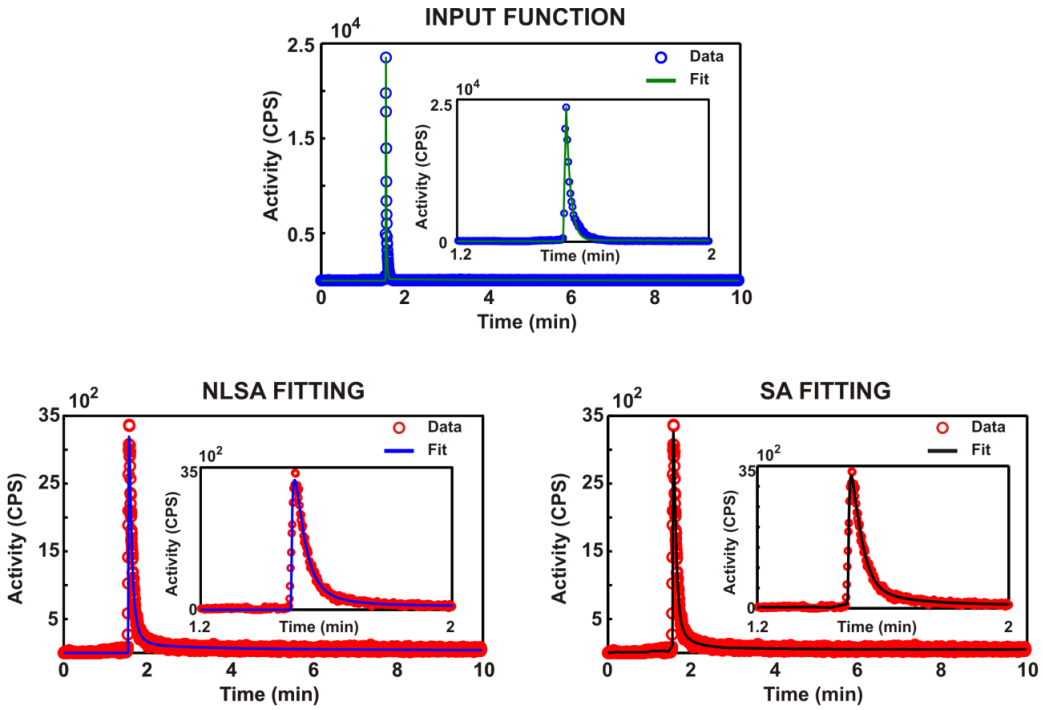

Figure 6.5: (A) Experimental input function (blue dots) with overlaid fit (green). (B-C) Experimental heart data (red dots) with overlaid NLSA (blue) and SA (black) fits.

Figure 6.6 A shows the mean ± SD of the trapping quantified with NLSA and SA. The value of α_0 estimated with NLSA significantly increased from 0.04min^{-1} ± 0.02min^{-1} in normoxia to 0.20min^{-1} ± 0.11min^{-1} at 15min hypoxia ($p < 0.05$). The mean of the trapped component estimated with SA did not change significantly between normoxia and hypoxia and was associated with larger error. The coefficient of variation ($CV\alpha_0$ (%)) associated with the estimation of the trapped component was smaller for NLSA than SA. The $CV\alpha_0$ in normoxia was 3.4% ± 2% for NLSA and 181.2% ± 308.9% for SA. At 15min hypoxia it was 8.2% ± 7% and 36.3% ± 41.8% for NLSA and SA, respectively.

Figure 6.7 A shows the mean ± SD of Patlak and NA calculated for [^{18}F]-FDG. The value of Patlak increased, but not significantly, from 0.06min^{-1} ± 0.02min^{-1} in normoxia to 0.19min^{-1} ± 0.09min^{-1} at 15min hypoxia. NA also increased from 0.03 ± 0.01 (a.u.) in normoxia to 0.04 ± 0.02 (a.u.) at 15min hypoxia, but not significantly. Table 6.4 shows the results from the NLSA and SA quantification for [^{18}F]-FMISO datasets (n=3). The NLSA algorithm always identified a trapped component α_0, whereas SA determined a null trapped component for one of the dataset (run 2, Normoxia). The number of kinetic components different from α_0 identified is 4 using NLSA and between 2 and 4 with SA.

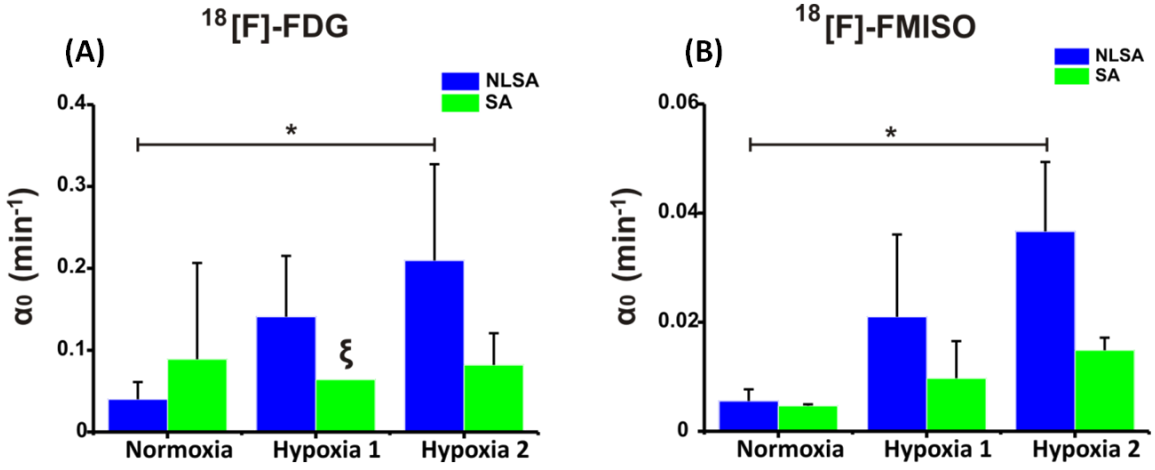

Figure 6.6: Mean ± SD of the trapping estimated with the NLSA (blue) and SA (green) algorithm in normoxia and hypoxia for (A) [^{18}F]-FDG and (B) [^{18}F]-FMISO experimental datasets. ξ indicates n=1 and * p < 0.05. α0 indicates the trapping of the tracer.

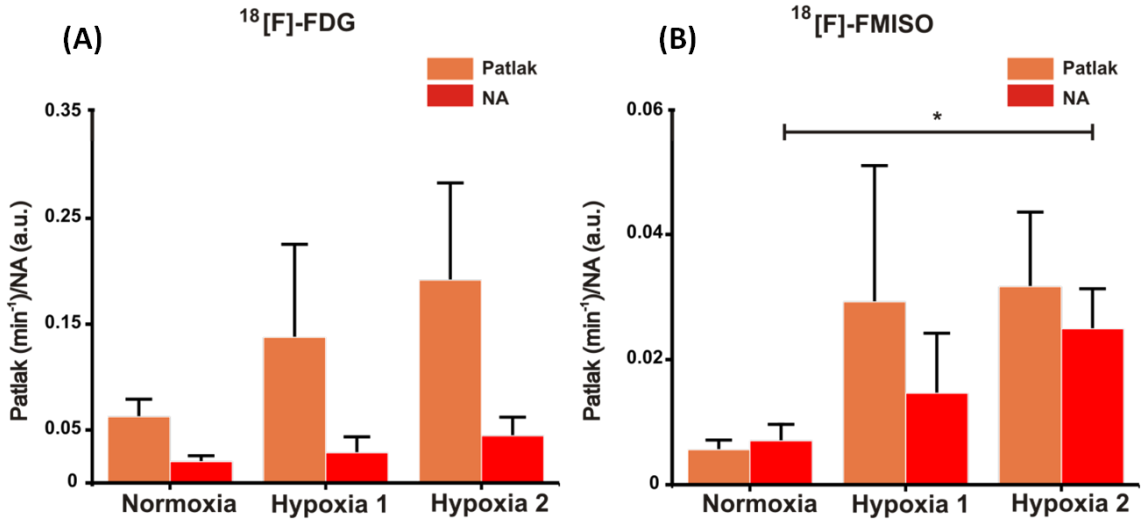

Figure 6.7: Mean ± SD of Patlak (orange) and NA (red) in normoxia and hypoxia for (A) [^{18}F]-FDG and (B) [1^{8}F]-FMISO experimental time-activity curve acquired ex vivo from perfused rat hearts. * p < 0.05.

Table 6.3: Results from the NLSA and SA quantification for [^{18}F]-FDG ex vivo datasets

	[^{18}F]-FDG datasets											
	Normoxia				Hypoxia 1				Hypoxia 2			
	1	2	3	4	1	2	3	4	1	2	3	4
α_0 NLSA (min^{-1})	0.037	0.070	0.023	0.025	0.084	0.160	0.200	-	0.310	0.260	0.220	0.042
α_0 SA (min^{-1})	0.038	0.005	0.037	-	0.064	-	-	-	-	0.130	0.050	0.060
Patlak (min^{-1})	0.066	0.080	0.066	0.040	0.100	0.150	0.250	0.046	0.200	0.180	0.300	0.077
NA (a.u.)	0.015	0.025	0.025	0.015	0.023	0.050	0.020	0.020	0.040	0.040	0.072	0.021

α_0 indicates the tracer trapping. Numbers 1, 2, 3, and 4 indicate the run number.

Table 6.4: Results from the NLSA and SA quantification for [18F]-FMISO ex vivo datasets

	[^{18}F]-FMISO datasets								
	Normoxia			Hypoxia 1			Hypoxia 2		
	1	2	3	1	2	3	1	2	3
α_0 NLSA (min^{-1})	0.004	0.008	0.004	0.033	0.025	0.011	0.050	0.040	0.023
α_0 SA (min^{-1})	0.004	-	0.005	0.010	0.016	0.002	0.020	0.015	0.013
Patlak (min^{-1})	0.005	0.007	0.004	0.015	0.018	0.054	0.450	0.025	0.024
NA (a.u.)	0.004	0.007	0.010	0.020	0.020	0.004	0.028	0.028	0.017

α_0 indicates the tracer trapping. Numbers 1, 2, 3, and 4 indicate the run number

Figure 6.6 B shows the mean ± SD of the trapping quantified with NLSA and SA. The value of α_0 estimated with NLSA significantly increased from $0.005min^{-1} \pm 0.002min^{-1}$ in normoxia to $0.03min^{-1} \pm 0.0002min^{-1}$ at 15min hypoxia ($p < 0.05$). The mean ± SD of the trapped component derived through SA also changed from $0.004min^{-1} \pm 0.00025min^{-1}$ in normoxia to $0.0148min^{-1} \pm 0.0023min^{-1}$ at 15min hypoxia, but not significantly. As found for the [^{18}F]-FDG time-activity curves, the $CV\alpha_0$ reported for NLSA was much smaller than that reported for SA. The $CV\alpha_0$ in normoxia was 4% ± 0.6% for NLSA and 16.1% ± 18.3% for SA. At 15min hypoxia it was 1.3% ± 0.2% and 13.7% ± 7% for NLSA and SA, respectively. In Figure 6.7 B the mean ± SD of Patlak and NA calculated for [^{18}F]-FMISO time-activity curves is reported. The value of Patlak increased from $0.005min^{-1} \pm 0.001min^{-1}$ in normoxia to $0.031min^{-1} \pm 0.01min^{-1}$ at 15min hypoxia, but was not significant. NA increased significantly from 0.007 ± 0.002 (a.u.) in normoxia to 0.02 ± 0.006 (a.u.) at 15min hypoxia ($p<0.05$).

6.7 Discussion

The results from the Monte Carlo simulations suggest that both quantitative and semi-quantitative analysis methods are adequate for the kinetic characterisation of time-activity curves acquired *ex vivo* from perfused hearts. NLSA was found to be more accurate than SA in estimating the absence of trapping ($\alpha_0 = 0min^{-1}$) for the SNRs considered and for both tri- and bi-exponential kinetics. NLSA was also superior to SA in quantifying the trapped component at low values of α_0, while for higher values of trapping the performance of the two algorithms was comparable.

The difference in performance of NLSA and SA in the identification and quantification of the trapped component is due to the different implementation of the two algorithms. In SA the possible values of the exponents β_j (Equation 4.57) that best describe the experimental data are chosen from a fixed grid of values and only the values of α_j are estimated. The optimal number of exponents is therefore not chosen *a priori* and is given by the number of rates β_j for which a non-zero α_j is estimated. The presence of noise can significantly reduce the accuracy of SA in identifying and quantifying very low frequency (e.g. trapping) and high frequency components (Veronese et al. 2010) as well as introducing phantom kinetic components (Cunningham and Jones 1993; Turkheimer et al. 1994) . For the NLSA algorithm, the experimental data are fitted with exponential curves of increasing order, and both β_j and α_j are derived using a non-linear least square estimator. In this case, all the kinetic components, specified *a priori*, are estimated and the model that best fits the experimental data is chosen *a posteriori* using a standard model parsimony criteria (Bertoldo et al. 1998). This means that the very low-frequency and high-frequency components are always estimated and the presence of noise can only affect the quantification of the value of the components, but not their identification.

SA was more accurate than NLSA in quantifying the number of components different from α_0, regardless the value of the trapping and SNR for tri-exponential curves. To determine whether the ability to estimate the correct number of kinetic components using the NLSA algorithm was dependent on the standard model parsimony criterion used, the NLSA algorithm was implemented and the optimal model was chosen using either the AIC or BIC. However, the accuracy of the NLSA algorithm in

estimating the number of kinetic components different from trapping was similar for both parsimony criteria used.

The accuracy of both algorithms in determining the correct number of exponentials appeared significantly better for bi-exponential dynamics, with accuracy close to 100% for all cases studied. Two or more kinetic components with close values are likely to be seen by SA and NLSA as a unique component. The greater the spread of kinetic values, the easier it is for the algorithms to discern the exponentials as separate components. In the simulations, the values of the kinetic components β_j were more spaced in the bi-exponential than tri-exponential curves, meaning that it was easier for SA and NLSA to discern the two components as distinct β_s.

The values estimated for Patlak and NA were found to be linearly proportional to the simulated values of trapping, but like spectral analysis, their estimation was affected by the presence of the noise. The %BIAS associated with the estimation of Patlak was always higher than that reported for the semi-quantitative index NA, for all SNRs and trapping considered. Patlak is derived by calculating the ratio between tissue retention of the tracer and the delivery input function which decays rapidly to zero. Both curves exhibit noise and therefore dividing two noisy quantities amplifies the noise and reduces the accuracy of the method. The mean of the %BIAS reported for NA becomes smaller with increasing values of trapping and SNRs, but the standard deviation does not change. In the Monte Carlo simulations for a given SNR the same amount of noise was added to the time-activity curves with different values of the trapped component. The standard deviation of the bias is dependent on the noise variance of the time-activity curve fitted and therefore it does not change with increasing values of trapping for a given SNR.

For experimental datasets the values reported for $CV\alpha_0$ suggest that the NLSA is more accurate than SA for the kinetic characterisation on *ex vivo* time-activity curves. NLSA identified a trapped component for the [^{18}F]-FDG datasets 11 times out of 12 and consistently indicated the presence of trapping for the [^{18}F]-FMISO datasets. Additionally, the trapped component quantified using NLSA significantly increases with the level of hypoxia for both [^{18}F]-FDG and [^{18}F]-FMISO in agreement with previous studies (Handley et al. 2011). In contrast the Patlak values estimated from the experimental time-activity curves of [^{18}F]-FDG and [^{18}F]-FMISO (Figure 6.6) are characterised by a large variability due to the noise exhibited by both tissue and input curves. An additional source of variability is associated with the nature of the *ex vivo* experiment where there is no recirculation. Bolus injection of radiotracer leads to a plasma activity that decays rapidly to zero leading to a input function $C_p(t)$ mainly characterised by background noise at later times.

Ex vivo time-activity curves have to be corrected for the contribution of radioactivity from previous injections to the residual tissue background signal in successive injections. For both spectral-based algorithms, the residual activity was corrected for by fitting the previous injection, and then subtracting the contribution of the first injection to the second, and the contribution of the first and second to the third. This approach assumes that (1) the tracer studied is irreversibly trapped or, if reversible has decayed entirely before the subsequent injection, (2) the concentration of exchangeable (reversible) tracer in the tissue is negligible before the next injection and (3) the trapped component in a previous injection remains trapped when the condition of the heart is changed. With the tracers (irreversible) used in this study and the timing of their injections relative to their washout kinetics, the tracer activity

in the heart contributing to each subsequent time-activity curve was very small, and was mainly represented by trapped tracer with the activity of the tracer in the equilibrating compartments almost zero (<3% of the total measured signal). These conditions are necessary to guarantee that the trapping rates quantified after the first injection are associated with changes in tissue metabolism rather than the presence of residual activity in the tissue.

Monte Carlo simulations showed that both NLSA and SA are not able to reliably estimate the number of non-trapped components characterising the tracer kinetics especially when the number of rates is high. As a result, the kinetic analysis of time-activity data acquired *ex vivo* from perfused hearts gives reliable information regarding the trapped component of the tracer studied, but no information of its transport/diffusion through the capillary membrane or of its transport from the intracellular space into the cells can be gained.

In PET *in vivo* studies each dynamic point in the time-activity curve, which represent the evolution in time of the radioactive signal point by point of within a ROI, is commonly acquired using different acquisition times. Each experimental point in the time-activity curve will be therefore characterised by a different level of noise and the different measurement error is usually taken into account by weighing the experimental data. In the *ex vivo* PET experiments presented in this thesis the radioactive signal is detected using two γ-detectors which measure all the radioactive decays that occur within their FOV. In this case, each point in the time-activity curve is acquired with the same acquisition time and is characterised by the same amount of noise. The error associated with the measurement can be therefore considered

equal at each time point. For this reason un-weighted estimators were chosen for the analysis of ex vivo time-activity curves in this thesis.

The Langendorff perfused heart has been the model of choice of cardiologist for years and has greatly increased our understanding of cardiac physiology. Nevertheless, this experimental model has a number of limitations. *Ex vivo* tissue time-activity curves are, for example, a heterogeneous measure of the tracer kinetics in the whole heart, as opposed to data acquired from more spatially homogeneous imaging studies. It is expected that the number of kinetic components returned by SA approaches are higher than found within a given region of tissue (Bertoldo et al. 1998) due to heterogeneity of tracer kinetics. While *in vivo* the coronary flow through the rat heart is 3ml/min, in the buffer-perfused Langendorff heart this increases to ~14ml/min at the same perfusion pressure, due to the lower oxygen carrying capacity of Krebs buffer. Because the flow rate defines tracer delivery to the tissue, this might complicate interpretation of semi-quantitative results where the bolus input is not accounted for. However, semi-quantitative approaches are simple to apply, and whilst less informative and more sensitive to experimental conditions, the use of NA offers a useful surrogate descriptor of tracer retention when datasets are acquired under identical experimental set up and protocol.

When investigating the pharmacokinetics of metabolic tracers like [^{18}F]-FDG, buffer substrate composition is also a critical consideration. In the present study, hearts were perfused with glucose as a sole energy substrate. The lack of fatty acids in the perfusion medium, and their influence on glucose transport and or downstream glycolysis mean that [^{18}F]-FDG uptake may be different than that seen *in vivo*. More

elaborate perfusion media and the use of membrane oxygenators would be required to study [^{18}F]-FDG metabolism under more physiologically appropriate conditions.

6.8 Conclusions

Accurate quantification of radiotracer kinetics in the Langendorff perfused heart is highly desirable for the characterisation and development of novel radiotracers and for the exploitation of existing tracers to probe biological processes in greater detail. In this Chapter the performance of three quantitative (SA, NLSA and Patlak) and one semi-quantitative (NA) analysis methods for the kinetic characterisation of *ex vivo* perfused heart time-activity curves was compared. SA and NLSA algorithms were tested in terms of their accuracy in identifying and quantifying the trapped component, and in estimating the kinetics of non-trapped components. Results from both Monte Carlo simulations and experimental data suggest that NLSA is the algorithm of choice when the aim of the kinetic analysis is to assess whether the radiotracer injected in the perfused heart is irreversible trapped or not. Once the presence of a fully trapped component has been identified, it can be quantified using either NLSA or the semi-quantitative index NA. Neither analysis methods were adequate for estimating the number of non-trapped components characterising the kinetics of *ex vivo* time-activity curves probably due to the heterogeneity of the experimental preparation.

Chapter 7 : MR Dynamic Spectroscopic Imaging of Cardiac Metabolism using [1-$^{13}C_1$] Pyruvate

7.1 Introduction

In Chapter 5 hyperpolarised ^{13}C pyruvate has been introduced as a potential valuable tool for studying changes to cardiac metabolism within the whole heart. However it is known that many pathophysiological changes in cardiac metabolism occur locally within a given region of the myocardium rather than globally across the entire heart.

Hyperpolarised ^{13}C pyruvate has been shown to be a promising tool for assessing alterations in cardiac metabolism during ischemia (Schroeder et al. 2010). As mentioned in Section 1.3, myocardial ischemia is defined as a reduction or cut-off of the amount of blood normally delivered to the myocardium and is typically associated with the formation of atherosclerotic plaques within the wall of one or more coronary arteries. Depending on the severity and duration of the ischemic event, myocytes located in the region of myocardium supplied by the occluded artery may become irreversibly injured and undergo necrosis. Myocyte death, also called myocardial infarction (MI), progresses following a transmural wave front from the subendocardium to subepicardium (Reimer and Jennings 1991). Previous studies

have shown that the extent of the transmurality of the infracted region is strongly dependent upon the duration of the ischemic event before reperfusion (Tarantini et al. 2005) and therefore its early detection and accurate monitoring is essential for both prognosis and treatment (von Knobelsdorff-Brenkenhoff and Schulz-Menger 2012). The response of the enzymatic complex PDH to myocardial ischemia and subsequent reperfusion has been extensively studied using hyperpolarised ^{13}C pyruvate, labelled in C1 and/or C2 position, both in *ex vivo* perfused hearts and *in vivo* in small and medium size animals (Merritt et al. 2008; Schroeder et al. 2009; Schroeder et al. 2010; Lau et al. 2013). In these studies a decrease in PDH activity associated with the ischemic event and a switch from aerobic to anaerobic metabolism were observed by measuring the hyperpolarised metabolic products of the injected pyruvate such as $H^{13}CO_3^-$, lactate or glutamate (Golman et al. 2008; Schroeder et al. 2010).

Global information on cardiac metabolism can be obtained using non-selective hyperpolarised ^{13}C MRS, as discussed in Chapter 4, that allows the detection of the metabolic conversion of pyruvate to its metabolites within a volumetric region (voxel) covering the whole heart (Santarelli et al. 2012). Alternatively, heterogeneity of myocardial metabolism can be studied through dynamic spatial-spectral imaging techniques and ischemic regions identified (Lau et al. 2010; Lau et al. 2013). In order to derive quantitative information on the underlying metabolic activities, the time-series corresponding to the injected molecule and its metabolites, extracted voxel by voxel or within a ROI, are commonly fitted with mathematical models (Menichetti et al. 2012). Regardless of the approach chosen for the data fitting, kinetic modelling is challenged by a trade-off between SNR, spatial resolution and

extent of the transmural ischemia. Increasing the in-plane resolution by 2 fold, for example, results in a 4 fold reduction in SNR. On the other hand, reducing the spatial resolution not only enhances the SNR but also increases the partial volume effect that prevents the detection of myocardial ischemia characterised by a low degree of transmurality. For this reason the knowledge of the minimum SNR_B and in-plane resolution necessary for the detection of small percentage of transmural ischemia using hyperpolarised ^{13}C MRSI in combination with kinetic modelling would be desirable for the optimisation of the imaging protocol.

7.2 Aims

The studies presented in this Chapter were carried out in collaboration with the Institute for Biomedical Engineering at ETH Zurich. The aims were to extend non-selective measurements to imaging of cardiac metabolism in physiological and pathophysiological condition (e.g. ischemia) using hyperpolarised ^{13}C MRSI. A protocol for the acquisition of MR spectroscopic dynamic images of hyperpolarised [1-$^{13}C_1$] pyruvate and its metabolites was developed *ex vivo* in healthy perfused rat hearts (Section 3.4.5) at KCL. Results are presented in Section 7.3.

Winning the Peter Baker's fellowship allowed the candidate to join the group headed by Prof. Kozerke at ETH Zurich for three months. In this period a series of simulation studies were carried out in order to support the translation of the ^{13}C MRSI protocol from *ex vivo* to *in vivo*. Through Monte Carlo simulations the accuracy in identifying myocardial ischemic regions using hyperpolarised ^{13}C imaging combined with kinetic

modelling was assessed to study the influence of image spatial resolution, SNR and the extent of transmural ischemia (Section 7.4).

7.3 ^{13}C MR Spectroscopic Imaging *Ex vivo*

Figure 7.1 shows representative standard ^{1}H cine images in short axis and four chamber view acquired at the beginning of each experiment in order to visualise the position of the perfused heart within the coil.

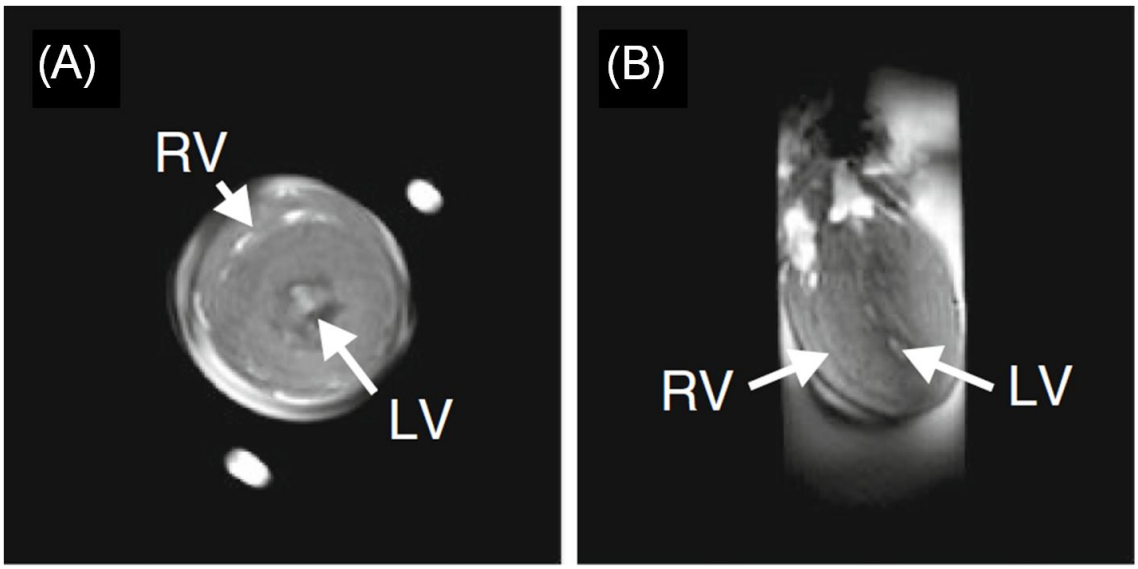

Figure 7.1: (A) Time frame from a short axis ^{1}H cine image acquired as reference for the ^{13}C images. The left ventricle (LV) can be seen in the middle of the image, while the right ventricle (RV) on the top left. The white dots outside the heart are incoming (bottom) and outgoing (top) perfusion line. (B) Four chamber view of the isolated perfused rat heart form a ^{1}H cine scan. The LV can be seen on the right while the RV on the left. The closed aortic valve is visible as a bright spot at the top of the left ventricle. Adapted from reference (Weiss and Mariotti et al. 2012).

Time-series of images of [1-$^{13}C_1$] pyruvate, [1-$^{13}C_1$] lactate and $H^{13}CO_3^-$ from two individual experiments are shown in Figure 7.2 A and B overlaid onto a time frame of a ^1H cine image in short axis view (Figure 7.1 A). The time frame t = 0s was chosen to be the last image without ^{13}C signal before the appearance of the hyperpolarised signal. Starting with injection of hyperpolarised solution into the perfusion line, the signal of pyruvate is visible in the inlet line indicated by the arrow in the pyruvate image at t = 5s (top of Figure 7.2 A). Signal in the outflow tube can be found at t = 30s, indicated by the arrow (bottom of Figure 7.2 A). The metabolic products lactate (via LDH) and $H^{13}CO_3^-$ (via PDH) are visible in the myocardium from t = 10s. To increase the SNR of the images the average of the signal of the images from t = 5s to t = 20s was calculated and shown for experiment 1 and 2 in Figure 7.2 C and D, respectively. In experiment 1 (Figure 7.2 A and C) the distributions of pyruvate perfusion and the production of lactate and $H^{13}CO_3$ are not homogeneous over the whole myocardium, while experiment 2 (Figure 7.2 B and D) shows a more homogeneous distribution of the metabolic products lactate and $H^{13}CO_3^-$. The regions indicated by the arrows 1 and 2 in the lactate and $H^{13}CO_3$ images of experiment 1 (Figure 7.2 C) reveal enhanced production of lactate and $H^{13}CO_3^-$, respectively.

Time-series from the regions of experiment 1 characterised by high lactate and $H^{13}CO_3^-$ production (indicated with arrow 1 and 2 in Figure 7.2 C) were extracted and shown in Figure 7.3 A and B, respectively. Figure 7.3 C shows the time-series representing the mean of the hyperpolarised signal of the three metabolites over the whole myocardium for experiment 2.

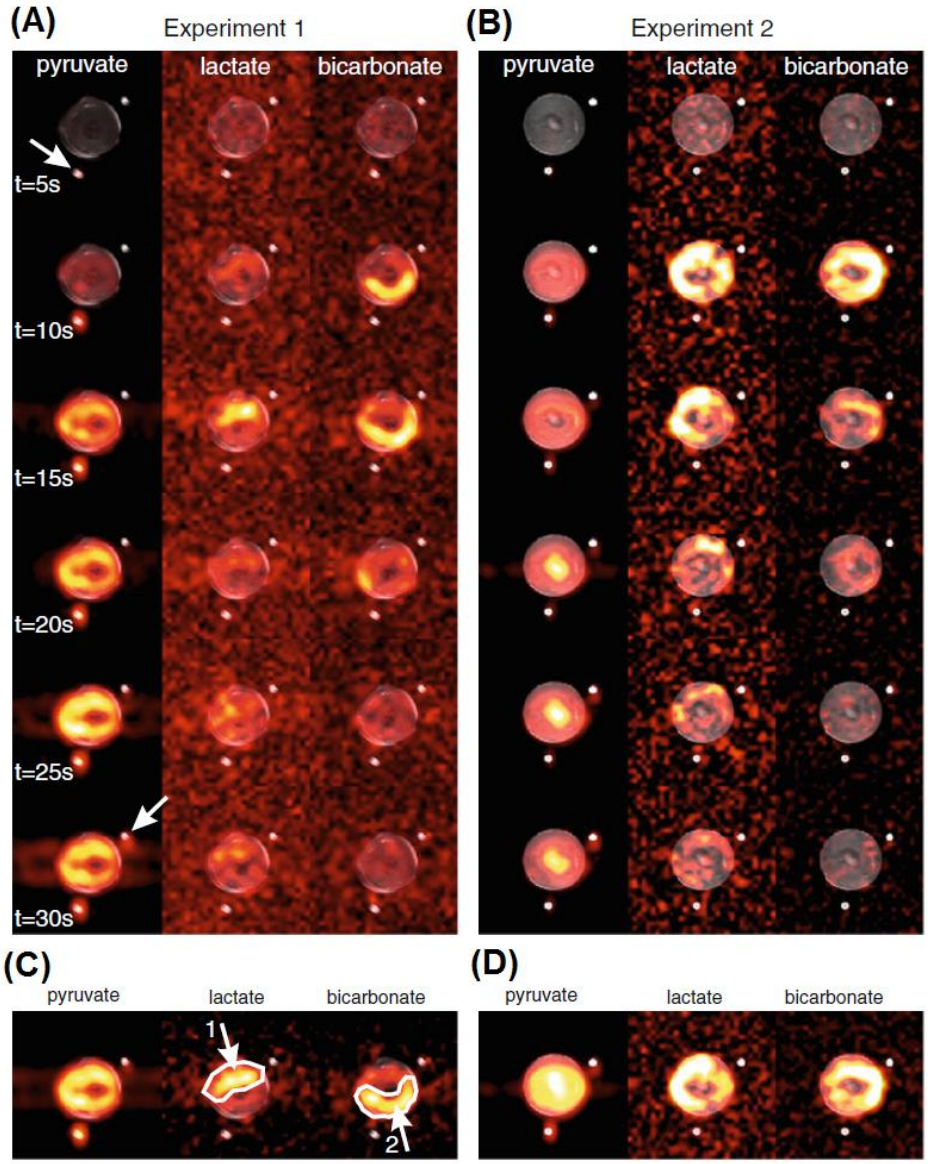

Figure 7.2: (A) and (B) Time-series of ^{13}C images from a slice in short axis view of the myocardium overlaid onto the ^{1}H reference image (Figure 7.1 A) for two different perfused hearts. Images of pyruvate lactate and $H^{13}CO_3^-$ signals are shown in the 1st, 2nd and 3rd column, respectively. Δt = 5s, where time t = 0s is defined as the last image without ^{13}C signal before appearance of hyperpolarised [1-$^{13}C_1$] pyruvate. The arrows in time frame t = 5s and t= 30s in (A) indicates the incoming perfusion line and outgoing tubing, respectively. (C) and (D) Mean images of time frames from t = 5s to t = 20s from the image series in (A) and (B), respectively. The images show a clear heterogeneous distribution of lactate and $H^{13}CO_3^-$ signals in experiment 1 ((A) and (C)). In experiment 2 the distribution of lactate and $H^{13}CO_3^-$ is more homogeneous ((B) and (D)). The region of high lactate and bicarbonate production in experiment 1 is indicated by arrow 1 and 2 respectively. Adapted from reference (Weiss and Mariotti et al. 2012).

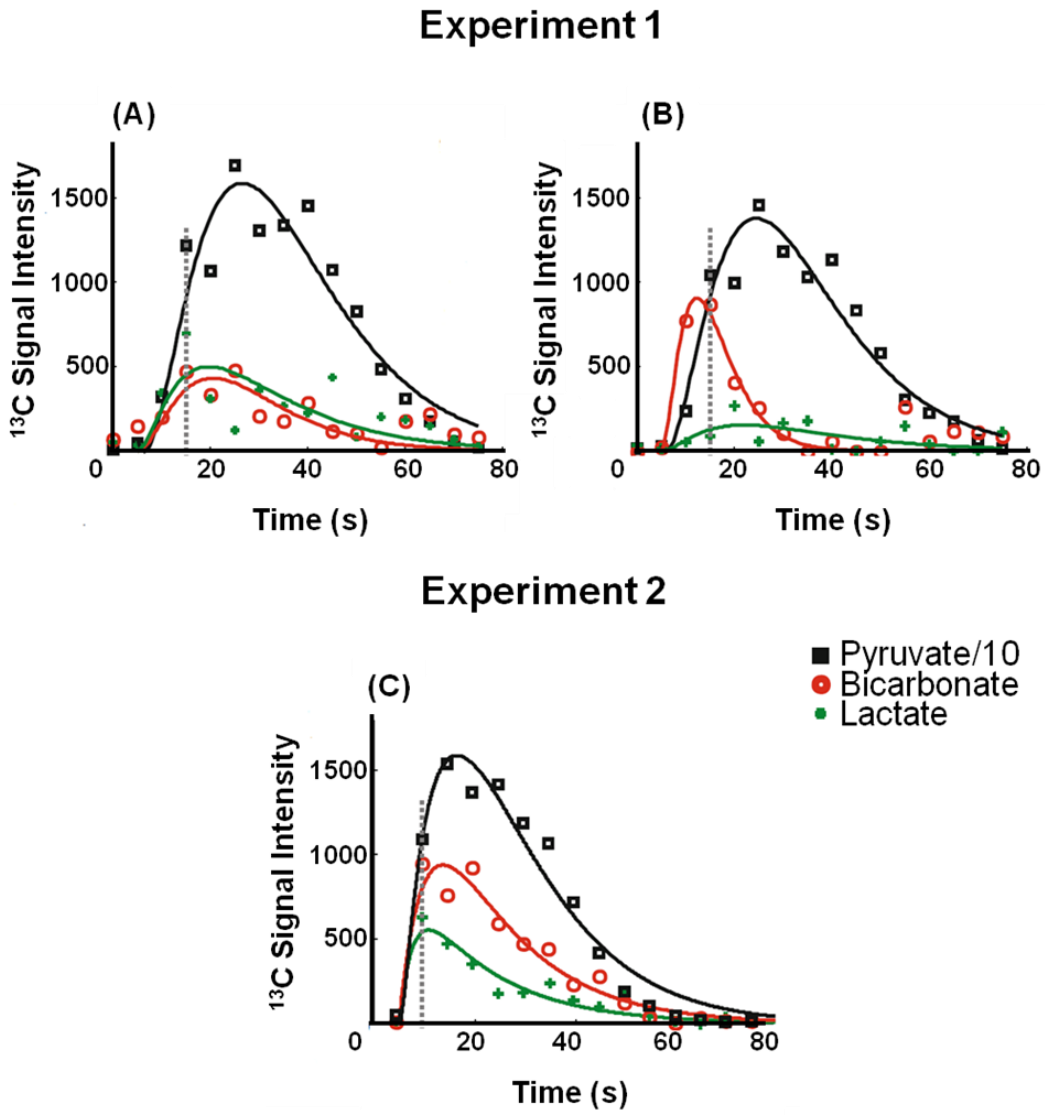

Figure 7.3: Time courses of the pyruvate, lactate and $H^{13}CO_3^-$ signals from the two experiments shown in Figure 7.2. Time-series from the region of high (A) lactate production and (B) bicarbonate production for experiment 1 indicated with arrow 1 and 2 in Figure 7.2, respectively. (C) time-series of the mean hyperpolarised signal over the whole myocardium presented for experiment 2. The solid lines show a fit of the data using a bi-exponential equation for interpolation and display purposes only. Adapted from reference (Weiss and Mariotti et al. 2012).

The early upslope of the $H^{13}CO_3^-$ signal in experiment 1 compared to the pyruvate signal (Figure 7.3 B) is a visual effect due to the down scaling of the pyruvate

signals. In experiment 1 the bicarbonate signal reaches its maximum point about 5s earlier in region 2 (between t = 10s and t = 15s) compared to region 1 (between t = 15s and 25s) suggesting a faster conversion of pyruvate to $H^{13}CO_3^-$, catalysed by PDH, in region 2.

Overall the signals from spectroscopic imaging are clearly limited by SNR as can be seen in the images shown in Figure 7.2. For this reason it was not possible to derive quantitative information by fitting the time-series with kinetic modelling on a pixel-by-pixel basis. However the SNR can be improved by summing within a ROI and data were interpolated for only display purpose using a bi-exponential function according to:

$$S(t) = ae^{-bt}(1 - e^{-ct}) \qquad 7.1$$

Where S is the observed signal and a, b, c are free fitting parameters.

The buffer used to perfuse both groups of heart was well oxygenated and therefore the heterogeneous distribution of metabolites in the myocardium reported for experiment 1 should not be related to the presence of hypoxic or ischemic regions but rather to regional variations of the pyruvate perfusion and related differences in regional metabolism. Spatial differences in metabolism may also be caused by regional differences in PDH activity, for example partial ischemia due to imperfect experimental conditions. Similar metabolic changes would be expected in a true ischemic region.

The methodology presented in this Section are characterised by some limitations that have to be considered. Imaging experiments were carried out without monitoring

cardiac function, meaning that we were unable to assess the consistency of our heart perfusion protocol after it is inserted into the spectrometer. Moreover, a lack of ECG triggering leads to image blurring along the phase encoding direction (left, right), due to residual motion as seen in the ^{13}C images in Figure 7.2 A and B.

7.4 Exploring Detection Limits of Cardiac Ischemia Using MR Dynamic Spectroscopic Imaging of Hyperpolarised ^{13}C Pyruvate Combined with Compartmental Modelling

Firstly, the accuracy and reproducibility of a two-compartment, unidirectional kinetic model based on the Bloch-McConnell equations for the conversion of hyperpolarised [1-$^{13}C_1$] pyruvate to $H^{13}CO_3^-$ via PDH were assessed using Monte Carlo simulations. After its validation, the proposed compartmental model was used to fit simulated dynamic ^{13}C images voxel by voxel in order to explore the detection limit of hyperpolarised metabolic imaging in identifying local myocardial ischemia depending on ischemic transmurality, SNR and image resolution. Usually the lowest SNR detected *in vivo* in small animals is associated with the $H^{13}CO_3^-$ peak, for this reason in this Chapter the desirable SNR is always presented with reference to this metabolite (SNR_B).

7.4.1 Monte Carlo Simulations

7.4.1.1 Hyperpolarised ^{13}C Time-Series

Datasets were simulated reproducing the characteristics of hyperpolarised ^{13}C time-activity curves (single voxel) that contain information of the metabolic conversion catalysed by PDH. A two-compartment, unidirectional kinetic model (Figure 4.5), whose dynamics is described by Equations 4.30 and 4.31 (k_{AB} = 0), was used to simulate *in vivo* ^{13}C dynamic curves of hyperpolarised [1-$^{13}C_1$] pyruvate (compartment A) and $H^{13}CO_3^-$ (compartment B). In this study the input function $C_p(t)$ representing the delivery of the hyperpolarised pyruvate to the heart was modelled as a γ-variate function (Equation 7.2).

$$C_p(t) = A(t - t_{arrival})^{alpha} * e^{\frac{(t - t_{arrival})}{beta}} \quad 7.2$$

A, alpha and beta are parameters that characterise the shape of the input function and $t_{arrival}$ is the time point of arrival of the pyruvate bolus. To obviate further sources of variability between one dataset and another, the same $C_p(t)$ was used for all simulations. Two *in vivo* systems characterised by a low a high value of k_{AB} (k_{AB_low} = 0.006s^{-1}, k_{AB_high} = 0.02s^{-1}) were simulated. The values of the effective relaxation rates r_{1A} and r_{1B} were maintained constant (r_{1A}= 0.0179s^{-1} and r_{1B} = 0.0293s^{-1}) and chosen in agreement with previous studies (Schroeder et al. 2009; Atherton et al. 2011; Chen et al. 2012; Santarelli et al. 2012). A representative dataset for each system simulated is shown in Figure 7.4 together with the chosen input function $C_p(t)$.

To investigate the effect of the random noise, normally exhibited by experimental data, hyperpolarised pyruvate and $H^{13}CO_3^-$ time-series were simulated for two $H^{13}CO_3^-$ SNR_Bs (SNR_{B_low} = 3 and SNR_{B_high} = 12), consistently with the experimental data. N = 100 and a time resolution Δt = 2s were chosen.

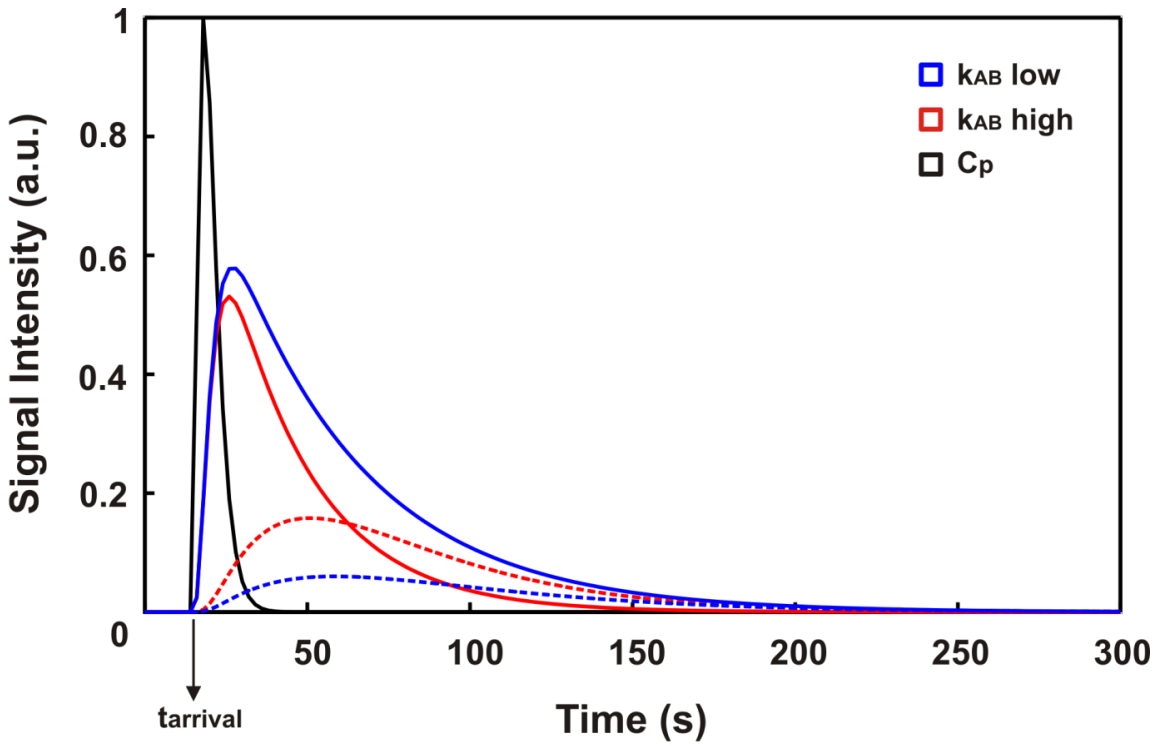

Figure 7.4: Representative synthetic ^{13}C time-series for pyruvate (continuous line) and $H^{13}CO_3^-$ (dashed line) for the two different systems simulated (k_{AB_low} = 0.006s^{-1} and k_{AB_high} = 0.02s^{-1}). The input function $C_p(t)$ used in the simulation is shown in black. All time-series are normalised for the peak value of the input function. $t_{arrival}$ represents the time point at which the hyperpolarised ^{13}C signal associated from the injected molecule is first detected.

7.4.1.2 Hyperpolarised ^{13}C Dynamic Images

A numerical signal model based on a short axis view of the rat heart was used to simulate *in vivo* hyperpolarised ^{13}C dynamic images of pyruvate and bicarbonate using a mask obtained from *in vivo* high resolution ^{1}H images of the rat heart (Figure 7.5).

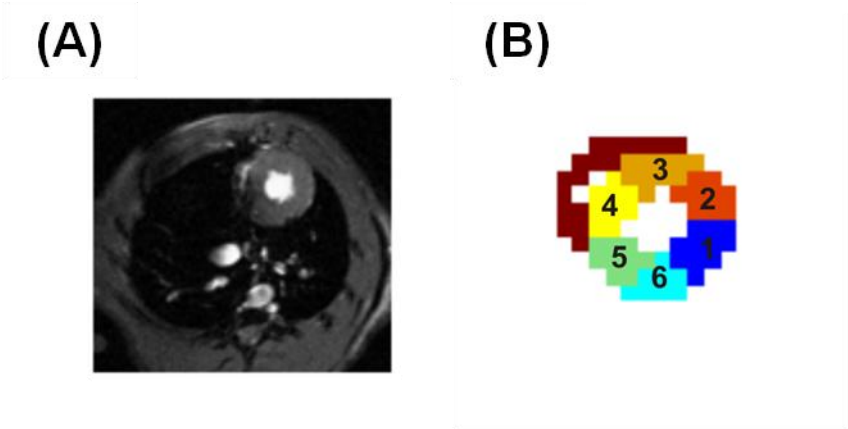

Figure 7.5: (A) Short axis ^{1}H high resolution image from a rat heart *in vivo* used to derive the left ventricle mask used in the Monte Carlo simulations and shown in (B).

Images characterised by four SNR_Bs ($3 \leq SNR_B \leq 12$) and six spatial resolutions (2 x 2 - 0.25 x 0.25 mm^2) were simulated. Additionally, to assess which is the minimum size of ischemia that can be detected for a chosen SNR_B spatial resolution, transmural ischemia (18%, 40%, 64% and 100% transmurality) was simulated in the myocardial anterior segment in agreement with the left ventricle segmentation proposed by the American Heart Association (AHA) (segment 3 in Figure 7.5) (Cerqueira et al. 2002). The values for k_{AB}, r_{1A} and r_{1B} used to generate the synthetic

hyperpolarised ^{13}C dynamic curves, voxel by voxel, were chosen in agreement with the study presented by *Lau and colleagues* where the rate of enzymatic conversion of PDH at 45min after reperfusion was reported to be approximately five times smaller than the baseline value (Lau et al. 2013) ($k_{AB\_baseline}$ = 0.018s^{-1}, k_{AB_45min} = 0.0035s^{-1}, r_{1A}= 0.0179s^{-1} and r_{1B} = 0.0293s^{-1}). A Δt = 2s was chosen for all simulated time-series. Representative simulated hyperpolarised ^{13}C images are presented in Figure 7.6 for the entire range of ischemic transmurality and SNR_Bs explored at a spatial resolution equal to 1 x 1 mm^2 and a representative time point (t = 30 s).

7.4.2 Data Analysis

7.4.2.1 Hyperpolarised ^{13}C Time-series

The accuracy and reproducibility of two-compartment, unidirectional kinetic model, was assessed by fitting synthetic hyperpolarised ^{13}C time-series of pyruvate and $H^{13}CO_3^-$ (Figure 7.4) with the proposed compartmental model. The percent bias (%BIAS) associate with the estimation of the kinetic rates (k_{AB}, r_{1A} and r_{1B}) was calculated as a performance index (Equation 7.3).

$$\%\mathrm{BIAS}_{\mathrm{p}} = 100 * \sum_{\mathrm{j}=1}^{\mathrm{k}} \frac{(\mathrm{p_j} - \mathrm{p_{TRUE}})}{\mathrm{p_{TRUE}}} \qquad 7.3$$

p_j and p_{TRUE} are the estimated and true value of the indices p.

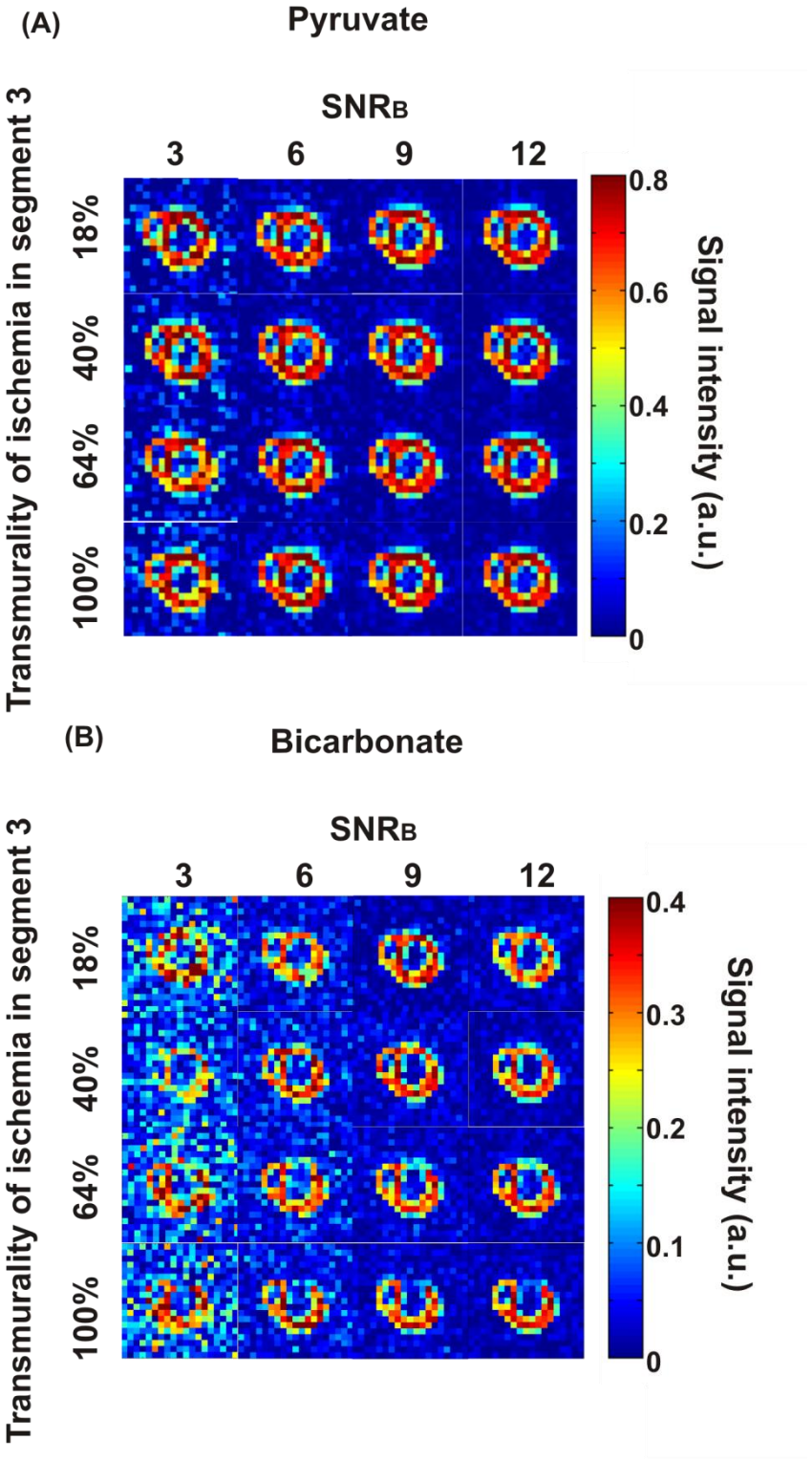

Figure 7.6 : Representative synthetic ^{13}C images of (A) pyruvate and (B) $H^{13}CO_3^-$ presented for the entire range of SNR_Bs and ischemic transmurality studied, 1 x 1 mm^2 spatial resolution and t = 30s.

7.4.2.2 Hyperpolarised ^{13}C Dynamic Images

In order to determine the minimum size of transmural ischemia that is detectable using hyperpolarised ^{13}C dynamic imaging for a given SNR_B and spatial resolution, simulated ^{13}C dynamic images of pyruvate and $H^{13}CO_3^-$ were fitted, voxel by voxel, to a two-compartment, unidirectional kinetic model.

A one way ANOVA with Dunnett's test was used to compare the values of k_{AB} derived through the kinetic model in the anterior segment of the left ventricle (ischemic segment) with those in a healthy segment for each simulated image (Dunnett 1955). All Monte Carlo simulations and kinetic analysis were performed through a custom-made Matlab (MathWorks®) code.

7.4.3 Results

7.4.3.1 Hyperpolarised ^{13}C Time-Series

Results from Monte Carlo simulations suggested that the chosen two-compartment, unidirectional kinetic model is able to accurately estimate the values of kinetic rates of the conversion of pyruvate to $H^{13}CO_3^-$ (k_{AB}, r_{1A} and r_{1B}) at the rates and SNR_B values characteristic of *in vivo* hyperpolarised ^{13}C time-series.

The mean ± SD of %Bias reported for k_{AB} and for the effective relaxation rates of pyruvate and $H^{13}CO_3^-$ (r_{1A} and r_{1B}) are presented in Figure 7.7. Regardless the SNR_Bs studied the error in parameter estimation of the proposed kinetic model increased with increasing values of k_{AB}. Additionally the performance of the proposed analysis method improved with increasing values of SNR_B. The maximum

%Bias estimated for k_{AB} was 3.4% ± 12.9% at SNR_B = 3 and k_{AB} = 0.02s^{-1}, while the minimum value equal to 1.1% ± 13% was reported at SNR = 12 and k_{AB} = 0.006s^{-1} (see Figure 7.7 A). The chosen kinetic model was able to accurately estimate r_{1A} with a maximum %Bias equal to - 2.6% ± 26.1% at SNR_B = 3 and k_{AB} = 0.02s^{-1} and a minimum value reported at SNR_B = 12 and k_{AB} = 0.006s^{-1} equal to - 0.5% ± 4% (see Figure 7.7 B). The values estimated for the %Bias of r_{1B} were comparable to those reported for k_{AB} with a maximum value equal to 5% ± 25.1% at SNR_B = 3 and k_{AB} = 0.02s^{-1} and a minimum value equal to 1.5% ± 12.1% at SNR_B = 12 and k_{AB} = 0.006s^{-1} (see Figure 7.7 C).

7.4.3.2 Hyperpolarised ^{13}C Dynamic Images

As expected the ability of detecting myocardial ischemia using hyperpolarised ^{13}C imaging combined with kinetic modelling depends on SNR_B, in-plane resolution and the extent of transmural ischemia. The values of k_{AB} derived by fitting the simulated ^{13}C dynamic images in Figure 7.6 voxel by voxel with the validated two-compartment, unidirectional kinetic model are presented in Figure 7.8 for two representative in-plane resolutions and all the SNR_Bs studied. In dynamic ^{13}C images characterised by an in-plane resolution of 1 x 1 mm^2 the ischemic segment (number 3 in Figure 7.8 A) is well defined only for the highest percentage of transmurality simulated (100%) regardless the SNR_B assessed (Figure 7.8 B). However, in images simulated with 0.25 x 0.25 mm^2 in-plane resolution even the smallest percentage of transmural ischemia (18%) at the lowest SNR_B (SNR_B = 3) can be delineated (Figure 7.8 C).

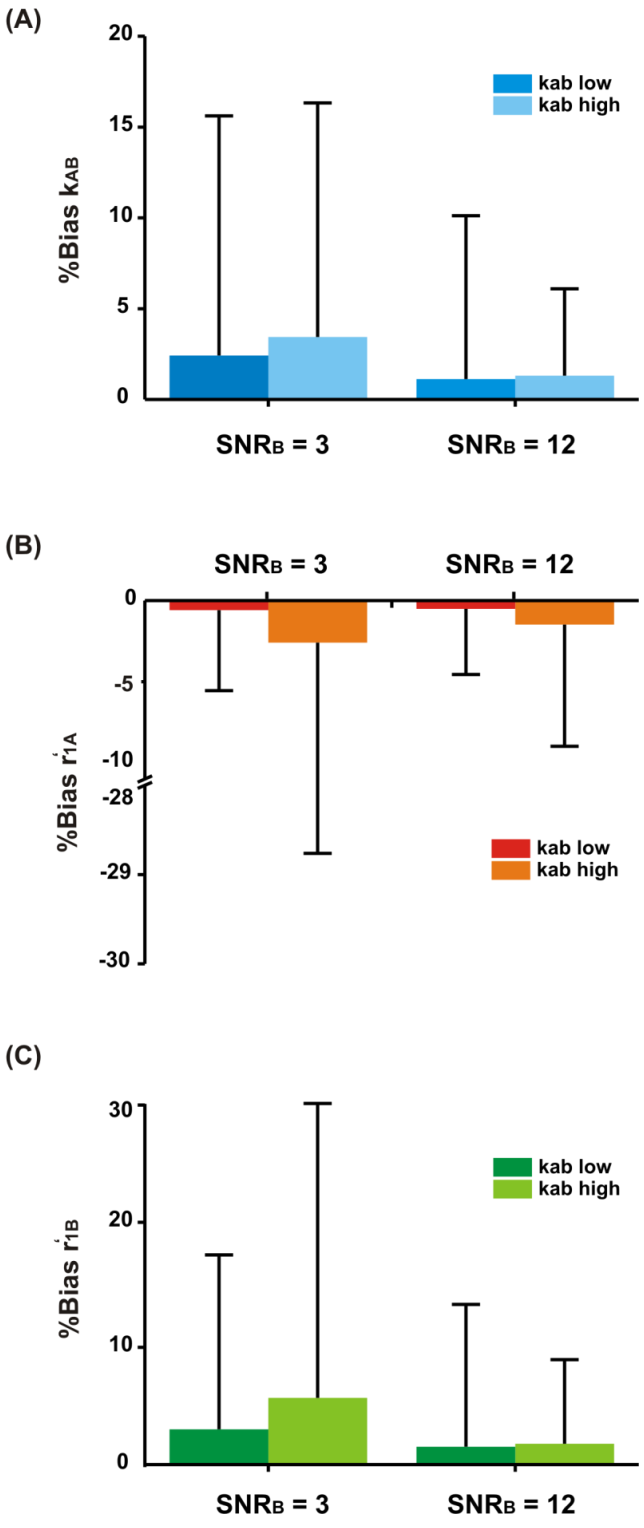

Figure 7.7: Mean ± SD for the %Bias reported for the characteristic kinetic rates of a two-compartment, unidirectional kinetic model. Values are reported for two values of SNR_B and k_{AB} characteristic of experimental datasets.

The minimum resolutions required to observe significant difference in k_{AB} between the ischemic and healthy myocardium for the range of SNR_Bs simulated are summarised in Figure 7.9. Results suggest that to detect 18% of transmural ischemia it is necessary to acquire the dynamic images with a minimum in-plane resolution of 0.4 x 0.4 mm^2 for a $SNR_B = 3$, whereas a resolution of 0.75 x 0.75 mm^2 is enough at $SNR_B > 6$. A transmurality of 40% in the ischemic segment can be discerned with a minimum resolution of 0.75 x 0.75 mm^2 at the lowest SNR_B studied, while 1 x 1 mm^2 is sufficient at $SNR_B > 6$. Results also suggest that an in-plane resolution of 1 x 1 mm^2 is adequate to detect 64% of ischemic transmurality when $3 < SNR_B < 6$, whereas for $SNRs_B > 6$ the same degree of ischemia can be detected with a minimum resolution of 2 x 2 mm^2. Finally, 1 x 1 mm^2 resolution is sufficient to detect 100% of transmural ischemia at $SNR_B = 3$, whereas an in-plane resolution of 2 x 2 mm^2 is sufficient to discern a 100% transmural ischemic segment from healthy myocardium if $SNR_B > 6$.

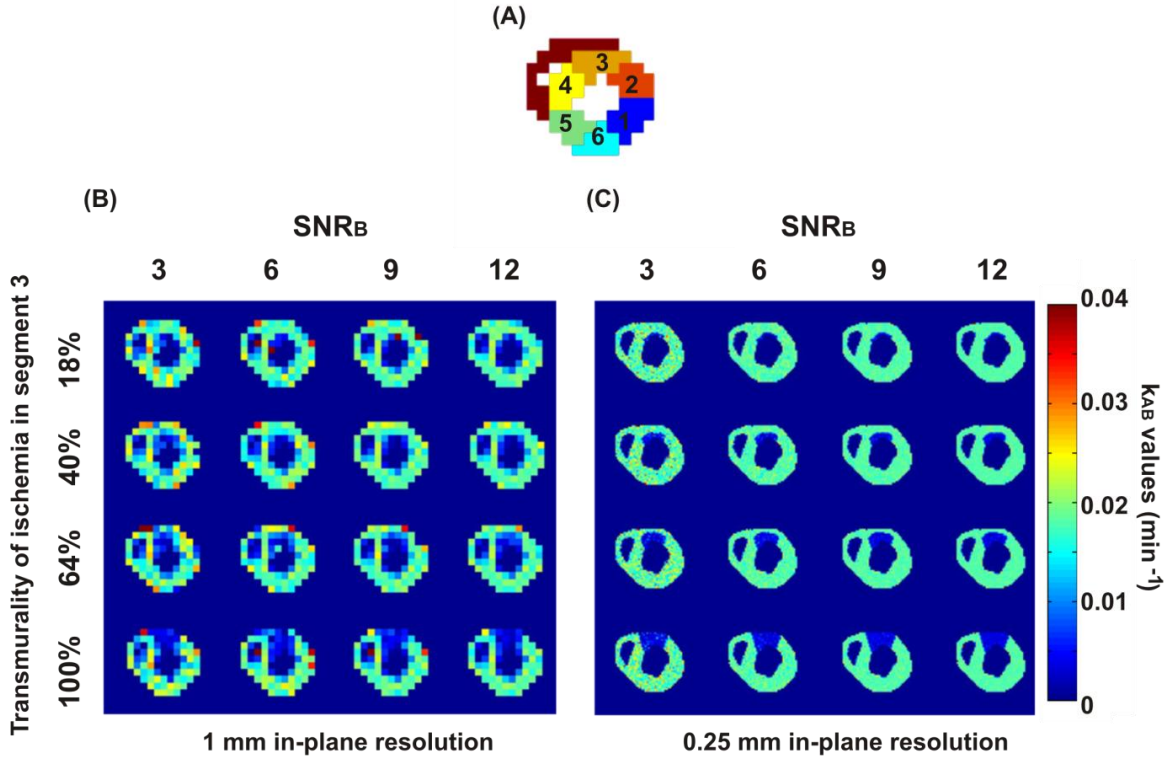

Figure 7.8: (A) AHA segmentation of the left ventricle used in the simulation. (B) and (C) k_{AB} maps obtained by using a two-compartment, unidirectional kinetic model to fit simulated ^{13}C dynamic images of pyruvate and $H^{13}CO_3^-$ characterised by an in-plane resolution of 1 x 1 mm^2 and 0.25 x 0.25 mm^2, respectively.

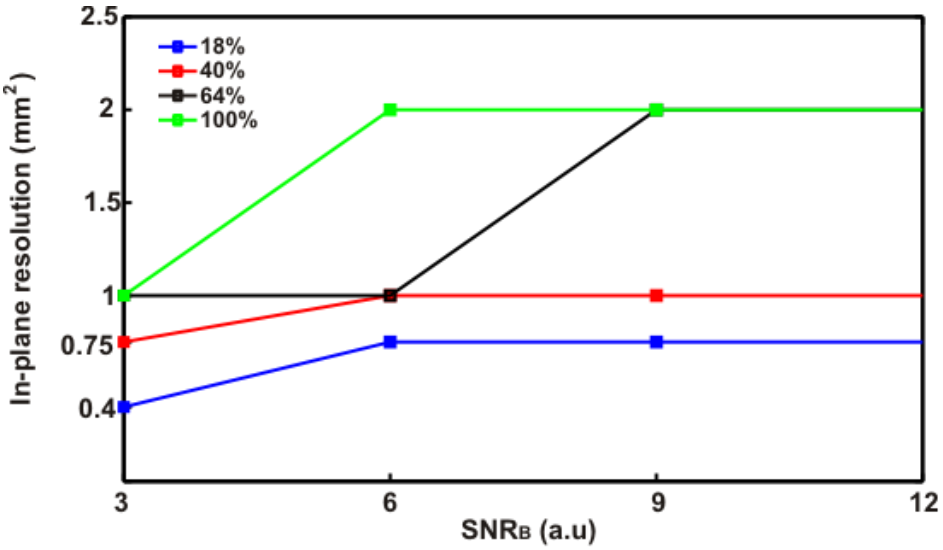

Figure 7.9: Minimum in-plane resolutions necessary to detect the four different percentage of ischemic transmurality simulated at the four SNR_Bs assessed.

7.4.4 Discussion

The first aim of the study presented in this Section was to assess the accuracy and reproducibility in parameter estimation of a kinetic model based on the modified Bloch-McConnell equations for the conversion of hyperpolarised ^{13}C pyruvate to $H^{13}CO_3^-$ via PDH at the rates and SNR_B values characteristic of *in vivo* experiments. ^{13}C time-series were simulated for a high and a low value of k_{AB} and SNR_Bs. The simulated curves were fitted with the chosen compartmental model and the %BIAS associate with the kinetic rates (k_{AB}, r_{1A} and r_{1B}) was calculated as a performance index. Results from the Monte Carlo simulations showed that the kinetic model has a good accuracy and reproducibility at the values of k_{AB} and SNR_Bs studied. However, its performances are sensitive to the noise level that characterised the hyperpolarised pyruvate and $H^{13}CO_3^-$ time-series. This results in an increase of the %Bias associated with the estimation of the kinetic parameters with decreasing values of SNR_Bs. Results also suggested that the error associated with the parameter estimation increases with increasing values of $k_{AB.}$ This is due to how the synthetic time-series of pyruvate and $H^{13}CO_3^-$ were simulated in this study. The standard deviation of the noise added to the pyruvate and $H^{13}CO_3^-$ curves was calculated as the ratio between the maximum value of the $H^{13}CO_3^-$ peak and the desirable SNR_B. Increasing the values of the rate of enzymatic conversion k_{AB}, the injected hyperpolarised pyruvate is depleted faster and therefore its peak value is diminished compared to that obtained at lower values of k_{AB}, whereas the $H^{13}CO_3^-$ maximum value is increased (Figure 7.4). For a given SNR_B the resulted SNR_A will therefore be lower for higher values of k_{AB} affecting the performances of the kinetic model.

To explore which is the minimum size of transmural ischemia in the left ventricle that can be detected using hyperpolarised ^{13}C dynamic imaging, a series of ^{13}C dynamic images of pyruvate and bicarbonate were simulated. Different percentages of transmural ischemia, in-plane resolutions and SNR_Bs were simulated and a summary of the results obtained from these simulations is shown in Figure 7.9. Results suggested that it is possible to discern the lowest percentage of ischemia simulated in segment 3 (18%) from the healthy myocardium at $SNR_B = 3$ with a minimum in-plane resolution of 0.4 x 0.4 mm^2. This means that even if the accuracy and reproducibility of a two-compartment, unidirectional kinetic model is affected by the presence of the noise, the k_{AB} estimation is accurate enough to allow one to discern regions with low values of k_{AB} (ischemic myocardium) from those characterised by high values of k_{AB} (healthy myocardium).

The highest in-plane resolutions that have been reported so far for imaging of hyperpolarised compounds are in the order of 1 x 1 mm^2 in the rat heart (Weiss et al. 2013) using a dedicated small animal scanner and 7.5 x 7.5 mm^2 in the pig heart using a human clinical MRI system (Lau et al. 2010). According to the results just presented, at these resolutions the percentage of transmural ischemia that can be detected is equal to 40% at $SNR_B > 6$ in the rat heart and $SNR_B > 3$ in the pig heart. However, the study presented in this Chapter is characterised by a number of limitations that have to be considered. All simulations, for example, assume ideal experimental conditions. Variations in coil sensitivities over the field of view, large slice thicknesses and motion artefacts, not considered in this study, may compromise the quality of the dynamic images and reduce the accuracy in parameter estimation of the proposed kinetic model.

The successful completion of the phase I clinical trial using hyperpolarised ^{13}C pyruvate as imaging agent for prostate cancer (UCSF, San Francisco, CA) has risen expectations for potential other clinical applications such as the early detection of MI. The usage of hyperpolarised tracers in cardiology is still at the very early stages and many research studies are aimed at the optimisation of the imaging protocol. The simulations presented in this Chapter were aimed to help engineers at ETH Zurich in designing an optimal imaging protocol that would allow the detection of small degrees of transmural ischemia in the left ventricle *in vivo* in rat hearts. Similar studies could be performed to help the design and optimisation of the imaging protocol in humans.

7.5 Conclusions

In this Chapter the feasibility of detecting information on the spatial distribution of hyperpolarised [1-$^{13}C_1$] pyruvate, [1-$^{13}C_1$] lactate and $H^{13}CO_3^-$ *ex vivo* in perfused rat hearts using slice selective spectroscopic imaging employing an echo planar readout was shown. Spatial distributions of the ^{13}C metabolite signals were measured and heterogeneous metabolism within the myocardium was detected. In order to facilitate the translation of the developed spectroscopic imaging protocol from *ex vivo* to *in vivo* experiments it would be desirable to have an a priori knowledge of the minimum SNR_B and in-plane resolution necessary for the detection of small percentage of transmural ischemia using hyperpolarised ^{13}C imaging combined with kinetic modelling. Monte Carlo simulations presented in this Chapter showed that a two-compartment, unidirectional model is accurate enough in estimating the kinetic rate

of conversion of pyruvate to $H^{13}CO_3^-$ at the values of SNR_Bs and k_{AB} characteristic of *in vivo* experiments in small animals. Results also suggested that in order to detect the smallest percentage of ischemic transmurality simulated (18%) by fitting the synthetic ^{13}C dynamic images of pyruvate and $H^{13}CO_3^-$ to the validated analysis model is necessary to achieve at least a SNR_B equal to 3 and an in-plane resolution equal to 4 x 4 mm^2.

Chapter 8 : Conclusions

The aim of this thesis was to develop experimental protocols and analysis methods for the real-time assessment of cardiac metabolism.

8.1 Major Findings in this Thesis

The first step towards achieving the aim of this thesis was to set up the HyperSense DNP polariser at KCL and validate its performance. Metabolically active molecules such as [1-$^{13}C_1$] pyruvate, [1,2-$^{13}C_2$] pyruvate and [1,4-$^{13}C_2$] fumarate were hyperpolarised and the longitudinal relaxation time constants T_1 as well as the polarisation enhancements obtained for each molecule was measured in solution and compared to the values previously reported in the literature. A hyperpolarised MR protocol was developed for the detection of metabolism *in vitro* in live cells and the conversion of hyperpolarised [1-$^{13}C_1$] pyruvate to [1-$^{13}C_1$] lactate was observed in real-time in whole blood cells. Dynamic time courses were analysed using quantitative and semi-quantitative methods. A hybrid MEM/NLS algorithm was applied to the kinetic analysis of hyperpolarised ^{13}C metabolic data acquired *in vitro*. The accuracy and reproducibility of the proposed method was determined using

Monte Carlo simulations and compared to those of compartmental modelling which represents the gold standard method for the analysis of hyperpolarised ^{13}C data.

An MR compatible Langendorff perfused rat heart system was developed together with an experimental protocol for ^{13}C MRS and MRSI to measure cardiac metabolism in real-time *ex vivo*. The conversion of hyperpolarised [1-$^{13}C_1$] pyruvate to its downstream metabolites was observed in two groups of isolated hearts perfused with two Krebs-Henseleit buffers with different compositions. The conversion of [1-$^{13}C_1$] pyruvate to [1-$^{13}C_1$] lactate via LDH, [1-$^{13}C_1$] alanine via ALT and $H^{13}CO_3^-$ via PDH was observed in both groups of hearts, whereas the conversion of [1-$^{13}C_1$] pyruvate to aspartate C1 and C4 was detected only in the Langendorff hearts perfused with glucose only buffer. This last metabolic conversion was detected for the first time in perfused hearts in real-time in this thesis. Previous cardiac studies employing hyperpolarised pyruvate have suggested that it is possible to estimate PDH activity by fitting the hyperpolarised ^{13}C time series of [1-$^{13}C_1$] pyruvate and $H^{13}CO_3^-$ to a two-compartment, first-order, unidirectional model. This compartmental model assumes that the metabolic conversion catalysed by PDH approximates to first order kinetics and does not depend on the availability of the enzymatic cofactors NAD^+ and CoA. The validity of this assumption was explored for hyperpolarised experiments carried out *ex vivo* by fitting the ^{13}C time-series of [1-$^{13}C_1$] pyruvate and $H^{13}CO_3^-$ with both first and second-order compartmental models. Results suggested that the metabolic conversion in perfused hearts follows second-order rather than first-order kinetics and therefore depends on the availability of the enzymatic cofactors. This result has been supported by a preliminary study carried out by Dr. Coert Zuurbier at University of Amsterdam in which the NADH dynamics were

measured using fluorescence during the injection of a 50mM pyruvate solution mimicking that used for the hyperpolarised experiments at KCL. This study suggested for the first time that the injection of a hyperpolarised pyruvate solution into a perfused heart may perturb the biological kinetics assessed.

Information on the local distribution of hyperpolarised [1-$^{13}C_1$] pyruvate and its metabolites was obtained using ^{13}C MRSI techniques developed in collaboration with Dr. Kilian Weiss. In these experiments a heterogeneous distribution of [1-$^{13}C_1$] pyruvate, [1-$^{13}C_1$] lactate and $H^{13}CO_3^-$ were detected in the myocardium. In order to support the translation of the ^{13}C MRSI protocol from *ex vivo* to *in vivo*, compartmental modelling was used to explore the detection limits of transmural myocardial ischemia *in vivo* in small rodents using hyperpolarised ^{13}C MRSI depending on SNR, spatial resolution and extent of ischemia. Results suggested that in order to detect the smallest percentage of ischemic transmurality simulated (18%) by fitting the synthetic ^{13}C dynamic images of pyruvate and $H^{13}CO_3^-$ with a two-compartment, first-order kinetic model it is necessary to achieve at least a SNR equal to 3 and an in-plane resolution equal to 4 x 4 mm^2.

A study was carried out to develop and validate quantitative and semi-quantitative analysis methods for time-activity curves of PET tracers acquired *ex vivo*. PET dynamic data were acquired by Dr. Richard Southworth and Dr. Rodolfo Medina as part of a study aimed at the characterisation of the uptake in the perfused heart of two PET tracers, namely [^{18}F]-FDG and [^{18}F]-FMISO, in normoxia and hypoxia. The performance of NLSA, SA, Patlak and the semi-quantitative index NA in

characterising the kinetics of these two PET tracers was assessed using both Monte Carlo simulations and experimental time-activity curves. The results showed that none of the analysis methods proposed is able to identify the number of the non-trapped kinetic components due to the heterogeneity of the measurement. However, NLSA is adequate to identify the presence of the trapping. Once identified, the trapped component can be estimated using either NLSA or the semi-quantitative index NA.

8.2 Future Work

In this thesis *ex vivo* dynamic data were acquired during the development and optimisation of the Langendorff perfused heart system and ^{13}C MR experimental protocols. This has resulted in high variability between measurements and the unavailability of cardiac contractility for some of the perfused hearts. In future all the Langendorff perfused heart experiments will be carried out under the same experimental conditions and the cardiac contractility will be monitored throughout the experiments in order to correlate the metabolic changes with cardiac function.

The possibility of injecting Langendorff perfused hearts with hyperpolarised ^{13}C urea, or another non metabolically active molecule, at the same time as [1-$^{13}C_1$] pyruvate will be explored in the future. The ^{13}C time-series of urea contains information on the perfusion of the hyperpolarised solution and will be used as input function in the modelling of this type of data. The possibility of using the hybrid MEM/NLS algorithm

for the kinetic analysis of *ex vivo* and *in vivo* hyperpolarised data will also be explored by deconvoluting the experimental dynamic data with the input function.

The hypothesis that the metabolic conversion of hyperpolarised [1-$^{13}C_1$] pyruvate to $H^{13}CO_3^-$ via PDH in perfused hearts is limited by the availability of the coenzyme NAD^+ will be further investigated. An experimental set up will be developed at KCL in order to investigate the dynamics of the cofactor NAD^+ using NADH fluorescence.

The analysis methods for characterising the conversion of hyperpolarised [1-^{13}C] pyruvate to $H^{13}CO_3^-$ will be extended using a second-order compartmental model including the non-hyperpolarised ^{13}C pools of [1-$^{13}C_1$] pyruvate and $H^{13}CO_3^-$, which are not detectable but are subject to metabolic conversion, together with the hyperpolarised ^{13}C pools.

In future work a compartmental model including the metabolic conversion of pyruvate to all its metabolites identified in the hyperpolarised ^{13}C MR spectrum (Figure 5.7 and Figure 5.8) will be implemented. This will allow obtaining a more complete overview of pyruvate metabolism in Langendorff perfused rat hearts. However, to describe such a complex metabolic pathway a large number of unknown parameters are necessary and the accuracy of compartmental model parameters estimates may be affected.

A PET insert is available for the 9.4T MR spectrometer used in this thesis. In future PET/hyperpolarised ^{13}C studies will be performed on the same perfused heart. This

will allow a more complete picture of the metabolic and functional state of the heart in physiological and pathophysiological conditions. A series of PET/MR experiments will be, for example, performed in order to investigate whether the injection of a hyperpolarised ^{13}C pyruvate solution at non-tracer concentration saturates the uptake of pyruvate across the mitochondria membrane making the metabolic conversion of pyruvate to $H^{13}CO_3^-$ transport-limited rather than limited by the rate of enzymatic conversion. In order to do so the distribution of the uptake of radioactive ^{11}C pyruvate (PET), injected at tracer concentration, and that of hyperpolarised ^{13}C pyruvate (MR) will be detected in one or more axial slices during the same experiment. Anatomical ^{1}H MR reference acquired for the same Langendorff perfused rat heart will be used to register the pyruvate uptake acquired with the two imaging modalities. This type of experiment will be performed both in normoxic and in hypoxic or ischemic perfused hearts to investigate whether the effect of the hyperpolarised solution on the pyruvate uptake depends on the level of oxygenation of the hearts. Additionally, cardiac metabolism and perfusion will be assessed in the same Langendorff heart using hyperpolarised ^{13}C pyruvate and radioactive ^{11}C ammonia, respectively. Metabolic and perfusion information will be integrated with the anatomical information of the same heart acquired using ^{1}H MR imaging.

The *ex vivo* imaging experimental protocol developed in this thesis at St. Thomas' hospital is being translated to *in vivo* studies in small animal (rats) at ETH Zurich were a MR scanner adequate to this type of experiments is installed next to a DNP polariser. Many efforts have been done by this group in the last five years in order to develop fast MRSI sequences able to detect the conversion of hyperpolarised ^{13}C

pyruvate to its metabolites *in vivo* in real time (Weiss et al. 2013; Sigfridsson et al. 2014). An experimental protocol for the injection of a hyperpolarised solution into a living animal has been also developed and optimised in the same group. The next step towards the translation to *in vivo* MRSI studies will be to acquire hyperpolarise images of pyruvate and its metabolites in healthy animals using different spatial resolutions and measuring the SNR_b obtained. Results will be compared with those obtained from the Monte Carlo simulation performed in this thesis (Section 7.4) to evaluate the effects of the variations in coil sensitivities over the field of view, large slice thicknesses and motion artefacts, not considered in this thesis, may have on the quality of the dynamic images on the accuracy in parameter estimation of the proposed kinetic model. Subsequently an experimental protocol for inducing different level of transmural myocardial ischemia through the ligation of the left descending coronary artery will be developed and validated. Finally a number of experiments aimed at the detection of myocardial ischemia using hyperpolarised ^{13}C MR combined with kinetic modelling will be performed.

After optimising the hyperpolarised imaging for cardiac metabolic studies Professor Kozerke's group aims to translate the experimental protocol validate for small animals to humans. They have recently bought a DNP polariser able to produce hyperpolarised sample for human studies. This machine is able to check, soon after the dissolution, the PH, purity and temperature of the hyperpolarised solution and releases only those samples suitable for injection. The aim for the future it is obtained the approval to start a clinical trial using hyperpolarised ^{13}C pyruvate as imaging agent for MI. Metabolic images of the human hearts will be acquired using 3T Philips scanner placed in a room next to that in which the DNP polariser is

located. Before starting the clinical trial it will be necessary to develop and optimise an experimental protocol for the safe injection of the hyperpolarised solution into humans as well as fast MR sequences for the detection of the hyperpolarised ^{13}C pyruvate metabolism in to the heart as previously done for the *in vivo* experiments performed in small animals.

References

Akaike, H. (1971). On a decision procedure for system identification. Engineering approach to computer control.

Arai, A. E. (2011). "Magnetic Resonance Imaging for Area at Risk, Myocardial Infarction, and Myocardial Salvage." Journal of Cardiovascular Pharmacology and Therapeutics **16**(3-4): 313-320.

Ardenkjaer-Larsen, J. H., B. Fridlund, et al. (2003). "Increase in signal-to-noise ratio of > 10,000 times in liquid-state NMR." Proceedings of the National Academy of Sciences of the United States of America **100**(18): 10158-10163.

Ardenkjar-Larsen, J. H., K. Golman, et al. (2003). "Increase of signal-to-noise of more than 10,000 times in liquid state NMR." Discovery medicine **3**(19): 37-39.

Atherton, H. J., M. S. Dodd, et al. (2011). "Role of Pyruvate Dehydrogenase Inhibition in the Development of Hypertrophy in the Hyperthyroid Rat Heart A Combined Magnetic Resonance Imaging and Hyperpolarized Magnetic Resonance Spectroscopy Study." Circulation **123**(22): 2552-U2134.

Barnes, A. B., G. D. Paepe, et al. (2008). "High-Field Dynamic Nuclear Polarization for Solid and Solution Biological NMR." Appl Magn Reson **34**(3-4): 237-263.

Bertoldo, A., P. Vicini, et al. (1998). "Evaluation of compartmental and spectral analysis models of [18F]FDG kinetics for heart and brain studies with PET." IEEE Trans Biomed Eng **45**(12): 1429-1448.

Bessho, R. and D. J. Chambers (2001). "Myocardial protection: the efficacy of an ultra-short-acting beta-blocker, esmolol, as a cardioplegic agent." J Thorac Cardiovasc Surg **122**(5): 993-1003.

Bloch, F. (1946). "Nuclear Induction." Physical Review **70**(7-8).

Blomley, M. J., J. C. Cooke, et al. (2001). "Microbubble contrast agents: a new era in ultrasound." BMJ **322**(7296): 1222-1225.

Brownlee, M. (2001). "Biochemistry and molecular cell biology of diabetic complications." Nature **414**(6865): 813-820.

Cerqueira, M. D., N. J. Weissman, et al. (2002). "Standardized myocardial segmentation and nomenclature for tomographic imaging of the heart. A statement for healthcare professionals from the Cardiac Imaging Committee of the Council on Clinical Cardiology of the American Heart Association." Int J Cardiovasc Imaging **18**(1): 539-542.

Chatham, J. C., B. Bouchard, et al. (2003). "A comparison between NMR and GCMS C-13-isotopomer analysis in cardiac metabolism." Molecular and Cellular Biochemistry **249**(1-2): 105-112.

Chen, A. P., R. E. Hurd, et al. (2012). "Simultaneous investigation of cardiac pyruvate dehydrogenase flux, Krebs cycle metabolism and pH, using hyperpolarized [1,2-(13)C2]pyruvate in vivo." NMR Biomed **25**(2): 305-311.

Cunningham, C. H., A. P. Chen, et al. (2007). "Double spin-echo sequence for rapid spectroscopic imaging of hyperpolarized 13C." Journal of magnetic resonance **187**(2): 357-362.

Cunningham, C. H., A. P. Chen, et al. (2008). "Pulse sequence for dynamic volumetric imaging of hyperpolarized metabolic products." Journal of magnetic resonance **193**(1): 139-146.
Cunningham, V. J. and T. Jones (1993). "Spectral analysis of dynamic PET studies." J Cereb Blood Flow Metab **13**(1): 15-23.
Dahlbom, M. (2002). "Estimation of image noise in PET using the bootstrap method." Ieee Transactions on Nuclear Science **49**(5): 2062-2066.
Damadian, R. (1971). "Tumor detection by nuclear magnetic resonance." Science **171**(3976): 1151-1153.
Damadian, R., M. Goldsmith, et al. (1977). "NMR in cancer: XVI. FONAR image of the live human body." Physiol Chem Phys **9**(1): 97-100, 108.
DiStefano, J. J., 3rd (1981). "Optimized blood sampling protocols and sequential design of kinetic experiments." Am J Physiol **240**(5): R259-265.
Dobrucki, L. W. and A. J. Sinusas (2010). "PET and SPECT in cardiovascular molecular imaging." Nat Rev Cardiol **7**(1): 38-47.
Dunnett, C. W. (1955). "A Multiple Comparison Procedure for Comparing Several Treatments with a Control." Journal of the American Statistical Association **50**(272): 1096-1121.
Fain, S. B., F. R. Korosec, et al. (2007). "Functional lung imaging using hyperpolarized gas MRI." J Magn Reson Imaging **25**(5): 910-923.
Frydman, L. and D. Blazina (2007). "Ultrafast two-dimensional nuclear magnetic resonance spectroscopy of hyperpolarized solutions." Nature Physics **3**(6): 415-419.
Fujibayashi, Y., H. Taniuchi, et al. (1997). "Copper-62-ATSM: A New Hypoxia Imaging Agent with High Membrane Permeability and Low Redox Potential." J Nucl Med **38**(7): 1155-1160.
Garlick, P. B., H. G. Parkes, et al. (2000). "A new system for the metabolic investigation of the isolated, perfused rat heart." J Mol Cell Cardiol **32**(5): 853-858.
Godfrey, K. (1982). Compartmental Models and Their Application. London, Accademic Press.
Golman, K., J. S. Petersson, et al. (2008). "Cardiac metabolism measured noninvasively by hyperpolarized 13C MRI." Magn Reson Med **59**(5): 1005-1013.
Gordon, J. W., S. B. Fain, et al. (2012). "Effect of lanthanide ions on dynamic nuclear polarization enhancement and liquid-state T1 relaxation." Magn Reson Med **68**(6): 1949-1954.
Gunn, R. N., S. R. Gunn, et al. (2001). "Positron emission tomography compartmental models." Journal of Cerebral Blood Flow and Metabolism **21**(6): 635-652.
Handley, M. G., R. A. Medina, et al. (2014). "Cardiac Hypoxia Imaging: Second-Generation Analogues of 64Cu-ATSM." J Nucl Med.
Handley, M. G., R. A. Medina, et al. (2011). "PET imaging of cardiac hypoxia: opportunities and challenges." J Mol Cell Cardiol **51**(5): 640-650.
Harris, T., G. Eliyahu, et al. (2009). "Kinetics of hyperpolarized 13C1-pyruvate transport and metabolism in living human breast cancer cells." Proceedings of the National Academy of Sciences of the United States of America **106**(43): 18131-18136.

Heather, L. C. and K. Clarke (2011). "Metabolism, hypoxia and the diabetic heart." J Mol Cell Cardiol **50**(4): 598-605.
Heijman, E., W. de Graaf, et al. (2007). "Comparison between prospective and retrospective triggering for mouse cardiac MRI." Nmr in Biomedicine **20**(4): 439-447.
Hill, D. K., Y. Jamin, et al. (2013). "(1)H NMR and hyperpolarized (1)(3)C NMR assays of pyruvate-lactate: a comparative study." NMR Biomed **26**(10): 1321-1325.
Hill, D. K., M. R. Orton, et al. (2013). "Model free approach to kinetic analysis of real-time hyperpolarized 13C magnetic resonance spectroscopy data." PLoS One **8**(9): e71996.
Hillman, E. M., O. Bernus, et al. (2007). "Depth-resolved optical imaging of transmural electrical propagation in perfused heart." Opt Express **15**(26): 17827-17841.
Huang, S. C. (2000). "Anatomy of SUV. Standardized uptake value." Nucl Med Biol **27**(7): 643-646.
James, T. (1998). Fundamentals of NMR, Biophysics Textbook Online.
Jensen, P. R., T. Peitersen, et al. (2009). "Tissue-specific Short Chain Fatty Acid Metabolism and Slow Metabolic Recovery after Ischemia from Hyperpolarized NMR in Vivo." Journal of Biological Chemistry **284**(52): 36077-36082.
Jerosch-Herold, M. (2010). "Quantification of myocardial perfusion by cardiovascular magnetic resonance." J Cardiovasc Magn Reson **12**: 57.
Kazan, S. M., S. Reynolds, et al. (2013). "Kinetic Modeling of Hyperpolarized C-13 Pyruvate Metabolism in Tumors Using a Measured Arterial Input Function." Magnetic Resonance in Medicine **70**(4): 943-953.
Kubota, K., T. Matsuzawa, et al. (1985). "Lung tumor imaging by positron emission tomography using C-11 L-methionine." J Nucl Med **26**(1): 37-42.
Lammertsma, A. A., R. De Silva, et al. (1992). "Measurement of regional myocardial blood flow using C15O2 and positron emission tomography: comparison of tracer models." Clin Phys Physiol Meas **13**(1): 1-20.
Lau, A. Z., A. P. Chen, et al. (2013). "Reproducibility study for free-breathing measurements of pyruvate metabolism using hyperpolarized (13) C in the heart." Magnetic resonance in medicine : official journal of the Society of Magnetic Resonance in Medicine / Society of Magnetic Resonance in Medicine **69**(4): spcone-spcone.
Lau, A. Z., A. P. Chen, et al. (2010). "Rapid multislice imaging of hyperpolarized 13C pyruvate and bicarbonate in the heart." Magnetic Resonance in Medicine **64**(5): 1323-1331.
Lauterbur, P. C. (2003) "Autobiography." Nobel Prize official website.
Lehtio, K., V. Oikonen, et al. (2003). "Quantifying tumour hypoxia with fluorine-18 fluoroerythronitroimidazole ([18F]FETNIM) and PET using the tumour to plasma ratio." Eur J Nucl Med Mol Imaging **30**(1): 101-108.
Liang, H. D. and M. J. Blomley (2003). "The role of ultrasound in molecular imaging." Br J Radiol **76 Spec No 2**: S140-150.
Logan, J., J. S. Fowler, et al. (1990). "Graphical analysis of reversible radioligand binding from time-activity measurements applied to [N-11C-methyl]-(-)-cocaine PET studies in human subjects." J Cereb Blood Flow Metab **10**(5): 740-747.

Lopaschuk, G. D., J. R. Ussher, et al. (2010). "Myocardial fatty acid metabolism in health and disease." Physiol Rev **90**(1): 207-258.
Malloy, C. R., A. D. Sherry, et al. (1988). "EVALUATION OF CARBON FLUX AND SUBSTRATE SELECTION THROUGH ALTERNATE PATHWAYS INVOLVING THE CITRIC-ACID CYCLE OF THE HEART BY C-13 NMR-SPECTROSCOPY." Journal of Biological Chemistry **263**(15): 6964-6971.
Mansfield, P. (2003). "Autobiography." Nobel Prize official website.
Mariotti, E., M. Veronese, et al. (2013). "Assessing radiotracer kinetics in the Langendorff perfused heart." EJNMMI Res **3**(1): 74.
Massoud, T. F. and S. S. Gambhir (2003). "Molecular imaging in living subjects: seeing fundamental biological processes in a new light." Genes Dev **17**(5): 545-580.
McRobbie D. W., M. E. A., Graves M.J., Prince M.R., Ed. (2006). MRI from Picture to Proton, Cambridge University Press.
Menichetti, L., F. Frijia, et al. (2012). "Assessment of real-time myocardial uptake and enzymatic conversion of hyperpolarized 1-C-13 pyruvate in pigs using slice selective magnetic resonance spectroscopy." Contrast Media & Molecular Imaging **7**(1): 85-94.
Merritt, M. E., C. Harrison, et al. (2011). "Flux through hepatic pyruvate carboxylase and phosphoenolpyruvate carboxykinase detected by hyperpolarized (13)C magnetic resonance." Proceedings of the National Academy of Sciences of the United States of America **108**(47): 19084-19089.
Merritt, M. E., C. Harrison, et al. (2007). "Hyperpolarized 13C allows a direct measure of flux through a single enzyme-catalyzed step by NMR." Proc Natl Acad Sci U S A **104**(50): 19773-19777.
Merritt, M. E., C. Harrison, et al. (2007). "Hyperpolarized C-13 allows a direct measure of flux through a single enzyme-catalyzed step by NMR." Proceedings of the National Academy of Sciences of the United States of America **104**(50): 19773-19777.
Merritt, M. E., C. Harrison, et al. (2008). "Inhibition of Carbohydrate Oxidation During the First Minute of Reperfusion After Brief Ischemia: NMR Detection of Hyperpolarized (CO2)-C-13 and (HCO3-)-C-13." Magnetic Resonance in Medicine **60**(5): 1029-1036.
Mitkovski, S., V. L. Villemagne, et al. (2005). "Simplified quantification of nicotinic receptors with 2[18F]F-A-85380 PET." Nucl Med Biol **32**(6): 585-591.
Mohammad-Djafari, A., J. F. Giovannelli, et al. (2002). "Regularization, maximum entropy and probabilistic methods in mass spectrometry data processing problems." International Journal of Mass Spectrometry **215**(1-3): 175-193.
Moreno, K. X., S. M. Sabelhaus, et al. (2010). "Competition of pyruvate with physiological substrates for oxidation by the heart: implications for studies with hyperpolarized 1-(13)C pyruvate." American Journal of Physiology-Heart and Circulatory Physiology **298**(5): H1556-H1563.
Motulsky, H. and A. Christopoulos (2004). Fitting Models to Biological Data Using Linear and Nonlinear Regression. *A practical guide to curve fitting*.
Neubauer, S. (2007). "The failing heart--an engine out of fuel." N Engl J Med **356**(11): 1140-1151.

Ng, C. K., A. J. Sinusas, et al. (1995). "Kinetic analysis of technetium-99m-labeled nitroimidazole (BMS-181321) as a tracer of myocardial hypoxia." Circulation **92**(5): 1261-1268.
Oh, S. J., D. Y. Chi, et al. (2005). "Fully automated synthesis of [18F]fluoromisonidazole using a conventional [18F]FDG module." Nucl Med Biol **32**(8): 899-905.
Opie, L. H., Ed. (1991). The Heart: Physiology and Metabolism, Raven Press.
Osborn, E. A. and F. A. Jaffer (2013). "The Advancing Clinical Impact of Molecular Imaging in CVD." JACC Cardiovasc Imaging **6**(12): 1327-1341.
Paans, A. M., W. Vaalburg, et al. (1985). "A comparison of the sensitivity of PET and NMR for in vivo quantitative metabolic imaging." Eur J Nucl Med **11**(2-3): 73-75.
Patlak, C. S., R. G. Blasberg, et al. (1983). "Graphical evaluation of blood-to-brain transfer constants from multiple-time uptake data." J Cereb Blood Flow Metab **3**(1): 1-7.
Pennell, D. J., D. N. Firmin, et al. (2011). "Review of journal of cardiovascular magnetic resonance 2010." J Cardiovasc Magn Reson **13**: 48.
Plesniak, J. (2011). "Single Photon Emission Computed Tomography as a diagnostic method in ischemic heart disease - basic technical aspects." Pol J Radiol **76**(3): 49-52.
Purcell, E. M., H. C. Torrey, et al. (1946). "RESONANCE ABSORPTION BY NUCLEAR MAGNETIC MOMENTS IN A SOLID." Physical Review **69**(1-2): 37-38.
Rabi, II, J. R. Zacharias, et al. (1938). "A new method of measuring nuclear magnetic moment." Physical Review **53**(4): 318-318.
Raftos, J. E., B. T. Bulliman, et al. (1990). "Evaluation of an electrochemical model of erythrocyte pH buffering using 31P nuclear magnetic resonance data." J Gen Physiol **95**(6): 1183-1204.
Rahmim, A. and H. Zaidi (2008). "PET versus SPECT: strengths, limitations and challenges." Nucl Med Commun **29**(3): 193-207.
Reimer, K. A. and R. B. Jennings (1991). The Heart and Cardiovascular System. Scientific Foundations, Raven Press
Rider, O. J. and D. J. Tyler (2013). "Clinical implications of cardiac hyperpolarized magnetic resonance imaging." J Cardiovasc Magn Reson **15**(1): 93.
Santarelli, M. F., V. Positano, et al. (2012). "How the signal-to-noise ratio influences hyperpolarized 13C dynamic MRS data fitting and parameter estimation." Nmr in Biomedicine **25**(7): 925-934.
Saraste, A., S. G. Nekolla, et al. (2009). "Cardiovascular molecular imaging: an overview." Cardiovasc Res **83**(4): 643-652.
Schmidt, K. (1999). "Which linear compartmental systems can be analyzed by spectral analysis of PET output data summed over all compartments?" J Cereb Blood Flow Metab **19**(5): 560-569.
Schmidt, K., G. Mies, et al. (1991). "Model of kinetic behavior of deoxyglucose in heterogeneous tissues in brain: a reinterpretation of the significance of parameters fitted to homogeneous tissue models." J Cereb Blood Flow Metab **11**(1): 10-24.

Schroeder, M. A., H. J. Atherton, et al. (2009). "Real-time assessment of Krebs cycle metabolism using hyperpolarized C-13 magnetic resonance spectroscopy." Faseb Journal **23**(8): 2529-2538.
Schroeder, M. A., H. J. Atherton, et al. (2011). "Determining the in vivo regulation of cardiac pyruvate dehydrogenase based on label flux from hyperpolarised 1-C-13 pyruvate." Nmr in Biomedicine **24**(8): 980-987.
Schroeder, M. A., L. E. Cochlin, et al. (2008). "In vivo assessment of pyruvate dehydrogenase flux in the heart using hyperpolarized carbon-13 magnetic resonance." Proceedings of the National Academy of Sciences of the United States of America **105**(33): 12051-12056.
Schroeder, M. A., P. Swietach, et al. (2010). "Measuring intracellular pH in the heart using hyperpolarized carbon dioxide and bicarbonate: a C-13 and P-31 magnetic resonance spectroscopy study." Cardiovascular Research **86**(1): 82-91.
Schwarz, G. (1978). "Estimating the Dimension of a Model." The annals of Statistics **6**(2): 461-464.
Shan, L. (2004). "Hyperpolarized [1,4-13C2]fumarate as an imaging agent of tumor cell death in vivo."
Shelton, M. E., C. S. Dence, et al. (1989). "Myocardial kinetics of fluorine-18 misonidazole: a marker of hypoxic myocardium." J Nucl Med **30**(3): 351-358.
Sigfridsson, A., K. Weiss, et al. (2014). "Hybrid multiband excitation multiecho acquisition for hyperpolarized C spectroscopic imaging." Magn Reson Med.
Skrzypiec-Spring, M., B. Grotthus, et al. (2007). "Isolated heart perfusion according to Langendorff---still viable in the new millennium." J Pharmacol Toxicol Methods **55**(2): 113-126.
Sokoloff, L., M. Reivich, et al. (1977). "The [14C]deoxyglucose method for the measurement of local cerebral glucose utilization: theory, procedure, and normal values in the conscious and anesthetized albino rat." J Neurochem **28**(5): 897-916.
Sourbron, S. P. and D. L. Buckley (2012). "Tracer kinetic modelling in MRI: estimating perfusion and capillary permeability." Phys Med Biol **57**(2): R1-33.
Southworth, R. (2009). "Hexokinase-mitochondrial interaction in cardiac tissue: implications for cardiac glucose uptake, the 18FDG lumped constant and cardiac protection." Journal of Bioenergetics and Biomembranes **41**(2): 187-193.
Southworth, R., K. A. Davey, et al. (2007). "A reevaluation of the roles of hexokinase I and II in the heart." Am J Physiol Heart Circ Physiol **292**(1): H378-386.
Southworth, R., J. L. Dearling, et al. (2002). "Dissociation of glucose tracer uptake and glucose transporter distribution in the regionally ischaemic isolated rat heart: application of a new autoradiographic technique." Eur J Nucl Med Mol Imaging **29**(10): 1334-1341.
Steinbach, P. J., R. Ionescu, et al. (2002). "Analysis of kinetics using a hybrid maximum-entropy/nonlinear-least-squares method: application to protein folding." Biophysical Journal **82**(4): 2244-2255.
Stewart, I. M., B. E. Chapman, et al. (1986). "Intracellular pH in stored erythrocytes. Refinement and further characterisation of the 31P-NMR methylphosphonate procedure." Biochim Biophys Acta **885**(1): 23-33.

Sutherland, F. J. and D. J. Hearse (2000). "The isolated blood and perfusion fluid perfused heart." Pharmacol Res **41**(6): 613-627.

Tarantini, G., L. Cacciavillani, et al. (2005). "Duration of ischemia is a major determinant of transmurality and severe microvascular obstruction after primary angioplasty: a study performed with contrast-enhanced magnetic resonance." J Am Coll Cardiol **46**(7): 1229-1235.

Turkheimer, F., R. M. Moresco, et al. (1994). "The use of spectral analysis to determine regional cerebral glucose utilization with positron emission tomography and [18F]fluorodeoxyglucose: theory, implementation, and optimization procedures." J Cereb Blood Flow Metab **14**(3): 406-422.

Veronese, M., A. Bertoldo, et al. (2010). "A spectral analysis approach for determination of regional rates of cerebral protein synthesis with the L-[1-(11)C]leucine PET method." J Cereb Blood Flow Metab **30**(8): 1460-1476.

von Knobelsdorff-Brenkenhoff, F. and J. Schulz-Menger (2012). "Cardiovascular magnetic resonance imaging in ischemic heart disease." J Magn Reson Imaging **36**(1): 20-38.

von Morze, C., P. E. Z. Larson, et al. (2012). "Investigating tumor perfusion and metabolism using multiple hyperpolarized C-13 compounds: HP001, pyruvate and urea." Magnetic Resonance Imaging **20**(3): 305-311.

Wang, W., J. C. Georgi, et al. (2009). "Evaluation of a compartmental model for estimating tumor hypoxia via FMISO dynamic PET imaging." Phys Med Biol **54**(10): 3083-3099.

Weiss and Mariotti, D. K. Hill, et al. (2012). "Developing Hyperpolarized C-13 Spectroscopy and Imaging for Metabolic Studies in the Isolated Perfused Rat Heart." Applied Magnetic Resonance **43**(1-2): 275-288.

Weiss, K., A. Sigfridsson, et al. (2013). "Accelerating hyperpolarized metabolic imaging of the heart by exploiting spatiotemporal correlations." Nmr in Biomedicine: n/a-n/a.

Wells, P. N. (2001). "Physics and engineering: milestones in medicine." Med Eng Phys **23**(3): 147-153.

Appendix A

Natural abundance ^{13}C MR spectra of the main metabolites involved in cardiac metabolism used to assign the peaks in the hyperpolarised ^{13}C spectra acquired from Langendorff perfused rat hearts and shown in Figure 5.7and Figure 5.8. 128 spectra were acquired for each compound using a flip angle θ = 30°, TR = 21s (total experimental time = 45min) and then added together.

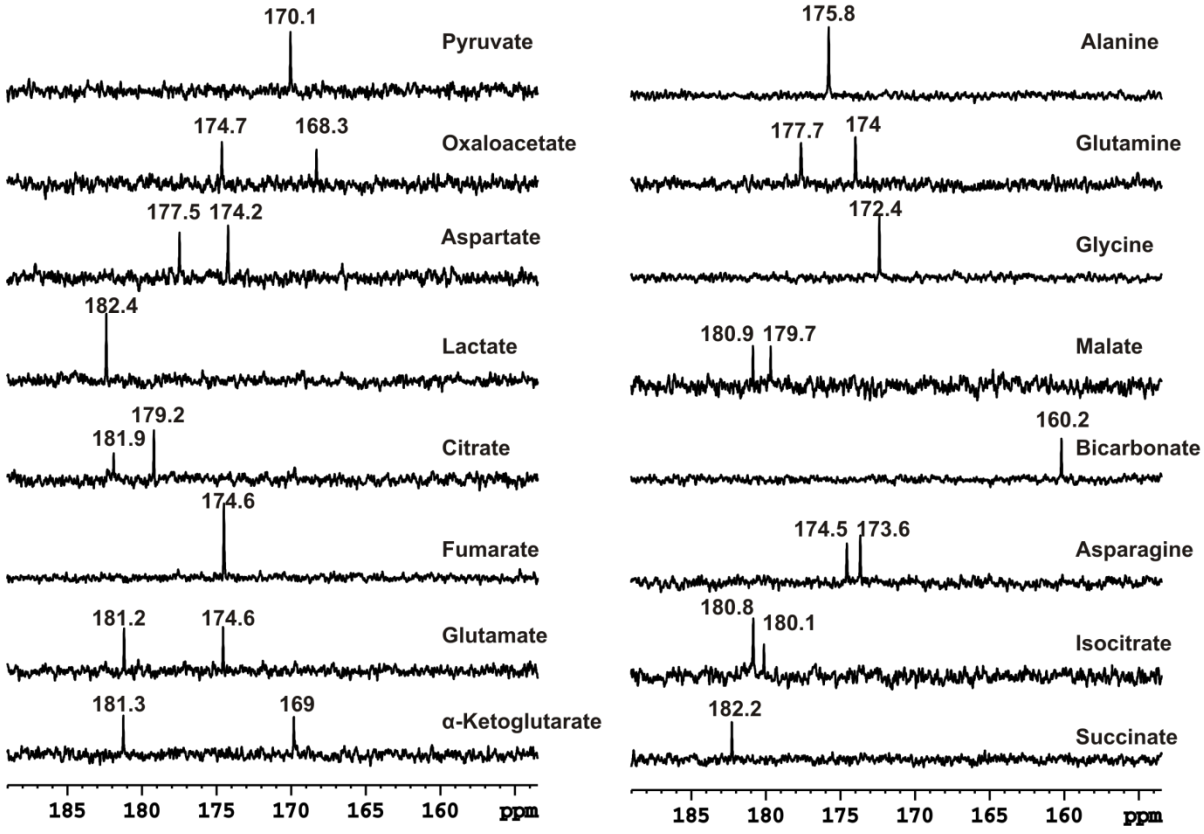

Appendix B

Publications Arising from the Work Presented in this Thesis

Research Articles

E. Mariotti, M.R. Orton, J.T. Dunn, R. Southworth, T.R. Eykyn. *Kinetic analysis of hyperpolarized data without a priori knowledge: hybrid maximum entropy and nonlinear least squares (MEM/NLS) method*. Magn Reson Med (under review).

F. Shaughnessy, **E. Mariotti**, K. P. Shaw, P. J. Blower, R. Siow, R. Southworth. *Intracellular thiol status does not govern the hypoxia selectivity of ^{64}Cu-ATSM*. J Nucl Med (under review).

R.A. Medina, E. Mariotti, D. Pavlovic, K.P. Shaw, T.R. Eykyn, P.J. Blower, R. Southworth ^{64}Cu-CTS for the PET identification of low grade cardiac hypoxia. Circ. Res (under review).

M.G. Handley, R.A. Medina, **E. Mariotti**, G.D. Kenny, K.P Shaw, R. Yan, T.R. Eykyn, P.J. Blower, R. Southworth. *PET imaging of cardiac hypoxia: second generation analogues of ^{64}Cu-ATSM*. J Nucl Med 2014. jnumed.113.129015. Pubblished head of print.

E. Mariotti, M. Veronese, J.T. Dunn, R.A. Medina, P.J. Blower, R. Southworth, T.R. Eykyn. *Assessing radiotracer kinetics in the Langendorff perfused heart*. EJNMMI Research 2013; **3**:74.

D.K. Hill, M.R. Orton, **E. Mariotti**, J. K. R. Boult, R. Panek, M. Jafar, H. G. Parkes, Y. Jamin, M. Falck Miniotis, N. M. S. Al-Saffar, M. Beloueche-Babari, S. P. Robinson, M. O. Leach, Y-L. Chung, T. R. Eykyn. *Model Free Approach to Kinetic Analysis of Real-Time Hyperpolarized ^{13}C Magnetic Resonance Spectroscopy Data*. PLOS ONE 2013; **8**: 9.

K. Weiss, **E. Mariotti**, D. K. Hill, M.R. Orton, J.T. Dunn, R. A. Medina, R. Southworth, S. Kozerke, T. R. Eykyn. *Developing Hyperpolarized ^{13}C Spectroscopy and Imaging for Metabolic Studies in the Isolated Perfused Rat Heart*. Applied Magnetic Resonance 2012; **43:**1-2 (Joint first author).

Conference proceedings

E. Mariotti, Joel T. Dunn, Rodolfo A. Medina, Z. Md Safee, M. G. Handley, F. Shaughnessy, P. J. Blower, T. R. Eykyn, R. Southworth. *Model-free analysis of PET and SPECT tracer kinetics in the isolated perfused rat heart using a hybrid maximum entropy method /non-linear least square algorithm*. In Proceedings of World Molecular Imaging Congress 2013, Savannah, Georgia, USA.

R. A. Medina, **E. Mariotti**, K. P. Shaw, Maxwell G. Handley, F. Shaughnessy, T. R. Eykyn, P. J. Blower, R. Southworth. The relationship between O2 concentration, ^{64}Cu-BTSC retention & cardiac metabolism in graded hypoxia in isolated perfused hearts. In Proceedings of World Molecular Imaging Congress 2013, Savannah, Georgia, USA.

F. Shaughnessy, R. A. Medina, **E. Mariotti**, T. R. Eykyn, P. J. Blower, R. Siow, R. Southworth. *The importance of cardiac acidosis on the dissociation of hypoxia selective PET tracer ^{64}CuATSM*. In Proceedings of World Molecular Imaging Congress 2013, Savannah, Georgia, USA.

Z. Md Safee, **E. Mariotti**, R. A. Medina, F. Shaughnessy, T. R. Eykyn, P. J. Blower, R. Southworth. *The potential use of Tc-99m MIBI as an imaging agent for cardiac mitochondrial toxicity: A preliminary study in isolated perfused hearts*. In Proceedings of World Molecular Imaging Congress 2013, Savannah, Georgia, USA.

E. Mariotti, F. Shaughnessy, R. A. Medina, J. T. Dunn, R. Southworth, T. R. Eykyn. *Laplace Inversion for Kinetic Analysis of Hyperpolarized ^{13}C data without a priori knowledge using Hybrid Maximum Entropy Method (MEM)/Non-Linear Least Square (NLS). I*n Proceedings of the International Society Magnetic Resonance in Medicine 21 (2013) (#3939), Salt Lake City, Utah, USA.

E. Mariotti, K. Weiss, S. Kozerke, T. R. Eykyn. *Exploring detection limits of cardiac ischemia using dynamic imaging of hyperpolarized ^{13}C pyruvate.* In Proceedings of the International Society Magnetic Resonance in Medicine 21 (2013) (#3930), Salt Lake City, Utah, USA.

E. Mariotti, K. Weiss, J.T. Dunn, M.R. Orton, A. Sigfridsson, S. Kozerke, T.R. Eykyn. *Evaluation of Robustness of Kinetic Analysis to Noise for Hyperpolarized [1-^{13}C] Pyruvate Metabolism in the Heart*. In Proceedings of The Third International Workshop on Metabolic Imaging, Philadelphia, PA, 2012.

D. K. Hill, **E. Mariotti**, M. R. Orton, J. K. R. Boult, Y. Jamin, S. P. Robinson, M. O. Leach, Y-L. Chung, T. R. Eykyn. *Model Free approach to Kinetic Analysis of Real*

Time hyperpolarised ^{13}C MRS Data-Area under Curve. In Proceedings of The Third International Workshop on Metabolic Imaging, Philadelphia, PA, 2012.

E. Mariotti, K. Weiss, J.T. Dunn, M.R. Orton, S. Kozerke, R. Southworth, Thomas R. Eykyn. *Kinetic Analysis of Hyperpolarized [1-^{13}C] pyruvate metabolism in the isolated perfused rat heart.* In Proceedings of 3rd International Symposium on Dynamic Nuclear Polarization 2011, Lausanne, Switzerland.

K. Weiss, **E. Mariotti**, L. Wissmann, R. Southworth, T.R. Eykyn, S. Kozerke. *Echo planar spectroscopic imaging of hyperpolarised 1-^{13}C pyruvate in perfused rat heart.* In Proceedings of 3rd International Symposium on Dynamic Nuclear Polarization 2011, Lausanne, Switzerland.

E. Mariotti, K. Weiss, J.T. Dunn, N.H.M. Hogg, D.K. Hill, M.R. Orton, S. Kozerke, R. Southworth, T.R. Eykyn*. Kinetic Analysis of Metabolism in isolated perfused heart using Hyperpolarised 1-^{13}C Pyruvate.* In Proceedings of BHF/MEC meeting, Royal Pharmaceutical Society 2011, London.

E. Mariotti, J. Dunn, N. Hogg, R. Southworth, T.R. Eykyn, *Kinetic Analysis of Blood Metabolism using Hyperpolarised 1-^{13}C Pyruvate.* In Proceedings of 20th British Chapter ISMRM Postgraduate Symposium 2011, Cambridge.